

**UNIVERSITE DE YAOUNDE I**

\*\*\*\*\*

**FACULTE DES SCIENCES**

\*\*\*\*\*

**CENTRE DE RECHERCHE ET  
DE FORMATION DOCTORALE  
EN SCIENCES, TECHNOLOGIE  
ET GEOSCIENCES**

\*\*\*\*\*

**UNITE DE RECHERCHE ET DE  
FORMATION DOCTORALE EN  
GEOSCIENCES ET  
APPLICATIONS**



**THE UNIVERSITY OF YAOUNDE I**

\*\*\*\*\*

**FACULTY OF SCIENCE**

\*\*\*\*\*

**POSTGRADUATE SCHOOL FOR  
SCIENCE, TECHNOLOGY AND  
GEOSCIENCES**

\*\*\*\*\*

**DOCTORATE RESEARCH UNIT  
FOR GEOSCIENCES AND  
APPLICATIONS**

**DEPARTEMENT DES SCIENCES DE LA TERRE**

*DEPARTMENT OF EARTH SCIENCES*

**LABORATOIRE DE GEOSCIENCES DES FORMATIONS PROFONDES ET APPLICATIONS**

*LABORATORY OF GEOSCIENCES FOR INTERNAL FORMATIONS AND APPLICATIONS*

**PETROLOGY OF METAVOLCANOSEDIMENTARY  
ROCKS AND ASSOCIATED IRON FORMATIONS OF  
THE ANYOUZOK IRON DEPOSIT, AKOM II AREA,  
SOUTH CAMEROON**

*Thesis submitted in fulfilment of the requirements for the degree of  
Doctor of Philosophy (Ph. D)*

*Speciality: Petrology and Structural Geology*

By

**ISAAC SWIFFA FAJONG**

*Reg. Number 05Y345*

*(M.Sc. Earth Sciences)*

Co-supervised by

**NZENTI Jean Paul**

*Professor*

University of Yaounde I

**SUH CHEO Emmanuel**

*Professor*

University of Bamenda



**Year 2023-2024**



**DEPARTEMENT DES SCIENCES DE LA TERRE**  
**DEPARTMENT OF EARTH SCIENCES**

**UNITE DE FORMATION ET DE RECHERCHE DOCTORALE**  
**EN GEOSCIENCES ET APPLICATIONS**

**ATTESTATION DE CORRECTION DE THESE DE DOCTORAT/Ph.D**

\*\*\*\*\*

**Option : Géosciences des Formations Profondes et Applications**  
**Spécialité : Pétrologie et Géologie Structurale**

**Nom et Prénoms du candidat : ISAAC SWIFFA FAJONG**

**Matricule : 05Y345**

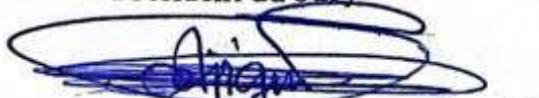
**Titre de la Thèse: "PETROLOGY OF METAVOLCANOSEMENTARY ROCKS AND ASSOCIATED IRON FORMATIONS OF THE ANYOUZOCK IRON DEPOSIT, AKOM II AREA, SOUTH CAMEROUN".**

**Date de soutenance : Mercredi, 29 Mai 2024.**

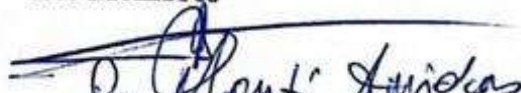
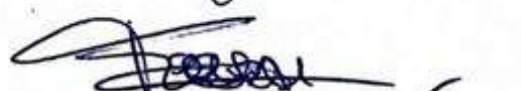
Nous, membres du jury, après avoir lu le document qui nous a été présenté, attestons que le candidat a effectué toutes les corrections, conformément aux observations formulées lors de la soutenance.

En foi de quoi, la présente Attestation de correction lui est délivrée, pour servir et valoir ce que de droit.

**Le Président du Jury**

  
NDJIGUI Paul Désiré

**Les Membres**

  
P. G. M. L. Amadou  
  
R. YONGUE

## DEDICATION

This thesis is dedicated to the memory of my parents, Deborah and Amos Fajong.

## ACKNOWLEDGEMENTS

Blessed be the name of the Lord Almighty, great things He hath done! I am indebted to Professor **Jean Paul Nzenti**, Head of Laboratory, for the patience, persistent coaching and encouragements over the years that enabled me to successfully go through this study program. I appreciate the tireless efforts of Professor **Suh Emmanuel Cheo.**, who co-supervised this work. Many thanks to the Head of Department of Earth Sciences, University of Yaounde I, Professor **Paul Désiré Ndjigui** for the multiple counsels and for creating the favourable environment for study and collaboration. I am equally grateful to the teaching core (lecturers) of the Department of Earth Sciences for their availability and careful guidance over the years. I am thankful to Professor **Ganno Sylvestre** and Dr. **Nzepang Tankwa Marvine** for proof-reading the manuscript. I acknowledge the International Mining and Infrastructure Corporation (IMIC) for logistic support and for the provision of samples. I am particularly thankful to Mr. **Steve Blunsdon** and Mr. **Khalifa Beyah**, the respective Chief operation officers for Afferro Mining Inc. and IMIC, for providing logistic support. I appreciate my seniors and mates of the Laboratory, Professors **Evine Laure Njiosseu**, **Kouankap Nono Djibril**, and **Ndema Mbongué Jean Lavenir**, Drs. **Ekah Ndime**, **Nga Essomba Philomene**, **Takoudjo Jonas**, **Tchatchueng Robinson**, **Kamguia Woguia Brice**, **Mvodo Hermine**, **Hamdja Ngniri Alexis**, **Djoukouo Soh Arlette**, **Ayonta Patrick** and also **Ngong Divine**, **Sepwouo Alex**, **Kouayep Lysianne**, **Suiven Terrence**, **Rosita**, and **William**, for the advice and assistance that helped in the realization of this work. I thank my friends and collaborators, Drs. **Donald Fossi Hermann**, **Moudioh Cyriel** and **Soh Tamehe Landry** whose comments and suggestions greatly improved on this work. I appreciate my sisters, brothers and their spouses for their continuous and sacrificial support, love and encouragements throughout the course of this work; indeed, “family is gold”. I am grateful to Reverend Dr. **Joe Jikong** of Etoug Ebe Baptist Church, Yaounde and to my father-in-law, Daddy **Mfon Patrick**, for your fervent prayers. I recognize the immeasurable contribution, love and support of my beloved wife, Mrs. **Olive Fajong**. It would have been impossible to realize this work, without you taking care of our home and children, **Danny**, **Keila**, **Shade** and **Seelay**. Finally, I am grateful to all those who in one way or the other contributed to the success of this work, but whose names have not been mentioned here. You are highly acknowledged and appreciated.



## TABLE OF CONTENTS

TABLE OF CONTENTS.....	iii
List of figures.....	vi
List of tables.....	viii
List of abbreviations .....	ix
ABSTRACT.....	x
RÉSUMÉ .....	xi
GENERAL INTRODUCTION.....	1
I. Background and Problem statement .....	2
II. Objectives.....	4
III. Thesis structure .....	4
CHAPTER I. GEOGRAPHIC AND GEOLOGIC SETTING .....	6
I. 1. Geographic Setting .....	7
I.1.1. LOCATION AND ACCESSIBILITY .....	7
I.1.2. CLIMATE .....	8
I.1.3. VEGETATION .....	8
I.1.4. FAUNA .....	9
I.1.5. GEOMORPHOLOGY .....	9
<i>I.1.5.1. Orography</i> .....	9
<i>I.1.5.1. Hydrography</i> .....	10
I.1.6. SOIL .....	11
I.1.7. POPULATION AND HUMAN ACTIVITY .....	12
I.2. Geological Setting .....	13
1.2.1. PANAFRICAN NORTH EQUATORIAL FOLD BELT (PANEFB).....	14
1.2.2. CONGO CRATON (CC) .....	17
1.2.3. GEOLOGY OF THE IRON ORE DEPOSIT .....	20
CHAPTER II. MATERIAL AND METHODS .....	22
II.1. Desktop / Preliminary studies .....	23
II.2. Field work .....	23

II.3 Laboratory studies .....	24
II.3.1. LITHOSTRATIGRAPHY AND PETROGRAPHIC STUDY .....	24
II.3.2. MINERALOGICAL ANALYSIS .....	25
II.3.3. GEOCHEMICAL ANALYTICAL METHODS .....	25
CHAPTER III. LITHOSTRATIGRAPHY AND PETROGRAPHY .....	27
III.1. Lithostratigraphy .....	28
III.1.1. NORTHERN PROSPECT .....	29
a) <i>Iron formations unit</i> .....	29
b) <i>Country rock unit</i> .....	32
III.1.2 SOUTHERN PROSPECT .....	32
a) <i>Iron formation unit</i> .....	32
b) <i>Country rock unit</i> .....	33
III.2 Petrographic study .....	36
III.2.1 PYROXENE BIOTITE GNEISS .....	36
III.2.2 EPIDOTE GNEISS .....	39
III.2.3. MAFIC GRANULITE .....	39
III.2.4. <i>GARNET AMPHIBOLITE</i> .....	42
III.2.5. <i>IRON FORMATIONS</i> .....	45
a) <i>Banded iron formations (BIFs)</i> .....	45
b) <i>Sheared banded iron formations (SBIFs).</i> .....	47
III.2.8. ORE TYPES.....	49
III.3. Mineralogy of IFs .....	50
III.3.1 XRD STUDIES FOR BIF .....	50
III.3.2 XRD STUDIES FOR SBIF.....	50
III.4. Structural aspects of the Anyouzok iron deposit .....	51
CHAPTER IV. GEOCHEMISTRY .....	56
IV.1. Host rock geochemistry: Nature of Protolith.....	57
IV.2. Geochemical properties .....	59
IV.2.1. METAVOLCANIC ROCKS .....	59
IV.2.1.1. <i>Mafic granulite</i> .....	59
IV.2.1.2. <i>Garnet amphibolite</i> .....	63

IV.2.2. METASEDIMENTARY ROCKS .....	64
IV.2.2.1. <i>Pyroxene biotite gneiss</i> .....	64
IV.2.3. <i>Iron formations</i> .....	69
CHAPTER V. INTERPRETATION AND DISCUSSION .....	74
V.1. Lithology .....	75
V.2. Alteration, metamorphism, and element mobility assessment.....	75
V.2.1. EFFECTS ON METAVOLCANIC ROCKS.....	76
V.2.2. EFFECTS ON CLASTIC METASEDIMENTARY ROCKS.....	77
V.2.3. EFFECTS ON IFs .....	78
V.3. Petrogenesis and tectonic setting of Anyouzok country rocks .....	79
V.3.1. METAVOLCANIC ROCKS.....	79
V.3.1.1. <i>Petrogenesis</i> .....	79
V.3.1.2. <i>Tectonic setting</i> .....	80
V.3.2. METASEDIMENTARY ROCKS .....	82
V.3.2.1. <i>Weathering and sediment maturity</i> .....	82
V.3.2.2. <i>Sediment Provenance</i> .....	82
V.3.2.3. <i>Tectonic setting</i> .....	83
V.4. Origin and depositional environment of the Anyouzok IFs.....	83
V.4.1. DETRITAL INPUT ASSESSMENT DURING THE ANYOUZOK IF DEPOSITION.....	83
V.4.2. SEAWATER AND HYDROTHERMAL FLUID CONTRIBUTION .....	86
V.4.3. PALEOREDOX STATE OF IF .....	88
V.4.4. DEPOSITIONAL SETTING.....	88
V.5 Comparison of the Northern and the southern prospects.....	89
V.6. Ore potential, environmental and socio-economic considerations .....	90
V.6.1. ORE POTENTIAL OF THE ANYOUZOK IRON ORE DEPOSIT .....	90
V.6.2. ENVIRONMENTAL AND SOCIO-ECONOMIC CONSIDERATIONS OF THE ANYOUZOK IRON ORE DEPOSIT.....	91
GENERAL CONCLUSION .....	92
REFERENCES .....	95
APPENDIX.....	A

## List of figures

<b>Figure 1.</b> Location map of study area. ....	7
<b>Figure 2.</b> Ombrothermic diagram applying data from Eseka meteorological station. ....	8
<b>Figure 3.</b> Block diagram of study area. ....	10
<b>Figure 4.</b> Hydrographic map of study area. ....	11
<b>Figure 5.</b> Reconstruction map of the Panafrican NE-Brazilian and West Africa domain, showing the continuity between the Sergipano and North Equatorial Range. ....	13
<b>Figure 6.</b> Geological map of Cameroon showing the location of the Anyouzok area and the main tectonic domains. ....	16
<b>Figure 7.</b> Sketch geological map of SW Cameroon. ....	20
<b>Figure 8.</b> Samples and drillholes location map of study area showing the northern and southern prospects. ....	29
<b>Figure 9.</b> Anyouzok northern prospect ....	31
<b>Figure 10.</b> Anyouzok southern prospect. ....	34
<b>Figure 11.</b> Petrographic features of pyroxene biotite gneiss. ....	37
<b>Figure 12.</b> Photomicrographs of pyroxene biotite gneiss under crossed polars. ....	38
<b>Figure 13.</b> Photographs of epidote gneiss. ....	40
<b>Figure 14.</b> Photograph of drill core sample and photomicrographs of mafic granulite. ....	42
<b>Figure 15.</b> Drill core sample and photomicrographs of garnet amphibolite. ....	44
<b>Figure 16.</b> Drill core samples and photomicrographs of BIFs. ....	46
<b>Figure 17.</b> Drill core sample and photomicrographs of SBIF. ....	48
<b>Figure 18.</b> Photography of ore types. ....	49
<b>Figure 19.</b> X-ray diffraction spectra for the Anyouzok BIF. ....	51
<b>Figure 20.</b> Structural features in pyroxene biotite gneiss and SBIF ....	52
<b>Figure 21.</b> Brittle deformation (fracturing) in drill core, preserved in SBIF hole TH25 ....	52
<b>Figure 22.</b> Stereonet projection of Anyouzok S <sub>1</sub> /S <sub>2</sub> foliations. ....	53
<b>Figure 23.</b> Sketch geologic map of Anyouzok area. ....	54
<b>Figure 24.</b> Protolith reconstruction and classification of Anyouzok country rocks. ....	57
<b>Figure 25.</b> Classification plots for the Anyouzok rocks. ....	58
<b>Figure 26.</b> Binary plots of major element variations with respect to MgO. ....	59
<b>Figure 27.</b> Binary plots of trace element variations with respect to MgO. ....	61
<b>Figure 28.</b> Anyouzok chondrite-normalised and primitive mantle normalised plots for mafic granulite and garnet amphibolite ....	63
<b>Figure 29.</b> Binary plots of major element variations with respect to Al <sub>2</sub> O <sub>3</sub> . ....	66

<b>Figure 30.</b> Binary plots of trace element variations with respect to Al <sub>2</sub> O <sub>3</sub> .....	67
<b>Figure 31.</b> REE and multi-element plots of Anyouzok pyroxene biotite gneiss.....	69
<b>Figure 32.</b> Binary plots of BIF and SBIF samples for major elements.....	71
<b>Figure 33.</b> Chondrite- (a) and (b) PAAS- normalized REE-Y of the Anyouzok iron formations (BIFs and SBIFs).....	72
<b>Figure 34.</b> Alteration box plot (after Large et al., 2001) for the Anyouzok metavolcanic rocks. ....	77
<b>Figure 35.</b> IFs hydrothermal alteration effect. ....	78
<b>Figure 36.</b> REE (a and c) and multi-element (b and d) diagrams of Anyouzok metavolcanic rocks plotted with rocks from nearby studies for comparison. ....	80
<b>Figure 37.</b> Tectonic discrimination plots of the Anyouzok metavolcanic rocks. ....	81
<b>Figure 38.</b> Tectonic discrimination plots of the Anyouzok pyroxene biotite gneiss. ....	83
<b>Figure 39.</b> Detrital input assessment of the Anyouzok IFs .....	85
<b>Figure 40.</b> Contribution of seawater and hydrothermal fluids in the Anyouzok IFs precipitation.....	87
<b>Figure 41.</b> Whole-rock geochemistry discrimination diagram for BIF, altered BIF, medium- and high-grade ore.....	90

## **List of tables**

<b>Table 1.</b> Table showing rainfall and temperature data for study area (2002 to 2022). .....	8
<b>Table 2.</b> Anyouzok iron deposit drillhole collars .....	28
<b>Table 3.</b> Anyouzok Northern prospect deposit drillhole logging details. ....	30
<b>Table 4.</b> Anyouzok southern prospect deposit drillhole logging details. ....	33
<b>Table 5.</b> Table showing sample ID, drillhole code and other sample parameters.....	35
<b>Table 6.</b> Petrographic characteristics of the Anyouzok geologic formations .....	48
<b>Table 7.</b> Table summarising characteristic peak values for all minerals detected through X-ray diffraction (XRD) for BIF and SBIF. ....	50
<b>Table 8.</b> Major element (wt.%) compositions of the Anyouzok metavolcanic rocks. ....	58
<b>Table 9.</b> Trace element (ppm) compositions of the Anyouzok metavolcanic rocks. ....	60
<b>Table 10.</b> Rare earth element (ppm) compositions and element ratios of the Anyouzok metavolcanic rocks. ....	62
<b>Table 11.</b> Major elements (wt%) and trace elements (ppm) compositions of the Anyouzok pyroxene biotite gneiss. ....	65
<b>Table 12.</b> Rare earth elements (ppm) compositions of the Anyouzok pyroxene biotite gneiss.	68
<b>Table 13.</b> Major elements (wt.%) and trace elements (ppm) compositions of the Anyouzok Iron formations. ....	70
<b>Table 14.</b> Rare earth element (ppm) compositions of the Anyouzok Iron formations.....	72



## **List of abbreviations**

### **List of mineral abbreviations** (after [Whitney and Evans, 2010](#))

Act: actinolite	Tr: tremolite
Afs: alkali feldspar	
Aln: Allanite	
Amp: amphibole	
Bt: biotite	
Cal: calcite	
Chl: chlorite	
Cpx: clinopyroxene	
Ep: epidote	
Fsp: feldspar	
Grt: garnet	
Hem: hematite	
Hbl: hornblende	
Ilm: ilmenite	
Kfs: K-feldspar	
Mag: magnetite	
Mc : microcline	
Ms : muscovite	
Opq: opaque	
Opx: orthopyroxene	
Or: orthoclase	
Pl: plagioclase	
Py: pyrite	
Qz: quartz	
Rl: rutile	
Ser: sericite	
Spn: sphene (titanite)	

## ABSTRACT

The iron formations of Anyouzok outcrop in the northwest margin of the Congo Craton (CC) in Cameroon and are part of the greenstone belts of the Nyong complex. This work aims at determining the geodynamic context and genetic model of the Anyouzok iron formations and the associated country rocks in an effort to contribute to the overall understanding of the tectonic evolution of the Nyong Complex and the associated iron ore. Drill core logging and field mapping were done to determine lithostratigraphy. From drill core samples, thin and polished sections were observed for petrography. ICP-AES and ICP-MS methods were employed to determine the rock geochemical properties, while XRD studies was used to determine ore mineralogy. This area is essentially made up of a metamorphosed rock unit, comprising iron formations (IFs) and country rocks. The iron formations consist of banded iron formations (BIF) and sheared banded iron formations (SBIF). The country rocks are made up of metasedimentary (pyroxene biotite gneiss) and metavolcanic (mafic granulite and garnet amphibolite) rocks. The metavolcanic rocks generally are interlayered with the iron formations, while the metasedimentary rocks are more frequently encountered as footwall and / or hanging wall. Mineral associations show that the area has been subjected to green schist, amphibolite, and granulite facies metamorphism. Basic structural analyses highlight several deformational phases which involve regional scale folding and shearing. Mafic granulites and garnet amphibolites are of basaltic protoliths. Pyroxene biotite gneiss was derived from greywacke and arkose protoliths, deposited in an active continental margin. The abundance of cavities, higher Fe contents (59.60-55.20 wt%) and the strong positive Eu anomalies ( $(\text{Eu}/\text{Eu}^*)_{\text{SN}}=2.14-3.17$ ) within the SBIFs compared to the BIF (26.05-48.40 wt%) with Eu anomalies of  $(\text{Eu}/\text{Eu}^*)_{\text{SN}}=1.86-2.68$ ). REE signatures indicate the contribution of both seawater and hydrothermal fluids during BIF precipitation. The overall variations in composition of the iron formations of Anyouzok, along with the metasediments primarily constituting the host rocks, and interstratified metavolcanics, reveal that the formations in the study area are of Algoma type and were deposited in a back-arc basin under suboxic to anoxic conditions.

**Keys words:** Petrology; metavolcanosedimentary rocks; iron formations; lithostratigraphy; hydrothermal fluids; back-arc; Anyouzok; Nyong Complex; Congo craton.

## RÉSUMÉ

Les formations ferrifères d'Anyouzok affleurent dans la bordure nord-ouest du craton du Congo (CC) au Cameroun et font partie des ceintures des roches vertes du complexe du Nyong. Ce travail a pour but de déterminer le contexte géodynamique et le modèle génétique des formations ferrifères d'Anyouzok et des roches encaissantes associées afin de contribuer à une meilleure compréhension de l'évolution tectonique du complexe du Nyong et du minerai de fer associée. Les études des carottes et la cartographie sur le terrain ont été effectuées pour déterminer la lithostratigraphie. À partir des échantillons de carottes de forage, des lames minces et les sections polies ont été observées pour la pétrographie. Les méthodes ICP-AES et ICP-MS ont été utilisées pour déterminer les propriétés géochimiques de la roche, tandis que des études XRD ont été utilisées pour déterminer la minéralogie du minerai. Le secteur d'étude est constitué de formations ferrifères et de roches encaissantes. Les formations ferrifères sont composées de formations ferrifères rubanées (BIF) et de formations ferrifères cisailées (SBIF). Les roches hôtes sont faites de roches métasédimentaires (gneiss à pyroxène et biotite) et de roches métavolcaniques (granulite mafique et amphibolite à grenat). Les métavolcanites sont généralement intercalées avec les formations ferrifères, tandis que les métasédiments sont plus fréquemment rencontrés en éponte inférieure et/ou en éponte supérieure. L'étude pétrographique des roches étudiées montrent des associations minérales typiques des faciès schistes verts, amphibolite et granulite. Les analyses structurales mettent en évidence plusieurs phases de déformation montrant des plissements et des cisaillements à l'échelle régionale. Les granulites mafiques et les amphibolites à grenat proviennent des protolites basaltiques. Les gneiss à pyroxène et biotite proviennent des grauwackes et des arkoses, déposés dans une marge continentale active. Des teneurs en Fe plus élevées (59, 60 à 55, 20% en poids), les fortes anomalies en Eu ( $(Eu / Eu^*)_{SN} = 2,14 \text{ à } 3,17$ ) dans les SBIF par rapport aux BIF (26.05-48.40% en poids, les anomalies en Eu de  $(Eu/Eu^*)_{SN}=1.86-2.68$ ). Les signatures des terres rares indiquent la contribution de l'eau de mer et des fluides hydrothermaux lors de la précipitation des BIF. Les variations globales de la composition des formations ferrifères d'Anyouzok, des métasédiments qui constituent principalement les épontes, ainsi que des métavolcanites interstratifiées révèlent que les formations du secteur d'étude sont de type Algoma et se sont déposées dans un bassin arrière-arc dans des conditions suboxiques à anoxiques.

**Mots clés :** Pétrologie ; métavolcanosédiments ; formations ferrifères ; lithostratigraphie ; fluides hydrothermaux ; bassin arrière-arc ; Anyouzok ; complexe du Nyong ; Craton du Congo.

# **GENERAL INTRODUCTION**

## I. Background and Problem statement

The cratonic basement of Cameroon mainly consists of Archean rocks (ca. 3500-2500 Ma; Shang et al., 2004, 2010; Takam et al., 2009; Li et al., 2016; Ndimé et al., 2019; Kamguia Woguia et al., 2022; Kouankap et al., 2022; Mvodo et al., 2022; Toteu et al., 2022; Deassou et al., 2022; Akame et al., 2023), which are associated with Paleoproterozoic rocks (Toteu et al., 1994; Feybesse et al., 1998; Soh Tamehe et al., 2022; Kamguia Woguia et al., 2022). This cratonic basement which constitutes the north western margin of the Congo craton in south Cameroon was reworked during the Eburnean/Transamazonian and Panafrican orogenies (Toteu et al., 1994; Lerouge et al., 2006; Nzepang Tankwa et al., 2020; Djoukouo Soh et al., 2021; Mvodo et al., 2022). It is represented by the Ntem and Nyong Complexes (Maurizot et al., 1986; Nedelec et al., 1990; Tchameni et al., 2001; Penaye et al., 2004; Toteu et al., 2004; Lerouge et al., 2006; Suh et al., 2009; Shang et al., 2010; Soh Tamehe et al., 2022; Owona et al., 2022). The Ntem complex is located to the centre south, while the Nyong complex lies to the south west of Cameroon, all bounded to the north by the Yaounde group (Nzenti et al., 1988; Barbey et al., 1990; Mvondo et al., 2003; Ngnotué et al., 2012), which thrusts southwards onto these complexes (Nzenti et al., 1984; Nedelec et al., 1986; Mvondo et al., 2007; Owona et al., 2012).

Cratonic domains contain greenstone belts which are composed mainly of mafic-ultramafic metamorphosed igneous rocks associated with metapelites, chert, iron formations, and felsic rocks (Polat et al., 2002; Soh Tamehe et al., 2022; Owona et al., 2022). Similarly, the Nyong complex is mostly composed of gneisses which appear locally as grey gneisses of TTG composition, pyroxenites, amphibolites and iron formations (Maurizot et al., 1986; Lerouge et al., 2006; Ndema et al., 2014; Ganno et al., 2015; Soh Tamehe et al., 2022; Owona et al., 2022). This complex has experienced deformation and high-grade metamorphism, rendering the reconstruction of the depositional environment of the hosted IFs difficult. Also, In spite of the extensive studies in the last century, many controversies still persist on their origin as well as on how these formations are upgraded to iron ore (Taylor et al., 2001; Klein, 2005; Suh et al., 2009; Bekker et al., 2010; Duuring and Hagemann, 2013; Hagemann et al., 2016 and references therein). More specifically, most of the earlier studies on iron formations in Cameroon focused more on the use of surface outcrops, for geochemical analysis rendering the interpretations difficult due to the effects of surface weathering on the samples.

As a palliative, several workers worldwide have investigated interbedded metaigneous and/or metasedimentary rocks to better constrain the depositional settings of iron formations

(Wang et al., 2014; El-Shazly et al., 2019; Moudioh et al., 2020; Nzepang Tankwa et al., 2020; Ganno et al., 2015; 2020; Soh Tamehe et al., 2018, 2019, 2022; Moudioh et al., 2021; Djoukouo Soh et al., 2021; Deassou Sezine et al., 2022). In this study, fresh, deep seated diamond drill core samples of IFs, metavolcanic and metasedimentary rocks have been used over surface grab samples, in an effort to get more reliable interpretations on the mode of deposition and palaeoenvironment of the iron formations.

Iron formations (IFs) are Precambrian sedimentary rocks, typically thin-bedded or laminated, containing 15% or more iron of sedimentary origin and commonly but not necessarily containing chert layers (James, 1954). Iron ore is an essential raw material for several industrialization products especially for developing nations. Besides their high economic value in the steel and construction industry, IFs provide invaluable information in the understanding of the evolution of the atmosphere, biosphere, coeval ocean composition and also the origin and growth of continents (Bolhar et al., 2004; Bekker et al., 2010; Thurston et al., 2012; Wang et al., 2014; El-Shazly et al., 2019; Moudioh et al., 2020; Gourcerol et al., 2022). Early classifications divided IFs into Algoma- and Superior-types (Gross, 1980). Superior-type IFs are extensive, closely associated with clastic to carbonate rocks, and were deposited in near-shore continental shelf environments with no direct correlation to volcanic rocks (Gross, 1980). Conversely, Algoma-type IFs are less extensive, closely affiliated with volcanic rocks in greenstone belts and were generally deposited in intracratonic rifts or in back-arc/arc basins (Gross, 1980). Texturally, iron formations were also divided into two groups: banded iron formation (BIFs) widespread in Archaean to early Paleoproterozoic successions, and granular iron formations (GIFs), much more common in Paleoproterozoic successions (Bekker et al., 2010).

In spite of the fluctuations in the price of iron ore in the world market, and a consequent instability in activities in the iron ore industry, iron ore remains a valid raw material for the steel and related industries which are indispensable, particularly for emergent nations like Cameroon. Industries and policy makers are getting more interested in low grade iron ore whose nature, mode of emplacement and enrichment processes are still less well known. In Cameroon, IFs are mainly found within the Nyong and Ntem Complexes (Suh et al., 2008, 2009; Chombong and Suh, 2013; Ganno et al., 2015, 2016, 2017; Chombong et al., 2017; Teutsong et al., 2017; Ndime et al., 2018, 2019; Soh Tamehe et al., 2018, 2019, 2022; Moudioh et al., 2020; Nzepang Tankwa et al., 2020; Djoukouo Soh et al., 2021), which are still not well understood. Consequently, it was deemed necessary to search for answers to the following questions:



1. What is the lithostratigraphy of the Anyouzok area and how is the iron ore emplacement related with the country/host rocks?
2. What is the nature of the Anyouzok iron ore?
3. What is the relationship between banded iron formations and the sheared banded iron formations?
4. Are there any identifiable clues to ore enrichment related processes?
5. What are the source rocks and the palaeoenvironment of the Anyouzok rocks?

This study therefore provides a comprehensive geochemical dataset for IFs and interbedded metavolcanic and metasedimentary rocks which were intercepted in drillholes of the Anyouzok iron ore deposit. Lithostratigraphy and petrography are presented, in combination with bulk-rock major, trace and rare earth elements (REE) geochemistry, with the aim of determining the origin and depositional environment of the Anyouzok IFs, which is important for the understanding of the Nyong Complex geodynamic evolution.

## **II. Objectives**

The overall objective of this study is to determine the Petrogenetic characteristics of the metavolcano-sedimentary rocks and their relationship with associated iron formations within the Anyouzok area. The specific objectives of this work are to:

- Carry out geological mapping of the area;
- Deduce the origin and evolution of the crustal material and the geotectonic context through their geochemical characteristics;
- Elucidate the origin of IFs and identify possible ore re-concentration processes.

## **III. Thesis structure**

This thesis begins with an introduction and is made up of five chapters as follows:

- chapter one is the geographical and geological settings. Under the geographical setting, the location and accessibility of the study area are illustrated by way of location and topographic maps. Here, climate and vegetation of the Ntem area, the relief and drainage of the area are also presented. It ends with presentation of soil, human and mining activities. Under the geological setting, there is an overview of the regional geology, as well as the geology of the iron ore deposit;

- chapter two focuses on the material and methods applied on the field and in the laboratory. The field methods include desktop studies where several maps were studied, and

samples collected. The laboratory methods involved describing all the processes of sample preparation for thin/polished sections and geochemical analyses;

- chapter three deals with the lithostratigraphy, petrography, ore mineralogy, structural studies and microstructures;

- chapter four presents the geochemical features of the Anyouzok area iron formations and their host rocks;

- chapter five presents the interpretations and discussions;

The thesis ends with a general conclusion and recommendations for further studies with respect to the research area.

# **CHAPTER I. GEOGRAPHIC AND GEOLOGIC SETTING**

## Introduction

This chapter locates the study area within the natural setting, highlighting the associated physical characteristics such as the climate, vegetation, and soil. It also presents the human and economic contexts as well as the local and regional framework.

### I. 1. Geographic Setting

#### I.1.1. Location and accessibility

The study area is located in Akom II subdivision of the Ocean Division, South Region of the Republic of Cameroon. More specifically, it is found between longitudes 10°24'E to 10°29'E and latitudes 2°52'N to 2°58'N, covering a total surface area of about 120 km<sup>2</sup> (Fig. 1). It is 266 Km away from Yaoundé and 75 Km from the Kribi deep seaport. The Anyouzok area can be accessed by passing through 157 Km of tarmac road from Yaoundé to Ebolowa, 82 Km of fairly good earth road from Ebolowa to Akom II and another 27 Km of earth road from Akom II to the site.

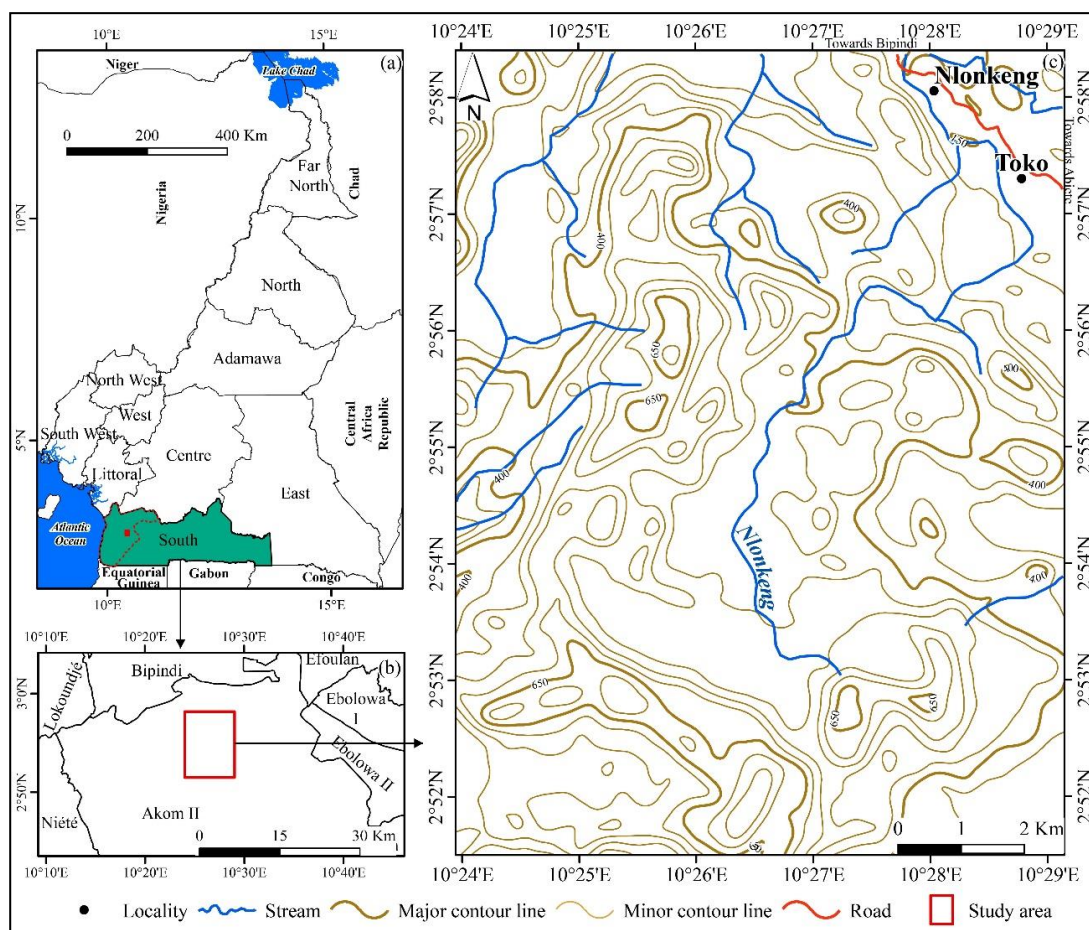


**Figure 1.** Location map of Study area. a) Cameroon administrative map locating the South region; b) Location of the study area within the Ocean Division administrative map; c) Topographic map of the study area; Extracted from the topographic map of Kribi (sheet NB32III) and SRTM image N°f03\_n002e010.

### I.1.2. Climate

Anyouzok falls within the equatorial climate of the Guinea subtype (Sighomnou, 2004). In the last two decades (2002 to 2022), the temperature and rainfall measurements registered from the Eseka meteorological station were as on table 1. According to this data, the average annual precipitation amounts to 2,273 mm and the temperature varies from 23.5°C to 25.9°C. The average annual temperature is 24.7°C. From the ombrothermic diagram, the region is subject to four seasons (Fig. 2):

- A long rainy season (August to November);
- A rainy season (March to June);
- A short dry season (December to February);
- A very short dry season (July).

**Table 1.** Table showing rainfall and temperature data for study area (2002 to 2022).

Month	Jan	Feb	Mar	Apr	May	Jun	Jul	Aug	Sep	Oct	Nov	Dec	Average
Precipitation (mm)	60.9	94.8	193.8	232.9	268.7	181.9	83.9	137.6	330	412	205.9	70.6	189.41
Temperature (°C)	25.5	25.9	25.2	25.4	25.2	24.4	23.5	23.5	23.9	24.2	24.8	25	24.70

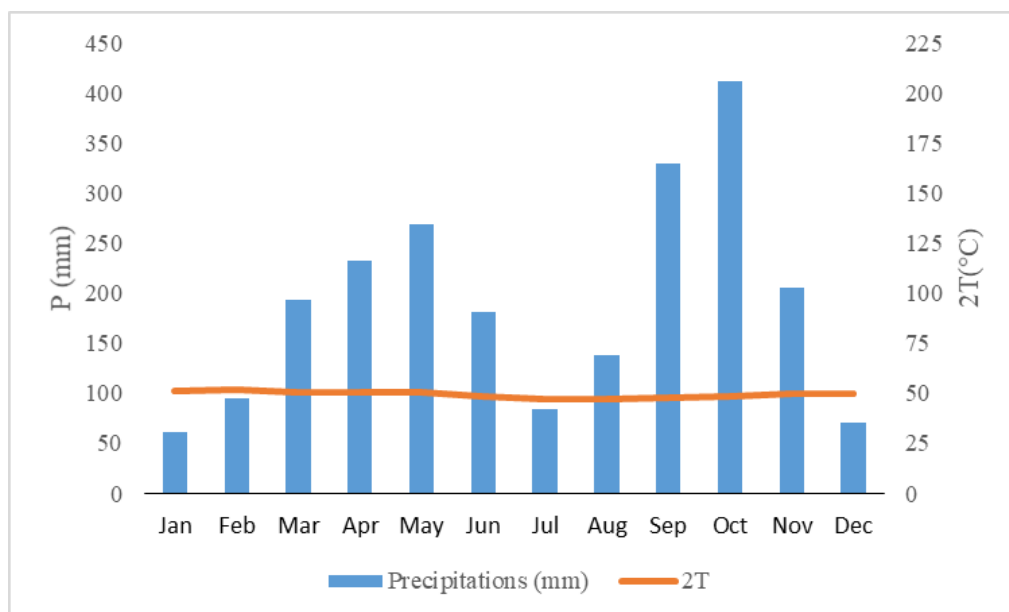


**Figure 2.** Ombrothermic diagram (after Bagnouls and Gaussen, 1957) applying data from Eseka meteorological station.

### I.1.3. Vegetation

The Anyouzok area in south Cameroon, is found in the equatorial evergreen rainforest. Primary forest is encountered to the northern section of the study area, with canopy heights of 15-20 m (Onguene and Kuyper, 2001). According to Letouzey (1985), the

primary forest is of the Atlantic Biafran type. Old secondary forests are located on slopes of hills and valleys, growing on shallow lateritic soils. The secondary forest contains numerous patches of wooden savannah and is characterized in places by the presence of species from savannah zones such as *Raphia regalis* (Letouzey, 1985). Swampy areas are also covered by *Raphia farinifera* (Raffia palm) bushes and *Bambusa tulda* (Indian Bamboo). Numerous tree species encountered include *Afzelia pachyloba* (White Doussie), *Lophira alata* (Azobe), *Baillonella toxisperma* (Moabi), *Entandrophragma cylindricum* (Sappeli), *Enantia chlorantha* (Yellow Moambe), *Irvingia gabonensis* (Bush mango), etc. Critically endangered and endangered categories are *Microbelinia bisculcata* and *Diospyros crassiflora* respectively (Onguene and Kuyper, 2001).

#### I.1.4. Fauna

The fauna of the study area is representative of the biogeographic characteristics of the forest zones. Due to the high undergrowth the equatorial forest provides a favourable habitat for abundant wildlife. Species encountered include reptiles and amphibians like *Vipera berus* (vipers), *Ophiophagus hannah* (cobra), *Dendroaspis angusticeps* (green mamba), *Conraua goliath* (frogs) *Didynamipus sjostedti* (toads), *Varanus ornatus* (forest Lizards) and *Kinixys erosa* (the Serrated Hinge-backed Tortois). Small mammals include *Antilocapra americana* (antelopes), *Thryonomys swinderianus* (cane rats), *Scalopus aquaticus* (moles), *Felis silvestris* (wildcat), *Erethizon dorsatum* (porcupine) etc. Medium and large size mammals present in this area tend to concentrate around the Campo-Ma'an National Park and include *Loxodonta africana* (elephants), *Syncerus caffer* (buffalos), *Gorilla gorilla* (Gorillas), *Pan troglodytes* (Chimpanzees), *Panthera pardus* (Panthers) and *Manis gigantea* (Giant Pangolin). Bird species include *Psittacus erithacus* (parrot), *Ramphastos toco* (toucan), *Perdrix perdrix* (the partridge) and *Accipitridae* (the eagle), which are the most represented bird species. The numerous rivers and streams flowing through this area are host to several and varied aquatic organisms which include *Hemichromis elongatus* (bony fish), *Panulirus Cygnus* (crayfish) and *Madagapotamon humberti* (crabs). Endangered species include the monkeys, parrots, the giant pangolina and the elephants.

#### I.1.5. Geomorphology

##### I.1.5.1. Orography

Southern Cameroon is relatively flat, with mean altitudes between 600 m and 700 m above sea level (Segalen, 1967). Areas with altitudes < 600 m are generally confined in



swampy U-shaped valleys that are interconnected into a dense dendritic hydrographic network (Fig. 3). Areas with altitudes greater than 700 m represent residual massifs with limited aerial extents and have concave rounded summits and convex steep to very steep slopes. The relief in Anyouzok is marked by sub-circular and elongated hills, all with steep slopes. The rounded hills are symmetrical, while the elongated hills are asymmetrical (Fig. 3).

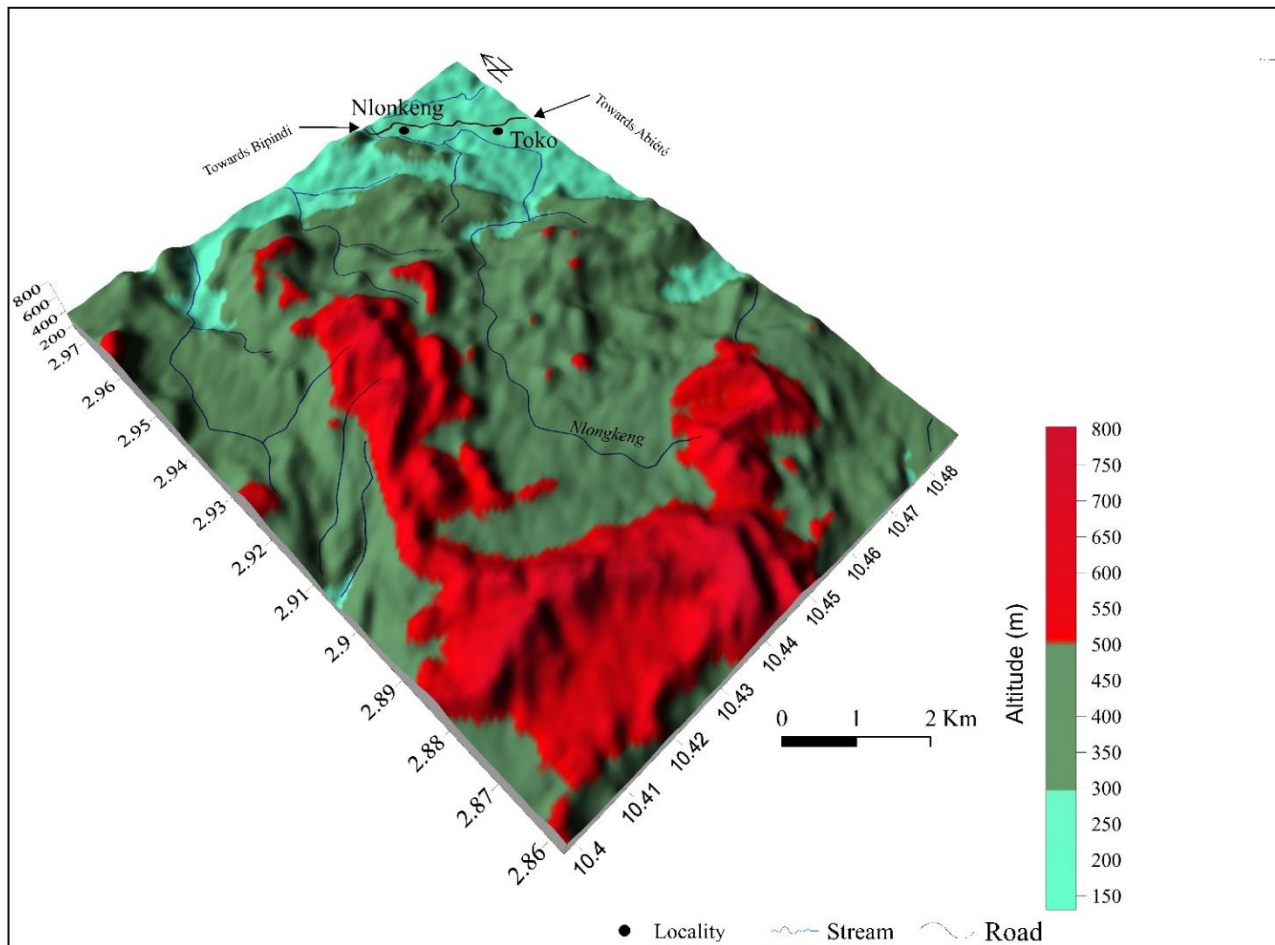


Figure 3. Block diagram of study area.

#### 1.1.5.1. Hydrography

South Cameroon is drained by two basins, namely the Congo and coastal river basins. Anyouzok area falls within the coastal river basin and consists of many streams which tend to flow in the SSW – NNE to NNW-SSE direction. One of the main rivers that drains this area is river *Nlongkeng* (Fig. 4). The streams are fed by the heavy rains that characterize the area. This high drainage intensity results in very high relative humidity which is further enhanced by low permeability of the soils which are underlain by shallow crystalline rocky formations.

Consequently, the stream and river flow levels are directly proportional to the precipitation with maximum flow rates in October and minimum in January.

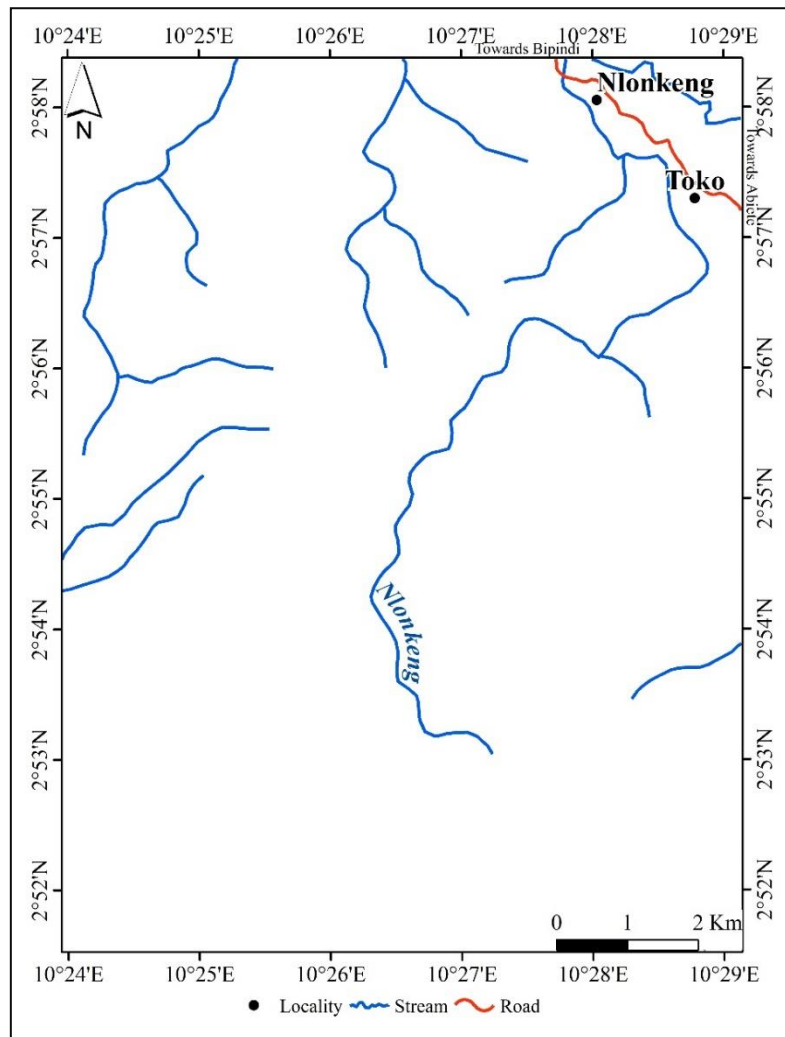


Figure 4. Hydrographic map of study area.

#### I.1.6. Soil

The development of the Anyouzok soil profile is generally favoured by a good drainage system in the humid tropical climate through the complete leaching of primary aluminosilicate minerals. They are developed on various parent rocks including iron formations (Ndjigui et al., 2013; Odigui Ahanda et al., 2019). However, unlike the deeply weathered horizons of neighbouring profiles, the Anyouzok profile is relatively shallow, averagely ranging from 10 to 20 m. This could be attributed to the nature of the protolith, topography and ground water dynamics (Odigui Ahanda et al., 2019).

#### I.1.7. Population and human activity

The South Region is the least populated Region of Cameroon with an estimated population of 634, 655 in 2005, rising to 745, 198 in 2015. The South Region accounts for 3.6% of Cameroon's total population with a population density of 13.4 inhabitants per km<sup>2</sup>. The populations for the Akom II and Bipindi Subdivisions were recorded at 7 544 and 13 257 respectively (RGPH, 2005). The surveys undertaken for the villages associated with the study area indicated a population of 4,543.

The populations of Bipindi and Akom II sub-divisions were estimated in 2005 at 14,118 and 8,802 inhabitants respectively. These populations are mainly rural youth and distributed over the 28 villages in the Bipindi subdivision and 55 villages in the Akom II subdivision. The area is made up of two main population groups, namely the pygmies and the Bantous. Each of these groups is subdivided into ethnic populations, clans and lineages (families). The indigenous Pygmies who were the earliest occupants of the forest are made up of the Bagyeli and the Bakola, while the Bantous are made up of the Bulu of Akom II subdivision, the Ngoumba, the Bulu and the Fang in Bipindi subdivision who live in harmony. The oral history of the people holds that the people occupying this area came from a diverse geographic origin. Though the pygmies constitute a minority, they were the first and therefore the oldest settlers in the area. The Ngoumbas originated from Congo while the Fang came from Gabon and Equatorial Guinea. The Bulus are of dual origin; one from the Adamawa and the other from the Central African Republic (CAR). Also included amongst these major groups are people from other parts of Cameroon who are transferred mainly to Akom II and Bipindi sub divisional headquarters for work purposes. The settlements are either in rural or semi-rural areas. In the rural areas, it is characterised by low population density and linear settlement along the roads. The semi-rural areas (Akom II and Bipindi) are characterized by a concentration of social infrastructure. Main economic activities are of the primary sector: agriculture (subsistence crops, e.g., cocoa), hunting, fishing, forest exploitation, and artisanal gold exploitation. The only mining activity recorded around this area till present is gold panning (artisanal mining). Gold panning has been one of the key activities in the area over the last decade. It is more intense around the Akom II subdivision (Nlonkeng and Toko villages). The exploitation is done along river and stream channels on stream sediments.

The Akom II area has a fairly good network infrastructure. The tarmac road from Yaoundé ends at Ebolowa. However, Ebolowa – Akom II is linked by laterite graded road which gets difficult sometimes in the rainy season. The villages are linked by road pavements

which are mostly accessible by motor bikes but are better in the dry seasons. Akom II centre, the seat of the sub-divisional headquarters is covered by telephone networks. Internet communication is further enhanced by the availability of optical fibre network. The area also happens to be a rail corridor for the access to the Kribi deep sea port thereby presenting promising communication options.

## I.2. Geological Setting

The Precambrian basement complex of Cameroon has recorded crustal evolution from the Mesoarchean to the Neoproterozoic, and consists of two major lithostructural units, namely, the Congo Craton (CC) and the Panafrican North Equatorial Fold Belt (PANEFB). The PANEFB is the major orogenic belt of central Africa, extending from Nigeria to the west, to Sudan and Uganda to the east (Fig. 5., [Casting et al., 1994](#)).

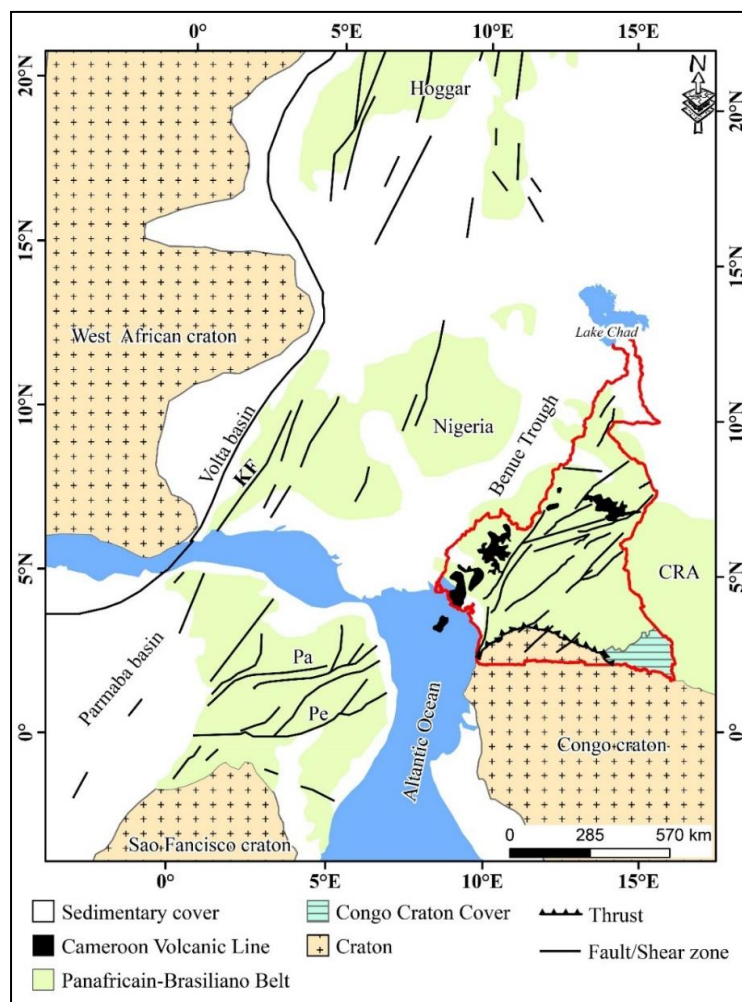


**Figure 5.** Reconstruction map of the Panafrican NE-Brazilian and West Africa domain, showing the continuity between the Sergipano and North Equatorial Range ([Casting et al., 1994](#)). Pe: Permian Shear Zone; Pa: Patos Shear Zone; KF: Kandi Fault.

### 1.2.1. Panafrican North Equatorial Fold Belt (PANEFB)

The PANEFB otherwise known as the Central African fold belt (CAFB) is an E-W oriented orogeny. In Cameroon, it has been reported by several authors (Nzenti et al., 1994, 2006; Ngnotué et al., 2000, 2012; Toteu et al., 2004; Nlomngan et al., 2019), with three distinct major geodynamic domains, namely, the northern domain, the central domain and the southern domain (Fig.6).

- **The northern domain** extends from the south of Poli to the extreme north of Cameroon (Penaye et al., 2006). It contains mostly of NE-oriented batholiths (gabbro, diorite, tonalite, trondhjemite, Panafrican granodiorite and monzodiorite), as well as the poli, Rey Bouba and Bibemi Zalbi intracontinental basins (Fig. 6). These batholiths are made up of pre-, syn-, and post-tectonic granitoids (Penaye et al., 2006; Houketchang Bouyo et al., 2016; Nomo Negue et al., 2017, Ngounouno et al., 2022). The ages of emplacement for the pre-, syn- and post-tectonic granitoids are between 735 and 670 Ma, 660 and 610 Ma and 600 and 560 Ma respectively (Penaye et al., 2006; Houketchang Bouyo et al., 2016; Nomo Negue et al., 2017; Hamdja Ngoniri et al., 2021). The intracontinental basins, consisting of Neoproterozoic schist and low to high grade gneisses of mafic to felsic, volcanic and sedimentary origins were dated (Toteu et al., 2006; Sep Nlomngan et al., 2019) at about 830 to 665 Ma (Poli basin), 670 to 634 (Rey Bouba basin) and 777 to 700 Ma (Bibemi Zalbi basin). The northern domain is affected by three to four deformation phases (Nzenti et al., 1992, 1999; Nlomngan et al., 2021, Ngounouno et al., 2022).

- **The central domain** is intermediary, linking the northern to the southern domain and extends from the south of Bafia to the South of Poli (Fig. 6). It is marked principally by several regional scale strike-slip faults, by the abundance of more or less deformed syn- to post-tectonic granitoids and by Paleoproterozoic relics of high grade continental crust (Tanko Njiosseu et al., 2005; Nzenti et al., 2007; Ganwa et al., 2016), intruded by syntectonic, high-K plutonic rocks of calc-alkaline affinity during the Neoproterozoic (Nzolang et al., 2003; Nzenti et al., 2006; Njiekak et al., 2008; Kouankap Nono et al., 2010). Several authors have reported three phases of ductile deformation (Toteu et al., 2001 ; Ngako et al., 2003; Tanko Njanku et al., 2006; Nzenti et al., 1994, 1998, 1999, 2007; Tchakounte et al., 2007; Kankeu, 2008). More recently (Ganno et al., 2010; Saha-Fouotsa et al., 2019; Fozing et al., 2021) distinguished four deformation phases accompanied by major strike-slip faults, namely:- the central Cameroon shear zone (CCSZ), the Fouban-Tibati-Banyo shear zone (FTBSZ), which is seen as a transcurrent ductile fault (Nzenti et al., 1988; Ngako et al., 1991, 2003;

Nomo Negue et al., 2017), the Betare Oya fault (BOF) which is considered as a ductile-fragile deformation (Kankeu et al., 2010) and the Sanaga Fault (SF), considered as a fragile deformation (Dumont, 1986). According to some authors (Toteu et al., 2001, 2004; Schmus et al., 2008; Ganwa et al., 2016), the Tibati-Banyo shear zone is considered as a major unconformity, separating the Northern domain from the central. More recently, Tchakounté et al. (2017) from U-Pb on zircon dating showed that the protoliths of some igneous-derived gneisses from around the Adamawa-Yade frontiers were emplaced during distinct periods. The Makenene TTG suites of date from 3.0-2.5 Ga and was affected by partial fusion at 2.08-2.07 Ga during the Eburnean orogeny and by a magmatic event with metamorphic imprints at 0.64-0.61 Ga, during the Panafrican orogeny. The Maham dioritic gneisses were put in place at 2.07 Ga. The younger magma derived gneisses of Bafia, Bep and Ngaa-Bappe intruded at 0.64-0.63 Ga.

- **The southern domain** represented by the Yaounde group is bounded to the south by the Congo craton (Fig. 6). At the regional scale, two major lithological assemblages are defined (Nedelec et al., 1986; Nzenti et al., 1988), namely a weakly metamorphosed assemblage, made up of schists and quartzites (the Ayos-Mbalmayo-Bengbis and Yokadouma series) and the high metamorphic grade assemblage, consisting of gneiss, migmatites, and amphibolite micaschists as well as silicate calcite amphibolites (the Yaounde, Ntui-Batumba and the Bafia series). These major lithologic assemblages were intruded by diorites and granodiorites, and underwent high pressure and high temperature metamorphism (Nedelec et al., 1986; Nzenti et al., 1988). The tectonic evolution of the Yaounde group is characterised by the following: i) four Neoproterozoic metamorphic episodes dated at  $719 \pm 32$  Ma,  $661 \pm 21$  Ma,  $630 \pm 6$  Ma and  $561 \pm 8$  Ma (Betsi et al., 2020) and (ii) four major ductile deformation phases (D<sub>1</sub>-D<sub>4</sub>) (Mvondo et al., 2003, 2007). The first three stages, D<sub>1</sub>-D<sub>3</sub> correspond to East-West to Northwest-southeast shortening, and to crustal thickening caused by the nappe. The D<sub>2</sub> stage corresponds to the North-south to Northeast-southwest extension, thereby producing an orogenic sinking, and the exhumation of the Yaounde series. Phase D<sub>1</sub> represents the piling up of the nappe, associated with prograde metamorphism, leading to high pressure granulite conditions. On the other hand, the D<sub>2</sub> phase represents a compressive stage which occurred during the parallel extension of the orogeny. This was also associated to basic magmatism and to large scale boudinage of the foliations. The D<sub>4</sub> deformation phase is tentatively attributed to consecutive lateral flow of diachronic crustal extension.



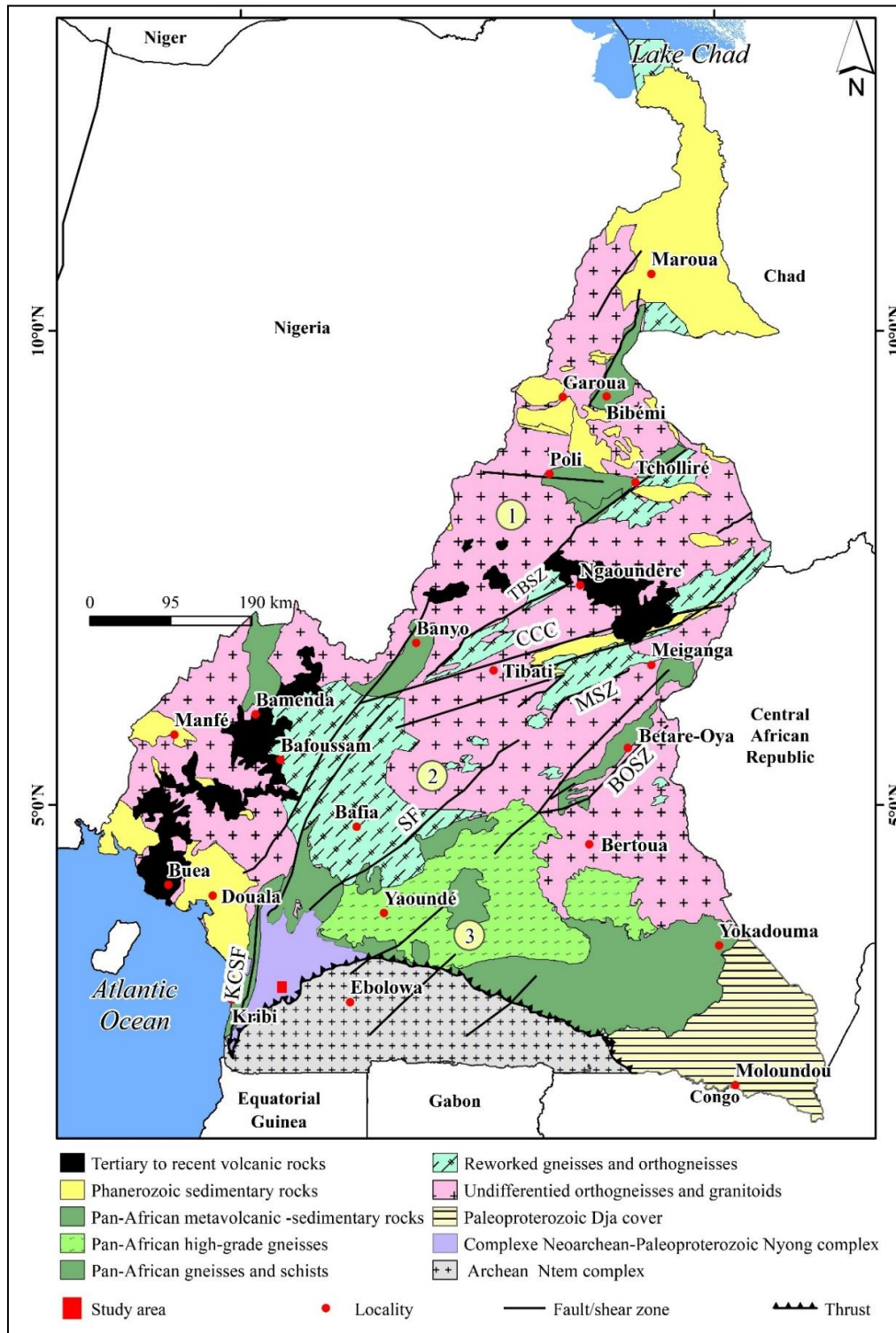


**Figure 6.** Geological map of Cameroon (after Kankeu et al., 2018) showing the location of the Anyouzok area and the main tectonic domains. 1: Northern domain; 2: Central domain; 3: Southern domain; BOSZ: Betare Oya Shear Zone; TBSZ: Tibati-Banyo Shear Zone; CCC: Central Cameroon Shear Zone; KCSZ: Kribi-Campo Shear Zone; MSZ: Meiganga Shear Zone.

### 1.2.2. Congo Craton (CC)

The Congo craton is a large sub-circular mass with a surface area of about 5.711,000 Km<sup>2</sup>, comprising an Archaean basement, early to Mid-Proterozoic fold belt and late Proterozoic cover (Goodwin, 1991). The Congo/São-Francisco craton broke up into two blocks separated by the Atlantic Ocean during the opening of the South Atlantic: (i) the São-Francisco craton in Brazil and (ii) the Congo-Zaire craton in Central Africa, whose northwestern edge outcrops in Cameroon and is represented by the Ntem Complex and the Nyong Complex (Fig 5; Maurizot et al., 1986).

❖ **The Nyong Complex** where lies the study area (Fig. 7) is the northwestern part of the Archaean Congo Shield (De Wit et al., 2008), remobilized in the Paleoproterozoic during the collision of the Congo and São-Francisco shields (Toteu et al., 1994; Feybesse et al., 1998; Lerouge et al., 2006; Aguilar et al., 2017; Alkmim and Teixeira, 2017). Earlier works on the Nyong complex show that it represents a reactivated part of the Archaean Congo craton throughout the Eburnean/Transamazonian (2400-1800 Ma; Penaye et al., 2004) and Pan-African/Brazilian (Feybesse et al., 1986; Maurizot et al., 1986) orogenies. The Nyong Complex represents a Paleoproterozoic suture zone coincident with a shear tectonic event between the Congo and São Francisco cratons (Ndema Mbongue et al., 2014; Kankeu et al., 2018; Houketchang Bouyo et al., 2019; Nga Essomba Tsoungui et al., 2020; Owona et al., 2021a). Preserved fragments of the Eburnean/Transamazonian orogeny have been uncovered in both north-eastern Brazil and Africa (Nigeria, north-central Cameroon, southern Gabon, Angola, Democratic Republic of Congo) forming the Sergipano-Central West African belt (Nzenti et al., 1988; Ledru et al., 1994; Tait et al., 2011).

The Nyong complex, based on several dating methods, has been found to contain Archaean, Paleoproterozoic and Neoproterozoic material. Following U-Pb dating on detrital zircon, rock material of volcano-sedimentary origin (Lerouge et al., 2006) were found to be of Archaean age (2500 -2900 Ma) (Pouclet et al., 2007; Nga Essomba Tsoungui et al., 2020; Nzepang Tankwa et al., 2020; Soh Tamehe et al., 2021; Owona et al., 2020, 2021a, 2021b; Kamguia Woguia et al., 2022). These rocks are principally granulite facies gneisses associated with banded iron formations, plutonites (constituting TTG, charnockites, dolerites, alkaline syenites) and the green rocks (serpentinites and the chloritic rocks).

Following U-Pb on zircon and Sm-Nd on zircon dating (Toteu et al., 1994; Feybesse et al., 1998), Paleoproterozoic material dating 2050 Ma were found, corresponding to the emplacement of certain granitic and syenitic massifs (Pouclet et al., 2007), while the ages of

2100-2000 Ma through U-Pb-Hf-O on zircon dating (Soh Tamehe et al., 2022) are thought to correspond to the date of emplacement of siliciclastic rocks and BIF. From U-Pb on zircon method, Neoproterozoic formations were dated at  $626 \pm 26$  Ma, corresponding to the metamorphic Panafrican event which affected this complex (Pouclet et al., 2007). Recent works (Owona et al., 2020, 2021b;  $2065 \pm 25$  Ma: Kamguia Woguia et al., 2022) estimate the mean age of this Eburnean/Transamazonian orogeny in the Nyong complex between 2,180 and 1,985 Ma. SHRIMP U-Pb zircon ages on Archean to Paleoproterozoic metasedimentary and metaigneous rocks, demonstrate high-pressure, eclogite facies metamorphism at  $2093 \pm 45$  Ma (Loose and Schenk, 2018). This age is similar to that obtained for the Gouap pyrite amphibolites (Soh Tamehe et al., 2021), and demonstrate that the Nyong Complex underwent regional metamorphism accompanied by hydrothermal activity during the Paleoproterozoic, precisely at ca. 2.09 Ga (Chombong et al., 2017) and later recorded Neoproterozoic footprints at ca. 600 Ma interpreted as the Pan-African disruption event (Penaye et al., 1993).

Well-preserved retrograde eclogite facies metamorphic rocks (eclogite facies garnet-clinopyroxene bearing mafic rocks) have also been highlighted in the Nyong Complex (Houketchang Bouyo et al., 2019; Nga Essomba Tsoungui et al., 2020). The Nyong series rocks were deposited at 2194-2032 Ma and later underwent regional hydrothermal activity and metamorphism 330 Ma later during the Eburnean/Transamazonian orogeny, which overlaps with the age of metamorphism (2100-2000 Ma) in the Nyong Complex as reported by previous authors (Toteu et al., 1994; Lerouge et al., 2006; Loose and Schenk, 2018; Nzepang Tankwa et al., 2020; Owona et al., 2020, 2021b; Kamguia Woguia et al., 2022). Three phases of deformation are highlighted in the Nyong complex (Nedelec et al., 1993; Feybesse et al., 1998; Binam Mandeng et al., 2018; Moudioh et al., 2020) associated with a polycyclic metamorphism which attained its peak during the Eburnean/Transamazonian tectonothermal event (2050 Ma; U-Pb age on zircon), in the amphibolite-granulite facies (Nedelec et al., 1993; Toteu et al., 1994; Lerouge et al., 2006; Mvodo et al., 2022) highlighted in the western part of the complex by Pan-African recrystallizations.

- Paleoproterozoic-dated D<sub>1</sub> phase ( $1734 \pm 22$  -  $1893 \pm$  Ma; Th - U-Pb ages, Ndema Mbongue et al., 2014, 2022) highlighted by a horizontal S<sub>1</sub> regional foliation bearing a variably oriented stretching lineation, and broad open folds associated with N-S sinistral rifts (Lerouge et al., 2006).

- D<sub>2</sub> phase with a transcurrent or shearing character developed P<sub>2</sub> folds, S<sub>2</sub> schistosity associated with an L<sub>2</sub> stretching lineation and C<sub>2</sub> shears injected by more or less deformed

mobilitates and dolerites. This phase is dated at 2 Ga (U-Pb ages on zircons) and is attributed to the Eburnean orogeny (Feybesse et al., 1987);

- D<sub>3</sub> phase marked by shears, schistosity, lineation and sometimes quartz puddles and exudates. These elements are comparable to those of the Pan-African D<sub>2</sub> phase that affected the Nyong complex ( $577 \pm 12$  -  $677 \pm 36$  Ma, Ndema Mbongue et al., 2014). Therefore, we can characterize this phase as Pan-African in age. The ubiquitous horizontal foliation within the Nyong series as well as the Px +Grt+ Pl +Qtz +Kfs granulite assemblages led to the conclusion (Lerouge et al., 2006; Barbosa and Sabaté, 2002) that the Nyong series would be an extension in Central Africa of the Transamazonian granulite orogeny of Brazil. This Eburnean/Trans-Amazonian orogeny extends from Cameroon, Central African Republic, Equatorial Guinea and Gabon, forming the West Central African Fold Belt (WCAFB); from its high-pressure, high-temperature metamorphic mineral assemblages and the geochemistry of associated magmatic rocks it can be classified as a subduction-collision orogeny (Nzenti et al., 1994, 2007; Feybesse et al., 1998; Loose and Schenk, 2018; Houketchang Bouyo et al., 2019; Nga Essomba Tsoungui et al., 2020).

❖ **The Ntem Complex** is made up of supracrustal rocks (Fig. 7) associated with charnockites (hypersthene granites) within the centre, granulitic gneisses to the south, and TTG suite granitoids in the northern part (Shang et al., 2004, 2007). Potassic granites and doleritic dykes cut across the TTG-charnockitic suite and granulite gneisses (Tchameni et al., 2001; Shang et al., 2010; Akame et al., 2020). The granitoids and charnockites were deformed and metamorphosed at 2.9 Ga (U-Pb age on zircon: (Toteu et al., 1994, 2001; Shang et al., 2010), while granites were injected between 2.7 and 2.9 Ga (Pb-Pb age on zircon: Tchameni et al., 2001). The geochemical signature of the charnockites and TTG suite in the Sangmelima, Ngoulemakong, and Ebolowa localities is similar to that of other Archean granitoids around the world. These rocks derive from the same protolith that is thought to be Archean greenstone (3.10 - 2.93 Ga) and include metabasites (Pouclet et al., 2007). Most recently, charnockites and TTGs from the Sangmelima area have been dated by LA-ICP-MS U-Pb on zircon. The ages obtained are between 3155 and 2850 Ma, while the gabbro intrusions are dated at  $2866 \pm 6$  Ma (Akame et al., 2020). The Ntem complex bears the imprint of a D<sub>1</sub> deformation expressed by S<sub>1</sub> foliation and P<sub>1</sub> isoclinal folds. The paragenesis associated with this phase is pyroxene (hypersthene, salite, subcalcic augite) + amphibole (tschermakite) + plagioclase + oxides (magnetite and ilmenite) and corresponds to the thermobarometric conditions of a low pressure-high temperature granulite facies metamorphism (700-800°C; 5-6Kb: Tchameni, 1997).



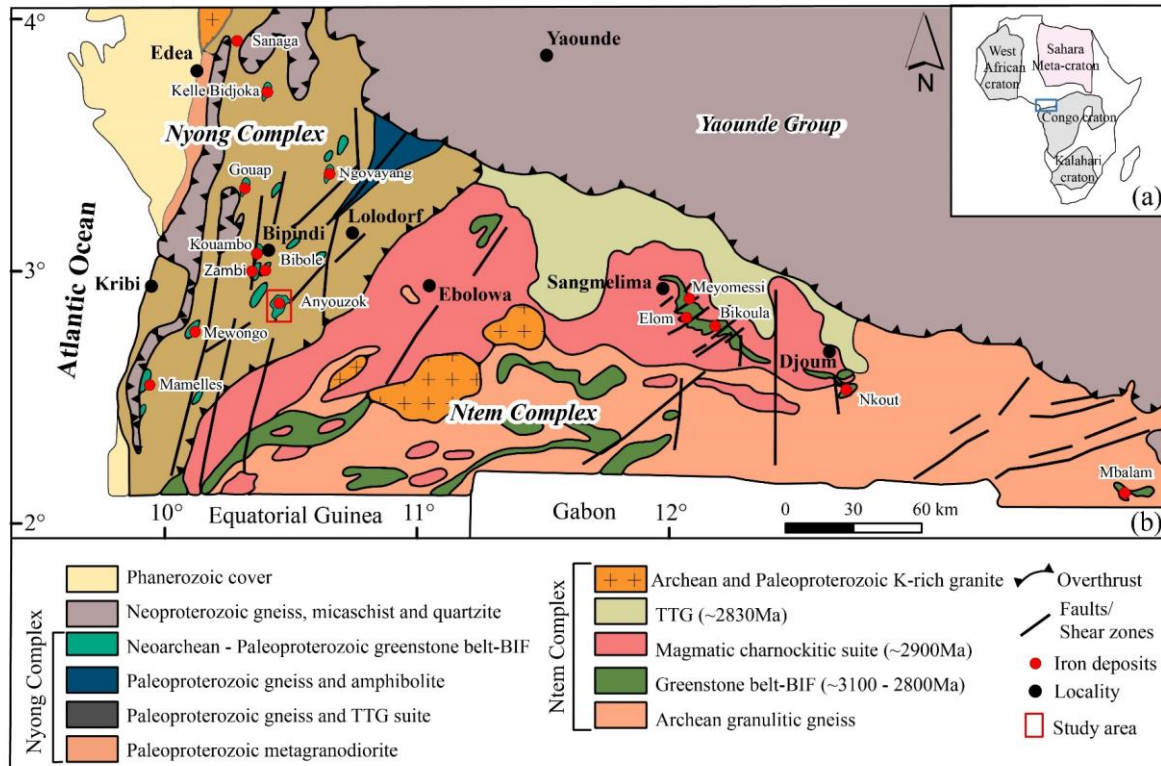


**Figure 7.** Sketch geological map of SW Cameroon (modified after [Maurizot et al., 1986](#); [Soh Tamehe et al., 2021](#)).

### 1.2.3. Geology of the iron ore deposit

The Anyouzok iron deposit found within the greenstone belts of the Nyong complex (Fig. 7), is one of the emerging iron ore provinces in Cameroon, west and central Africa. The Nyong complex consists of various gneisses, micaschists, amphibolites, IFs, metagranodiorites, charnockites, dolerites, quartzites, tonalite-trondhjemite-granodiorite suite, syenites, serpentinites and eclogites ([Lerouge et al., 2006](#); [Ebah Abeng et al., 2012](#); [Aye et al., 2017](#); [Houketchang Bouyo et al., 2016](#); [Nga Essomba Tsoungui et al., 2020](#); [Moudioh et al., 2020](#); [Nzepang Tankwa et al., 2020](#); [Kwamou Wanang et al., 2021](#); [Mvodo et al., 2022](#); [Owona et al., 2022](#); [Soh Tamehe et al., 2022](#)). Later on, New Resolution Energy in the effort to improve on the exploration effort of Caminex Sarl for the study area, through airborne surveys interpreted the geology of the area as comprising predominantly of E-W striking highly folded series of gneisses and amphibolites, divided on domains based on magnetic and radiometric character ([Peters, 2011](#)). These magnetic and radiometric characters of the various rock units could subsequently be used for full lithological interpretations if linked with ground geological investigations. [Owona et al. \(2021b\)](#) show that the metasedimentary rocks of the Nyong complex (including iron formations), derived

from the Meso-Neoproterozoic Congo shield (~2,800 Ma) were deposited between 2,400 and 2,200 Ma. They were then metamorphosed during the Paleoproterozoic orogeny (~2,200-2,000 Ma).

## **CHAPTER II. MATERIAL AND METHODS**

## **Introduction**

This chapter presents the materials and methods employed to attain the set objectives. The work was effected in three main stages which included preliminary/desktop studies, field work and laboratory work.

### **II.1. Desktop / Preliminary studies**

This work began with the collection and review of related literature as well as the assembly of existing maps. In this case, studies were carried out on global and African geology in general, and on the Precambrian geology of Cameroon. Attention was also focused on iron ore deposits related to Banded Iron Formations around the world, Africa, and Cameroon. Research thesis as well as publications in available journals were reviewed in the Laboratory of Geosciences for Internal Formations and Applications of the Earth Sciences department in the University of Yaoundé I. Existing regional geologic maps, topographic maps as well as airborne survey maps of the area were also acquired and studied together in prelude to the field work.

### **II.2. Field work**

Four field visits were done between 2013 and 2022. Outcrops were exposed along road cuttings and on river / stream channels. Due to deep weathering and the presence of the dense tropical forest, soil colour was also noted on field notebooks as index for the presence of underlying mineralized rock. With the aid of a handheld GPS, the geographic coordinates of the outcrops were registered. Using a compass clinometer and a measuring tape, the structural parameters of prominent outcrops were measured and recorded. The outcrops were also described in relation to the petrology, mineralogy, and structures (textures). Representative rock samples were then collected and sealed in sample bags. Subsequently, the sample bags were coded with unique identification codes for further studies and sample selection for thin sections, mineralogical and geochemical analysis.

Diamond drill cores were logged at the Caminex core shed. For each hole, drill cores were observed from beginning to end of hole. Based on color, texture and mineral composition, different rock units were distinguished, and rock boundaries delimited. Using a measuring tape, lithologic boundaries and thicknesses were measured and recorded progressively. Half and quarter core samples were systematically collected from the representative drillholes with respect to their lithology and texture. Drill core samples were carefully selected to ensure that the full variability of the iron mineralized unit (SBIFs and



BIFs) and interbedded none-mineralized unit (barren zones) were represented as required to reflect the geology of the deposit.

### **II.3 Laboratory studies**

To construct the lithostratigraphy, rocks were observed on the field at the outcrop scale for formations that were exposed, information from macroscopic and microscopic rock description were collected (texture, mineralogy, etc.), together with knowledge of field occurrence and interrelationships. Adjacent lithology's were then correlated based on depths of intercepts and lithology patterns.

Laboratory studies included several procedures amongst which were petrographic study, structural analysis, mineralogical analysis, and geochemical analytical methods. In most cases, each method had a particular procedure for sample preparation.

#### **II.3.1. Lithostratigraphy and petrographic study**

Laboratory work included the confectioning and study of rock thin sections under the polarizing and metallographic microscopes. Seventy-five standard thin sections (23 mafic granulites, 09 epidote gneiss, 24 garnet amphibolites and 20 pyroxene biotite gneiss) and fifteen polished thin sections (8 SBIFs, 4 BIFs) were made at the GeoTech Labs, Vancouver, Canada. The standard thin sections were studied under the polarized microscope at the Laboratory of Geoscience and internal formations and applications (LGPS), department of earth sciences, while the polished thin sections were studied at the GeoTech Labs, Vancouver, Canada. Microscopic observation made it possible to determine the mineralogical composition and mineral association in equilibrium. The mineral abbreviations used in this work is according to [Whitney and Evans \(2010\)](#), while the nomenclature and mineral assemblage follows the recommendations of [IUGS-SCRM \(International Union of Geological Sciences\), 2017](#).

For Mineral volume percentage calculations, petrographic and microstructural studies were done by observing representative sections of mineral associations under transmitted light and under reflected light for ore polished thin sections. Mineral modal estimations were done following the “Society for Geology Applied to Mineral Deposits” standards ([www.e-sga.org](http://www.e-sga.org)) to come out with modal percentages for each mineral.

### II.3.2. Mineralogical analysis

Iron formation (IF) mineral composition was further determined by the X-ray diffraction (XRD) method with the Bruker D8-Advanced Eco 1Kw diffractometer at AGES (University of Liège, Belgium). 100 g of fresh rock sample were carefully selected, cut, and manually crushed and sieved to 250µm, using a mortar and pestle. X-ray wavelengths  $X$  ( $0.1 < \lambda < 10 \text{ nm}$ ) are incident on the mineral sample. Excited atoms emit radiations consistent with Bragg's law,  $n\lambda = 2d(hkl)\sin\theta$ , where  $n$  = whole numbers corresponding to the order of diffraction;  $\lambda$  = incident wavelength,  $d$  = distance between layers, and  $\theta$  = angle of diffraction.

### II.3.3. Geochemical Analytical Methods

Based on the petrographic results, forty-five representative samples (eight mafic granulites, eleven garnet amphibolites, four pyroxene biotite gneiss, eight SBIFs and four BIFs) were selected for whole rock geochemical analysis. Due to the limited number of epidote gneiss samples as well as the highly altered nature, they were not analysed for geochemistry. After data curation, twenty-one altered samples were screened out and twenty-three samples (4 mafic granulites, 7 garnet amphibolites, 3 pyroxene biotite gneiss, 5 SBIFs and 4 BIFs) were selected for geochemical studies. Epidote gneiss samples were not considered for geochemical analysis because they were strongly weathered. Whole rock geochemical analysis for major elements was done using rock pulp by inductively coupled plasma-atomic emission spectrometry (ICP-AES) while inductively coupled plasma mass spectrometry (ICP-MS) was conducted for trace element and rare earth element (REE) analysis, at ALS Lab, Ireland. Samples were initially pulverized, and 50-60 g extracted for analysis. Rock powder (0.2 g) was then fused with  $\text{LiBO}_2$  and dissolved in 100 mm<sup>3</sup> of 5%  $\text{HNO}_3$ . Analytical uncertainties vary from 0.1% to 0.04% for major elements, 0.1 to 0.5 ppm for trace elements, and 0.01 to 0.5 ppm for rare earth elements. Loss on ignition (LOI) was determined by weight difference after ignition at 1000°C. Various standards were used and data quality assurance was verified by running these standards between samples as unknowns. Analysis precision for rare earth elements is estimated at 5% for concentrations > 10 ppm and 10% when lower. Since Y is more similar to Ho and has been extensively used in REE studies of aqueous solutions and their precipitates ([McDonough and Sun, 1995](#)), it has been inserted between Dy and Ho. REE-Y concentrations of IFs were normalized to Post Archaean Australian Shale (PAAS; [Taylor and McLennan, 1985](#)). The Eu, Ce, La, Gd, Y and Pr anomalies of IFs discussed in this study are calculated following the procedure of [Bau and](#)

Dulski (1996) and Bolhar et al. (2004):  $(Eu/Eu^*)_{SN} = (Eu)_{SN}/(0.67Sm_{SN}+0.33Tb_{SN})$ ;  $(Ce/Ce^*)_{SN} = Ce_{SN}/(0.5La_{SN} + 0.5Pr_{SN})$ ;  $(La/La^*)_{SN} = (La)_{SN}/(3Pr_{SN}-2Nd_{SN})$ ;  $(Gd/Gd^*)_{SN} = (Gd)_{SN}/(0.33Sm_{SN}+0.67Tb_{SN})$ ;  $(Y/Y^*)_{SN} = 2Y_{SN}/(Dy_{SN}+Ho_{SN})$ ;  $(Pr/Pr^*)_{SN} = Pr_{SN}/(0.5Ce_{SN}+0.5Nd_{SN})$  and  $(Eu/Eu^*)_{CN} = (Eu)_{CN} / \sqrt{Sm_{CN} \times Gd_{CN}}$ . The chemical index of alteration, CIA is calculated after Nesbitt and Young (1982):  $CIA = 100 \times [Al_2O_3/(Al_2O_3+CaO+Na_2O+K_2O)]$ ,  $CaO^*$  is the  $CaO$  in the silicate fraction only.

## **CHAPTER III. LITHOSTRATIGRAPHY AND PETROGRAPHY**

## Introduction

This chapter aims to identify the existing rock types, establish a relationship between them, and specify the main mineral phases through a stratigraphic and lithological inventory. It also deals with the petrographic and mineralogical characterization of the different geological formations within the study area. Field investigations show that the Anyouzok area is made up of a metamorphic unit consisting of iron formation (15 mod. %), in association with country rocks which are made up of pyroxene biotite gneiss (55 mod. %), mafic granulite (20 mod. %), and garnet amphibolite (10 mod. %).

### III.1. Lithostratigraphy

Based on IFs occurrences on the field, the Anyouzok iron deposit is subdivided into a northern and a southern prospect (Fig. 8). The northern prospect is an N-S trending ore body with a strike length of 2100 m by 800 m (Fig. 8). The southern prospect is a NW-SE trending ore body with a strike-length of 2000 m by 300 m (Fig. 8).

The lithostratigraphy of the study area was determined via the logging of thirteen representative holes drilled by Caminex SARL (Table 2). Eight drillholes (TH9, TD37, TD35, TD46, TH31, TD47, TD60 and TD65) were logged from the northern prospect (Fig. 9a), while five drillholes (TE4, TE5, TE6, TE9, TE22) were considered for the southern prospect (Fig. 9a). The drillhole details are presented on Tables 3 and 4. The cross sections A-A' (Fig. 9b) and B-B' (Fig. 9b), illustrate the litho-assemblages within the northern and the southern prospects respectively. The units intercepted along the stratigraphy in both prospects are metamorphosed and consist of an IF unit (BIF and SBIF) and a country rock unit (mafic granulite, garnet amphibolite epidote gneiss and pyroxene biotite gneiss).

**Table 2.** Anyouzok iron deposit drillhole collars

Hole ID	Easting	Northing	Elevation	End of Hole	Azimuth	Dip angle
TH9	657797	323609	545	83	180	-50
TH31	657607	324482	350	81	135	-50
TD35	657828	323809	575	281	180	-55
TD37	657809	323698	556	179	180	-55
TD46	658098	323893	573	306	180	-55
TD47	658400	324101	602	329	180	-55
TD60	657794	324605	385	110	140	-70
TE4	660816	317370	686	245	60	-50
TE5	660775	317343	687	182	60	-50
TE6	660705	317321	686	300	60	-50
TE9	660651	317460	680	220	55	-50
TE22	660886	317253	679	139	70	-50
TD65	657564	323327	467	111	140	-70

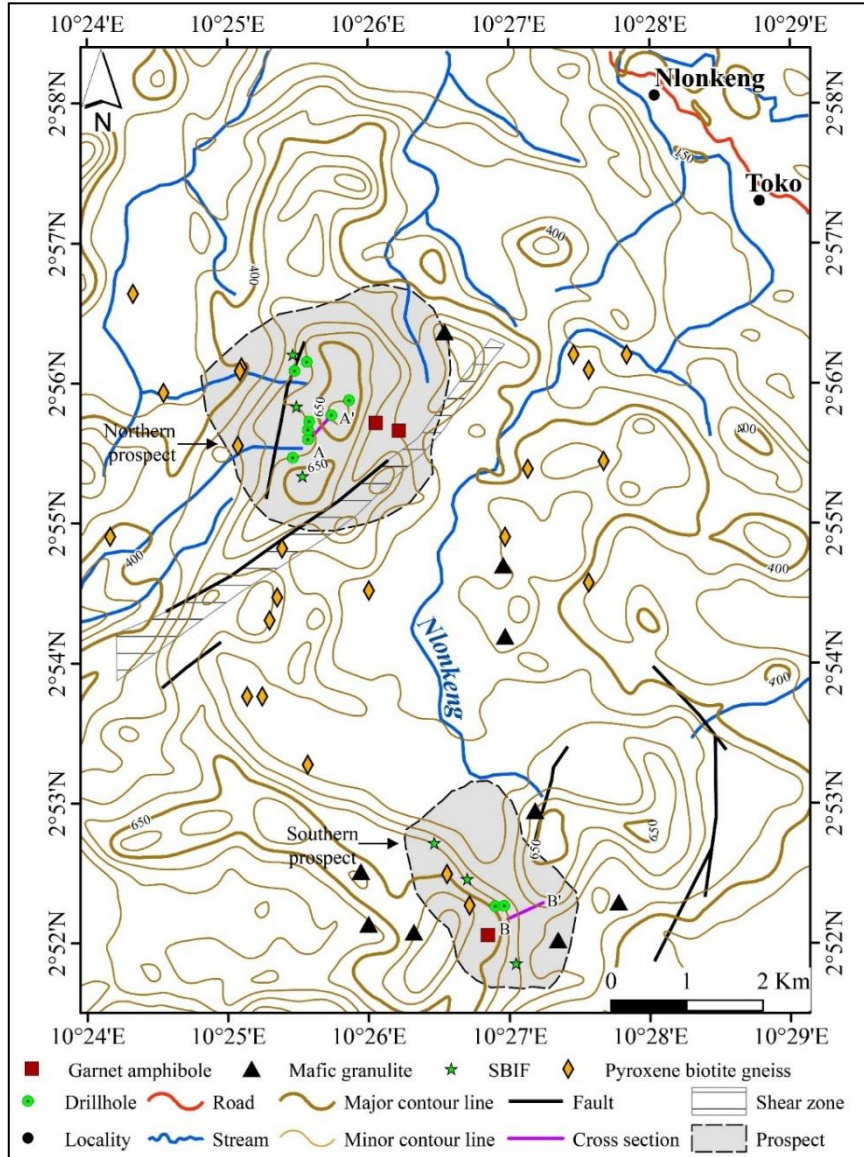


**Figure 8.** Samples and drillholes location map of study area showing the northern and southern prospects.

### III.1.1. Northern prospect

#### a) *Iron formations unit*

In this part of the deposit, IFs consist of SBIFs, intercepted below the surface at variable depths from 15 m (hole TD37), with their respective cumulative thicknesses varying from 10.30 m (hole TH60; Fig. 9a) to 147.3 m (hole TD47; Fig. 9a). SBIFs are found in sharp to gradational contact with interbedded pyroxene biotite gneiss, mafic granulite, and garnet amphibolite. Along section A-A' (Fig. 9b), SBIFs are found with no hanging wall, directly below the hematite cap, except for hole TD46. Core specimen consists mainly of medium- to coarse-grained magnetite and quartz.

**Table 3.** Anyouzok Northern prospect deposit drillhole logging details.

Drillhole	From	To (m)	Interval (m)	Rock type	Contact
TH9	0	3	3	Lateritic cover	Gradational
TH9	3	16.4	13.4	Hematite cap	Gradational
TH9	16.4	83	66.6	SBIF	EOH
TD37	0	3.3	3.3	Lateritic cover	Gradational
TD37	3.3	15	11.7	Hematite cap	Gradational
TD37	15	97.83	82.83	SBIF	Sharp
TD37	97.83	106.9	9.07	Pyroxene biotite gneiss	Sharp
TD37	106.9	143.41	36.51	SBIF	Sharp
TD37	143.41	179	35.59	Mafic granulite	EOH
TD35	0	4	4	Lateritic cover	Gradational
TD35	4	23.4	19.4	Hematite cap	Gradational
TD35	23.4	107.08	83.68	SBIF	Sharp
TD35	107.08	114.2	7.12	Garnet amphibolite	Sharp
TD35	114.2	120.74	6.54	SBIF	Sharp
TD35	120.74	133.4	12.66	Mafic granulite	Sharp
TD35	133.4	220.2	86.8	Pyroxene biotite gneiss	Sharp
TD35	220.2	281	60.8	Mafic granulite	EOH
TD46	0	5.44	5.44	Lateritic cover	Gradational
TD46	5.44	21.44	16	Hematite cap	Gradational
TD46	21.44	69.2	63.46	Pyroxene biotite gneiss	Sharp
TD46	69.2	70.3	1.1	Epidote gneiss	Gradational
TD46	70.3	84.9	14.6	Pyroxene biotite gneiss	Sharp
TD46	84.9	96.4	11.5	Mafic granulite	Sharp
TD46	96.4	102.4	6	SBIF	Sharp
TD46	102.4	110	7.6	Mafic granulite	Sharp
TD46	110	118	8	SBIF	Sharp
TD46	118	126.9	8.9	Mafic granulite	Sharp
TD46	126.9	154.3	27.4	SBIF	Sharp
TD46	154.3	186	31.7	Mafic granulite	Sharp
TD46	186	216	30	SBIF	Gradational
TD46	216	240	24	Garnet amphibolite	Sharp
TD46	240	306	66	Mafic granulite	EOH
TH31	0	3.6	3.6	Lateritic cover	Gradational
TH31	3.6	17.9	14.3	Garnet amphibolite	Gradational
TH31	17.9	31.9	14	SBIF	Sharp
TH31	31.9	49.9	18	Mafic granulite	Sharp
TH31	49.9	62.88	12.98	Garnet amphibolite	Sharp
TH31	62.88	81	18.12	Mafic granulite	EOH
TD47	0	25.4	25.4	Lateritic cover	Gradational
TD47	25.4	55.9	30.5	Garnet amphibolite	Gradational
TD47	55.9	70.2	14.3	SBIF	Gradational
TD47	70.2	82.9	12.7	Garnet amphibolite	Gradational
TD47	82.9	184.9	102	SBIF	Sharp
TD47	184.9	189.1	4.2	Pyroxene biotite gneiss	Sharp
TD47	189.1	195.1	6	Garnet amphibolite	Sharp
TD47	195.1	197	1.9	Pyroxene biotite gneiss	Sharp
TD47	197	204.7	7.7	Garnet amphibolite	Sharp
TD47	204.7	212.1	7.4	Pyroxene biotite gneiss	Sharp
TD47	212.1	214.6	2.5	Mafic granulite	Sharp
TD47	214.6	242	27.4	Pyroxene biotite gneiss	Gradational
TD47	242	273	31	SBIF	Sharp
TD47	273	315.9	42.9	Pyroxene biotite gneiss	Sharp
TD47	315.9	329	13.1	Garnet amphibolite	EOH
TD60	0	12.6	12.6	Lateritic cover	Gradational
TD60	12.6	16.9	4.3	Pyroxene biotite gneiss	Sharp
TD60	16.9	40	23.1	Mafic granulite	Sharp
TD60	40	67	27	Garnet amphibolite	Gradational
TD60	67	72.2	5.2	SBIF	Sharp
TD60	72.2	79.3	7.1	Garnet amphibolite	Sharp
TD60	79.3	84.4	5.1	SBIF	Gradational
TD60	84.4	110	25.6	Garnet amphibolite	EOH
TD65	0	1.3	1.3	Lateritic cover	Gradational
TD65	1.3	8.7	7.4	Hematite cap	Gradational
TD65	8.7	22.06	13.36	Mafic granulite	Gradational
TD65	22.06	56.55	34.49	SBIF	Sharp
TD65	56.55	111	54.45	Mafic granulite	EOH

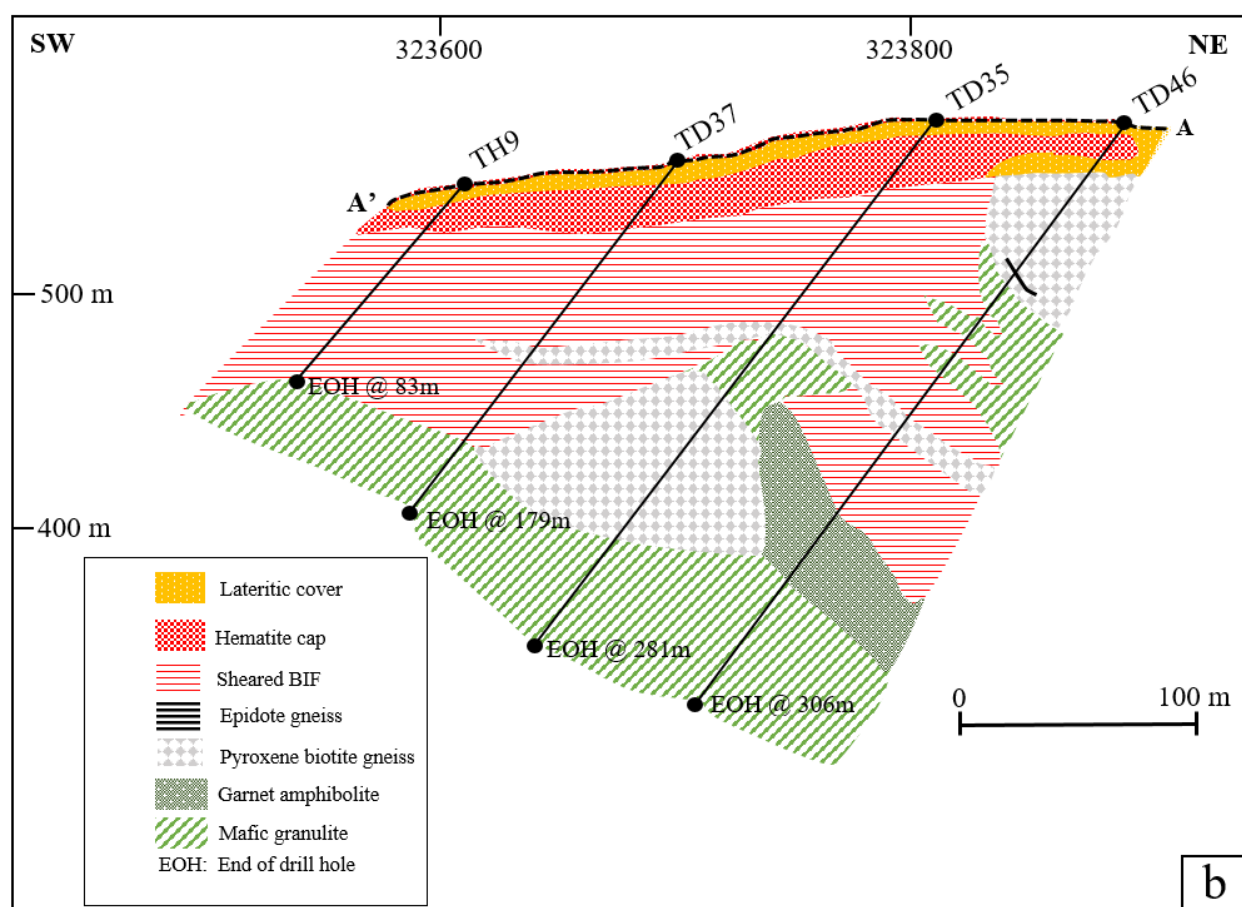
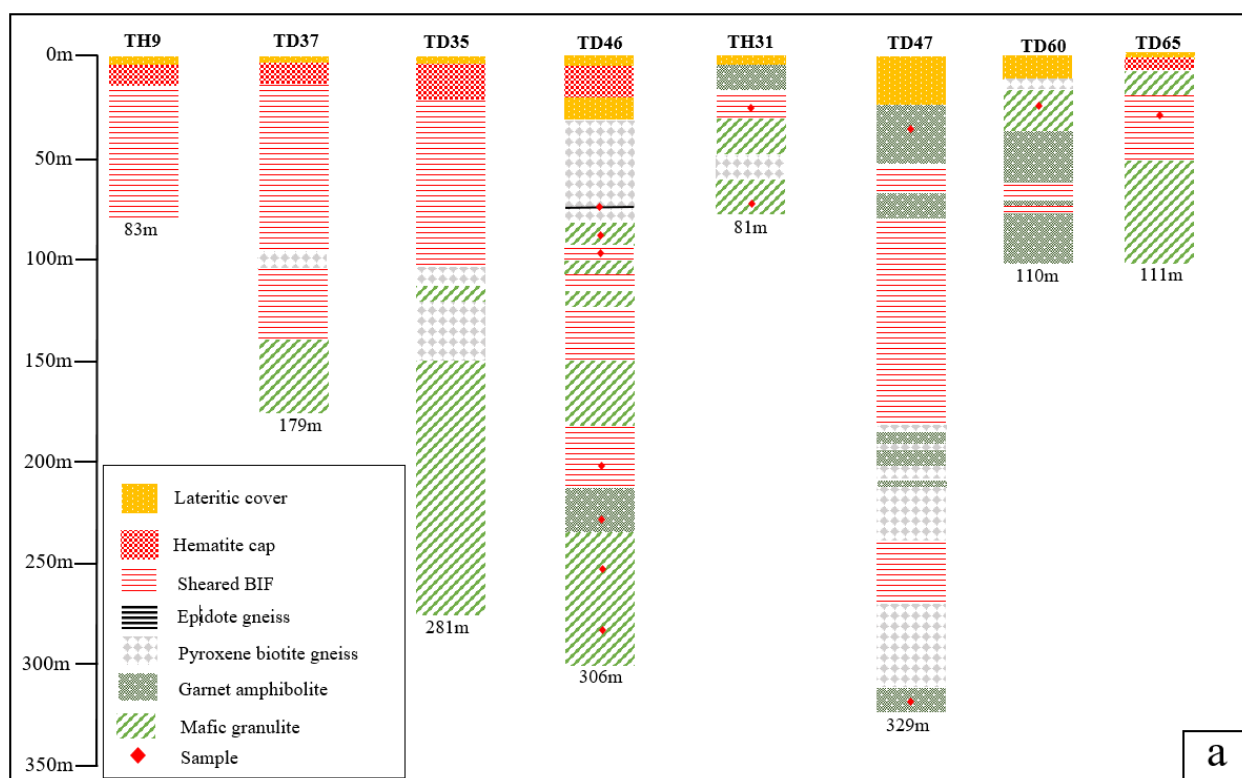


**Figure 9.** Anyouzok northern prospect (a) Litho-stratigraphic logs with sample locations. (b) Geological NE-SW cross section (A-A' in Fig. 8).



### *b) Country rock unit*

Pyroxene biotite gneiss is intercepted from 12.6 m depth (hole TD60) with various intercalations along section and cumulative thickness up to 86.80 m (hole TD35). Pyroxene biotite gneiss at the hanging wall was intercepted from ~ 32-84 m, just below the hematite cap (hole TD46; Fig. 9b). At the footwall, pyroxene biotite gneiss is found in sharp contact with mafic granulite and garnet amphibolite. The core specimen mainly made up of fine- to coarse-grained biotite, quartz, pyroxene, and feldspar.

Mafic granulite represents the major lithotype along the stratigraphy of the northern prospect (Fig. 9b) and generally shows a sharp and conformable contact with the SBIFs and the other country rocks. At the hanging wall it is intercepted in holes TD46, TD60 and TH31 with thicknesses of 11.5 m, 23.1 m, and 13.36 m respectively. The core specimen consists of medium- to coarse-grained pyroxene, garnet, amphibole, and quartz.

Garnet amphibolite represents the least abundant lithotype along the stratigraphy of the northern prospect (Fig. 9b). It is intercepted from 3.60 m below surface (hole TH31) to 329.16 m depth (hole TD47), with cumulative thickness ranging from 7.12 m (hole TD35) to 70.16 m (hole TD47). Hand specimen shows visible amphibole, garnet and quartz crystals.

## III.1.2 Southern prospect

### *a) Iron formation unit*

IFs unit within the southern prospect comprises ubiquitous SBIFs and minor BIFs, the latter only intercepted along section of the drillhole, TE22.

SBIF is exposed in drill core at various depths from 19.4 m (hole TE22) below the surface and show cumulative thicknesses ranging from 46.0m (hole TE4) to 92.6m (hole TE22; Fig. 9a). In this prospect, SBIFs show sharp and conformable contacts with intercalated mafic granulite and garnet amphibolite. Along section B-B' (Fig. 8), SBIFs are intercalated with mafic granulite, with the hanging wall and foot wall marked by prominent pyroxene biotite gneiss, except along hole TE6 where the hanging wall shows mafic granulite and garnet amphibolite intercalations. Likewise, on the northern prospect, drill core specimen mainly consists of magnetite and quartz.

BIF was not encountered during field work, but it is exposed in drill core of the hole TE22 from 46.5 to 48 m, with a thickness of 1.5 m. It occurs in between mafic granulite with gradational contacts (Fig. 9a). BIF core specimen is banded, with alternating white and dark millimetre to centimetre thick quartz-rich and magnetite-rich bands respectively. Within the

dark bands, the magnetite is fine- to medium-grained while the white bands show fine grained quartz.

**Table 4.** Anyouzok southern prospect deposit drillhole logging details.

Drillhole	From	To (m)	Interval (m)	Rock type	Contact
TE6	0	11	11	Lateritic cover	Gradational
TE6	11	91.3	80.3	Pyroxene biotite gneiss	Gradational
TE6	91.3	95.9	4.6	Mafic granulite	Gradational
TE6	95.9	125	29.1	Pyroxene biotite gneiss	Sharp
TE6	125	153.8	28.8	Garnet amphibolite	Sharp
TE6	153.8	192.8	39	SBIF	Sharp
TE6	192.8	218.3	25.5	Mafic granulite	Gradational
TE6	218.3	246.9	28.6	SBIF	Gradational
TE6	246.9	300	53.1	Pyroxene biotite gneiss	EOH
TE5	0	6.56	6.56	Lateritic cover	Gradational
TE5	6.56	88.93	82.37	Pyroxene biotite gneiss	Gradational
TE5	88.93	123.25	34.32	SBIF	Sharp
TE5	123.25	155	31.75	Mafic granulite	Sharp
TE5	155	168.4	13.4	SBIF	Sharp
TE5	168.4	182	13.6	Pyroxene biotite gneiss	EOH
TE4	0	8.5	8.5	Lateritic cover	Gradational
TE4	8.5	44.65	36.15	Pyroxene biotite gneiss	Sharp
TE4	44.65	81.35	36.7	SBIF	Sharp
TE4	81.35	106.25	24.9	Mafic granulite	Sharp
TE4	106.25	115.55	9.3	SBIF	Sharp
TE4	115.55	245	129.45	Pyroxene biotite gneiss	EOH
TE9	0	11.65	11.65	Lateritic cover	Gradational
TE9	11.65	80.7	69.05	Pyroxene biotite gneiss	Gradational
TE9	80.7	93.7	13	Garnet amphibolite	Gradational
TE9	93.7	119.5	25.8	SBIF	Gradational
TE9	119.5	134.75	15.25	Garnet amphibolite	Gradational
TE9	134.75	141	6.25	Mafic granulite	Gradational
TE9	141	186.4	45.4	SBIF	Sharp
TE9	186.4	220	33.6	Pyroxene biotite gneiss	EOH
TE22	0	19.4	19.4	Lateritic cover	Gradational
TE22	19.4	21.6	2.2	SBIF	Sharp
TE22	21.6	33.4	11.8	Mafic granulite	Sharp
TE22	33.4	37.3	3.9	SBIF	Sharp
TE22	37.3	42	4.7	Mafic granulite	Sharp
TE22	42	45.5	3.5	SBIF	Sharp
TE22	45.5	46.5	1	Mafic granulite	Gradational
TE22	46.5	48	1.5	BIF	Gradational
TE22	48	50.5	2.5	Mafic granulite	Sharp
TE22	50.5	133.5	83	SBIF	Sharp
TE22	133.5	137.6	4.1	Mafic granulite	Sharp
TE22	137.6	139	1.4	Pyroxene biotite gneiss	EOH

#### *b) Country rock unit*

Pyroxene biotite gneiss is intercepted at various depths from 8.5 m (hole TE4) below the surface (Fig. 9a) and show cumulative thicknesses ranging from 1.51 m (hole TE22) to 165.95 m (hole TE4). It represents the most abundant lithology of the Southern prospect (Fig. 9b). Pyroxene biotite gneiss mainly shows gradational contacts with interbedded mafic granulite, SBIF and garnet amphibolite (Table 5). It is mainly made up of fine to coarse biotite, quartz, and feldspar crystals.

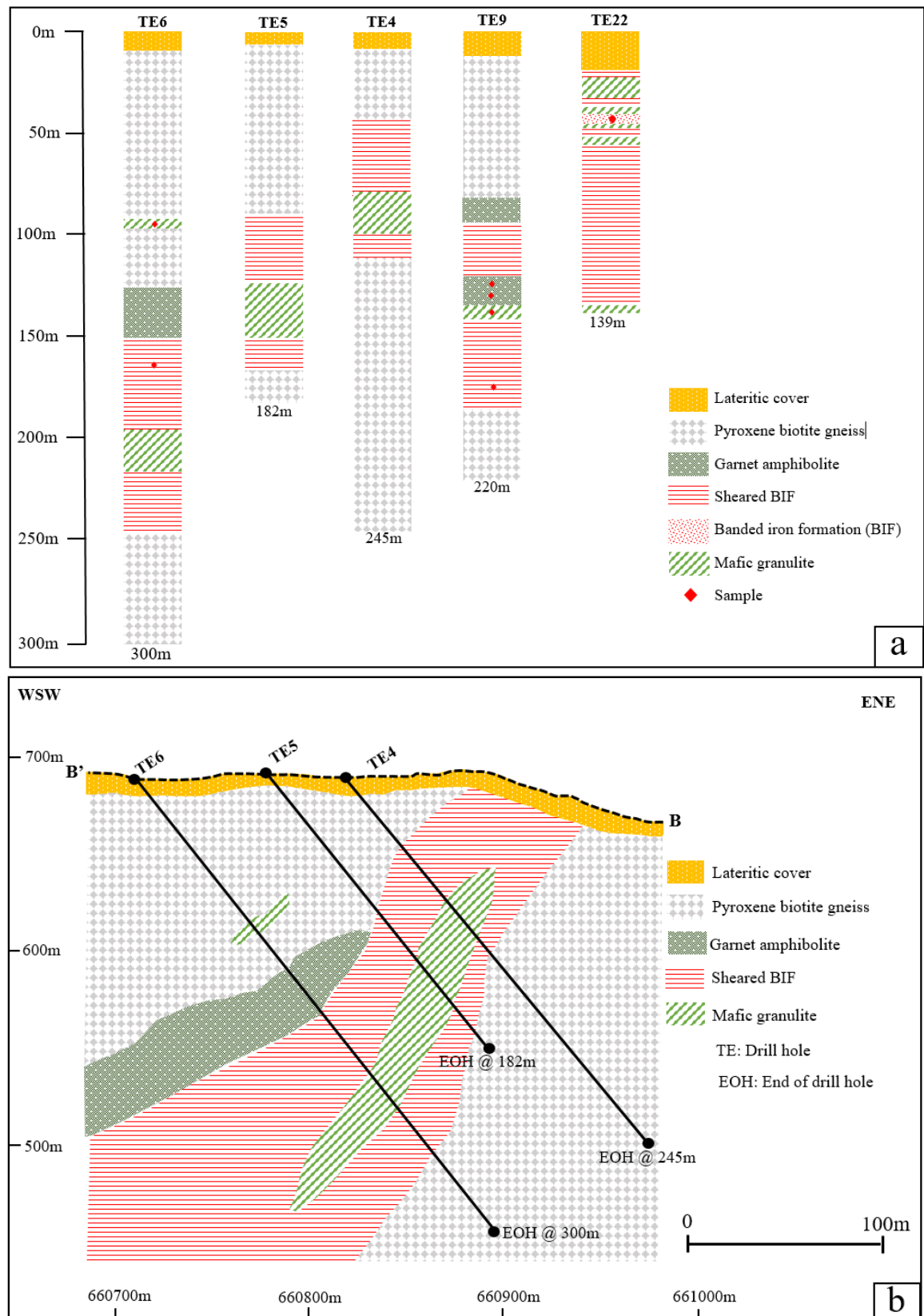


**Figure 10.** Anyouzok southern prospect (a) Lithostratigraphic logs with sample locations. (b) Geological ENE-WSW cross section (B-B' in Fig. 8).

Mafic granulite mainly occurs as intercalations between SBIFs with generally sharp contacts and have cumulative thicknesses ranging from 6.25 (Hole TE9) to 31.75 (hole TE5). Along section of hole TE22, mafic granulite represents the only lithology intercalated between SBIFs and BIFs. The core specimen consists of medium- to coarse-grained pyroxene, garnet, amphibole, and quartz.

Garnet amphibolite in the southern prospect represents the least abundant lithotype as well (Fig. 10b). The intercepts extend from 80.7 m (hole TE9) below the surface to 125 m (hole TE6), with cumulative thicknesses ranging from 28.25 m (Hole TE9) to 28.8 m (hole TE6). Drill core shows medium to coarse amphibole, garnet, and quartz.

**Table 5.** Table showing sample ID, drillhole code and other sample parameters.

SN	Sample ID	Drillhole	Coordinates			Azimuth	Dip angle	Sample depth (m)	EOH	Rock type
			Easting	Northing	RL					
1	IS6		659307	321593	413			Surface		Pyroxene biotite gneiss
2	IS11a		657578	323501	505			Surface		Pyroxene biotite gneiss
3	IS11b		657578	323501	505			Surface		Pyroxene biotite gneiss
4	IS12	TH31	657606	324482	349	135	-50	10.5	81.4	Pyroxene biotite gneiss
5	IS44		657370	323262	467			Surface		Epidote gneiss
6	IS16	TD46	658097	323893	573	180	-55	70.3	305.9	Epidote gneiss
7	IS17	TD46	658097	323893	573	180	-55	93.5	305.9	Mafic granulite
8	IS20	TD46	658097	323893	573	180	-55	236.4	305.9	Mafic granulite
9	IS22	TD46	658097	323893	573	180	-55	280.8	305.9	Mafic granulite
10	IS23	TD46	658097	323893	573	180	-55	305.7	305.9	Mafic granulite
11	IS26	TD47	658399	324101	602	180	-55	159	329.16	Mafic granulite
12	IS34	TE6	660705	317321	685	60	-50	108.8	300.35	Mafic granulite
13	IS40	TE9	660651	317460	679	55	-50	138.4	220.2	Mafic granulite
14	IS18b	TD46	658097	323893	573	180	-55	154.3	305.9	Garnet amphibolite
15	IS21	TD46	658097	323893	573	180	-55	272.9	305.9	Garnet amphibolite
16	IS24	TD47	658399	324101	602	180	-55	25.9	329.16	Garnet amphibolite
17	IS27b	TD47	658399	324101	602	180	-55	197.2	329.16	Garnet amphibolite
18	IS28	TD47	658399	324101	602	180	-55	327	329.16	Garnet amphibolite
19	IS29	TD60	657793	324604	385	140	-70	16.9	110	Garnet amphibolite
20	IS14	TH31	657606	324482	349	135	-50	36.6	81.4	Garnet amphibolite
21	IS27	TD47	658399	324101	602	180	-55	197.2	329.16	Garnet amphibolite
22	IS15	TH31	657606	324482	349	135	-50	77.3	81.4	Garnet amphibolite
23	IS33	TE6	660705	317321	685	60	-50	95.5	300.35	Garnet amphibolite
24	IS37	TE9	660651	317460	679	55	-50	134.2	220.2	Garnet amphibolite
25	IS39	TE9	660651	317460	679	55	-50	136.7	220.2	Garnet amphibolite
26	IS50	TE22	660887	317250	670	70	-50	46.71	139.11	BIF
27	IS51	TE22	660887	317250	670	70	-50	47	139.11	BIF
28	IS52	TE22	660887	317250	670	70	-50	47.5	139.11	BIF
29	IS13	TE22	660887	317250	670	70	-50	48	139.11	BIF
30	IS41	TE9	660651	317460	679	55	-50	173.7	220.2	SBIF
31	IS54	TD65	657558	323320	484	140	-70	25.5	111.1	SBIF
32	IS18	TD46	658097	323893	573	180	-55	154.3	305.9	SBIF
33	IS19	TD46	658097	323893	573	180	-55	212.65	305.9	SBIF
34	IS35	TE6	660705	317321	685	60	-50	155.8	300.35	SBIF
35	IS30	TD60	657793	324604	385	140	-70	67.30	110	SBIF
36	IS31	TD47	658399	324101	602	180	-55	150	329.16	SBIF
37	IS42	TD47	658399	324101	602	180	-55	159	329.16	SBIF

## III.2 Petrographic study

### III.2.1 Pyroxene biotite gneiss

The pyroxene biotite gneiss samples (Table 5) were collected both from surface outcrops (IS6, IS11, IS11b) and from drill core (sample IS12 from hole TH31, sampled at depth of 10.5m). Surface outcrops of pyroxene biotite gneiss occur as slabs on road surface (Fig. 11a) and as road cuttings, leading to drill pads (Fig. 11b). Grab sample (Fig. 11c) and drill core (Fig. 11d) are light grey, foliated, folded and generally fine-grained. Visible minerals are quartz and feldspar with dotted dark biotite and pyroxene.

Under the microscope, the rock is banded shows a granoblastic heterogranular microstructure (Fig. 12a and b), consisting of feldspar, quartz, biotite, pyroxene, amphibole, sericite, microcline, garnet, opaque, apatite and allanite (Fig. 12a to f).

**Alkali feldspar** (20-30 mod.%) is generally coarse-grained, perthitic and represented by orthoclase. Its crystals are subhedral to anhedral, with sizes ranging between 0.4 mm and 2 mm. It occurs in association with quartz, plagioclase and biotite (Fig. 12a to f). Feldspar shows several opaque and quartz mineral inclusions (Fig. 12b and c). Alkali feldspar manifests quartz and plagioclase exsolutions. Some crystals show transformation to sericite (Fig. 12a to e).

**Quartz** (15-20 mod.%) Quartz occurs as anhedral grains of up to 1 mm long or as sub-millimetric crystals. Quartz is mostly associated with biotite, feldspar, amphibole and pyroxene (Fig. 12a - h). It also occurs as tiny inclusions in alkali feldspar and orthopyroxene.

**Biotite** (15-20 mod.%) generally appears as lamellae (Fig. 12a – f). It is the most abundant ferromagnesian mineral in the rock. The sizes of the lamellae are variable, up to 1.5 mm (Fig. 12e) for large crystals, while the smaller crystals are less than 0.5 mm (Fig. 12a, b, c, d and f). It occurs in association with quartz, K-feldspar and amphibole. Biotite sometimes contains accessory minerals such as zircon (Fig. 12e).

**Amphibole** (10-15 mod.%) is green hornblende which occurs as anhedral crystals and is associated with biotite, K-feldspar, sericite, orthopyroxene and quartz (Fig. 12a and e). Crystals have average dimensions of  $0.2 \times 0.4$  mm. Amphiboles are also found as secondary minerals derived from pyroxene (Fig. 12d). In this situation, pyroxene is being transformed into amphibole around the peripheries.

**Plagioclase feldspar** (5-10 mod.%) is anhedral, fine-to medium grained about 0.4 x 0.6 mm and associated with quartz and K-feldspar (Fig. 12a and f).

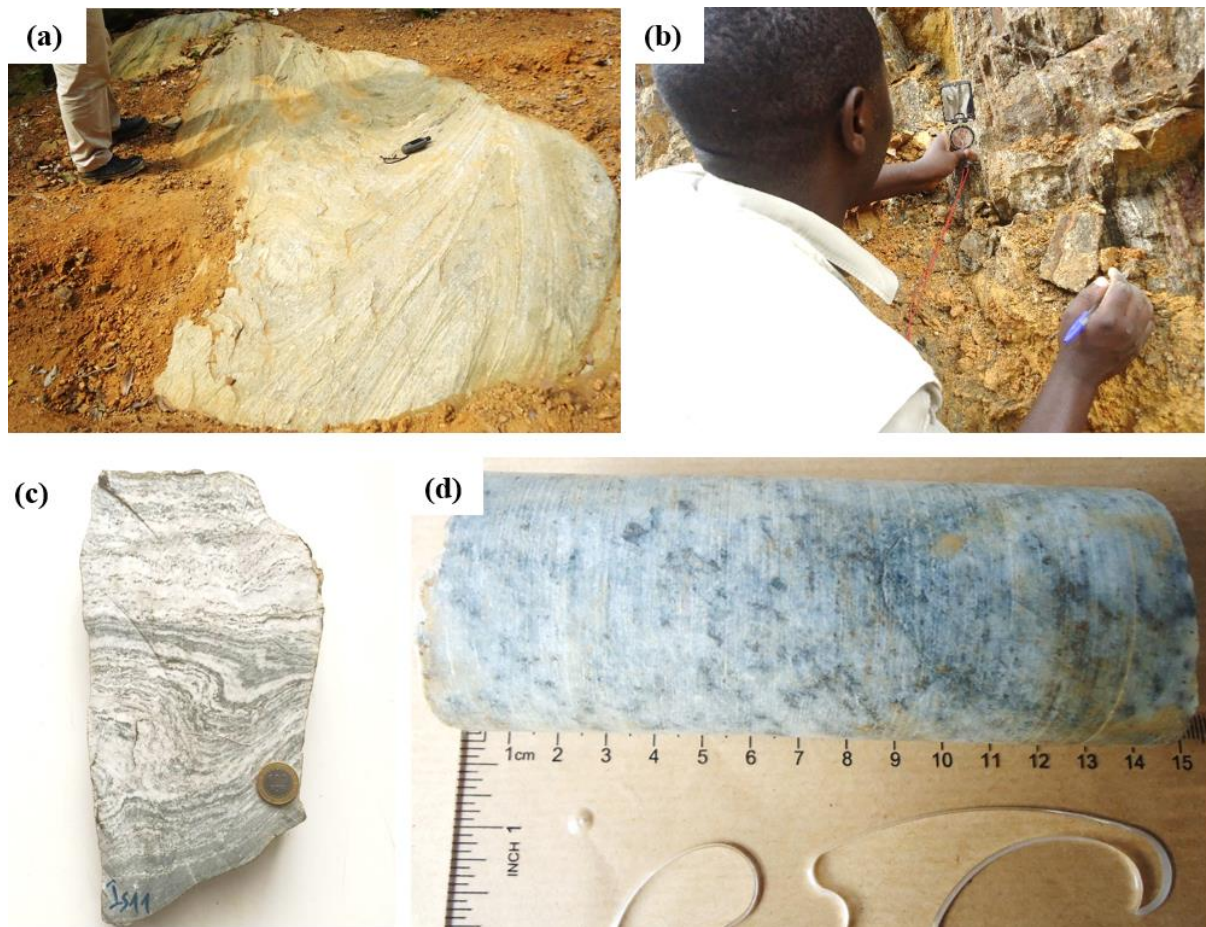


**Figure 11.** Petrographic features of pyroxene biotite gneiss a) Shallow dipping outcrop gneiss occurring as slabs to the north of the deposit b) Steeply dipping outcrop occurring as road cutting to the south of the road deposit; c) Hand specimen of folded and foliated pyroxene biotite gneiss; d) Drill core of pyroxene biotite gneiss.

**Pyroxene** (5-10 mod.%) consists of orthopyroxene and clinopyroxene. Clinopyroxene occurs as anhedral crystals and are greenish under plane polarised light. Orthopyroxene is anhedral, with crystal sizes from  $0.2 \times 0.1\text{mm}$  to  $2 \times 1\text{mm}$  (Fig. 12d). Some crystals are riddled with inclusions of quartz and opaque (Fig. 12f). They are in frequent association with quartz, feldspar and biotite. Clinopyroxene shows alteration to amphibole around the peripheries (Fig. 12d). Pyroxene is also found, being transformed into an opaque mineral (Fig. 12d).

**Opaque minerals** (5-10 mod.%) are disseminated in the rock matrix and appear as anhedral crystals. The grain sizes vary from sub-millimeter to millimeter and occur as inclusions within quartz, pyroxene and perthitic feldspar (Fig. 12a-f).



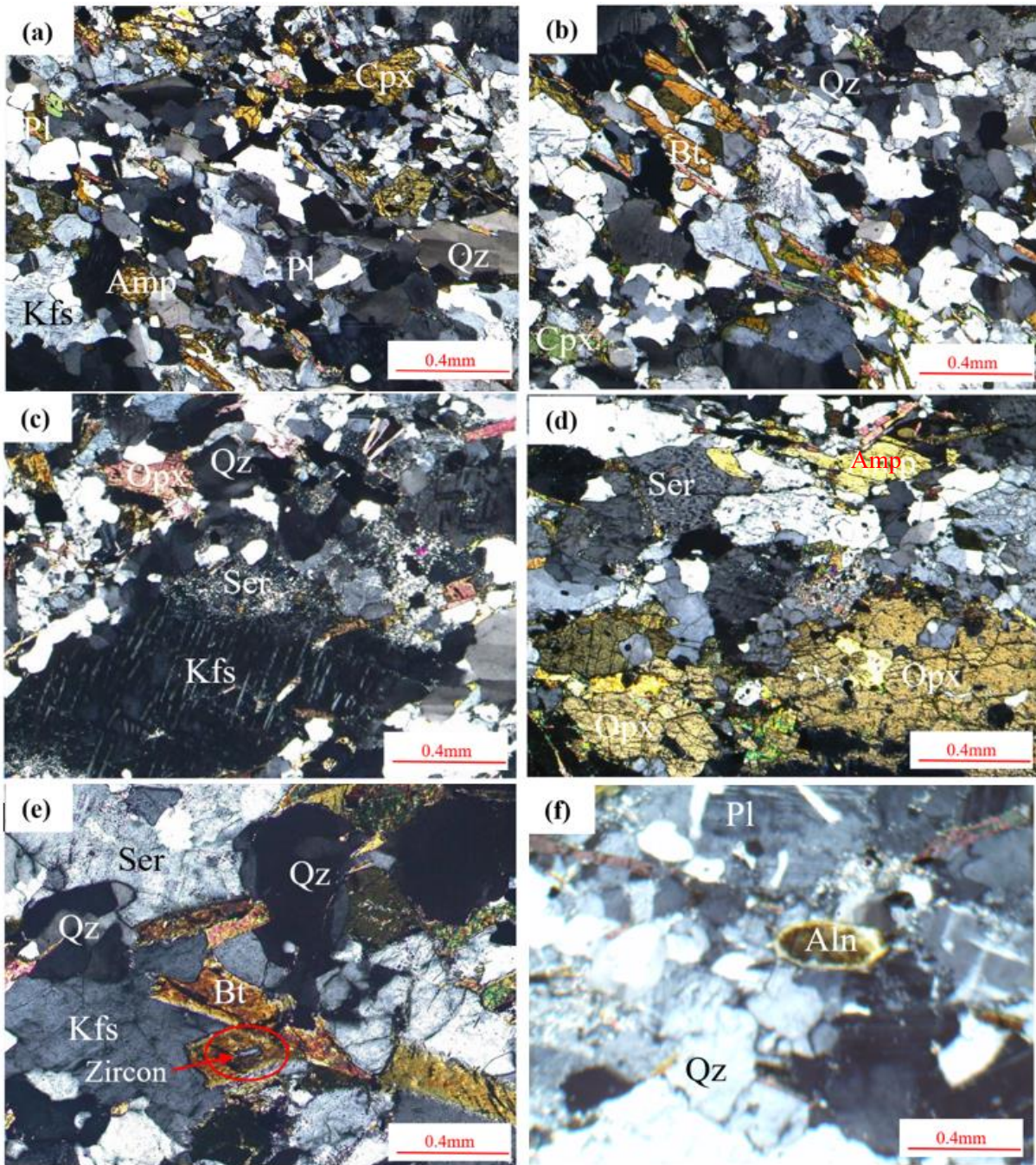


**Figure 12.** Photomicrographs of pyroxene biotite gneiss under crossed polars a) showing microbanding and mineral lineation, with granoblastic heterogranular texture (b) granoblastic heterogranular microstructure also showing banding and an association of quartz, clinopyroxene and acicular biotite crystals c) Perthitic feldspar porphyroblasts in association with orthopyroxene and Quartz d) Photograph showing orthopyroxene megacrystal e) Photograph showing biotite crystal with zircon crystal as inclusion f) Allanite inclusion within plagioclase.

**Allanite** (<1 mod.%) is oval-shaped with a radioactive auriol (Fig. 12f). Crystal size is  $0.3 \times 0.6$  mm and occurs as an inclusion within plagioclase.

**Zircon** (<1 mod.%) is accessory, and found as inclusion in biotite crystals (Fig. 12e).

### III.2.2 Epidote gneiss

Epidote gneiss sample (IS16) was collected from hole TD46 at 70.30 m (Table 4). Core specimen is dark grey, foliated and generally fine-to-medium grained. Visible minerals are quartz, epidote, and feldspar (Fig. 13a). Under the microscope, the rocks show banding with quartz-rich bands alternating with epidote-rich bands (Fig. 13b and c). Texture is granoblastic heterogranular consisting of quartz, alkali feldspar and epidote.

**Quartz** (20-30 mod.%) is fine-to medium grained < 0.5 mm and appears as stretched aggregate crystals (Fig.13 b and c) in association with epidote and alkali feldspar (Fig. 13d). Quartz also occurs as quartz veins (Fig. 13c); the process of silicification. Minute quartz crystals are found as inclusions within the epidote minerals.

**Epidote** (20-30 mod.%) is generally fine-grained (~0.1 mm long), and are found concentrated within the epidote-rich band (Fig. 13b, c, e and f).

**Alkali Feldspar** (10-15 mod.%) consists of coarse grained, anhedral perthitic plagioclase crystals (1mm x 1.5 mm). they are mostly found undergoing sericitisation and are closely associated with quartz and epidote crystals (Fig. 13d).

**Sericite** (10-15 mod.%) is very fine-grained, mostly found associated with epidote and quartz. It is a secondary mineral from the alteration of K-feldspar (Fig. 13 c, d). Wallrock alteration therefore associated here is that of epidotisation, sericitisation and silicification.

### III.2.3. Mafic granulite

Twenty mafic granulite core samples were initially collected at various depths (Table 5). Samples IS17 and IS20 were collected from hole TD46 at 93.50 m and 236.40 m respectively. Sample IS26 was collected from hole TD47 at 159.0 m and sample IS40 from hole TE9 at 138.40 m.

Drill core specimen is dark grey with coarse pyroxene grains associated with garnet crystals (Fig.14a).



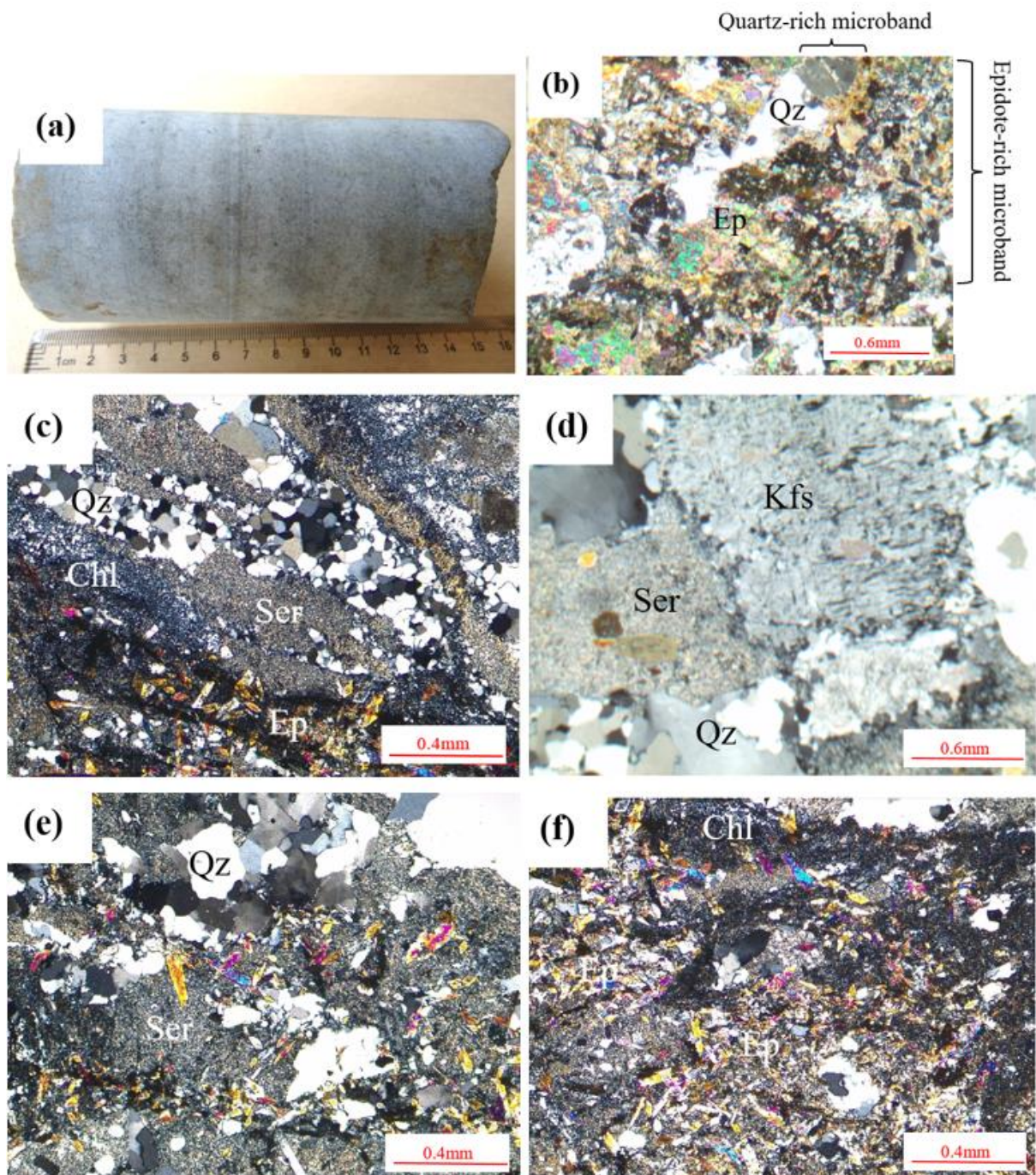


**Figure 13.** Photographs of Epidote gneiss. a) Drill core of Epidote gneiss b) and c) Photomicrographs of epidote gneiss showing microbanding (XPL) d) Photomicrograph showing alkali feldspar undergoing sericitisation e) Photomicrograph of epidote gneiss showing quartz, epidote, and sericite in association f) Photomicrograph of epidote gneiss showing chlorite, epidote and sericite association.

In thin section, the rock shows a granoblastic heterogranular microstructure consisting of pyroxene, garnet, quartz, plagioclase, opaque, amphibole, and zircon (Fig. 14b- f).

**Pyroxene** (35-40 mod.%) occurs as clinopyroxene (inclined extinction) and orthopyroxene (parallel extinction). Crystals are subhedral and of variable sizes, with the largest having dimensions between  $2 \times 1$  mm and  $3 \times 2$  mm. They are associated with garnet, amphibole, and quartz, but sometimes with garnet and plagioclase (Fig. 14b-f). Some pyroxene crystals contain opaque inclusions (Fig. 14e and f). Pyroxene crystals also show transformation into amphibole and opaque minerals along their rims and cleavages (Fig. 14b, e and f). At some points, pyroxene reacts with garnet at the peripheries to produce amphibole (Fig. 14d).

**Garnet** crystals (30-35 mod.%) are rounded (Fig. 14d), and medium- to coarse-grained ( $0.2 \text{ mm} \times 0.3 \text{ mm}$  to  $0.8 \text{ mm} \times 1.5 \text{ mm}$ ). Garnet crystals often bear reaction corona around the rims (Fig. 14d, e and f). Some garnet porphyroblasts contain several biotite, quartz, opaque and zircon inclusions (Fig. 14d, e and f). Most pyroxene and opaque crystals are in the process of transformation. Garnet crystals are associated with quartz and plagioclase (Fig. 14d). Garnet crystals contain minute zircon, quartz and opaque inclusions showing internal schistosity (Fig. 14d).

**Quartz** (5-10 mod.%) is fine to coarse grained (0.2-1 mm in diameter) and either appears as aggregates mixed with opaque minerals, or is found occupying interstices between minerals, usually garnet, pyroxene and sometimes biotite. Quartz also occurs as minute inclusions in garnet and pyroxene (Fig. 14d, e and f).

**Plagioclase** (<5 mod.%) is anhedral, fine-to medium grained (up to 1 mm) and shows transformation into sericite (Fig. 14d). It is mostly found, being formed around the peripheries of garnet crystals (Fig. 14d and e).

**Opaque minerals** (5-10 mod.%) occur as inclusions within pyroxene, garnet and amphibole (Fig. 14b-d). Some opaque minerals (Fig. 14b, c and f) show borders with corona.

**Zircon** (<0.1 mod.%) is anhedral and occurs as anhedral inclusions within garnet crystals (Fig. 14d and e).



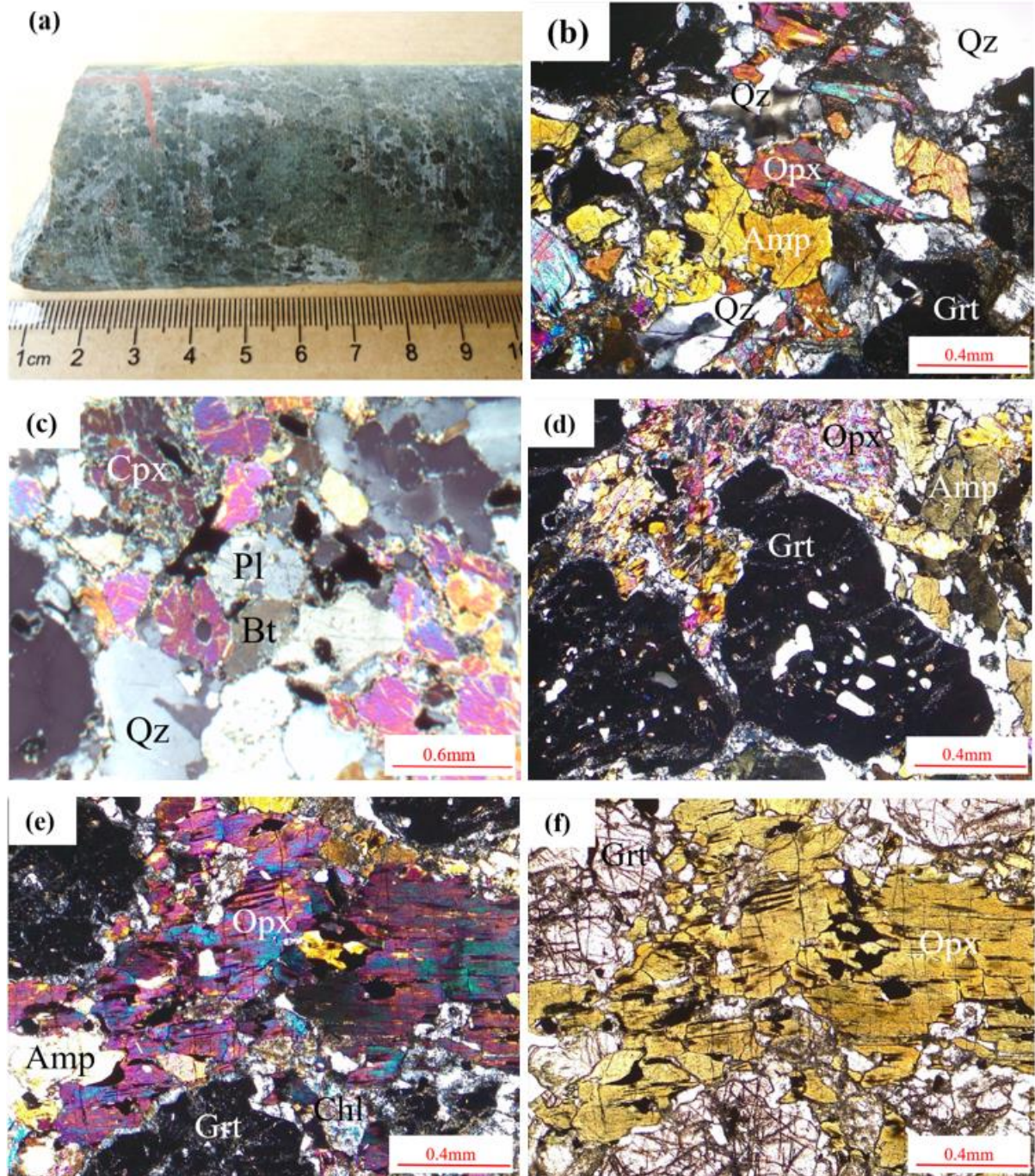


**Figure 14.** Photograph of drill core sample and photomicrographs of mafic granulite. a) Drill core b and c) Granoblastic heterogranular microstructure showing various mineral associations. c) Garnet with corona around borders d) Garnet contains quartz inclusions e) Pyroxene megacrystal in association with garnet (XPL) f) Pyroxene megacrystal in association with garnet (PPL).

#### III.2.4. *Garnet amphibolite*

Twenty four garnet amphibolite samples were initially collected at various depths from 4 different holes (Table 4). Sample IS15b was collected from hole TH31 at 77.30 m. Samples IS24, IS27b and IS28 were collected from hole TD47 at 25.90 m, 197 m and at 327

m respectively. Both samples IS37 and IS39 were collected from TE9 at 134.2 m and 136.7 m respectively while sample IS33 was collected from hole TE6 at 95.5 m. In drill core (hand specimen), garnet amphibolite is greenish brown and medium to coarse grained. Visible minerals are garnet, amphibole and pyroxenes (Fig. 15a). Whitish quartz specks are also visible.

In thin section, garnet amphibolite shows granoblastic heterogranular texture with garnet, amphibole, quartz, pyroxene, and biotite as main constituents and accessories minerals comprising opaque, and rutile.

**Amphibole** (55-65 mod.%) is green hornblende. It is the most abundant ferromagnesian mineral in the rock. It appears as large subhedral to anhedral crystals (Fig. 15b-f) of variable dimensions (0.4 mm × 0.6 mm to 1.5 mm × 2.5 mm). Some amphibole crystals show destabilization into biotite and opaque along cleavages (Fig. 15b and e). Amphibole is mostly associated with garnet, pyroxene, quartz and opaque.

**Garnet** (10-15 mod.%) appears as anhedral, heavily fractured porphyroblasts (Fig. 15b, c and d). Grain sizes vary from 0.2 mm × 0.5 mm to 1 mm × 2 mm. It contains quartz inclusions, defining an internal schistosity (Fig. 15c). Garnet is generally associated with pyroxene, amphibole and quartz crystals (Fig. 15b, c and d).

**Quartz** (5-10 mod.%) is anhedral and crystal sizes are generally inframillimetric to millimetric. The larger crystals (0.2 × 0.5 mm) are associated with amphibole, pyroxene and opaque crystals (Fig. 15b, c, d and f), while the microcrystals are found in the interstices between minerals (Fig. 15b-f). Some crystals are found as inclusions in garnet porphyroblasts (Fig. 15c and d).

**Pyroxene** (10-15 mod.%) is represented by orthopyroxene. Pyroxene crystals are generally anhedral and frequently associated with amphibole, garnet, and quartz crystals (Fig. 15b, c and f). Pyroxene crystals are of variable sizes but are generally fine to medium grained ( $\leq 0.6$  mm × 0.8 mm).



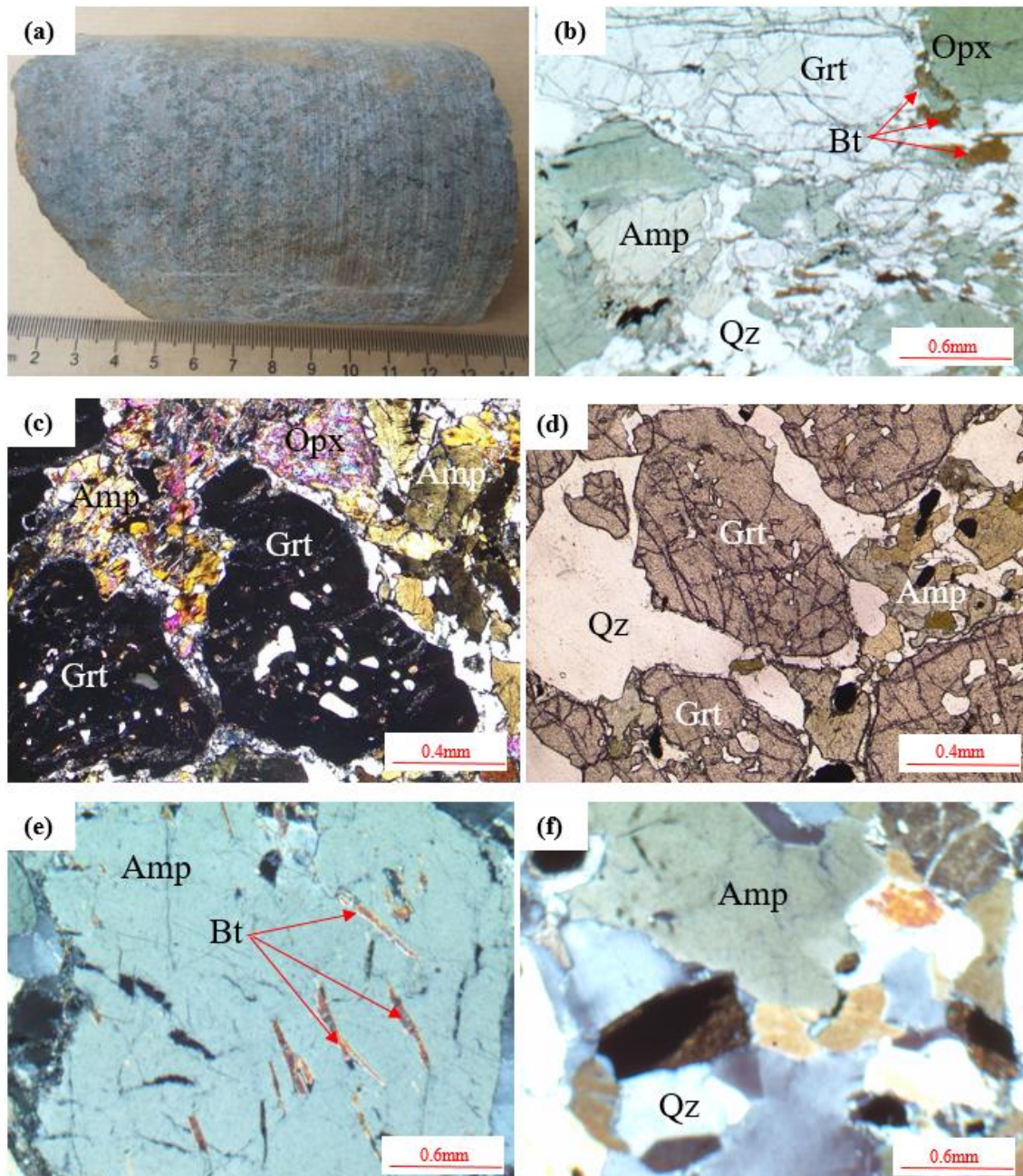


**Figure 15.** Drill core sample and photomicrographs of Garnet amphibolite. a) Drill core. b) Photomicrograph of garnet amphibolite showing various mineral associations (PPL), c) Photomicrograph of garnet porphyroblast with plagioclase corona showing quartz and rutile inclusions (XPL), d) Garnet porphyroblast with quartz and opaque inclusions (PPL). e) photomicrograph showing transformation of amphibole into biotite needles along fractures. f) Photomicrograph of garnet amphibolite showing opaque mineral crystals with rutile corona.

**Biotite** (<5 mod.%) appears as a secondary mineral derived from amphibole (Fig. 15b and e). It is found either at the rims of amphibole, or within amphibole porphyroblasts as small lamellae (Fig. 15e).

**Opaque** (<5 mod.%) are anhedral and appear as minute inclusions (<0.2-0.5 mm) in garnet and amphibole crystals or along their rims (Fig. 15b-f). Opaque crystals also occur as corona around rutile crystal rims (Fig. 15f).

**Rutile** (<1 mod.%) is anhedral and occurs as fine crystals (<0.2-0.4 mm). These crystals are mostly associated with opaque minerals and mostly constitute a corona around the opaque minerals (Fig. 15f).

### ***III.2.5. Iron formations***

The Anyouzok IFs comprise banded iron formations (BIFs) and sheared banded iron formations (SBIFs).

#### ***a) Banded iron formations (BIFs)***

Four BIF samples were collected from 46.71 m to 48 m (IS13, IS50, IS51, IS52) from hole 22. Core specimen is medium to fine grained, foliated and made up of alternating white silica rich bands and dark magnetite rich bands (Fig. 16a). The white bands range from 1 mm-10 mm while the dark bands range from 2 mm-16 mm in thickness. Seven thin sections were prepared from these samples.

In thin section, the rock portrays a granoblastic heterogranular microstructure consisting of quartz, magnetite, amphibole, pyrite, biotite, chlorite and hematite (Fig. 16b-e).

**Magnetite** (30 mod.%) is fine (0.5 x 0.5 mm in average), anhedral and in association with quartz, biotite and amphibole which exists as tremolite and actinolite (Fig. 16c). Magnetite sometimes intergrows with pyrite and less likely with hematite (Fig. 16d). Some magnetite crystals contain minute quartz inclusions (Fig. 16b and c).

**Amphibole** (15 mod.%) crystals are generally stretched, occurring as tremolite and actinolite. Tremolite and actinolite range from 1-1.5 mm in diameter (Fig 16c and e). They are mostly found partly altered into chlorite and contain diffuse magnetite inclusions (Fig. 16c and e).

**Biotite** (1 mod.%) is anhedral, closely associated with amphibole, magnetite and less frequently quartz. It is generally fine to medium grained (0.25 x 0.5 mm). It sometimes shows transformation into chlorite, mostly along the rims (Fig. 16c).

**Quartz** (50 mod.%) crystals are anhedral and in close association with amphibole, magnetite and biotite. Quartz is also coarse grained, constituting quartz-rich bands (Fig. 16b and e).

**Pyrite** (2 mod.%) is fine to medium grained, yellowish brown anhedral to subhedral. It is mostly associated with magnetite, where it mostly grows around the peripheries of magnetite crystals (Fig. 16c).



**Hematite** (<1 mod.%) is brownish and occurs as traces of intimate intergrowths with pyrite and magnetite. It is also found around the rims of magnetite megacrystals (Fig. 16d).

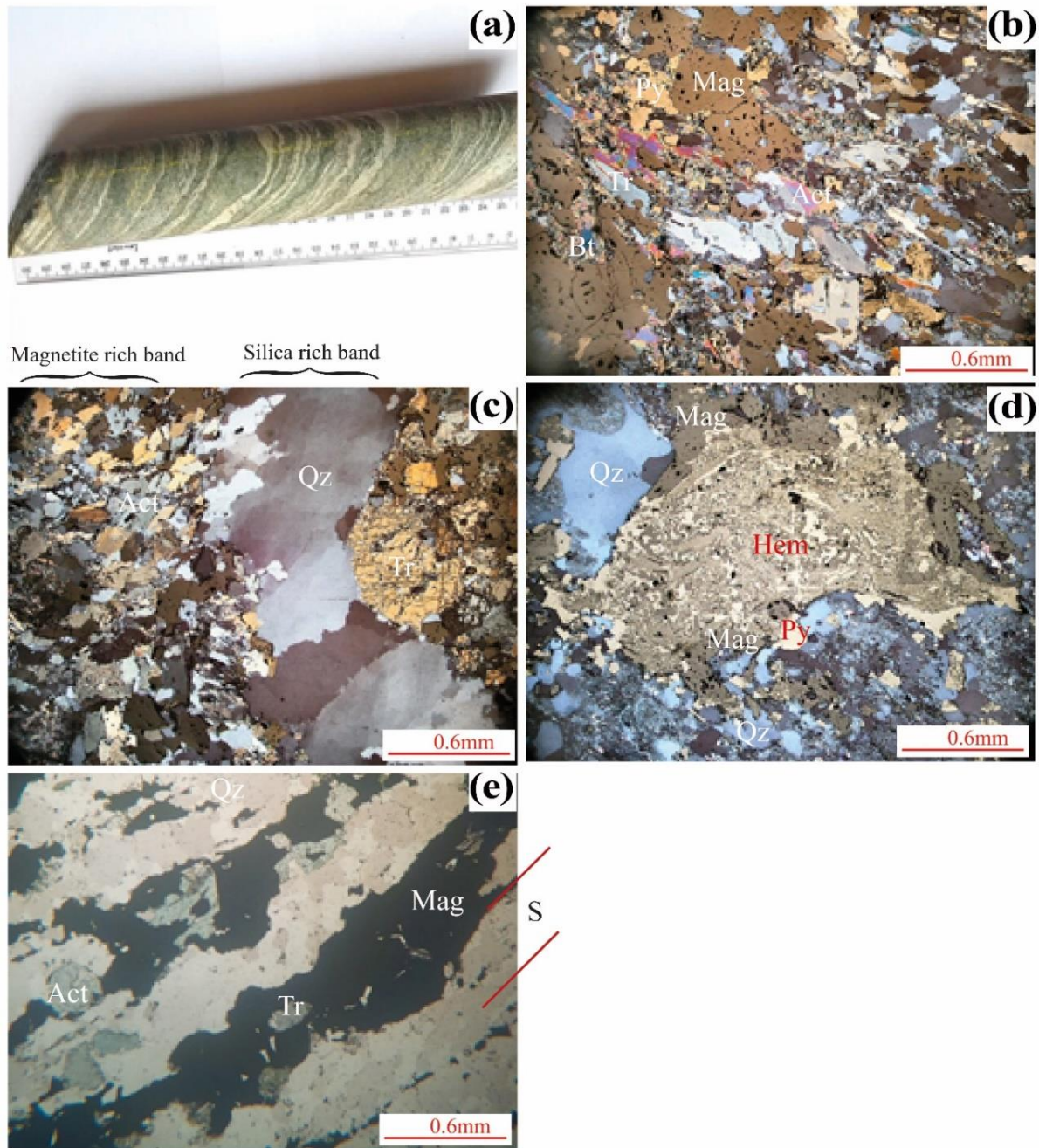


**Figure 16.** Drill core samples and photomicrographs of BIFs. (a) Drill core (hand specimen) of Banded iron formation (BIF) showing alternating silica and magnetite rich bands; (b) photomicrograph (partially crossed and reflected light) of BIF showing mineral composition; (c) Photomicrograph (polished section) of BIF showing Magnetite-rich microbands alternating with quartz and actinolite/tremolite-rich microbands (d) anhedral magnetite crystal partially replaced by hematite and pyrite; (e) Photomicrograph showing microbanding.

*b) Sheared banded iron formations (SBIFs).*

Eight SBIF samples were collected from holes TD65 at 25.50 m (IS 54), TD46 at 212.65 m (IS19), TD46 at 154.30 m (IS18), hole TE6 at 155.80 m (IS35), hole TE9 at 173.70 m (IS41), TE47 at 150 m (IS31) and TE47 at 159 m (IS42). SBIF in hand specimen is dark grey, medium to coarse grained, massive, highly strained, and mainly composed of magnetite and quartz (Fig. 17a). Eight thin sections were made from these samples.

In thin section, the rock shows mylonitic and granoblastic heterogranular textures (Fig. 17b, c and d), consisting of magnetite, quartz, amphibole, plagioclase, ilmenite, biotite, chlorite, calcite and K-feldspar. **Magnetite** (60 mod.%) is anhedral to subhedral, with very few euhedral grains (Fig. 17b). It contains several cavities and is occasionally altered to ilmenite (Fig. 17c). Magnetite is closely associated with quartz, amphibole, biotite, K-feldspar and plagioclase. Where magnetite crystals lack cavities, quartz is found as minute inclusions.

**Ilmenite** (2 mod.%) is anhedral, medium to coarse grained ( $0.5 \times 1$  mm), found within the core of magnetite (Fig. 17c).

**Quartz** (20 mod.%) is anhedral, generally coarse-grained and associated with magnetite and amphibole. (Fig. 17b-d).

**Plagioclase** (2 mod.%) is anhedral, medium to coarse-grained (1-1.5 mm). It is closely associated with magnetite, K-feldspar and quartz (Fig. 17b). Plagioclase is altered into sericite.

**K-feldspar** (<1 mod.%) is anhedral, medium to coarse grained (1-1.5 mm) and is associated with magnetite, biotite and quartz (Fig. 17b). Like plagioclase, the crystals are altered into sericite.

**Amphibole** (10 mod.%) occurs as medium to coarse crystals which occur as tremolite and actinolite (Fig. 17d). Tremolite and actinolite are closely associated to magnetite and quartz. The amphibole megacrystal also contains quartz inclusions (Fig. 17d).

**Biotite** (2 mod.%) is lamina, fine- to medium-grained, associated with plagioclase, K-feldspar, quartz and to a lesser extent magnetite (Fig. 17b).

**Calcite** (1 mod.%) is anhedral, generally found at the rims of magnetite crystals (Fig. 17c).

Characteristics of the respective lithological units were summarized below, in Table 6. From the respective mineral assemblages portrayed by each rock type, the Anyouzok rocks have registered metamorphic conditions of the amphibolite, granulite and green schist facies (Table 6).



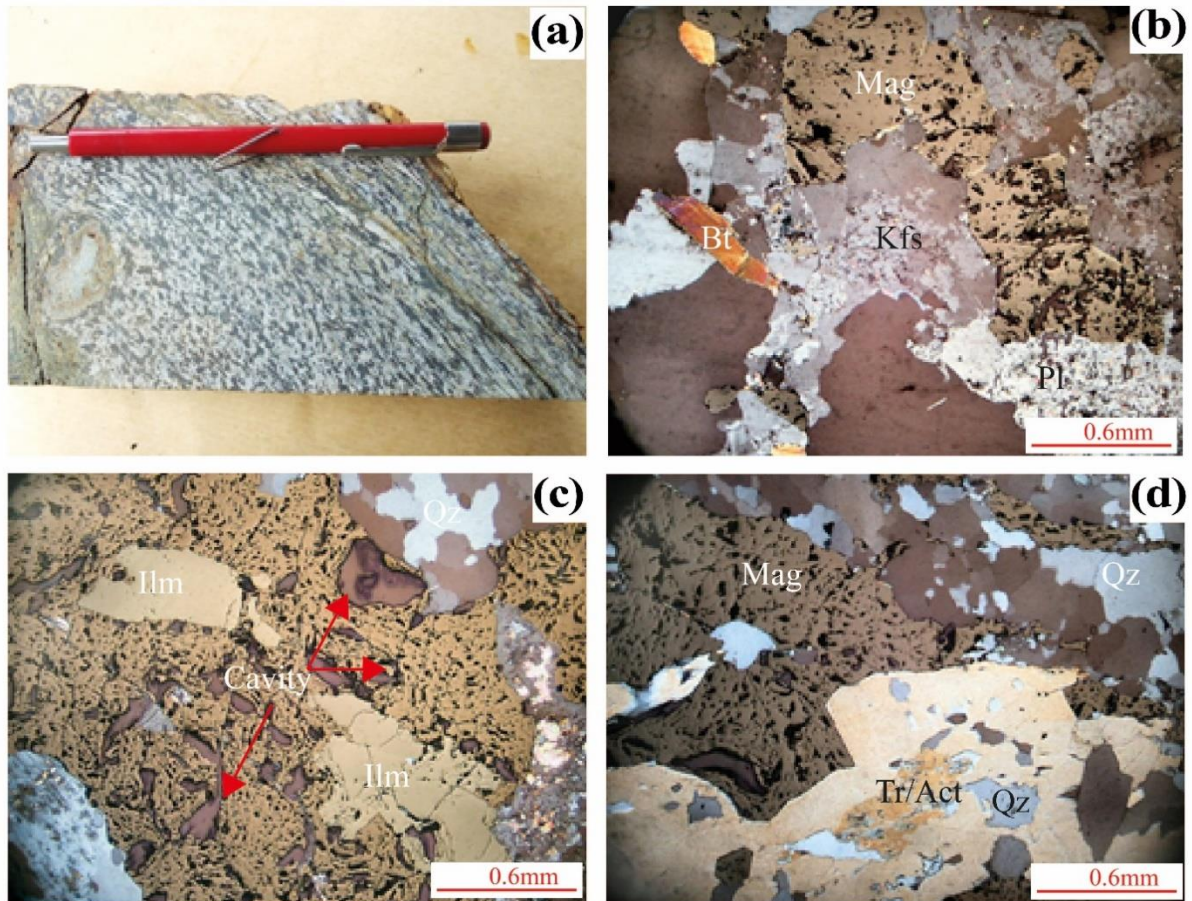


**Figure 17.** Drill core sample and photomicrographs of SBIF. (a) Hand specimen of SBIF; (b) granoblastic magnetite associated with biotite and intensely sericitized plagioclase and K-feldspar; (c) Anhedral magnetite exhibiting cavities in association with ilmenite and secondary calcite; (d) Photomicrograph showing quartz-amphibole-magnetite association with amphibole and development of tremolite/actinolite during metamorphism.

**Table 6.** Petrographic characteristics of the Anyouzok geologic formations

Petrographic type	Outcrop mode	Microstructures	Mineral associations	Facies
Pyroxene biotite gneiss	Road cutting	Granoblastic heterogranular	i) Qz + Bt + Kfs + Opx + Cpx ii) Qtz + Amp + Sph	- Granulite - Amphibolite
Epidote gneiss	Found exclusively in drill core		Qz + Ep + Pl	- Amphibolite
Mafic granulite	Boulders and domes		(i) Cpx + Opx + Grt + Qz + Pl (ii) Amp + Opq	- Granulite - Ampibolite
Garnet amphibolite			Grt + Amp + Pl + Qz + Bt	- Amphibolite
BIF	Found exclusively in drill core.		Mag + Tr + Act + Bt + Qz + Py + Hem	- Greenschist
SBIF	Road cuttings and as domes		(i) Mag + Il + Qz + Pl + Kfs + Bt (ii) Mag + Qz + Cal + Ser + Tr + Act	- Amphibolite - Greenschist

### III.2.8. Ore types

Based on state, texture, and competence, four main iron ore types have been identified at the Anyouzok iron ore deposit, namely the blue dust and the foliated hematite BIF which are all weathered products of supergene enrichment, the banded magnetite iron formation ore material and the massive to sheared BIF magnetite ore (Fig. 18).

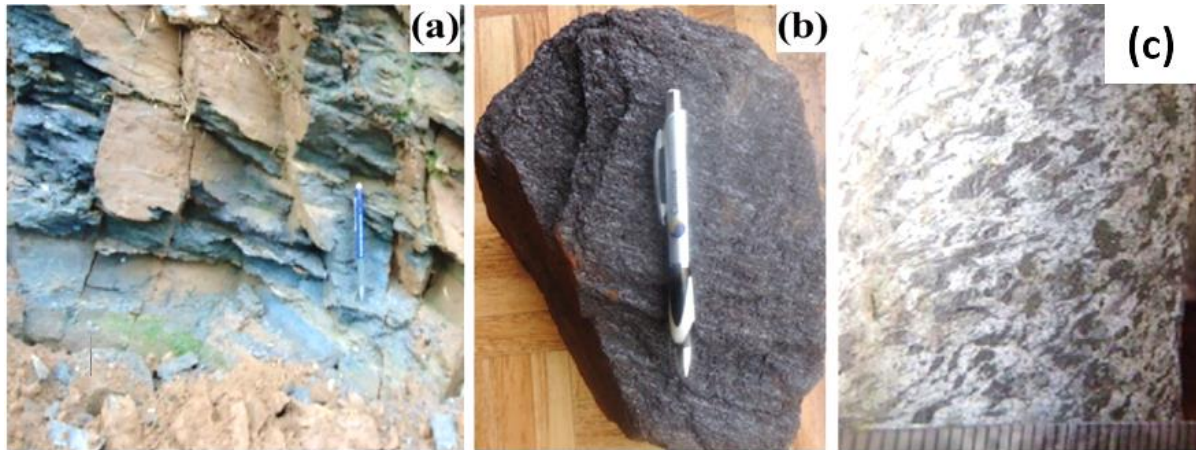


**Figure 18.** Photography of ore types. a) Blue dust outcrop on the hill flanks of the northern prospect b) Hand specimen (grab sample) of hematite-rich ore (spongy) with thin quartz bands. c) Disseminated magnetite ore

#### a) Blue dust

Blue dust is steel grey in colour and occurs near the top of the ore horizon as thin, but persistent beds (Fig. 18a). It is made up of fragile laminated, fine powdery material, mostly rich in hematite and martite. Hematite and martite originate from desilicification of banded iron formation. This occurs mostly at the base of slopes and within fracture pockets where there is abundant water especially during the wet seasons and leaching is constant and effective.

#### b) Foliated hematite ore

Foliated hematite ore is dark brown and foliated, showing hematite-rich bands alternating with laminated tinny quartz bands (Fig. 18b). The ore is fragile (biscuity), and very porous (spongy) due to leaching of silica and other mobile material.

#### c) Disseminated magnetite ore

Based on surface area intercepts encountered during drilling, this is the main (abundant) iron ore type of the Anyouzok deposit. It is dark grey in colour, and fine- to medium grained. It may be massive, weakly, or highly strained. Magnetite contents range of between 45% and 60%.

### III.3. Mineralogy of IFs

Considering the relatively simple mineralogy of the BIF and SBIF, compared with the complex country rock mineralogy of the country rocks, X-ray diffraction analysis method was used in this work to determine the mineralogical composition of BIF and SBIF (Table 7).

**Table 7.** Table summarising characteristic peak values for all minerals detected through X-ray diffraction (XRD) for BIF and SBIF.

Sample code	Mineral phase	Chemical Formula	D-Spacing (Å)
<b>Banded iron formation (IS51)</b>	Magnetite	$\text{Fe}_3\text{O}_4$	2.53, 2.97, 1.72, 1.62, 1.42
	Quartz	$\text{SiO}_2$	4.26, 3.34, 2.24, 2.13, 1.82, 1.67, 1.54
	Hematite	$\text{Fe}_2\text{O}_3$	1.49, 1.45, 2.7, 2.519, 1.69
	Pyrite	$\text{FeS}_2$	2.42, 1.92, 1.63
	Tremolite	$\text{Ca}_2\text{Mg}_5\text{Si}_8\text{O}_{22}(\text{OH})_2$	8.37, 2.70
	Actinolite	$\text{Ca}_2(\text{Mg,Fe})_5\text{Si}_8\text{O}_{22}(\text{OH})_2$	4.52, 3.27, 3.11, 8.41, 2.70
	Biotite	$\text{K}(\text{Mg,Fe})_3\text{AlSi}_3\text{O}_{10}(\text{F,OH})_2$	10.10, 2.45
<b>Sheared banded iron formation (IS30)</b>	Magnetite	$\text{Fe}_3\text{O}_4$	2.97, 2.53, 2.10, 1.72, 1.62, 1.42
	Quartz	$\text{SiO}_2$	4.26, 3.34, 2.24, 2.13, 2.02, 1.82, 1.67, 1.54
	Hematite	$\text{Fe}_2\text{O}_3$	3.68, 1.49, 1.45
	Pyrite	$\text{FeS}_2$	2.42, 1.91
	Tremolite	$\text{Ca}_2\text{Mg}_5\text{Si}_8\text{O}_{22}(\text{OH})_2$	2.7
	Chlorite	$(\text{Mg,Fe}^{2+})_5\text{Al}(\text{Si}_3\text{Al})\text{O}_{10}(\text{OH})_8$	14.11, 7.07, 4.72, 3.54, 2.84, 1.88, 1.56
	Biotite	$\text{K}(\text{Mg,Fe})_3\text{AlSi}_3\text{O}_{10}(\text{F,OH})_2$	10.10, 2.45, 2.00
	Calcite	$\text{CaCO}_3$	2.29, 2.10, 3.06, 2.85, 2.09
	K-feldspar	$\text{KAlSi}_3\text{O}_8$	3.77

#### III.3.1 XRD studies for BIF

Mineral phases identified in BIF as represented by sample IS51 (Table 7) were magnetite, quartz, hematite, pyrite, tremolite, actinolite, and biotite (Fig. 19a). Magnetite presents six mineral peaks, with a major peak at 2.53 Å. Quartz presents seven peaks, with major peak at 3.34 Å. Hematite presents major peak at 1.47 Å. Biotite and tremolite show trace occurrences with two peaks. Biotite shows major peak at 10.10 Å, while for tremolite, major peak occurs at 2.70 Å. Pyrite is represented by three peaks with major peak at 2.42 Å. Actinolite shows major peaks at 3.11 Å.

#### III.3.2 XRD studies for SBIF

SBIF is represented by sample IS30 (Table 7), with magnetite, quartz, hematite, pyrite, tremolite, chlorite, biotite, and K-feldspar as the mineral phases encountered (Fig. 19b). Magnetite, quartz, and hematite in SBIF like in BIF, present peak values at 2.53 Å, 3.34

Å and 1.47 Å respectively (Fig. 19a and b). Biotite shows peak value at 10.10 Å. Pyrite and tremolite show trace occurrences, with peak values of 2.42 Å and 2.70 Å respectively. Unlike in BIF, SBIF in addition, presents chlorite and K-feldspar minerals with peak values of 7.07 Å and 3.77 Å respectively (Table 7).

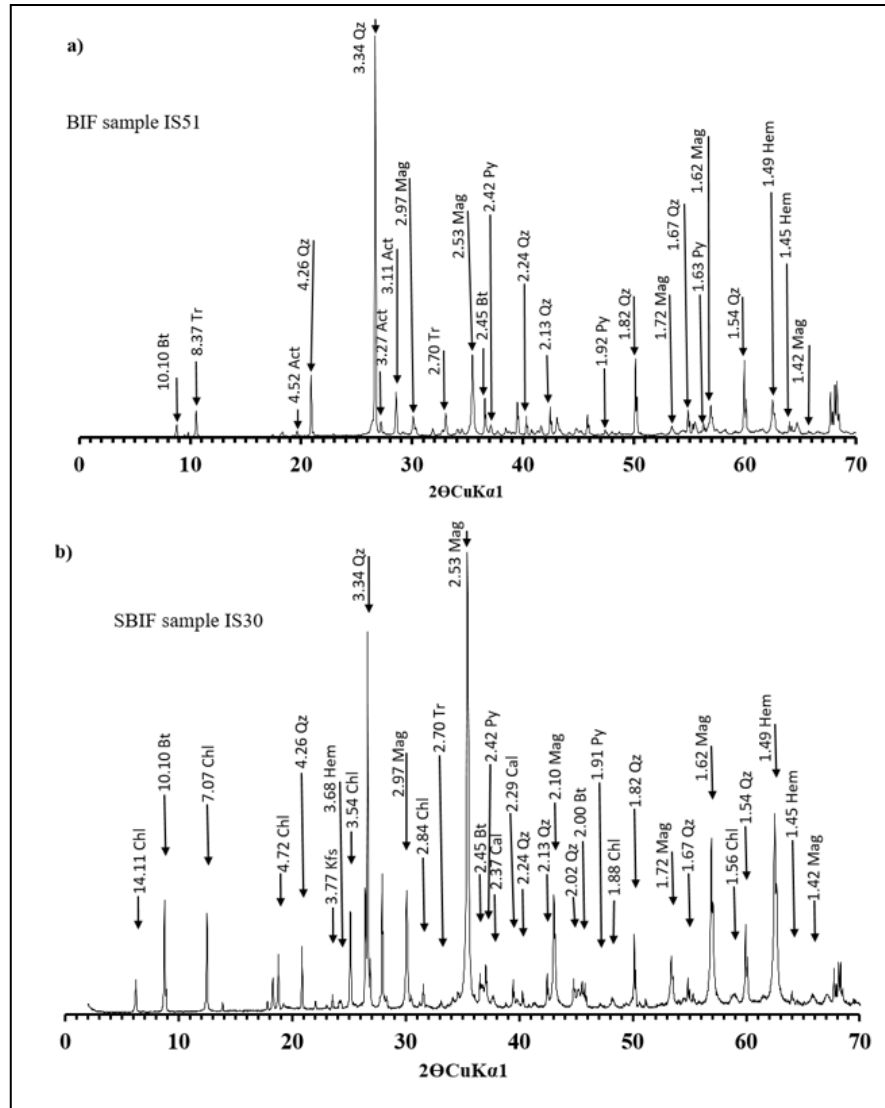


**Figure 19.** X-ray diffraction spectra for the Anyouzok BIF. (a) and SBIF (b) samples, indicating prominent quartz and magnetite peaks. Magnetite (Mag), biotite (Bt), hematite (Hem), quartz (Qz), chlorite (Chl), tremolite (Tr), actinolite (Act), pyrite (Py), Calcite (Cal).

#### III.4. Structural aspects of the Anyouzok iron deposit

Structural elements identified in the study area are foliations, folds and shear planes.

##### - Foliation

Compositional bedding (foliations) is observed in mafic granulite, garnet amphibolite, pyroxene biotite gneiss, and SBIFs, and are defined by alternating light quartz and feldspar



bands of millimeter thickness and dark biotite-rich bands of centimeter thickness (Fig. 20a). SBIFs portray a dominant  $S_2$  foliation, parallel to the  $S_1$  gneissic compositional layering (Fig. 20a). The  $S_1/S_2$  in the northern prospect represents an NW shallow-dipping composite fabric with a mean direction of  $N126^\circ E32^\circ NE$  (Fig. 22a and c), whereas, in the southern prospect,  $S_2$  (Fig. 22), which affected SBIFs and pyroxene biotite gneiss, is steeply dipping  $60\text{--}75^\circ$  towards the SW (Fig. 22b and c). The average direction of  $S_1/S_2$  is  $N145^\circ E66^\circ SW$ . The schistosity associated with the fold axial plane is underlined by the preferential orientation of feldspar, quartz and ferromagnesian crystals (Fig. 20d).

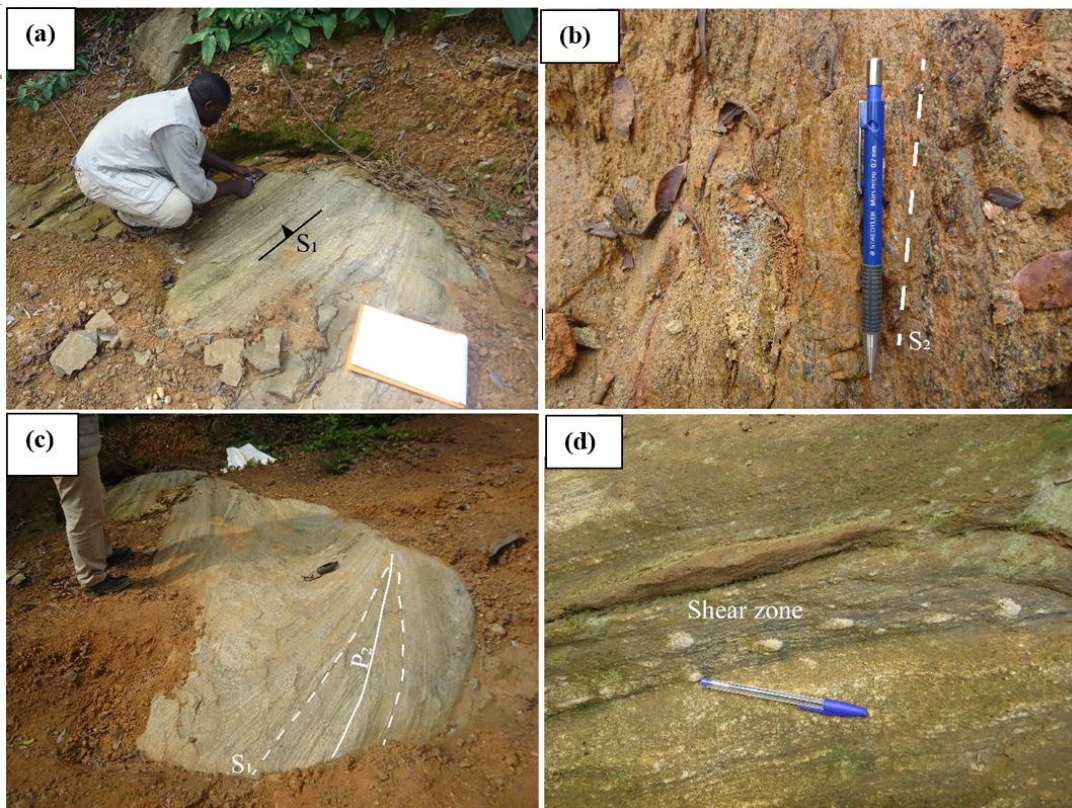


**Figure 20.** Structural features in pyroxene biotite gneiss and SBIF (a)  $S_1$  foliation in Pyroxene biotite gneiss; (b)  $S_2$  foliation in SBIF; (c)  $P_2$  fold in pyroxene biotite gneiss; (d) Shear zone in pyroxene biotite gneiss.



**Figure 21.** Brittle deformation (fracturing) in drill core, preserved in SBIF hole TH25.

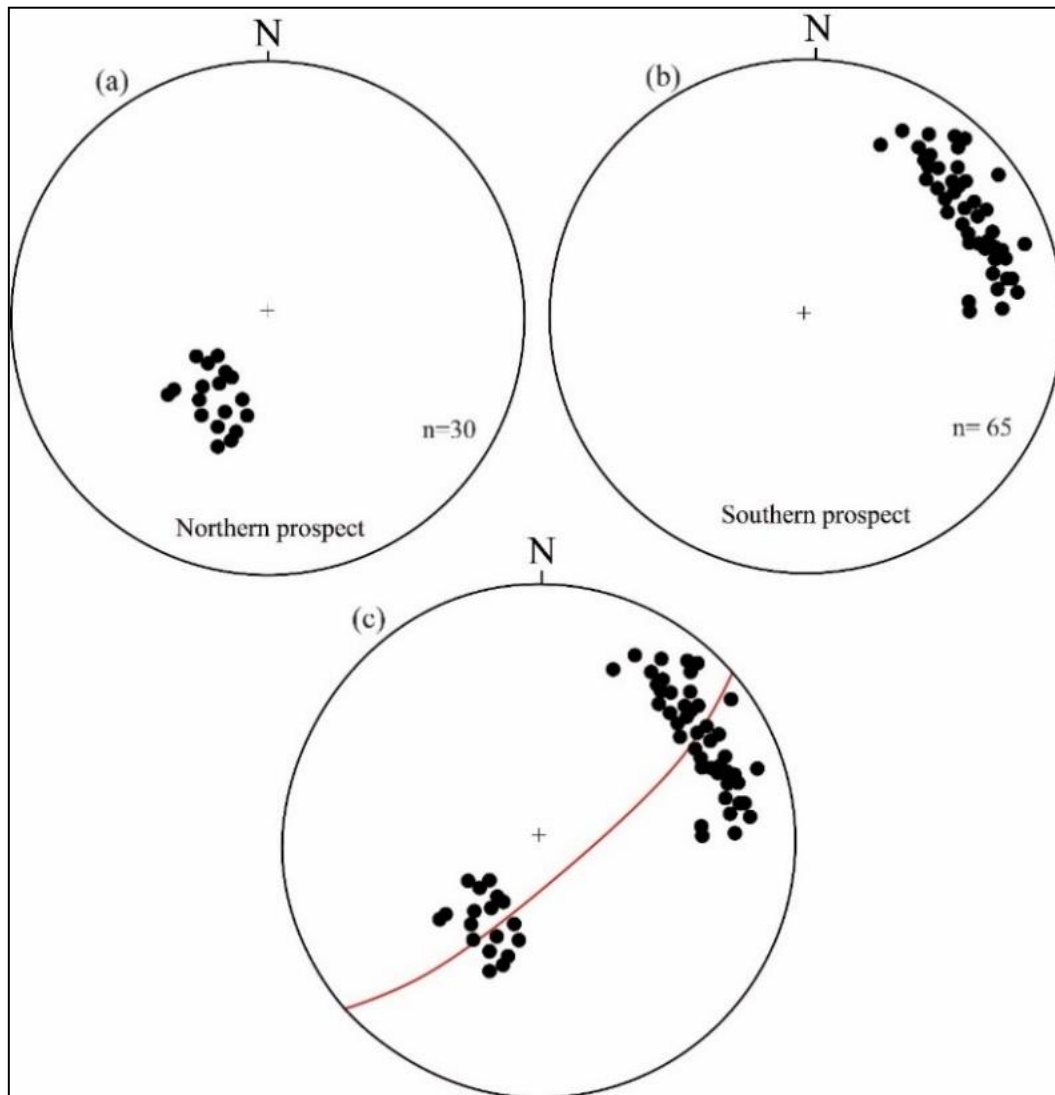


**Figure 22.** Stereonet projection of Anyouzok  $S_1/S_2$  foliations a) diagram of poles for Northern and b) southern prospect c) Northern and southern prospects combined.

#### - **Fold**

Variably oriented axial folds are observed on and pyroxene biotite gneiss (e.g. Fig. 20c). In pyroxene biotite gneiss, fold is manifested in quartz and feldspar minerals, with fold axis orientation of N50, 90.

#### - **Shearing**

Shearing is visible in feldspar megacrystals which are stretched and surrounded by pyroxenes which show pressure shadow zones. Sheared crystals are from 2.0 cm x 1.8 cm and 3.5 x 2.5 cm lengths and widths respectively. Shear plane measures N60, 48W and is slickensided,

indicative of movements. The C-planes are parallel to  $S_1/S_2$ , suggesting a component of layer parallel shearing (Fig. 20d).

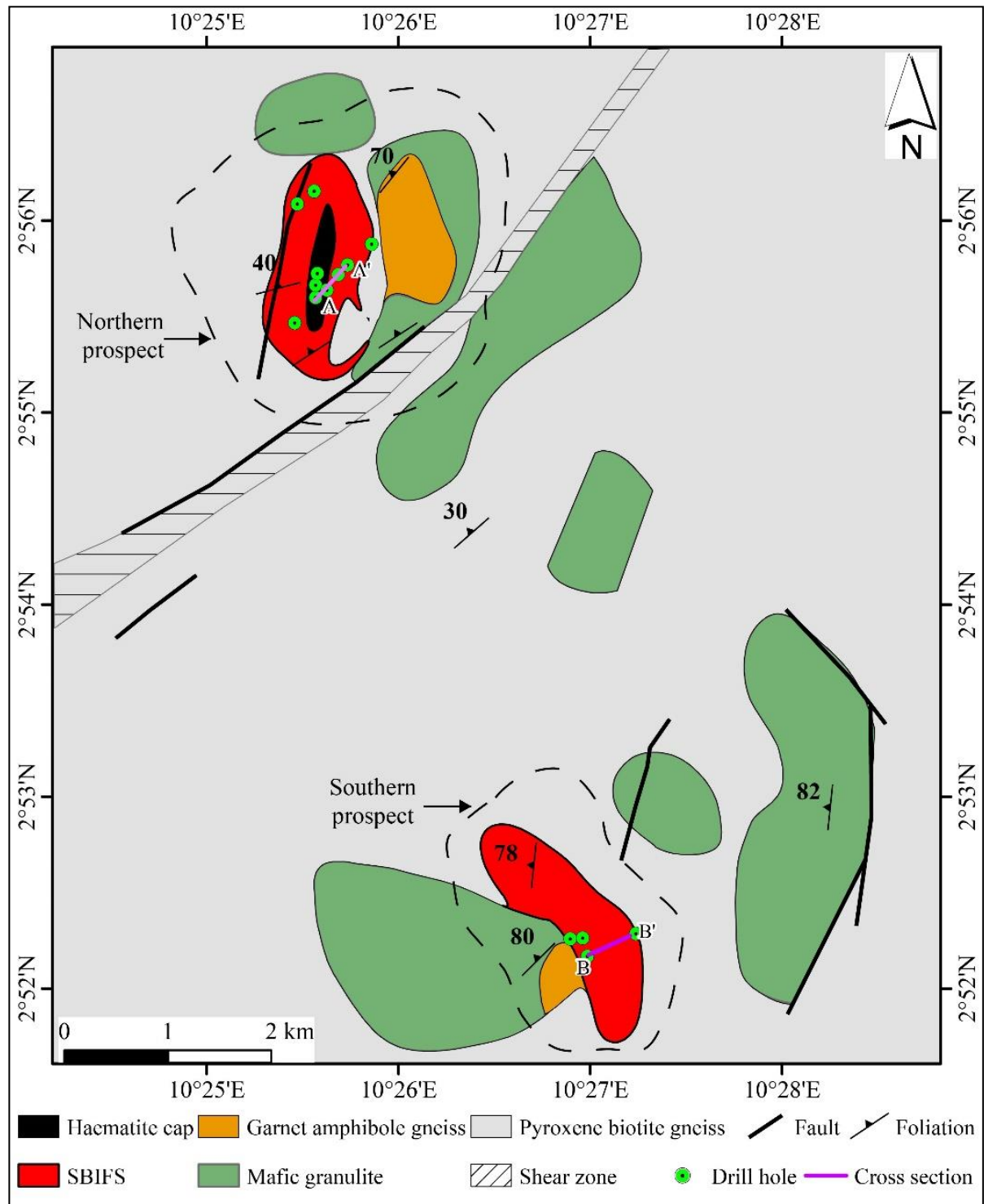


**Figure 23.** Sketch geologic map of Anyouzok area.

#### **- Brittle deformation (fracturing)**

Several moderate to low displacement fractures were identified in near surface drill core of pyroxene biotite gneiss and sheared BIF (Fig. 21, e.g. in hole TH25).

### **Conclusion**

The lithostratigraphy, petrography, mineralogy, and structural studies of the Anyouzok iron deposit reveal that the rocks are essentially metamorphic, made up of iron formations and the host rock units. The iron formations consist of BIF and SBIF while the host rock units are made up of pyroxene biotite gneiss, epidote gneiss, mafic granulite, and garnet amphibolite. The stratigraphic sections show some similarities and differences between the northern and the southern prospects. SBIF is intercepted in drillholes of both the northern and southern prospects. However, BIF is intercepted only on hole TE22 of the southern prospect. The holes of the northern prospect end mostly in mafic granulite as the basement, while the holes of the southern prospect end in pyroxene biotite gneiss as the basement. These rocks show heterogranular granoblastic and mylonitic microstructures with typical granulite and amphibolite facies assemblages. The lithostratigraphic and petrographic study revealed a geological outline of the study area (Fig. 23) which shows that over 60% of the surface area is covered by pyroxene biotite gneiss. Structurally, the rocks are foliated and shallow dipping within the northern prospect, while the rocks of the southern prospects are generally steeply dipping.



## **CHAPTER IV. GEOCHEMISTRY**

## Introduction

The geochemical characteristics of the various formations of the Anyouzok area are

presented in this chapter, to aid in deducing the deposition and enrichment processes, protolith of the country rock, possible depositional, and geotectonic environment. Still from the previous chapter (Chapter III), the geology of the Anyouzok area is made up of a metamorphic assemblage consisting of iron formations and the country rocks.

To determine the geochemistry of the various rock types, selected rock samples were analysed for major, trace and rare earth elements (REE). 15 samples were collected and analysed for country rock (Pyroxene biotite gneiss, mafic granulite, and garnet amphibolite) while 9 samples were collected and analysed for iron formation (BIF and SBIF).

### IV.1. Host rock geochemistry: Nature of Protolith

Whole rock geochemical compositions of fifteen representative host rock samples are recorded in Tables 8 to 12. The ternary plot (Fig. 24) of [De la Roche \(1965\)](#) shows that the study area is made up of metabasalts and arkoses to greywackes. In this diagram, pyroxene biotite gneiss follows a horizontal disposition with compositions close to those of greywackes and arkoses. The mafic granulite and the garnet amphibolite samples follow the dorsal trend and plot close to basalt.

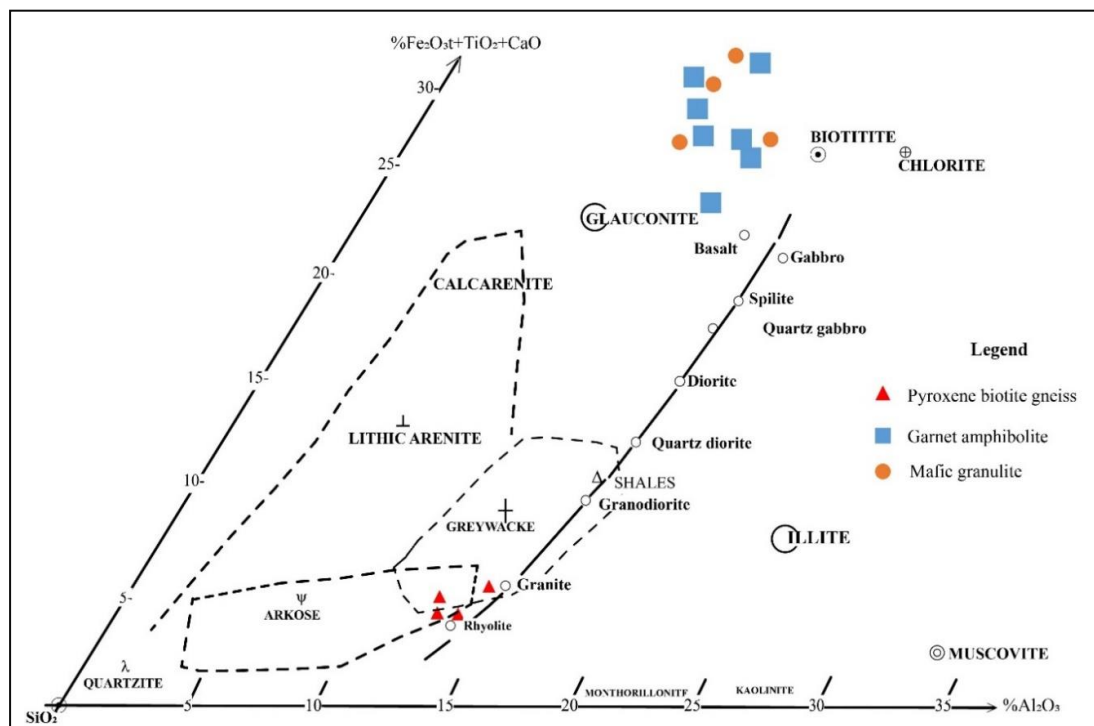


**Figure 24.** Protolith reconstruction and classification (after [De La Roche, 1965](#)) of Anyouzok country rocks, position of studied rock in the whole rock triangle ( $\text{Fe}_2\text{O}_3 + \text{TiO}_2 + \text{CaO}$ ) wt.% vs. ( $\text{Al}_2\text{O}_3$ ) wt.% showing meta-igneous and metasediment derived rock.

**Table 8.** Major element (wt.%) compositions of the Anyouzok metavolcanic rocks.

Rock type	Mafic granulite				Garnet amphibolite						
	IS20	IS40	IS26	IS17	IS15b	IS24	IS27b	IS28	IS33	IS37	IS39
SiO <sub>2</sub>	44.7	48.8	50.6	51.2	44.1	44.8	49.3	46.5	49.1	50.8	46.5
TiO <sub>2</sub>	0.57	0.9	2.24	1.77	1.84	0.64	1.37	1.46	1.34	0.99	0.77
Al <sub>2</sub> O <sub>3</sub>	14.25	14.75	11.95	13.5	12.9	14.05	13.2	14.35	12.05	13.3	13.65
Fe <sub>2</sub> O <sub>3</sub>	14.65	16.6	21.5	18.15	18.1	12.25	17.45	15.8	18.6	16.45	14.25
MgO	9.91	5.92	4.01	5.07	7.72	11.3	6.28	8.99	5.5	6.37	11.4
MnO	0.21	0.27	0.25	0.22	0.26	0.17	0.21	0.2	0.22	0.21	0.2
CaO	13.95	8.28	7.82	8.14	11.85	13.25	9.31	7.73	9.37	8.65	9.33
Na <sub>2</sub> O	1.7	1.48	0.41	1.16	1.25	1.7	1.06	2.04	1.58	1.15	1.73
K <sub>2</sub> O	0.29	0.55	0.07	0.48	0.53	0.54	0.43	0.75	0.45	0.57	0.91
Cr <sub>2</sub> O <sub>3</sub>	0.07	0.01	<0.01	0.01	0.02	0.06	0.01	0.02	0.02	0.02	0.12
P <sub>2</sub> O <sub>5</sub>	0.05	0.32	0.25	0.22	0.3	0.05	0.13	0.18	0.19	0.17	0.06
LOI	0.04	1.02	-0.97	0.05	0.38	0.49	-0.15	2.21	0.17	0.41	1.71
Total	100.39	98.92	98.13	99.98	99.26	99.3	98.61	100.24	98.6	99.1	100.65
mg#	57.27	41.4	26.98	35.62	45.8	64.63	41.62	52.99	36.94	43.41	61.31
K <sub>2</sub> O/Na <sub>2</sub> O	0.17	0.37	0.17	0.41	0.42	0.32	0.41	0.37	0.28	0.5	0.53
K <sub>2</sub> O + Na <sub>2</sub> O	1.99	2.03	0.48	1.64	1.78	2.24	1.49	2.79	2.03	1.72	2.64

Furthermore, considering the binary plot Zr/Ti versus Nb/Y (Floyd and Winchester, 1978), the protolith of mafic granulite and garnet amphibolite are basalts (Fig. 25a). Following the log(TFe<sub>2</sub>O<sub>3</sub>/K<sub>2</sub>O) vs. log (SiO<sub>2</sub>/Al<sub>2</sub>O<sub>3</sub>) binary plots (Pettijohn et al., 1987), Pyroxene biotite gneiss samples fall within the arkose and greywacke fields (Fig. 25b).

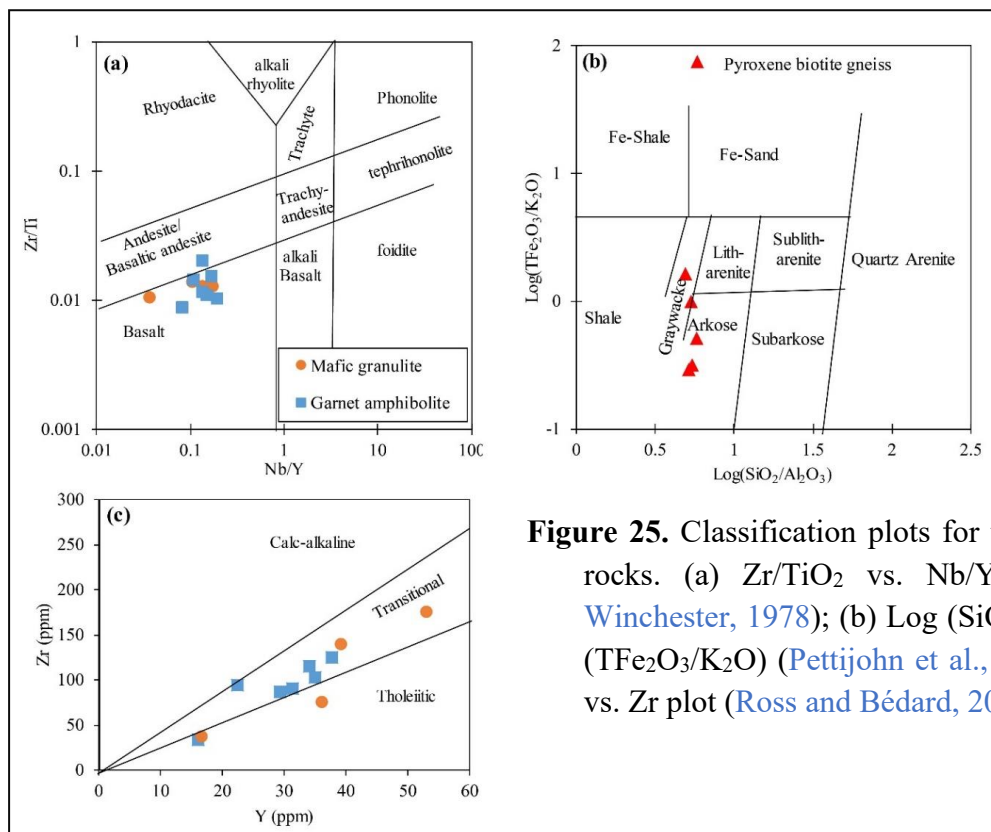


**Figure 25.** Classification plots for the Anyouzok rocks. (a) Zr/TiO<sub>2</sub> vs. Nb/Y (Floyd and Winchester, 1978); (b) Log (SiO<sub>2</sub>/Al<sub>2</sub>O<sub>3</sub>)/Log (TFe<sub>2</sub>O<sub>3</sub>/K<sub>2</sub>O) (Pettijohn et al., 1987); (c) Y vs. Zr plot (Ross and Bédard, 2009).

## IV.2. Geochemical properties

### IV.2.1. Metavolcanic rocks

#### IV.2.1.1. Mafic granulite

##### a) Major elements

The mafic granulites are characterized by variable contents of  $\text{SiO}_2$  (44.7-51.25 wt.%), high  $\text{Fe}_2\text{O}_3$  (14.65-21.2 wt.%),  $\text{MgO}$  (4.01-9.91 wt.%) and  $\text{CaO}$  (7.82-13.95 wt.%) contents.

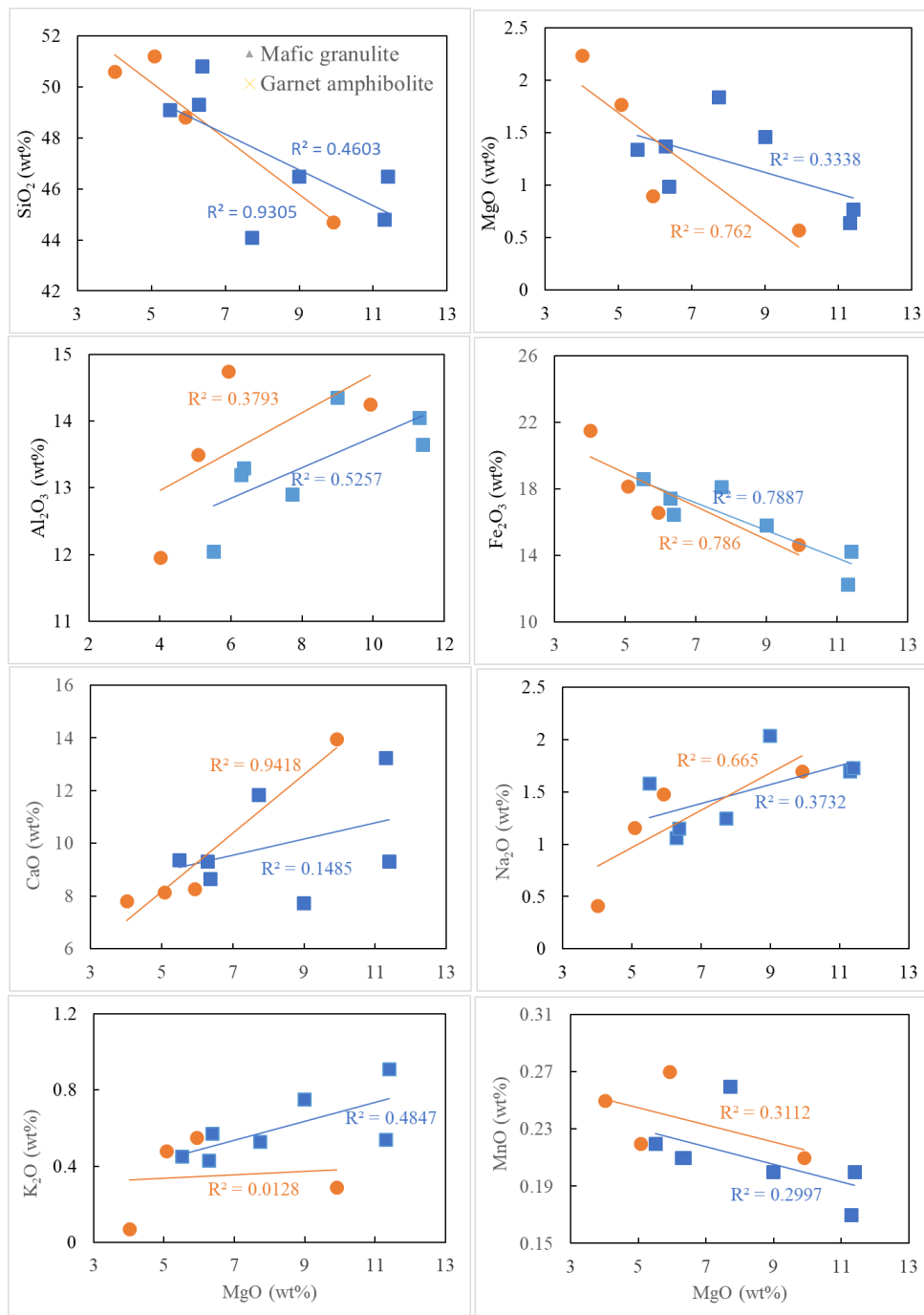


**Figure 26.** Binary plots of major element variations with respect to  $\text{MgO}$ .

Al<sub>2</sub>O<sub>3</sub> (11.95-14.75 wt.%) and TiO<sub>2</sub>(0.57-2.24 wt.%) contents are relatively low to moderate. They display low total alkali (Na<sub>2</sub>O + K<sub>2</sub>O = 0.48-2.03 wt.%) contents and low MnO (0.21-0.27 wt.%), P<sub>2</sub>O<sub>5</sub> (0.05-0.32 wt.%) and Cr<sub>2</sub>O<sub>3</sub> (<0.01-0.07 wt.%) contents. Compared to the basalt described by [Le Maitre \(1976\)](#), mafic granulite only differs by a slight depletion of SiO<sub>2</sub>, MgO and CaO and a slight enrichment in TiO<sub>2</sub>, Fe<sub>2</sub>O<sub>3</sub> and K<sub>2</sub>O for comparable content in other elements. In the Zr vs. Y diagram ([Ross and Bédard, 2009](#)) mafic granulite shows tholeiitic to transitional affinity (Fig. 25c). Variation of some major elements as a function of MgO shows a positive correlation with CaO, and Na<sub>2</sub>O and negative correlations with SiO<sub>2</sub>, and TiO<sub>2</sub> (Fig. 26).

#### *b) Trace elements*

The high field strength element (HFSE) concentrations for mafic granulite are generally low (<10 ppm), except for Zr (37-176 ppm) and Y (16.7-53.1 ppm) which are relatively higher (Table 9). Large iron lithophile elements (LILEs) such as Rb (1.2-15 ppm) show very low concentrations while Sr (20.7-86.4 ppm) and Ba (6-103.5 ppm) show slightly higher values. Cr contents range from 20-460 ppm. Following the variation of some trace elements as a function of MgO (wt.%), Cr correlates positively, while Hf, Nb, Th and Zr show negative correlations when plotted against MgO (Fig. 27).

**Table 9.** Trace element (ppm) compositions of the Anyouzok metavolcanic rocks.

Rock type	Mafic granulite				Garnet amphibolite						
	IS20	IS40	IS26	IS17	IS15b	IS24	IS27b	IS28	IS33	IS37	IS39
Cr	460	100	20	80	150	440	80	120	130	100	820
Sn	1	1	2	1	1	1	1	1	1	1	1
V	361	287	392	391	475	258	429	392	242	338	231
Ba	24.1	82.6	6	103.5	90.8	31.6	63.6	126.5	52.8	53.8	70.8
Rb	2.5	7.3	1.2	15	8.9	2.9	7.5	10	9.1	5.3	10.6
Ga	16.8	13.7	18.7	15	18.8	13.3	16.9	18.4	18.7	14.1	16.3
Cs	0.02	0.17	0.05	0.65	0.44	0.01	0.3	0.18	0.12	0.07	0.31
Th	0.15	0.93	1.33	1.64	<0.5	0.07	0.4	0.16	0.69	0.5	0.44
U	0.1	0.51	0.31	2.63	0.24	0.08	0.24	0.27	0.27	0.35	0.31
Sr	48.4	86.4	20.7	62.1	69.5	37.5	32.3	53.1	57	38.6	40.7
Nb	0.6	3.7	6.9	6.6	6.6	1.3	4.7	4.7	6.3	3.1	3
Ta	<0.1	0.3	0.3	0.3	0.3	<0.1	0.3	0.2	9.7	<0.1	0.1
Hf	1.3	1.8	4.8	3.8	3.4	1.1	2.6	2.8	3.8	2.4	2.5
Zr	37	76	176	140	115	34	91	103	125	87	94
Y	16.7	36.1	53.1	39.2	34.2	16.2	31.5	35.1	37.8	29.4	22.5

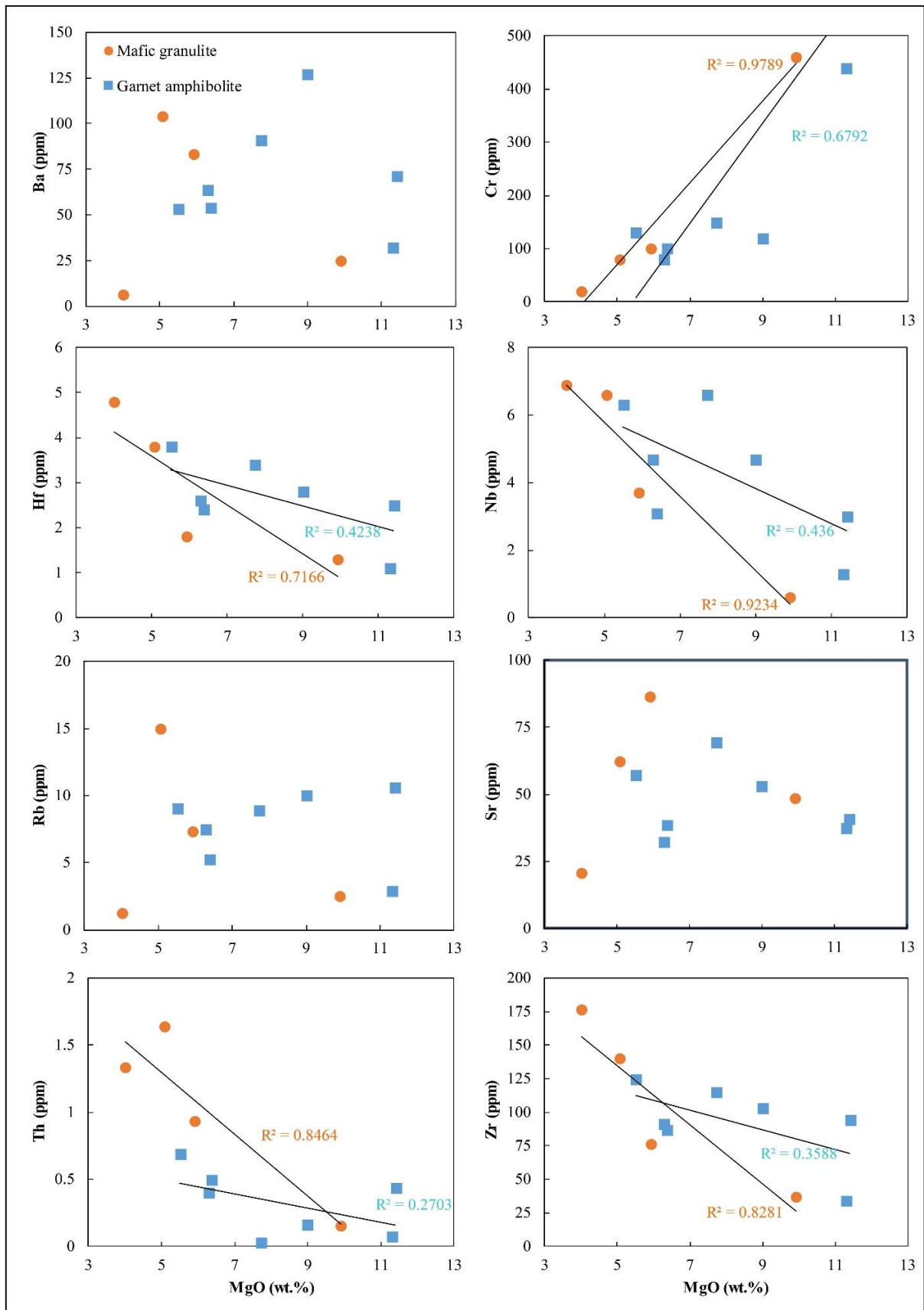


**Figure 27.** Binary plots of trace element variations with respect to MgO.

c) REE

The sum of REE ( $\Sigma$ REE) in mafic granulites (Table 10) vary from 32.01-100.74 ppm. Chondrite-normalized REE diagrams show homogeneous and coherent patterns for most of the analyzed samples, comparable to both NMORB and EMORB (Fig. 28a). The Anyouzok mafic granulite samples, show relatively flat patterns ( $(La/Yb)_{CN}=0.77-1.39$ ; Fig. 28a). They generally present slight negative to no Eu anomalies ( $(Eu/Eu^*)_{CN}=0.84-1.04$ ) and exhibit no Ce anomalies ( $Ce/Ce^*: 0.96-1.08$ ). Primitive mantle-normalized multi-element diagrams (Fig. 28b) show peaks in K and U and troughs in Nb, Ta, Sr, Ti.

**Table 10.** Rare earth element (ppm) compositions and element ratios of the Anyouzok metavolcanic rocks.

Rock type	Mafic granulite				Garnet amphibolite						
	IS20	IS40	IS26	IS17	IS15b	IS24	IS27b	IS28	IS33	IS37	IS39
La	2.1	7	9.8	8.7	6.6	2.1	4.6	7.3	6.6	5.1	4
Ce	6.8	16.3	26.1	20.9	19.5	6	13.2	21.3	18.1	13.4	10
Pr	1.19	2.43	3.51	2.82	2.97	0.93	2.09	3.24	2.68	1.87	1.54
Nd	7.3	11.3	18	14.6	15	4.8	10.8	17.1	14.5	9.2	7.1
Sm	2.58	3.19	5.78	4.35	4.37	1.63	3.77	5.19	4.04	2.8	2.19
Eu	0.89	1.14	1.89	1.59	1.54	0.69	1.49	1.5	1.56	0.99	0.64
Gd	2.62	4.07	8.14	6.14	5.11	2.3	4.97	5.63	5.99	3.69	2.72
Tb	0.43	0.81	1.48	1.07	0.88	0.41	0.84	0.93	1.03	0.69	0.56
Dy	3.14	5.49	9.93	7.8	6.44	2.86	5.74	6.33	6.88	5.2	3.66
Ho	0.64	1.29	2.06	1.49	1.29	0.63	1.27	1.3	1.42	1.15	0.76
Er	1.98	3.84	6.28	4.5	4.08	2.17	3.77	3.77	4.45	3.71	2.44
Tm	0.24	0.59	0.77	0.62	0.5	0.26	0.5	0.49	0.56	0.42	0.34
Yb	1.85	4.01	6.15	4.24	3.99	2.03	3.58	3.84	4.54	3.45	2.89
Lu	0.25	0.65	0.85	0.63	0.56	0.29	0.52	0.52	0.6	0.51	0.47
$\Sigma$ REE	32.01	62.11	100.74	79.45	72.83	27.1	57.14	78.44	72.95	52.18	39.31
$(La/Yb)_{CN}$	0.77	1.19	1.08	1.39	1.12	0.7	0.87	1.29	0.99	1	0.94
$(La/Sm)_{CN}$	0.51	1.37	1.06	1.25	0.94	0.8	0.76	0.88	1.02	1.14	1.14
$(Gd/Yb)_{CN}$	1.15	0.82	1.07	1.17	1.04	0.92	1.12	1.19	1.07	0.87	0.76
$(Eu/Eu^*)_{CN}$	1.04	0.96	0.84	0.94	0.99	1.09	1.05	0.85	0.97	0.94	0.8
$(Ce/Ce^*)_{CN}$	1.04	0.96	1.08	1.02	1.07	1.04	1.03	1.06	1.04	1.05	0.97
Th/Nb	0.25	0.25	0.19	0.25	0	0.05	0.09	0.03	0.11	0.16	0.15
Nb/Y	0.04	0.1	0.13	0.17	0.19	0.08	0.15	0.13	0.17	0.11	0.13
La/Nb	3.5	1.89	1.42	1.32	1	1.62	0.98	1.55	1.05	1.65	1.33
Dy/Yb	1.7	1.37	1.61	1.84	1.61	1.41	1.6	1.65	1.52	1.51	1.27
Zr/Nb	61.67	20.54	25.51	21.21	17.42	26.15	19.36	21.91	19.84	28.06	31.33
Zr/Hf	28.46	42.22	36.67	36.84	33.82	30.91	35	36.79	32.89	36.25	37.6
Th/Yb	0.08	0.23	0.22	0.39	0.01	0.03	0.11	0.04	0.15	0.14	0.15

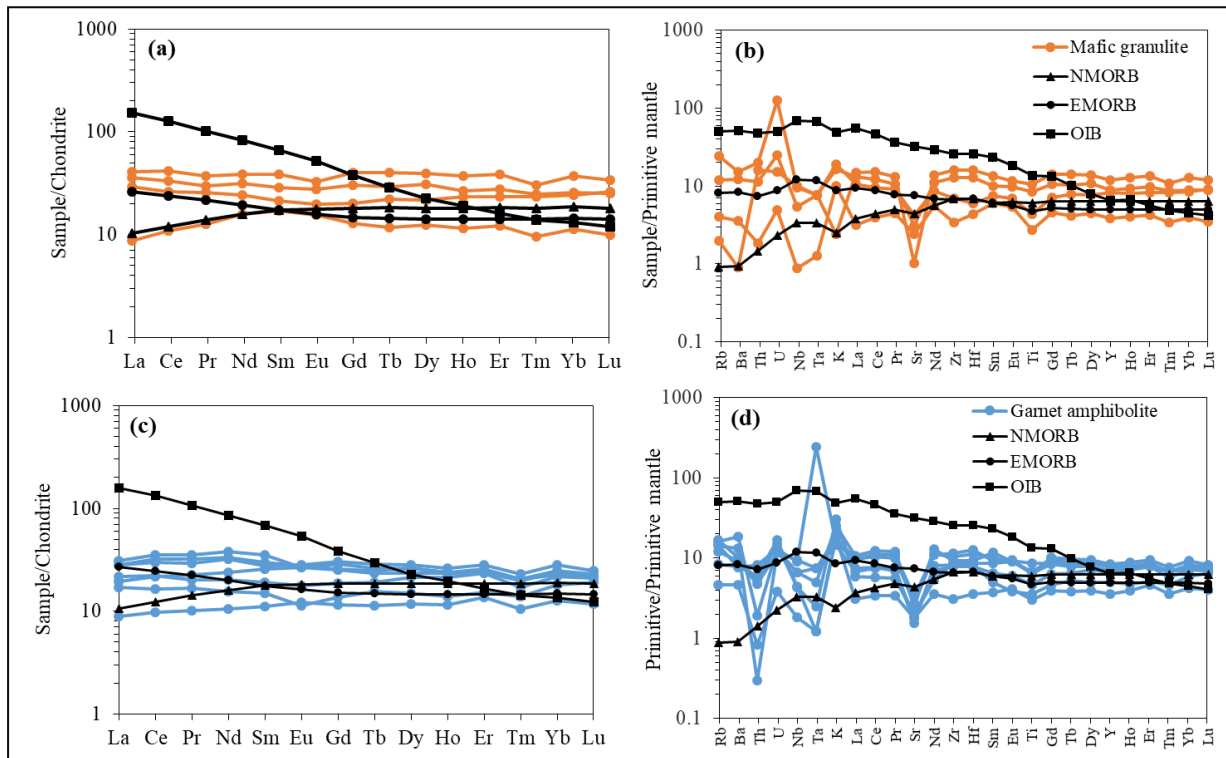


**Figure 28.** Anyouzok Chondrite-normalised and primitive mantle normalised plots for mafic granulite and garnet amphibolite (a and c) Chondrite-normalized (after [McDonough and Sun, 1995](#)) REE plots for the Anyouzok mafic granulite and garnet amphibolite respectively; (b and d) primitive mantle-normalized (after [Sun and McDonough, 1989](#)) multi-element diagrams for the Anyouzok mafic granulite and garnet amphibolite respectively.

#### IV.2.1.2. Garnet amphibolite

##### a) Major elements

The studied garnet amphibolite samples show basalt compositions ([Floyd and Winchester, 1978](#)) with variable  $\text{SiO}_2$  (44.1 - 50.8 wt.%) contents. These rocks display high  $\text{Fe}_2\text{O}_3$  (12.25 - 18.6 wt%),  $\text{MgO}$  (5.5 - 11.4 wt%),  $\text{Al}_2\text{O}_3$  (12.05 - 14.35 wt%) and  $\text{CaO}$  (7.73 - 13.25 wt%) contents. They are poor in alkalis ( $\text{Na}_2\text{O}+\text{K}_2\text{O}=1.49\text{-}2.79$  wt%). The analyzed samples show low contents in  $\text{TiO}_2$  (0.64 - 1.84 wt%),  $\text{MnO}$  (0.17 - 0.26 wt%),  $\text{P}_2\text{O}_5$  (0.05 - 0.30 wt%), and  $\text{Cr}_2\text{O}_3$  (0.01-0.12 wt%). Compared to the basalts described by [Le Maitre \(1976\)](#), garnet amphibolite only differs by a slight depletion of  $\text{SiO}_2$ ,  $\text{MgO}$  and  $\text{CaO}$  and a slight enrichment in  $\text{TiO}_2$ ,  $\text{Fe}_2\text{O}_3$  and  $\text{K}_2\text{O}$ . The major element diagram as a function of  $\text{MgO}$  (Fig. 26) shows positive correlation for  $\text{Al}_2\text{O}_3$ ,  $\text{Fe}_2\text{O}_3$  and  $\text{K}_2\text{O}$  on the one hand, and a negative correlation for  $\text{SiO}_2$  and  $\text{Fe}_2\text{O}_3$  on the other hand (Fig. 26).  $\text{TiO}_2$  content varies from 0.64 - 1.84; characteristic of rocks of the transitional affinity ([Shido et al., 1974](#)). This is



further confirmed with the Zr vs Y (Ross and Bédard, 2009) diagram, where the samples fall within transitional affinity (Fig. 25c).

#### *b) Trace elements*

Except for Zr (34 - 125 ppm) and Y (16.2 - 37.8 ppm), the HFSE contents in garnet amphibolite samples are generally low (< 10 ppm; Table 9). Large ion lithophile elements (LILEs) such as Rb (2.9 - 10.6 ppm) show very low concentrations, whereas Sr (32.3 - 69.5 ppm) and Ba (31.6 - 126.5 ppm) show slightly higher values. Cr contents range from 80 - 820 ppm in garnet amphibolite. In binary plots of trace elements against MgO, Cr shows positive correlation while Hf, Nb, Th and Zr tend to show negative correlations when plotted against MgO. Ba, Rb and Sr show scattered data points when plotted against MgO (Fig. 27).

#### *c) REE*

REE contents (Table 9) are variable ( $\Sigma$ REE: 27.1-78.44 ppm). Chondrite-normalized REE diagrams show homogeneous and coherent patterns for most of the analyzed samples, comparable to both NMORB and EMORB (Fig. 28a, and c). The Anyouzok garnet amphibolite samples generally present slight negative to no Eu anomalies ( $(\text{Eu}/\text{Eu}^*)_{\text{CN}} = 0.80\text{-}1.09$ ) and exhibit no Ce anomalies ( $\text{Ce}/\text{Ce}^* = 0.97\text{-}1.07$ ). Primitive mantle-normalized multi-element diagrams (Fig. 28b, and d) show peaks in K and U and troughs Th, Nb, Ta, and Sr.

### IV.2.2. Metasedimentary rocks

#### *IV.2.2.1. Pyroxene biotite gneiss*

##### *a) Major elements*

The Anyouzok pyroxene biotite gneiss is characterized by high  $\text{SiO}_2$  (73-75.50 wt.%) and  $\text{Al}_2\text{O}_3$  (13.2-14.50 wt.%), low  $\text{Fe}_2\text{O}_3$  (1.58-3.22 wt.%), MgO (0.22-0.96 wt.%) and CaO (0.96-1.33 wt.%). and moderate alkali ( $6.75 \leq \text{Na}_2\text{O} + \text{K}_2\text{O} \leq 8.47$ ) contents (Table 11). Other major elements such as  $\text{Cr}_2\text{O}_3$ , MnO,  $\text{P}_2\text{O}_5$  are very low in the rocks. The UCC (Rudnick and Gao, 2003), shows  $\text{SiO}_2$  contents of 64.8 wt%, and  $\text{Al}_2\text{O}_3$  content of 15.4 wt%, while for the NASC,  $\text{SiO}_2$  content is 64.8 wt% and 16.9 wt% for  $\text{Al}_2\text{O}_3$ . Therefore, the Anyouzok pyroxene biotite gneiss  $\text{SiO}_2$  and  $\text{Al}_2\text{O}_3$  contents are closer to those of the UCC. The  $\text{SiO}_2/\text{Al}_2\text{O}_3$  ratios vary slightly from 4.86 to 5.7 and are close to values known in the Kyanite garnet gneisses and garnet plagioclase gneisses of Yaounde (Nzenti et al., 1988), the garnet gneisses of Kpwa-Atog Boga (Soh Tamehe et al., 2018), the kyanite-garnet and biotite-muscovite garnet gneisses of Ntui-Betamba, Yaounde (Ngnotué et al., 2000) and the paragenesis and schists of Santa Quintéria, North East Brazil (De Carvalho Mendes et al., 2021). Major element variation diagrams show a negative correlation for  $\text{K}_2\text{O}$  and  $\text{SiO}_2$  with

Al<sub>2</sub>O<sub>3</sub>, positive correlation for CaO and Na<sub>2</sub>O with Al<sub>2</sub>O<sub>3</sub> and dispersed data points for MgO and TiO<sub>2</sub> with Al<sub>2</sub>O<sub>3</sub> (Fig. 29).

**Table 11.** Major elements (wt%) and trace elements (ppm) compositions of the Anyouzok pyroxene biotite gneiss.

Elements	IS6	IS11	IS11b	IS12	Mean
SiO <sub>2</sub>	73	75.5	74.1	75.3	74.48
TiO <sub>2</sub>	0.26	0.1	0.1	0.09	0.14
Al <sub>2</sub> O <sub>3</sub>	13.75	13.95	14.5	13.2	13.85
Fe <sub>2</sub> O <sub>3</sub>	3.22	1.73	1.58	2.57	2.28
MgO	0.96	0.32	0.22	0.49	0.5
MnO	0.03	0.03	0.02	0.02	0.03
CaO	1.28	0.96	1.33	1.08	1.16
Na <sub>2</sub> O	3.51	2.72	3.05	2.79	3.02
K <sub>2</sub> O	3.24	5.51	5.42	5.04	4.8
Cr <sub>2</sub> O <sub>3</sub>	0.01	<0.01	<0.01	0.01	0.01
P <sub>2</sub> O <sub>5</sub>	0.05	0.01	0.01	0.05	0.03
LOI	1.33	0.82	0.76	0.79	0.93
Total	100.64	101.65	101.09	101.43	101.2
SiO <sub>2</sub> /Al <sub>2</sub> O <sub>3</sub>	5.31	5.41	5.11	5.7	5.38
K <sub>2</sub> O/Na <sub>2</sub> O	0.92	2.03	1.78	1.81	1.63
K <sub>2</sub> O+Na <sub>2</sub> O	6.75	8.23	8.47	7.83	7.82
K <sub>2</sub> O/Al <sub>2</sub> O <sub>3</sub>	0.24	0.39	0.37	0.38	0.35
Al <sub>2</sub> O <sub>3</sub> /TiO <sub>2</sub>	52.88	139.5	145	146.67	121
TiO <sub>2</sub> /Al <sub>2</sub> O <sub>3</sub>	14.01	14.05	14.6	13.29	13.99
Na <sub>2</sub> O + K <sub>2</sub> O	6.75	8.23	8.47	7.83	7.82
Cr	60	10	20	20	27.5
Sn	2	<1	1	4	2.33
V	37	12	12	7	17
Ba	605	1280	1245	803	983.3
Rb	101	85.5	96.1	224	126.7
Ga	12.6	13.8	16.9	14.6	14.48
Cs	0.57	0.25	0.26	0.86	0.49
Th	29.1	3.31	4.55	41.8	19.69
U	4.79	0.51	0.44	8.72	3.62
Sr	144	168	195.5	84.1	147.9
Nb	5.8	0.9	1.4	19.5	6.9
Ta	<0.1	<0.1	<0.1	1.5	1.5
Hf	4	3.8	2.5	4.7	3.75
Zr	123	125	80	138	116.5
Y	7.1	3.2	2.5	20.7	8.38
K	26897	45741	44994	41840	39868
Ti	15599	5999.5	5999.5	5399.6	8249
K/Rb	266.31	534.99	468.2	186.78	364.1
Cr/Th	2.06	3.02	4.4	0.48	2.49
Th/U	6.08	6.49	10.34	4.79	6.92
La/Th	0.96	7.16	6.26	0.88	3.82
Y/Ho	22.9	24.62	25	29.15	25.42
Zr/Hf	30.75	32.895	32	29.362	31.07
Rb/Sr	0.7014	0.5089	0.4916	2.6635	0.856
Ti/Zr	126.82	47.996	74.994	39.127	70.81
Th/Yb	42.174	9.1944	14.219	37.658	31.76
Ti/V	421.59	499.96	499.96	771.36	485.3
(La/Sm)CN	5.87	7.69	10.81	4.34	7.18
(La/Yb)CN	27.29	44.44	60.12	22.32	38.54
(Gd/Yb)CN	2.59	2.69	2.47	3.7	2.86
(Eu/Eu*)CN	0.7	1.44	2.25	0.29	1.17
Eu/Eu*)SN	1.62	2.9	4.38	1.09	2.5

a) *Trace elements*

Concentrations for LILE, such as Sr (84.1 -195.5 ppm) are lower than those of Ba (605-1280 ppm), but the mean values for both Sr (147.9 ppm) and Ba (983.25 ppm) are generally higher than the average concentrations for adjacent BIF interbedded metasediments. Rb (85.5-224 ppm), Th (3.31-41.8 ppm) and U (0.44-8.72 ppm) generally show lower concentrations than the earlier cited LILEs.

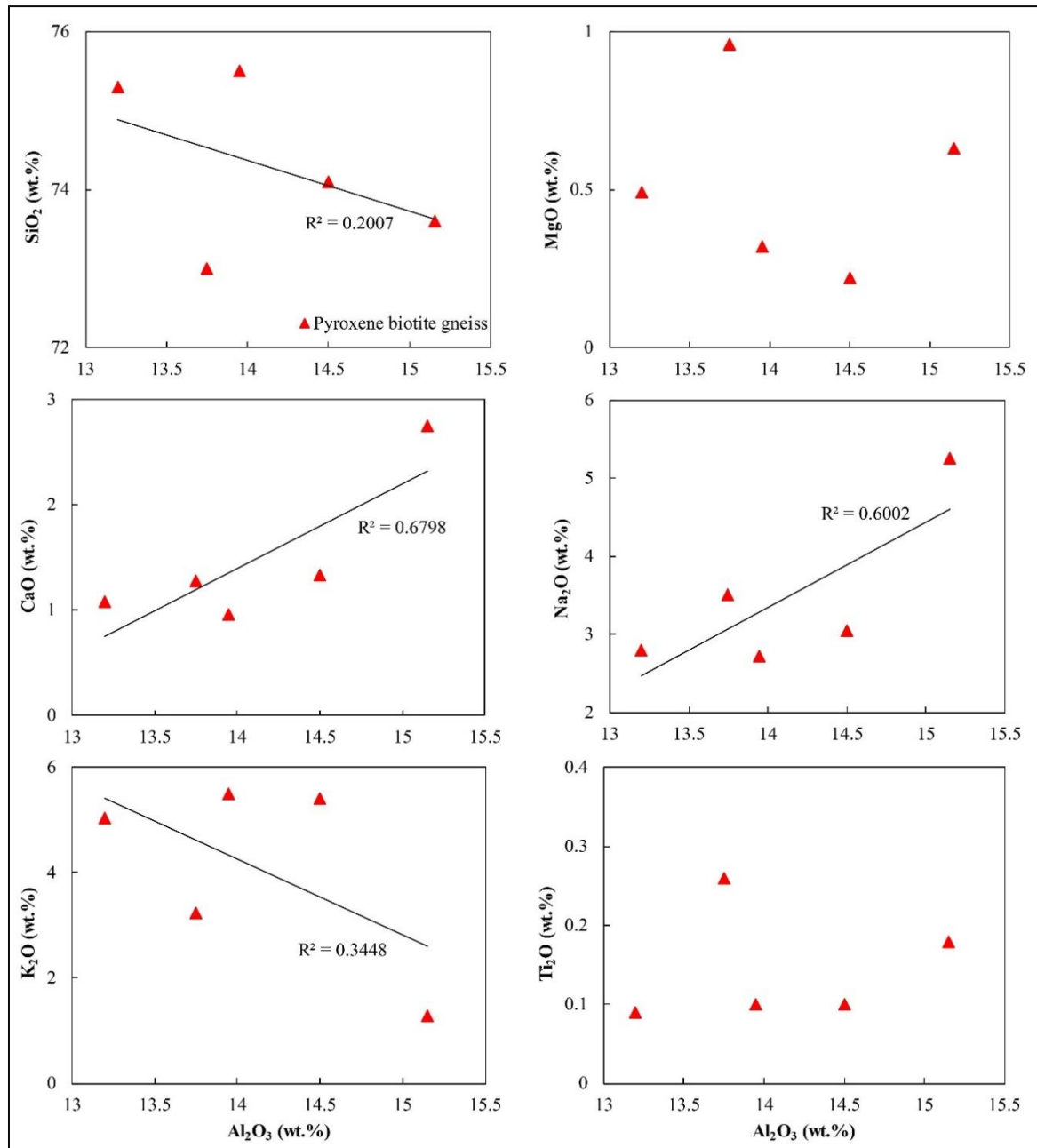


**Figure 29.** Binary plots of major element variations with respect to Al<sub>2</sub>O<sub>3</sub>.

The Anyouzok pyroxene biotite gneisses show very low concentrations in HFSEs, e.g., Zr which varies from 80 to 138 ppm. Hf shows much lower concentrations, ranging from 2.5 to 4.7 ppm. The average concentrations of Zr (116.5 ppm) and Hf (3.75 ppm) are generally lower for the Anyouzok pyroxene biotite gneisses than for metasediments of adjacent studies (Table 12). The UCC-normalised plot generally shows peaks in Rb, Th and Yb, and troughs in Sr and Tm (Fig. 31b). Binary plots for  $\text{Al}_2\text{O}_3$  versus some trace elements show negative correlations for Rb, Hf and Zr, and positive correlation for Sr (Fig. 30).

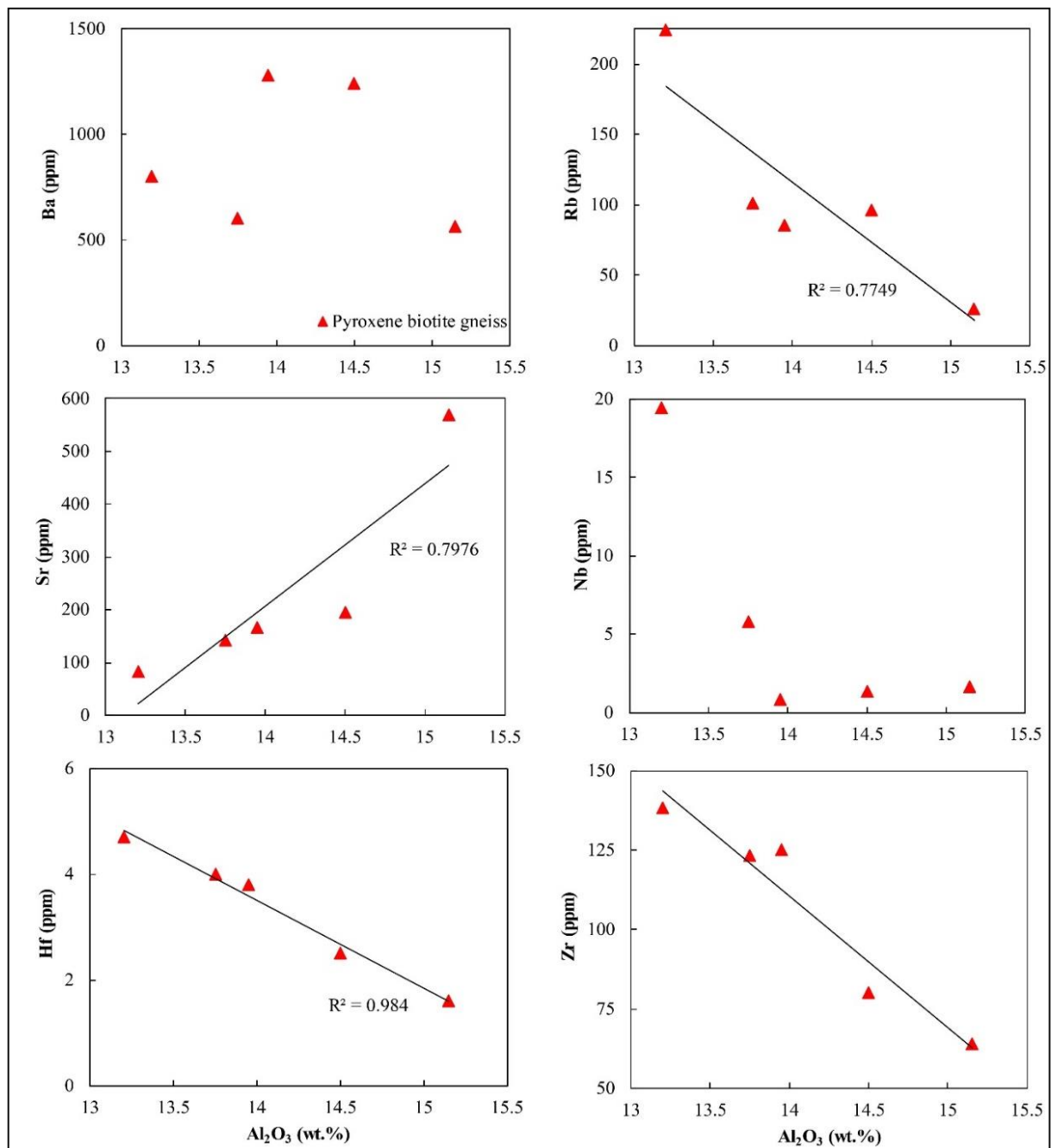


**Figure 30.** Binary plots of trace element variations with respect to  $\text{Al}_2\text{O}_3$ .

b) *REE*

The Anyouzok pyroxene biotite gneisses are characterized by low  $\Sigma\text{REE}$  ranging from 64.62 to 112.8 ppm, with an average concentration of 102.36 ppm. The PAAS-normalised (Taylor and McLennan, 1985) diagram for Anyouzok pyroxene biotite gneiss presents a generally weakly horizontal and coherent pattern, exhibiting slight enrichment in LREE and impoverishment in HREE (Fig 31a). The studied metasediments show very slight positive Eu anomalies, except for samples IS6  $(\text{Eu}/\text{Eu}^*)_{\text{SN}} = 1.62$  and IS12  $(\text{Eu}/\text{Eu}^*)_{\text{SN}} = 1.09$ , which rather portray slightly negative Eu anomalies (Fig. 31a).

**Table 12.** Rare earth elements (ppm) compositions of the Anyouzok pyroxene biotite gneiss.

	<b>IS6</b>	<b>IS11</b>	<b>IS11b</b>	<b>IS12</b>	<b>Mean</b>
<b>La</b>	27.9	23.7	28.5	36.7	29.2
<b>Ce</b>	52.1	19.3	19.5	72.6	40.88
<b>Pr</b>	5.16	3.65	4.27	7.37	5.11
<b>Nd</b>	18	12.3	13.1	24.8	17.05
<b>Sm</b>	2.99	1.94	1.66	5.33	2.98
<b>Eu</b>	0.59	0.72	0.94	0.5	0.69
<b>Gd</b>	2.21	1.2	0.98	5.08	2.37
<b>Tb</b>	0.26	0.13	0.08	0.87	0.34
<b>Dy</b>	1.63	0.8	0.47	4.81	1.93
<b>Ho</b>	0.31	0.13	0.1	0.71	0.31
<b>Er</b>	0.81	0.35	0.32	1.62	0.78
<b>Tm</b>	0.08	0.02	0.03	0.14	0.07
<b>Yb</b>	0.69	0.36	0.32	1.11	0.62
<b>Lu</b>	0.07	0.02	0.01	0.1	0.05
<b><math>\Sigma\text{REE}</math></b>	112.8	64.62	70.28	161.74	102.4
<b><math>(\text{La}/\text{Sm})_{\text{CN}}</math></b>	5.87	7.69	10.81	4.34	7.18
<b><math>(\text{La}/\text{Yb})_{\text{CN}}</math></b>	27.29	44.44	60.12	22.32	38.54
<b><math>(\text{Gd}/\text{Yb})_{\text{CN}}</math></b>	2.59	2.69	2.47	3.7	2.86
<b><math>(\text{Eu}/\text{Eu}^*)_{\text{CN}}</math></b>	0.7	1.44	2.25	0.29	1.17
<b><math>(\text{Eu}/\text{Eu}^*)_{\text{SN}}</math></b>	1.62	2.9	4.38	1.09	2.5

#### IV.2.3. Iron formations

The geochemical results for BIFs and SBIFs are presented in Tables 13 and 14.

##### IV.2.3.1. BIFs

###### a) Major elements

$\text{SiO}_2$  (44.4 - 60.78 wt%) and  $\text{Fe}_2\text{O}_3$  (26.05 - 48.40 wt%) are the main constituents of the Anyouzok BIFs, representing a total of about 87 wt% (Table 13).  $\text{MgO}$  (2.55 - 5.98 wt%) and  $\text{CaO}$  (1.46 - 3.39 wt%) contents are moderate, and similar with  $\text{Al}_2\text{O}_3$  (1.83 - 2.52 wt%).  $\text{MnO}$  (0.04 - 0.46 wt%) and  $\text{TiO}_2$  (0.05 - 0.12 wt%) are low, while  $\text{K}_2\text{O}$  in Anyouzok BIFs vary from 0.47 to 1.2 wt%.  $\text{P}_2\text{O}_5$  for Anyouzok BIFs are low in concentration and show a narrow range from 0.07 to 0.12 wt%. Loss on ignition (LOI) values are from -0.69 to 0.9 wt% in the Anyouzok BIFs. Binary plots of  $\text{SiO}_2$  and  $\text{Al}_2\text{O}_3$  vs  $\text{Fe}_2\text{O}_3$  both show negative correlations.

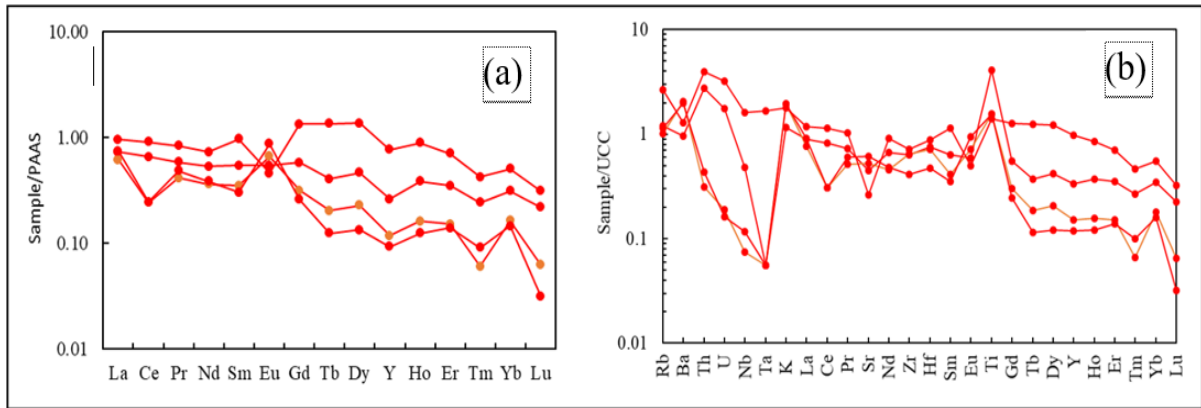


**Figure 31.** REE and multi-element plots of Anyouzok pyroxene biotite gneiss. Normalisation values (a) after Taylor and McLennan (1985), and (b) Rudnick and Gao, 2003 respectively.

###### a) Trace elements

The Anyouzok IFs generally show low trace element contents, < 10 ppm. However, relatively high values are observed in some LILEs such as Sr (6.6 - 11.5 ppm), Rb (23.6 - 88 ppm) and Ba (39 - 74 ppm; 3.8 - 134 ppm) contents. HFSE contents in BIF, such as Zr (12.4 - 18 ppm) and Th (1.1 - 1.5 ppm) are higher than in SBIF where Zr (3.7 - 7) and Th (<0.05 - 0.16) contents are lower (Table 12).

###### b) REE

The total REE-Y concentrations for BIF samples range from 37.43 ppm to 39.69 ppm (Table 14). Chondrite-normalized (McDonough and Sun, 1995) plot shows homogenous patterns with LREE enrichment over the HREE (Fig 30a) and positive Eu anomalies ((Eu/Eu\*)<sub>CN</sub>) ranging from 1.23 - 1.66. PAAS-normalized REE-Y plots (Taylor and



McLennan, 1985) are consistent (Fig. 31b). HREE are enriched over LREE with prominent positive Eu anomalies,  $(Eu/Eu^*)_{SN}$  ranging from 1.86 to 2.68. Y/Ho ratios range from 26.4 to 30.33, while Pr/Yb ratios vary between 1.22 and 2. BIFs show positive La  $((La/La^*)_{SN}=1.1-1.23)$  and Gd  $((Gd/Gd^*)_{SN}=1.21-1.35)$  anomalies.

**Table 13.** Major elements (wt.%) and trace elements (ppm) compositions of the Anyouzok Iron formations.

Rock type	BIF				SBIFs				
Elements	IS13	IS50	IS51	IS52	IS18	IS19	IS35	IS41	IS54
Major elements									
SiO <sub>2</sub>	44.4	60.8	59.02	59.45	43.7	43.5	43.3	45.7	47.26
TiO <sub>2</sub>	0.12	0.07	0.07	0.05	0.01	0.04	0.03	0.08	<0.01
Al <sub>2</sub> O <sub>3</sub>	1.83	2.37	2.52	1.84	0.26	0.94	0.7	0.99	0.74
Fe <sub>2</sub> O <sub>3</sub>	48.4	26.4	26.05	27.68	55.2	51.3	53.2	50.2	49.6
MgO	2.55	5.27	5.98	5.73	1.94	1.94	2.08	2.21	1.82
MnO	0.04	0.4	0.46	0.46	0.03	0.04	0.03	0.04	0.05
CaO	1.46	2.44	3.39	2.76	1.16	1.1	1.03	0.75	1.1
Na <sub>2</sub> O	0.52	0.14	0.18	0.1	0.04	0.27	0.1	0.01	0.2
K <sub>2</sub> O	0.47	1.16	1.2	0.84	0.06	0.4	0.08	0.03	0.32
Cr <sub>2</sub> O <sub>3</sub>	0.01	0	0	0	<0.01	0.01	0.01	0.01	0
P <sub>2</sub> O <sub>5</sub>	0.12	0.09	0.07	0.09	0.09	0.16	0.14	0.11	0.1
LOI	-0.69	0.8	0.9	0.9	-1.32	-1.2	-0.88	-0.58	-1.3
Total	99.2	99.9	99.87	99.87	101.17	98.51	99.82	99.56	99.96
Fe	33.9	18.5	18.24	19.38	38.64	35.91	37.24	35.14	34.72
Trace elements									
Sn	<1	<1	<1	<1	<1	<1	<1	<1	<1
V	28	<8	<8	<8	6	13	9	32	<8
Ba	66.1	71	74	39	9.7	134	5.1	3.8	74
Rb	23.6	85.4	88	54.5	2.8	33.7	3.4	1.9	15.9
Ga	3.5	1.5	2.4	1.4	0.5	1.9	1	3.4	3.6
Cs	0.77	8.7	8.7	4.4	0.07	0.88	0.1	0.14	0.4
Th	1.23	1.5	1.3	1.1	0.05	<0.05	0.13	0.16	<0.2
U	0.32	0.3	0.3	0.2	0.1	0.08	0.38	0.09	0.1
Sr	10.5	8.9	11.5	6.6	7.1	20.7	5	5.3	15
Nb	1	0.5	0.6	0.4	0.2	0.4	1	0.7	<0.1
Ta	<0.1	<0.1	<0.1	<0.1	<0.1	<0.1	0.1	<0.1	<0.1
Hf	0.5	0.4	0.5	0.3	0.2	0.2	0.2	0.2	0.1
Zr	18	17	16.9	12.4	4	7	7	5	3.7
Y	9.1	6.6	7.5	6.8	5.8	7.2	5.9	5.5	6.9

#### IV.2.3.2. SBIFs

##### a) Major elements

The major element compositions of the Anyouzok SBIFs, like for the BIFs also show that SiO<sub>2</sub> and Fe<sub>2</sub>O<sub>3</sub> are the main constituents, representing ca. 96% of the bulk composition of SBIFs (Table 13). SBIFs show relatively high SiO<sub>2</sub> (43.3-47.26 wt%) and higher Fe<sub>2</sub>O<sub>3</sub> (49.6 - 55.2 wt%) contents compared with BIFs. In SBIFs, MgO (1.82 - 2.21 wt%) contents are low, while the concentrations of CaO (0.75 - 1.16 wt%), Al<sub>2</sub>O<sub>3</sub> (0.26 - 0.99 wt%), MnO (0.03 - 0.05 wt%), TiO<sub>2</sub> (0.01 - 0.08 wt%) and K<sub>2</sub>O (0.03 - 0.08 wt%) are lower. P<sub>2</sub>O<sub>5</sub>

concentrations have a narrow range from 0.09 – 0.16 wt% in SBIFs. LOI values range from -1.32 to -0.58 wt% in SBIFs. In binary plots for major elements against  $\text{Fe}_2\text{O}_3$  (Fig. 32),  $\text{SiO}_2$ ,  $\text{Al}_2\text{O}_3$ ,  $\text{MgO}$  and  $\text{CaO}$  show negative correlations with  $\text{Fe}_2\text{O}_3$  while  $\text{TiO}_2$  and  $\text{P}_2\text{O}_5$  correlate positively with  $\text{Fe}_2\text{O}_3$  for BIF. For SBIF,  $\text{SiO}_2$ ,  $\text{Al}_2\text{O}_3$ ,  $\text{TiO}_2$ ,  $\text{MgO}$  and  $\text{P}_2\text{O}_5$  show negative correlations with  $\text{Fe}_2\text{O}_3$ , while  $\text{CaO}$  shows negative correlation with  $\text{Fe}_2\text{O}_3$ .

#### b) Trace elements

The Anyouzok SBIFs, like the BIFs, show low trace element contents, <10 ppm (Table 13). However, a few LILEs such as Sr (5.0 - 20.7 ppm), Rb (2.8 - 33.7 ppm) and Ba (3.8 - 134 ppm) show slightly high concentrations in SBIFs. Some HFSEs such as Zr (3.7 - 7 ppm) and Th (< 0.05 - 0.16 ppm), also present relatively low concentrations in SBIFs.

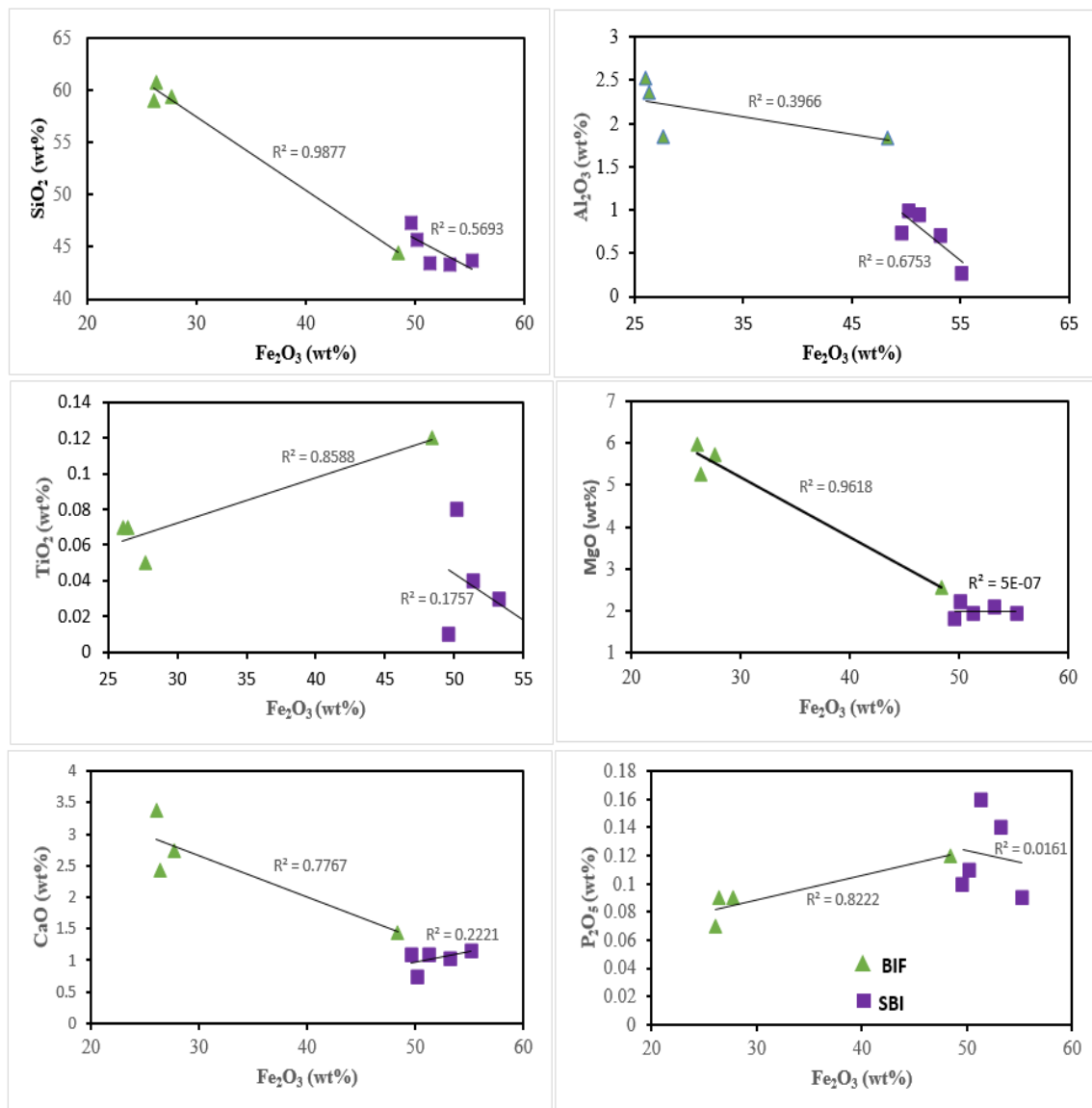


**Figure 32.** Binary plots of BIF and SBIF samples for major elements.

**Table 14.** Rare earth element (ppm) compositions of the Anyouzok Iron formations.

Rock type	BIF				SBIFs				
La	6	6.8	6.5	6.2	1.7	2.5	1.4	3.7	3.2
Ce	11.4	12.7	12.5	12	3.5	5.9	3.5	7.2	5.3
Pr	1.29	1.36	1.31	1.36	0.43	0.74	0.44	0.92	0.62
Nd	5	5.3	5.2	5.4	1.8	3.1	2.3	3.1	2.7
Sm	1.15	1	1.08	0.98	0.44	0.71	0.54	0.84	0.54
Eu	0.66	0.45	0.45	0.45	0.36	0.47	0.36	0.38	0.35
Gd	1.27	1.19	1.16	1.1	0.7	0.95	0.74	0.69	0.87
Tb	0.17	0.18	0.18	0.17	0.1	0.13	0.11	0.12	0.12
Dy	1.43	1.05	1.04	1.14	0.86	1.02	0.89	0.75	0.76
Ho	0.3	0.25	0.26	0.24	0.2	0.22	0.17	0.2	0.18
Er	0.93	0.74	0.79	0.7	0.59	0.64	0.56	0.43	0.55
Tm	0.09	0.1	0.11	0.1	0.05	0.05	0.05	0.07	0.08
Yb	0.81	0.74	0.82	0.68	0.66	0.66	0.56	0.41	0.51
Lu	0.09	0.11	0.13	0.11	0.06	0.04	0.04	0.09	0.08
$\Sigma$ REE-Y	39.7	38.6	39.03	37.43	17.25	24.33	17.56	24.4	22.76
$(Eu/Eu^*)_{SN}$	2.68	1.94	1.86	2.01	3.17	2.83	2.72	2.14	2.54
$(Ce/Ce^*)_{SN}$	0.94	0.96	0.99	0.95	0.94	0.99	1.02	0.9	0.86
$(La/La^*)_{SN}$	1.1	1.19	1.23	1.13	1.12	0.96	2.66	0.75	1.63
$(Gd/Gd^*)_{SN}$	1.35	1.26	1.21	1.22	1.41	1.4	1.32	1.03	1.45
$(Y/Y^*)_{SN}$	0.86	0.8	0.89	0.81	0.87	0.94	0.94	0.88	1.16
$(Eu/Eu)_{CN}$	1.66	1.26	1.23	1.32	1.98	1.74	1.74	1.52	1.56
$(Eu/Eu^*)_{NASC}$	2.7	1.97	1.88	2.04	3.26	2.88	2.78	2.16	2.61
Y/Ho	30.3	26.4	28.85	28.33	29	32.73	34.71	27.5	38.33

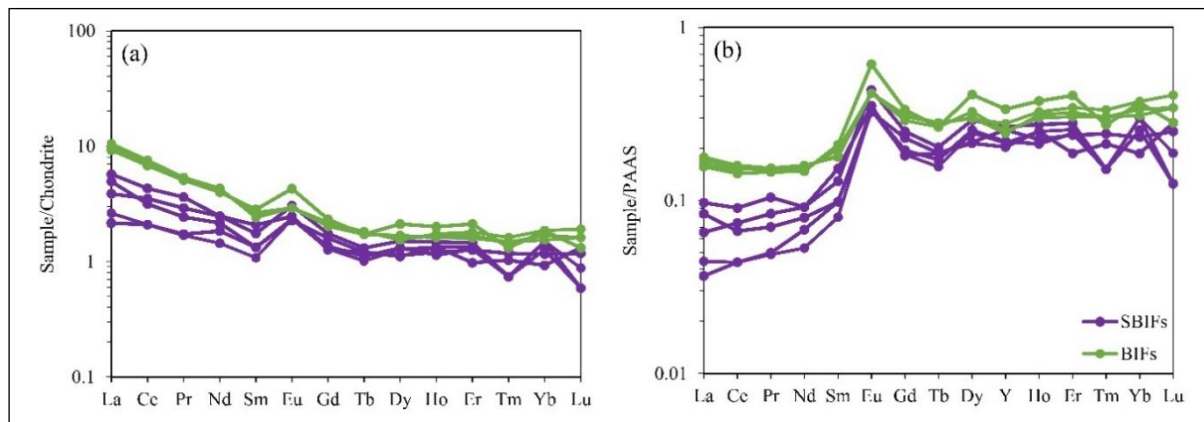


**Figure 33.** Chondrite- (a) and (b) PAAS- normalized REE-Y of the Anyouzok iron formations (BIFs and SBIFs). Normalization values after [McDonough and Sun \(1995\)](#) and [Taylor and McLennan \(1985\)](#).

### c) REE

SBIFs present total REE-Y concentrations ranging from 17.25 - 24.4 ppm (Table 14). Chondrite-normalized ([McDonough and Sun, 1995](#)) plot shows homogenous patterns with LREE enrichment over the HREE (Fig. 33a) and positive Eu anomalies ( $(Eu/Eu^*)_{CN}$ ) ranging from 1.52 to 1.98. The HREE tend to be fractionated and less consistent than the LREE.

PAAS-normalized REE-Y plots (after [Taylor and McLennan, 1985](#)) are consistent for SBIFs (Fig. 33b). HREE are enriched over LREE with prominent positive Eu anomalies,  $(Eu/Eu^*)_{SN}$  ranging from 2.14 to 3.17 in SBIFs while Y/Ho ratios range from 27.50 to 38.33. Pr/Yb ratios vary between 0.65 and 2.24. SBIFs show positive Gd  $((Gd/Gd^*)_{SN}=1.03-1.45)$  and negative to positive to negative La  $((La/La^*)_{SN}=0.75-2.66)$  anomalies. Except for one SBIF sample (IS54), all the analyzed SBIF samples present negative Y anomalies  $((Y/Y^*)_{SN} = 0.87-0.94)$ . Similar to the Chondrite-normalized ([McDonough and Sun, 1995](#)) plots, the HREE for the PAAS-normalized REE-Y plots (after [Taylor and McLennan, 1985](#)) are also more fractionated than the LREE.

## Conclusion

Geochemically, the Anyouzok area is made up essentially of metavolcanic and metasedimentary rocks. The metavolcanic (mafic granulites and garnet amphibolites) rocks are tholeiitic basaltic while the metasedimentary rocks (pyroxene biotite gneiss) are principally of greywacke and arkose. The chondrite-normalized plots and PAAS-normalized REE-Y plots are fairly coherent, for both BIF and SBIF, with an enrichment of LREE over HREE for the chondrite-normalised plot and a slight positive Eu-anomaly, while for the PAAS-normalised plot, there is HREE enrichment over LREE, with a pronounced positive Eu-anomaly.

## **CHAPTER V. INTERPRETATION AND DISCUSSION**

## Introduction

In this chapter, the main results are interpreted and discussed. Therefore, the results are compared with those of other studies to deduce their implications. The discussion then integrates the petrography, lithostratigraphy, ore mineralogy and geochemistry in an effort to determine the nature of the associated ore, the possible source (protolith) of the country rocks, palaeoenvironment of deposition, tectonic evolution and probable ore enrichment processes.

### V.1. Lithology

The lithology of the Anyouzok area comprises IFs and the country rocks. The Iron formations are made up of BIFs and SBIFs, while the country rocks are made up of mafic granulite, garnet amphibolite and pyroxene biotite gneiss. All these rocks show granoblastic, heterogranular microstructures characterized by typomorphic assemblages of granulite and amphibolite facies. The coexistence of granulite and amphibolite facies demonstrates the plurifacial character of metamorphism in this region. The granulitic metamorphism would be comparable to the high-grade metamorphism demonstrated at Bonguen and Lolodorf (Lerouge et al., 2006; Ndema Mbongue et al., 2014) and that of the Yaoundé series (Nzenti et al., 1988), while amphibolite metamorphism would be comparable to the Pan-African amphibolite facies metamorphism. Several authors have highlighted metamorphic rocks of sedimentary origin: (i) in the PNEFB, notably in the Poli and Lom series (Soba, 1989; Hamdja Ngoniri et al., 2021); the Yaoundé Group (Nzenti et al., 1988; Nzenti and Tchoua, 1996; Ngnotué et al., 2000; Yonta-Ngoune et al., 2010); Banyo (Nzenti et al., 2007); (ii) the Congo craton (Feybesse et al., 1987; Ndema Mbongue et al., 2014; Ganno et al., 2015; Soh Tamehe et al., 2018).

### V.2. Alteration, metamorphism, and element mobility assessment

Most Precambrian rocks have been affected by processes such as metamorphism, metasomatism and deformation, which tend to modify their primary geochemical features (Polat et al., 2002; Wang et al., 2017). In the current study, field investigations combined with petrographic, structural, and geochemical studies show that the rocks within the Anyouzok region have been subjected to some deformation, high grade metamorphism and alteration. Similar processes are widely reported within the whole Nyong complex (Lerouge et al., 2006; Ganno et al., 2017; Soh Tamehe et al., 2018; Nga Essomba Tsoungui et al.,



2020; Moudioh et al., 2020; Nzepang Tankwa et al., 2020; Owona et al., 2022). In this regard, effects of post-emplacement processes on the mobility of major, trace and rare earth elements should be assessed before any petrogenetic and geodynamic interpretations.

#### V.2.1. Effects on metavolcanic rocks

The Anyouzok metavolcanic rocks have experienced high grade metamorphism, and some alteration (Fig. 14b-f and Fig. 15b, c and f) and the occurrence of secondary sericite and chlorite (Fig. 14c and e). However, they mainly show low LOI (mean: 0.37 wt% and 0.90 wt% for mafic granulite and garnet amphibolite samples, respectively), indicating insignificant hydration or alteration, except for one mafic granulite sample IS26 (LOI: -0.97 wt%) and one garnet amphibolite sample IS27b (LOI: -0.15 wt%). The degree of alteration of the analyzed metavolcanic rock samples were quantified using the chlorite-carbonate-pyrite index (CCPI; Large et al., 2001) and the Ishikawa alteration index (AI; Ishikawa et al., 1976). The analyzed rocks show relatively low AI (33.14 - 39.86 and 35.21 - 52.67) and moderate CCPI (50.53 - 67.51 and 52.88 - 71.00) for mafic granulite and garnet amphibolite respectively, indicating moderate alteration. In the CCPI vs AI diagram (Fig. 34), overall samples plot within the least altered box for mafic to felsic rocks, although some samples follow the chlorite-pyrite-(sericite) alteration trend, which also suggests some degrees of alteration and weak compositional modification of the major elements. Polat et al. (2002) proposed that metavolcanic rock samples with  $0.90 < \text{Ce/Ce}^* < 1.10$  lack LREE mobility while samples with  $0.90 > \text{Ce/Ce}^* > 1.10$  had undergone high LREE mobility. In the case of the Anyouzok metavolcanic rocks, Ce anomalies range from 0.96 - 1.08 and from 0.97 - 1.07 respectively for mafic granulite and garnet amphibolite (Table 10), consistent with LREE immobility. Furthermore, according to these previous authors, positive correlation between Zr and other elements suggests lack of mobility of these elements via alteration, since Zr is generally considered to be immobile. The analyzed samples show positive correlations with REEs (such as La, Ce, Sm, Eu, Gd, Dy, Yb; not shown) and HFSEs (such Nb, Y, Hf; not shown) and scattered data points with some LILEs (such as Ba, Rb; not shown). In addition, their REE and HFSE patterns (Fig. 28) are generally homogeneous and coherent, suggesting insignificant mobility during post-igneous metamorphism and alteration. Therefore, immobile elements were considered to depict the igneous affinities, petrogenesis and tectonic setting of the investigated metavolcanic rocks.

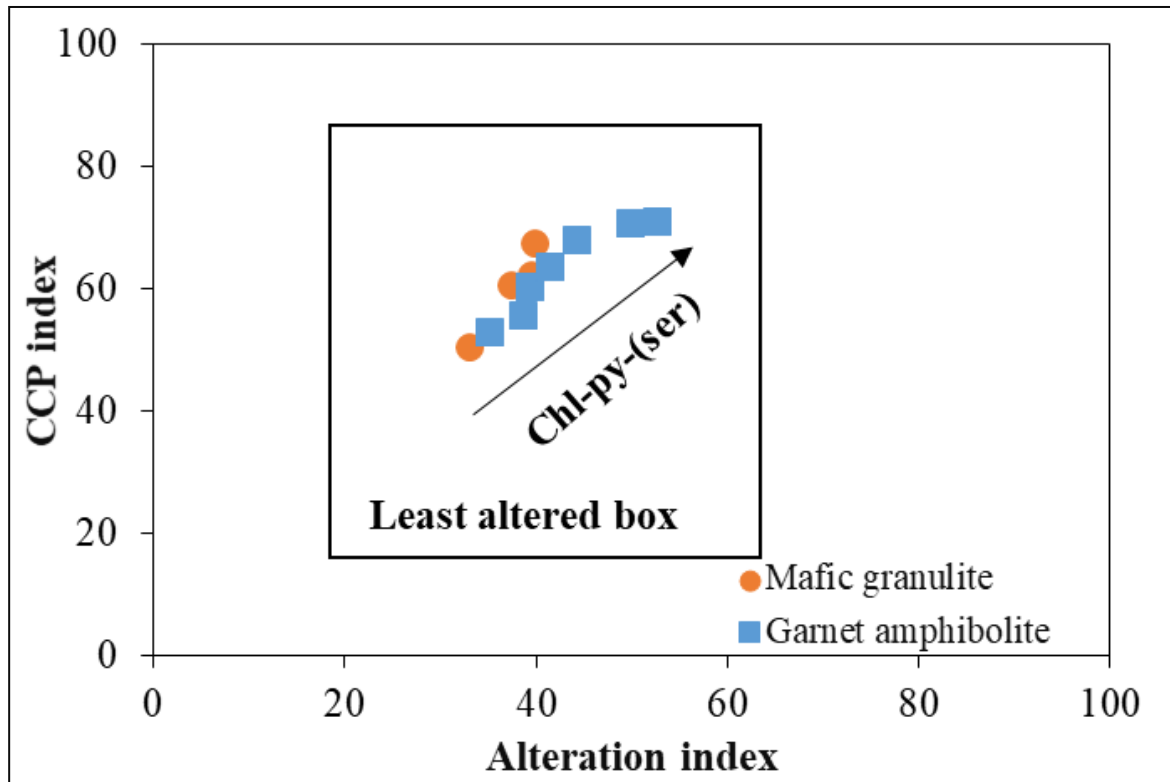


**Figure 34.** Alteration box plot (after Large et al., 2001) for the Anyouzok metavolcanic rocks. Overall samples fall within the least altered box and follow the chlorite alteration trend.

#### V.2.2. Effects on clastic Metasedimentary rocks

Pyroxene biotite gneisses like all other rock types, have been subjected to granulite-to amphibolite facies metamorphism. Because they are fairly stable during metamorphism, empirical element ratios such as K/Rb have been used as indices to determine depletion or enrichment of such elements, thus element mobility. According to [Paolo Sighinolfi \(1974\)](#), K/Rb ratios (R) for amphibolite facies rocks is 231 while for granulite facies rocks, mean is 505.

[Rudnick et al. \(1985\)](#) revealed that the R value of granulitic rocks is related to K content. Thus, these authors argued that granulites with K contents >1 wt% have R value varying from 50 to 500 while the R value of granulites with K content <1 wt% usually exceed 500. On the contrary, non-metamorphosed igneous rocks (except ocean tholeiitic) have average, R value of about 230 ([Rudnick et al., 1985](#)), while for shales it is 200 ([Rudnick et al., 1985](#)). In Anyouzok, the K/Rb ratio for the pyroxene biotite gneiss ranges from 186.78-468.2 with average of 364.07, IS11 is the exception, having an R value of 534.99. This implies that all the samples, but for sample IS11 show R values similar to those of non-metamorphosed

rocks, thus all the rocks, except sample IS11 have not undergone significant loss in K and Rb in the course of metamorphism.

### V.2.3. Effects on IFs

Effects of hydrothermal alteration on BIFs within the Nyong group have been recently reported by few authors (Soh Tamehe et al., 2018; Djoukouo Soh et al., 2021). Polished thin section observations of the Anyouzok IFs revealed secondary minerals such as calcite, sericite, and tremolite (Fig. 16 & 17). These secondary minerals are mainly encountered in SBIFs, which have experienced shearing, but less obvious in BIFs. Geochemical data present a general increase in  $\text{Fe}_2\text{O}_3$  and decrease in  $\text{SiO}_2$  within the SBIFs, in contrast to BIFs (except for sample IS13), resulting in the increase of Fe/Si ratios from 0.67 in BIFs to 1.72 in SBIFs. Moreover, the SBIFs matrix present numerous cavities (Fig. 17b, c and d), which are most likely a result of leaching of silica (Hagemann et al., 2016). Moreover, the widespread shearing which affected the Anyouzok SBIFs may have created paths for fluid circulation, facilitating hydrothermal alteration and leaching processes. The formation of calcite and epidote are generally linked with hydrothermal alteration (El-Shazly et al., 2019). In this view, these authors proposed the use of  $\text{Fe}_2\text{O}_3/\text{Al}_2\text{O}_3$  vs.  $\text{CaO}/\text{Al}_2\text{O}_3$  and  $\text{Fe}_2\text{O}_3/\text{TiO}_2$  vs.  $\text{CaO}/\text{TiO}_2$  binary diagrams to assess the effect of hydrothermal alteration. In these diagrams (Fig. 35a and 35b), SBIF samples show strong positive correlations ( $r^2 = 0.99$ ), suggesting that the rock was affected by hydrothermal alteration. In contrast, such correlations are not observed in BIFs.

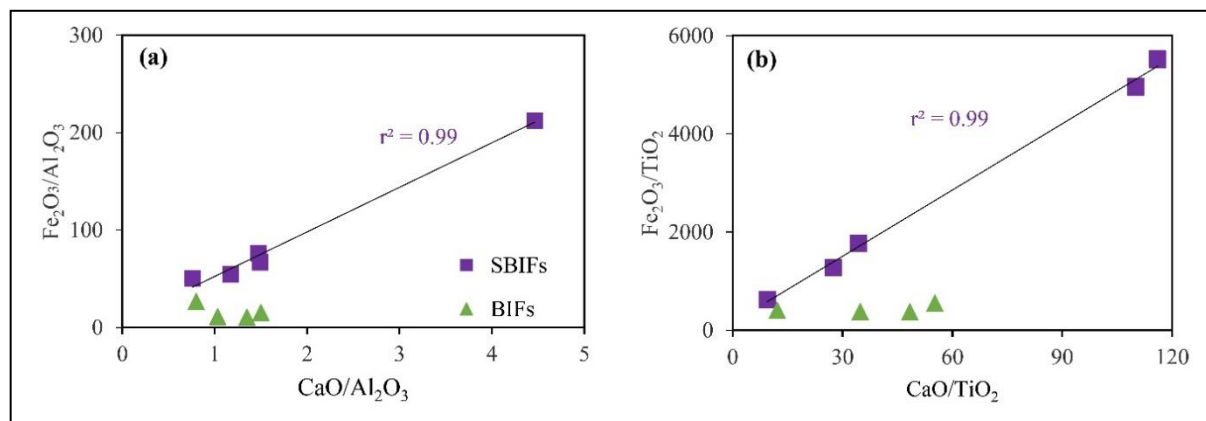


**Figure 35.** IFs hydrothermal alteration effect. (a)  $\text{Fe}_2\text{O}_3/\text{Al}_2\text{O}_3$  vs.  $\text{CaO}/\text{Al}_2\text{O}_3$  and (b)  $\text{Fe}_2\text{O}_3/\text{TiO}_2$  vs.  $\text{CaO}/\text{TiO}_2$  binary plots (after El-Shazly et al., 2019) for hydrothermal alteration effect on the Anyouzok IFs.

In addition, PAAS-normalized REE-Y patterns of the investigated IFs (Fig. 33b) exhibit prominent positive Eu anomalies and HREE enrichment over LREE comparable to many Archean to Paleoproterozoic IFs worldwide (Bau and Dulski, 1996; Bolhar et al., 2004; Thurston et al., 2012; Ganno et al., 2017; Ndime et al., 2019; El-Shazly et al., 2019; Gatsé Ebotehoua et al., 2021; Gourcerol et al., 2022), suggesting that most samples kept their primary REE-Y systematics. Based on the above discussion, we suggest that BIFs are more reliable in determining the characteristics of the Anyouzok IFs during their deposition, while SBIFs characteristics should be used with caution.

### V.3. Petrogenesis and tectonic setting of Anyouzok country rocks

#### V.3.1. Metavolcanic rocks

##### V.3.1.1. Petrogenesis

Considering the Zr/Ti vs. Nb/Y plot (Floyd and Winchester, 1978) all the Anyouzok metavolcanic rock samples are of basaltic origin (Fig. 25a) corroborating with previous investigations on the geochemical features of metabasic rocks within the Nyong Group greenstone belts (Ndema Mbongue et al., 2014; Fuanya et al., 2019; Moudioh et al., 2020; Kwamou Wanang et al., 2021; Mvodo et al., 2022; Owona et al., 2022). The Anyouzok mafic granulite and garnet amphibolite data points show tholeiitic to transitional affinities (Fig. 25c). These results are similar to those of Kribi (Mvodo et al., 2022) and Bipindi (Moudioh et al., 2020) mafic granulite and the Akom II garnet amphibolite (Aye et al., 2017) which show transitional to tholeiitic tendencies. The Anyouzok metavolcanic rock samples mainly show flat patterns in chondrite-normalized REE diagrams (Fig. 36a and c).

The Nyong group mafic granulites, from Kribi (Mvodo et al., 2022) and Bipindi (Moudioh et al., 2020), and the Nyong Group garnet amphibolites from Akom II (Aye et al., 2017) are plotted for comparison. Both Anyouzok mafic granulite and garnet amphibolite samples, as well as the Nyong Group mafic granulites show relatively flat patterns ( $(La/Yb)_{CN}=0.77-1.39$ ;  $0.70-1.29$  for mafic granulite and garnet amphibolite, respectively) (Fig. 36a, c). In contrast, the Nyong Group garnet amphibolite patterns are more fractionated, with LREE enriched over the HREE.

Mafic to ultramafic source magmas tend to assimilate crustal components during their ascent to the surface, resulting in variable degrees of crustal contamination (DePaolo, 1981; Pearce, 2008). The extent and nature of this input could be evaluated using elemental concentrations and various ratios, showing different variations in crustal- and mantle-derived

materials (DePaolo, 1981; Sun and McDonough, 1989; Barth et al., 2000; Rudnick and Gao, 2003; Pearce, 2008). For instance, troughs in Nb and Ta exhibited by most analyzed samples in multi-element diagrams (Fig. 34b and d) suggest crustal input (DePaolo, 1981; Barth et al., 2000; Pearce, 2008). Th/Nb (0.19 - 0.36; mean: 0.24 and 0.004 - 0.16; mean: 0.08 for mafic granulite and garnet amphibolite, respectively) and Nb/Y (0.036 - 0.17; mean: 0.11 and 0.08 - 0.19; mean: 0.14 for mafic granulite and garnet amphibolite respectively) ratios of the analyzed samples are lower than UCC values (Th/Nb: 0.87; Nb/Y: 0.57; Rudnick and Gao, 2003), suggesting insignificant to minor crustal contamination.

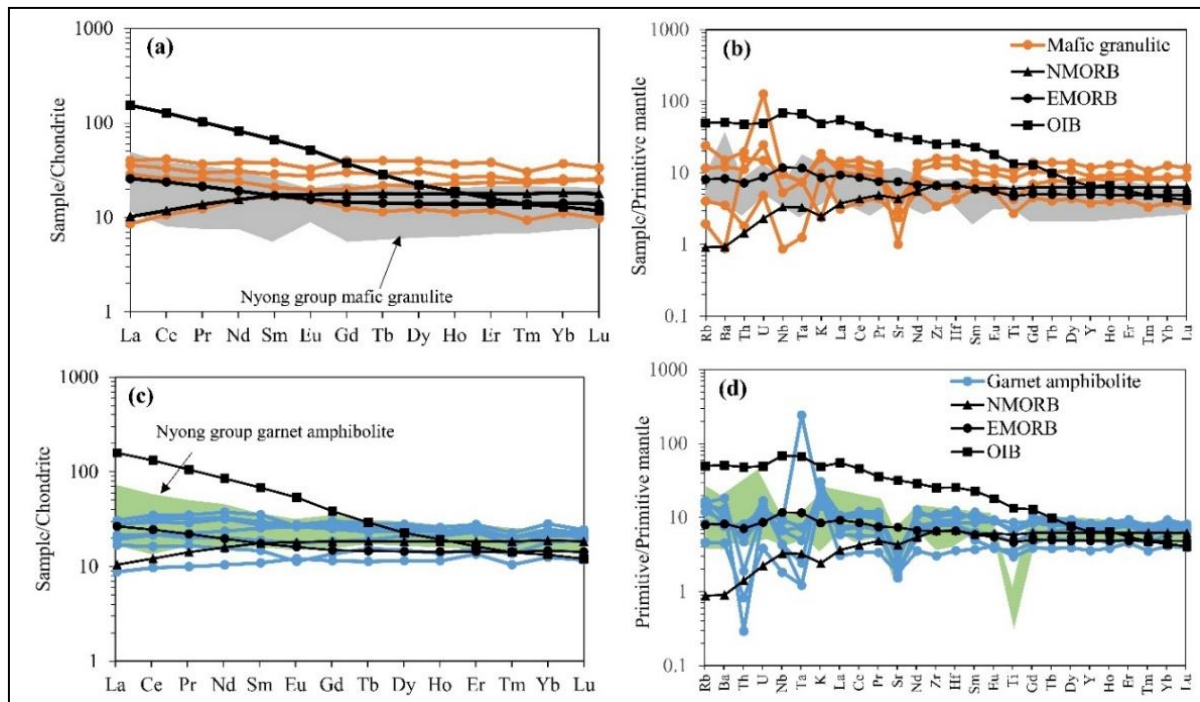


**Figure 36.** REE (a and c) and multi-element (b and d) diagrams of Anyouzok metavolcanic rocks plotted with rocks from nearby studies for comparison. Normalisation values after McDonough and Sun, (1995) and Sun and McDonough (1989) respectively. Nyong Group mafic granulite data are from (Moudioh et al., 2020) and (Mvodo et al., 2022). Nyong Group garnet amphibolite data are from (Aye et al., 2017).

### V.3.1.2. Tectonic setting

Previous workers reported various tectonic environments for the Nyong Group metabasic rocks including back-arc, within-plate, NMORB, EMORB and OIB settings (Fuanya et al., 2019; Moudioh et al., 2020; Kwamou Wanang et al., 2021; Mvodo et al., 2022; Owona et al., 2022 and references therein). Chondrite-normalized diagrams show that the Anyouzok metavolcanic rocks mainly show NMORB and EMORB affinities (Fig. 36a and c). Furthermore, in the primitive mantle-normalized multi-element plots (Fig. 36b and d),

most samples exhibit depletion in Nb, Ta, Ti and Zr, which are commonly observed in arc basalt setting (Kelemen et al., 2014; Meng et al., 2014; Wang et al., 2016). Various tectonic discrimination diagrams based on immobile elements are generally used to constrain the geodynamic setting of metamorphosed mafic rocks (Cabanis and Lecolle, 1989; Pearce, 2008). In the La/10-Nb/8-Y/15 ternary diagram (Fig. 37a) proposed by Cabanis and Lécolle (1989), the studied garnet amphibolite samples, likewise the Akom II garnet amphibolite plotted for comparison show back-arc and EMORB characteristics. In contrast, the analyzed mafic granulite samples mainly have arc tholeiitic and back-arc features, similar to other Nyong Group mafic granulites. In the Th/Yb vs. Nb/Yb discrimination diagram (Fig. 37b), the Anyouzok samples are scattered within and above the mantle array. Garnet amphibolite samples fall within the back-arc field and NMORB area, while mafic granulite plot along the arc field and follow the within plate enrichment trend defined by Pearce (2008). Based on these geochemical features and earlier studies of metabasic rocks within the Nyong Group, an association of back-arc and arc setting is suggested for the emplacement of the Anyouzok metavolcanic rocks precursors.

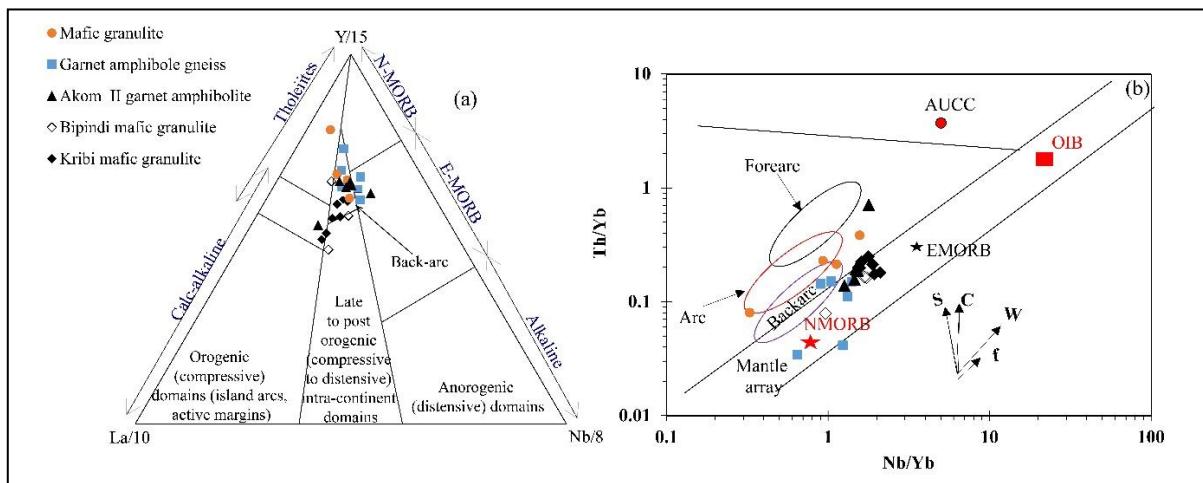


**Figure 37.** Tectonic discrimination plots of the Anyouzok metavolcanic rocks. (a) La/10-Nb/8-Y/15 (Cabanis and Lecolle, 1989); (b) Th/Yb vs. Nb/Yb. NMORB: normal mid-ocean ridge basalts, E-MORB: Enriched Mid Ocean Ridge Basalts, OIB: Ocean Island Basalts, AUCC: Archean Upper Continental Crust. The vectors f, W, C and S refer to fractional crystallization, within plate fractionation, crustal contamination and subduction zone component respectively (after Pearce, 2008). Forearc, arc, and backarc fields are from (Metcalf et al., 2008).



### V.3.2. Metasedimentary rocks

#### *V.3.2.1. Weathering and sediment maturity*

Previous studies have indicated that the chemical compositions of rocks are dependent on source compositions and can be affected by regional metamorphism and supergene geological processes such as transport sorting, diagenesis, and chemical alteration (Nesbitt and Young, 1982; Roser and Korsch, 1986; McLennan et al., 1993). The chemical index of alteration (CIA) is used to assess the degree of chemical weathering under which the intermediate to acidic protore of metasediments have been subjected. Generally, CIA values for weakly altered igneous and metamorphic rocks are in the order of 55 or less, whereas strongly altered rocks, which produce residual clay minerals, such as kaolinite and/or gibbsite, correspond to CIA values close to 100 (Nesbitt and Young, 1982). Values of 70 - 75 and ~ 56 are typical for shales and greywackes, respectively (McLennan et al., 1993; Motta Garcia et al., 2014). The average Chemical Index of Alteration (CIA) value for pyroxene biotite gneisses, at 61 (59.67 to 63.13), closely resembles the alteration index of greywackes (56), indicating an intermediate to acidic source rock that has undergone low to moderate chemical alteration. Additionally, the Th/U ratio of the examined pyroxene biotite gneiss suggests that these siliciclastic rocks likely experienced low to moderate weathering in their primary source area (McLennan et al., 1993).

Similar to the CIA, the index of chemical variability (ICV) can be useful as an index of recycling and compositional maturity in sedimentary rocks (Cox et al., 1979; Armstrong-Altrin et al., 2015). Clastic sediments with low ICV values (<1) are likely to be derived from a mature sedimentary source with large amounts of clay minerals, indicating sediment recycling in a passive tectonic setting. In contrast, clastic sediments with high ICV values (>1) indicate immature sediments (Kamp and Leake, 1985). The ICV values of pyroxene biotite gneiss ranges from 80.40 to 91.36 (with a mean of 84), indicating that they are metasediments derived from immature sediments. These sediments correspond to deposits resulting from moderate to weak weathering processes.

#### *V.3.2.2. Sediment Provenance*

The chemical composition of sedimentary rocks is controlled by a complex suite of parameters operating through erosion, transport, and deposition. The main first-order parameters include the composition of the source rock, modification by chemical weathering, mechanical weathering, and abrasion, authigenic inputs, hydraulic sorting and diagenesis (Johnson 1993). Various major and trace element ratios such as  $\text{Al}_2\text{O}_3/\text{TiO}_2$ , La/Co, Co/Th,

Cr/Th and Cr/Zr in siliciclastic rocks are reliable provenance indicators (Bhatia and Crook, 1986; Lazaro et al., 1995; Cullers and Berendsen, 1998). The  $\text{Al}_2\text{O}_3/\text{TiO}_2$  ratio for felsic rocks is generally between 10 and 100 (sometimes more), while for mafic rocks it is  $<20$  (Hayashi et al. 1997). In pyroxene biotite gneiss, the  $\text{Al}_2\text{O}_3/\text{TiO}_2$  ratio varies from 52.88 to 146.67, indicating that the sediments are derived from felsic rock sources.

### V.3.2.3. Tectonic setting

Major clastic sedimentary rock components like  $\text{SiO}_2$ ,  $\text{Al}_2\text{O}_3$ ,  $\text{K}_2\text{O}$  and  $\text{Na}_2\text{O}$ , can be used to define the tectonic setting of terrigenous sedimentary rocks.  $\text{SiO}_2/\text{Al}_2\text{O}_3$  and  $\text{K}_2\text{O}/\text{Na}_2\text{O}$  values (Fig. 38a) go from the volcanic arc through the active continental margin to the passive continental margin (Roser and Korsch, 1986). With the  $\text{SiO}_2$  and  $\text{K}_2\text{O}/\text{Na}_2\text{O}$  discriminant diagram (Fig. 38b), all samples from the Anyouzok area (Roser and Korsch, 1986) fall within the active continental margin (ACM).

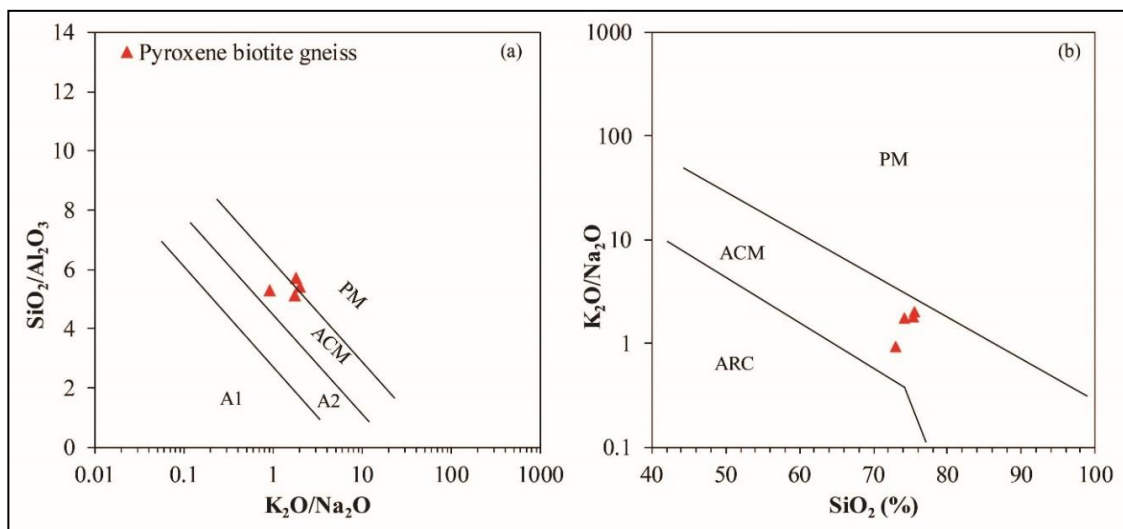


**Figure 38.** Tectonic discrimination plots of the Anyouzok pyroxene biotite gneiss. (a)  $\text{K}_2\text{O}/\text{Na}_2\text{O}$  vs.  $\text{SiO}_2$  and (b)  $\text{SiO}_2/\text{Al}_2\text{O}_3$  vs.  $\text{K}_2\text{O}/\text{Na}_2\text{O}$  diagrams (after Roser and Korsch, 1986). ACM (active continental margin), PM (passive margin), ARC (Oceanic island-arc margin), A1 (arc setting, basaltic and andesitic detritus), and A2 (evolved arc setting, felsic-plutonic detritus).

## V.4. Origin and depositional environment of the Anyouzok IFs

### V.4.1. Detrital input assessment during the Anyouzok IF deposition

The primary features of IFs could be influenced by the occurrence of clastic and/or volcanic components, yielding to high contents of some trace elements generally considered

immobile and which lack in seawater (e.g.  $\text{Al}_2\text{O}_3$ ,  $\text{TiO}_2$ , Zr, Th, Nb, Sc; Bolhar et al., 2004; Alexander et al., 2008; Basta et al., 2011; Thurston et al., 2012; Wang et al., 2014; Gourcerol et al., 2016). In addition, this detritus produce correlation between the former listed immobile elements and some REE and HFSE ratios such as Y/Ho, Pr/Yb (Thurston et al., 2012). Petrography study has revealed the presence of detrital components within the Anyouzok IFs depicted by minerals such as plagioclase and K-feldspar (Figs. 17 and 18). The Anyouzok BIFs show  $\text{Al}_2\text{O}_3$  (mean: 2.14 wt%),  $\text{TiO}_2$  (mean: 0.08 wt%), Zr (mean: 16.08 ppm) contents and Pr/Yb ratios (mean: 1.76) suggesting slight detritus contribution during the deposition of BIFs.

Estimation of the detrital input in the Anyouzok IFs was based on the Fe/Ti vs.  $\text{Al}/(\text{Al}+\text{Fe}+\text{Mn})$  diagram by Boström (1970), displaying the ideal mixing between terrigenous and metalliferous sediments. In this plot (Fig. 39a), the analyzed BIFs reveal up to 15% detritus in their composition whereas the SBIFs reflect insignificant contamination for most samples (except sample IS41 with ca. 10% crustal input). As discussed under the effects of alteration, metamorphism, and element mobility, increase in Fe within the SBIFs is associated with hydrothermal alteration, which facilitated leaching processes, thus the position of their data points closer to hydrothermal sediments area (Fig. 39a). Th/U ratios  $< 5$  have been proposed as indicator of the presence of phosphate (e.g. apatite, monazite) and contaminants during chemical sediment deposition (Thurston et al., 2012), since volcanic and clastic materials generally have values ranging from ca 3-5 (Sun and McDonough, 1989; Condie, 1993; Rudnick and Gao, 2003). In the current study, phosphate minerals such as monazite or apatite have neither been identified in thin sections, nor via XRD investigations. The studied BIFs have Th/U ratios ranging from 3.84-5.50, similar to volcanic and clastic materials 5 (Sun and McDonough, 1989; Condie, 1993; Rudnick and Gao, 2003). In addition, Fig. 39b, indicates increasing Th/U ratios with decreasing Zr concentrations in the Anyouzok BIFs, suggesting the influence of volcanic or clastic detritus in the Anyouzok BIFs. Lower concentrations and ratios, and lack of correlations between Zr and Th/U presented by the SBIF samples (Table 13), could be attributed to leaching of materials during hydrothermal activities (Hagemann et al., 2016).

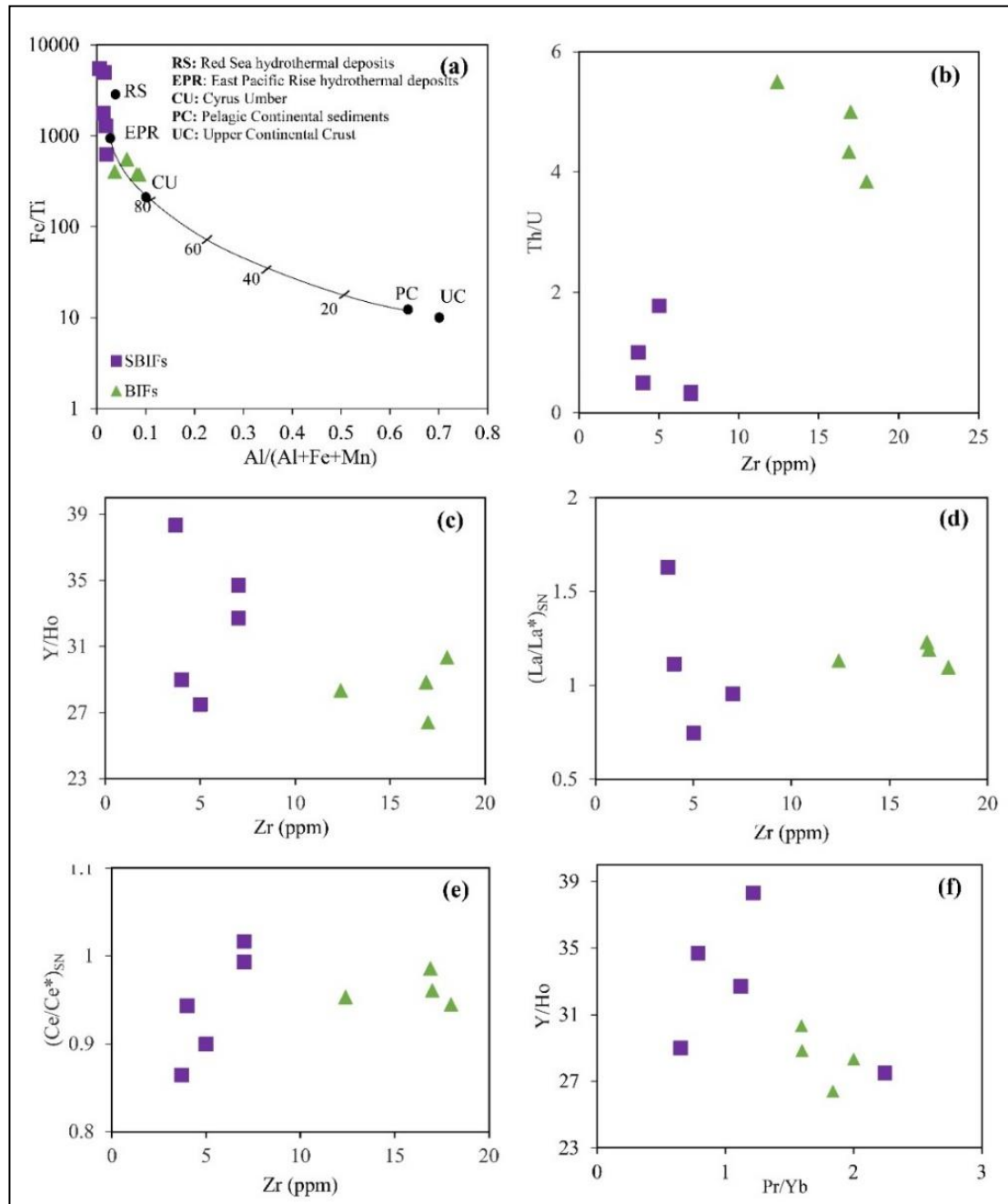


**Figure 39.** Detrital input assessment of the Anyouzok IFs: (a) Fe/Ti vs. Al/(Al + Fe + Mn). The curve represents mixing of pelagic continental sediments (PC) with East Pacific Rise deposits (EPR); approximate amount of EPR in the mixture ([adopted from Barrett, 1981](#)) is indicated by the numbers in percentage. CU: Cyprus umber, UC: Upper continental crust, RS: Red sea hydrothermal deposits ([Marchig et al., 1982](#); [Taylor and McLennan, 1985](#)); (b) Th/U vs. Zr; (c) Y/Ho vs. Zr; (d) (La/La\*)<sub>SN</sub> vs. Zr; (e) (Ce/Ce\*)<sub>SN</sub> vs. Zr; (f) Y/Ho vs. Pr/Yb; (g) (La/La\*)<sub>SN</sub> vs. Pr/Yb; (h) (Ce/Ce\*)<sub>SN</sub> vs. Pr/Yb.

To further evaluate the influence of detritus on the REE-Y systematics of the Anyouzok IFs, binary plots such as Zr and Pr/Yb vs. Y/Ho, (La/La\*)<sub>SN</sub> and (Ce/Ce\*)<sub>SN</sub> were

used (Fig. 39c-f). In fig. 39e,  $(Ce/Ce^*)_{SN}$  highlighted positive correlation against Zr for the SBIFs and no correlation against Pr/Yb. In contrast, no other important positive correlation is observed with Y/Ho and  $(La/La^*)_{SN}$ , suggesting that the presence of detritus and/or alteration have not significantly influenced the REE-Y systematics of the Anyouzok IFs.

#### V.4.2. Seawater and hydrothermal fluid contribution

REE-Y systematics is widely used to assess the origin of Si and Fe in IFs (Bau and Dulski, 1999; Bolhar et al., 2004; Alexander et al., 2008; Bekker et al., 2010; Planavsky et al., 2010; Basta et al., 2011; Gourcerol et al., 2022). Chemical sediments originated from seawater are characterized by super-chondritic Y/Ho ratios ( $>44$ ), shale-normalized REE-Y patterns exhibiting positive La, Y and Gd anomalies, negative Ce anomaly, and HREE enrichment over LREE and MREE (Bau and Dulski, 1999; Bolhar et al., 2004; Thurston et al., 2012). In PAAS-normalized REE-Y diagrams, the Anyouzok IFs show consistent patterns (Fig. 30b) with LREE depletion over HREE, positive Gd and La anomalies (except for two SBIF samples; IS19 and IS41) and negative Y anomalies (but for one SBIF sample IS54). They show chondritic to super-chondritic Y/Ho ratios in both BIFs (26.40-30.33) and SBIF (27.5-38.33) samples. Almost all BIF samples (except IS13) exhibit negative Y anomalies and chondritic Y/Ho ratios indicating they could be derived from slow rates of Fe oxyhydroxide precipitation (Bau, 1999; Bau and Dulski, 1999; Basta et al., 2011).

Several workers reported that prominent positive Eu anomalies in IFs reflect the influence of high temperature hydrothermal fluids, whereas lack of Eu anomalies are considered as low temperature hydrothermal fluid signatures (Danielson et al., 1992; Bau and Dulski, 1999; Bolhar et al., 2004; Alexander et al., 2008; Gourcerol et al., 2016). The Anyouzok IFs show positive  $(Eu/Eu^*)_{SN}$  anomalies ranging from 1.86-2.68 and from 2.14-3.17 for the BIFs and SBIFs respectively, suggesting influence of high temperature hydrothermal fluids. In addition, Bau and Dulski (1996) reported that high temperature hydrothermal fluids ( $> 250^{\circ}C$ ) have  $(Eu/Eu^*)_{CN} > 1$  and lower temperature hydrothermal fluids ( $< 250^{\circ}C$ ) have  $(Eu/Eu^*)_{CN} \approx 1$ . In this view, the Eu anomalies ( $(Eu/Eu^*)_{CN}=1.23-1.66$  and  $1.52-1.98$ ) observed in the analyzed BIFs and SBIFs respectively could account for high temperature hydrothermal fluids contribution. However, in the  $(Eu/Eu^*)_{SN}$  vs. LREE diagram (Fig. 40a), excluding sample IS13 showing secondary enrichment, all BIF samples lack correlation, suggesting hydrothermal fluid input during their precipitation (Danielson et al., 1992; Bau and Dulski, 1999; Bolhar et al., 2004; Alexander et al., 2008; Gourcerol et al., 2016). In contrast, the increase in Eu anomalies with decreasing LREE in SBIFs samples

could indicate the influence of post-depositional processes, such as hydrothermal alteration, as previously discussed.

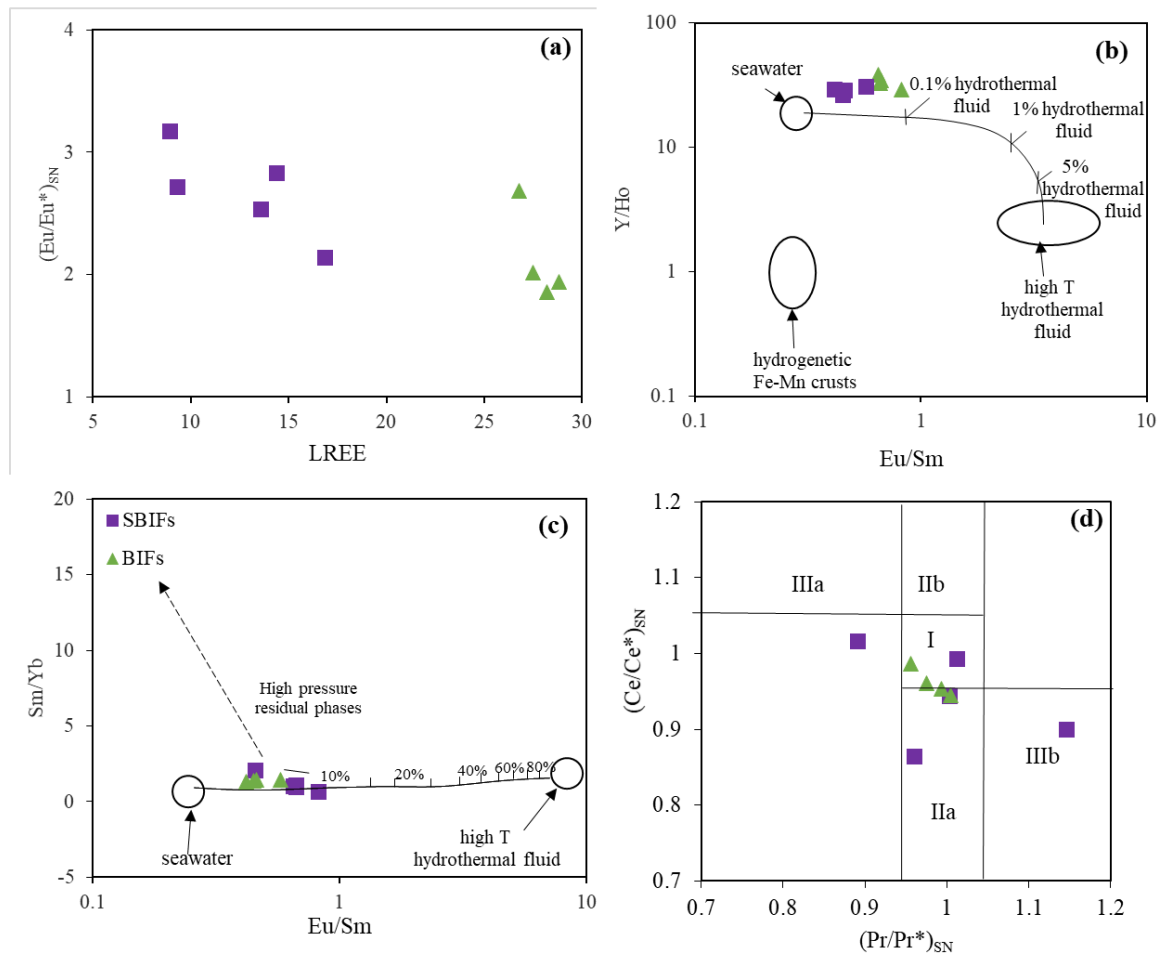


**Figure 40.** Contribution of seawater and hydrothermal fluids in the Anyouzok IFs precipitation: (a)  $(Eu/Eu^*)_{SN}$  vs. LREE diagram for the Anyouzok IFs; (b)  $Eu/Sm$  vs.  $Y/Ho$  (Alexander et al., 2008) with conservative mixing line of high-temperature hydrothermal fluid (Bau and Dulski, 1999) and seawater (Alibo and Nozaki, 1999); (c)  $Eu/Sm$  vs.  $Sm/Yb$  plot (Gourcerol et al., 2016) with conservative mixing line of high-temperature hydrothermal fluid (Thurston et al., 2012) and seawater (Alibo and Nozaki, 1999); (d)  $(Ce/Ce^*)_{SN}$  vs.  $(Pr/Pr^*)_{SN}$  plot (Bau and Dulski, 1996) for the Anyouzok IFs. I: neither Ce nor La anomaly; IIa: positive La anomaly, no Ce anomaly; IIb: negative La anomaly, no Ce anomaly; IIIa: positive Ce anomaly; IIIb: negative Ce anomaly.

Alexander et al. (2008) and Gourcerol et al. (2016) proposed binary diagrams based on  $Eu/Sm$ ,  $Y/Ho$  and  $Sm/Yb$ , and defined mixing line using seawater and high temperature hydrothermal fluid endmembers, to evaluate their contribution in the solute sources of IFs.



Fig. 40b shows that small quantities of high temperature hydrothermal fluids (0.1%) could account for the Eu/Sm and Y/Ho ratios presented by the Anyouzok IFs. Furthermore, the analyzed IFs fall along the mixing line (Fig. 40c) defined by [Gourcerol et al. \(2016\)](#) and suggest an input of ca. 5% of high temperature hydrothermal fluids in the Anyouzok BIFs and that they were deposited distal to the hydrothermal vent. It is therefore suggested that mixture of seawater, low quantities of high temperature hydrothermal fluids and variable quantities of detrital materials influenced the deposition of the Anyouzok IFs. Comparable results were reported for several IF occurrences within the Congo Craton in Cameroon ([Teutsong et al., 2017](#); [Soh Tamehe et al., 2018, 2021](#); [Ndime et al., 2019](#); [Nzepang Tankwa et al., 2020](#)) and Congo ([Gatsé Ebotehoua et al., 2021](#); [Gourcerol et al., 2022](#)).

#### V.4.3. Paleoredox state of IF

Ce anomalies in chemical sediments is widely used to assess the paleoredox state of the ancient seawater ([Bau and Dulski, 1996](#); [Klein, 2005](#); [Bekker et al., 2010](#); [Braga et al., 2015](#)). Suboxic and anoxic seawaters lack negative Ce anomalies unlike oxygenated seawater which displays strong negative Ce anomalies ([Bau and Dulski, 1996](#); [Bekker et al., 2010](#)). To distinguish “true” from “false” negative Ce anomalies, the  $(Ce/Ce^*)_{SN}$  vs.  $(Pr/Pr^*)_{SN}$  diagram (Fig. 40d) has been proposed by [Bau and Dulski \(1996\)](#). In this plot, most of the Anyouzok IF samples show no Ce anomalies, suggesting that they were deposited in a suboxic to anoxic environment. Only SBIF sample IS41, with chondritic Y/Ho ratios (27.5) coupled with negative La (0.75) and Y (0.88) anomalies, show oxic environment, which could be attributed to Fe oxyhydroxide influence on the REE-Y. Therefore, we suggest that the Anyouzok IFs were deposited under anoxic conditions, similar to most of the Nyong Group and Archean to Paleoproterozoic IFs worldwide ([Bekker et al., 2010](#); [Planavsky et al., 2010](#); [Chombong et al., 2017](#); [Ndime et al., 2019](#); [Gatsé Ebotehoua et al., 2021](#); [Deassou Sezine et al., 2022](#)).

#### V.4.4. Depositional setting

Based on associated or interbedded rocks, IFs have been classified as Algoma type, when deposited close to volcanic centers within greenstone belts or as Superior type when deposited distal from volcanic centres, on continental shelves or on submerged platforms ([Gross, 1980](#); [Klein, 2005](#); [Beukes and Gutzmer, 2008](#)). Previous workers suggested both superior- ([Ganno et al., 2017](#); [Soh Tamehe et al., 2018, 2021](#)) and Algoma-type ([Moudioh et al., 2020](#)) affinities for the Nyong Group IFs. Furthermore, several depositional environments were proposed for Nyong Group IFs, including island arc setting with MORB-like signatures

(Kwamou Wanang et al., 2021), volcanic arc setting (Nzepang Tankwa et al., 2020), back-arc or continental margin sea environments (Ganno et al., 2017; Soh Tamehe et al., 2018), large basin between a continental margin and an oceanic volcanic center (Soh Tamehe et al., 2021), extensional basin between a continental margin and back-arc setting (Moudioh et al., 2020). The Anyouzok IFs are interbedded with metasedimentary rocks (pyroxene biotite gneiss) and metavolcanic rocks comprising mafic granulite and garnet amphibolite along the stratigraphy (Figs. 9 and 10), suggesting an Algoma type deposit. Considering the conspicuous higher Shale-normalized Eu anomalies of the Algoma type IFs, Huston and Logan (2004) proposed a threshold with  $(\text{Eu}/\text{Eu}^*)_{\text{NASC}} > 1.8$  for Algoma type and values  $< 1.8$  for the superior type IFs. In this view, high  $(\text{Eu}/\text{Eu}^*)_{\text{NASC}}$  anomalies presented by the studied BIFs (1.88-2.7) and SBIFs (2.16-3.26) suggest an Algoma type deposit for the Anyouzok IFs, although higher values presented by SBIFs reflect influence of hydrothermal alteration. Taking into consideration our results and those of previous IF investigations within the Nyong Group, we suggest that the Anyouzok IFs are Algoma-type and were deposited distal to the hydrothermal vents, in an arc/back-arc setting.

## **V.5 Comparison of the Northern and the southern prospects**

The ore body of the northern prospect is N-S trending with a strike length of 2100 m by 300 m, while that of the southern prospect is NW-SE trending with a strike-length of 2000 m by 300 m, thus the northern prospect ore body is bigger.

The ore body and the host rocks of the Northern prospect is generally shallow-dipping to the North east while the ore body of the southern prospect is generally steeply dipping to the WNW.

As per the drill sections, all the drillholes to the northern prospect begin on the mineralised rock, drilling through it into a mafic granulite footwall while for the southern prospect, the hole begins on pyroxene biotite gneiss through the hanging wall, mineralisation and pyroxene biotite gneiss footwall with mafic granulite intercalations.

BIF is intercepted only on a drillhole of the southern prospect which therefore contains both BIF and SBIF, while only SBIF is intercepted on the Northern prospect.

The rocks of the northern prospect have experienced more shearing than those of the southern prospect, thus the ore body of the northern prospect appear more sheared than those of the southern prospect, thus the ore body of the northern prospect tends to show more enrichments when compared with those of the southern prospect.

## V.6. Ore potential, environmental and socio-economic considerations

### V.6.1. Ore potential of the Anyouzok Iron ore deposit

The demand for high grade ( $> 55$  wt% Fe), high purity (e.g. low phosphorus) Fe concentrates has been in a steady increase since the last decade. However, hematite / goethite-rich ore bodies are increasingly difficult to find. Consequently, industries and policy makers are getting more and more interested in low grade iron ore (Hagemann et al., 2016). Exploration efforts are thus geared towards Archaean and Paleoproterozoic IF-hosted magnetite-rich deposits (Duuring and Hagemann, 2013; Hagemann et al., 2016). Several exploration works have been carried out on the Anyouzok iron ore deposit (Peters, 2011; Baker and Haythornthwaite, 2015), the latest of them being the prefeasibility studies conducted by Caminex Sarl, the Cameroonian subsidiary of the British-based International Mining and Infrastructure Corporation (IMIC).

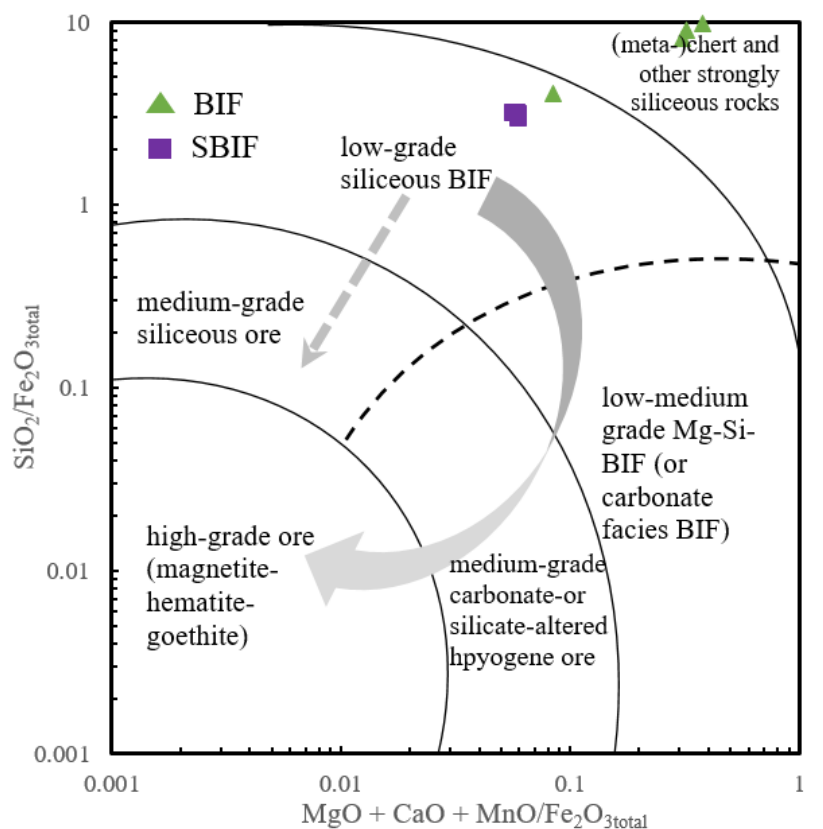


**Figure 41.** Whole-rock geochemistry discrimination diagram for BIF, altered BIF, medium- and high-grade ore, showing major and oxide ratios ( $\text{MgO} + \text{CaO} + \text{MnO} / \text{Fe}_2\text{O}_{3\text{total}}$  versus  $\text{SiO}_2 / \text{Fe}_2\text{O}_{3\text{total}}$  with discrimination fields and arrows showing alteration trends (after Angerer et al., 2012).

These studies reported magnetite ore deposit, with 96.9 Mt at 34.92% Fe indicated and 79.4 Mt at 35.04% Fe inferred reserves (Baker and Haythornthwaite, 2015). Three iron ore types have been identified within the Anyouzok iron deposit; the blue dust, the massive hematite ore and the disseminated magnetite ore (Fig. 16). Blue dust and massive hematite ore occur within the limited weathered horizon and for commercial reasons would not be economic. This is contrary to the Nkout iron ore deposit with deep, well developed soil horizon of up to 50 m below the surface (Odigui Ahanda, et al., 2019) where direct shipping ore occurrences have been reported. On the contrary, the disseminated magnetite ore shows relatively high  $\text{Fe}_2\text{O}_3$  contents (49.6-55.2%), lower gangue content (43.3-47.7%  $\text{SiO}_2$  and 0.26-0.99%  $\text{Al}_2\text{O}_3$ ) with low concentrations of deleterious elements ( $\text{P}_2\text{O}_5$  average of 0.12%). Consequently, the magnetite-rich, disseminated ore in terms of volume is a more favourable target. Following the  $(\text{MgO} + \text{CaO} + \text{MnO}) / \text{Fe}_2\text{O}_{3\text{total}}$  versus  $\text{SiO}_2 / \text{Fe}_2\text{O}_{3\text{total}}$  plot (Fig. 41), the Anyouzok BIF falls within the “meta-chert and other strongly siliceous rock” field while SBIF falls within the ‘low-grade siliceous BIF ore’ (after Angerer et al., 2012). Therefore the BIF may have been deposited as low-grade and was later subjected to ore re-concentration processes into a more enriched SBIF.

#### V.6.2. Environmental and socio-economic considerations of the Anyouzok Iron ore deposit

Environmental and social impact assessment studies was carried out during the exploration phase within the Ntem concession. Key environmental concerns identified include impacts resulting from site clearing and destruction of the forest and associated habitats, land uses and rehabilitation activities, post closure and the potential impact to water resources and contamination. Potential negative socio-economic impacts include population influx and associated impacts such as social ills and pressure on infrastructure, social unrest, conflict, air pollution and impacts associated with community health. However, positive impacts associated with the improvement of livelihood around the project area through direct and indirect economic advantages (e.g. increased job opportunities, procurement of goods and services, etc), development and improvement of infrastructure, as well as the training and provision of education for the local communities. These positive impacts are expected to be beneficial to the local communities directly, besides the effects it would have at the regional scale.

## **GENERAL CONCLUSION**

This work aimed at determining the petrographic characteristics of metavolcano-sedimentary rocks and their relationship with associated iron formations within the Anyouzok area. The results obtained in the study were interpreted and discussed and the following conclusions were arrived at: -

The lithostratigraphy combined with petrographic and mineralogical studies of both prospects reveal that the rocks are predominantly metamorphic, consisting of the iron formations and the host rock units. The iron formations consist of BIF and SBIF while the host rock units are made up of pyroxene biotite gneiss, epidote gneiss, mafic granulite and garnet amphibolites. The stratigraphic sections show some similarities and differences between the northern and the southern prospects. The northern prospect mostly portrays mafic granulite as the basement, while pyroxene biotite gneiss constitutes the basement for the southern prospect.

These rocks show heterogranular granoblastic, coronitic and mylonitic microstructures with typical granulite and amphibolite facies assemblages. In addition, SBIF photomicrographs show cavities which are indices of quartz leaching, unlike for BIF photomicrographs. XRD studies of the iron formations also show similarities with minerals studied under the metallographic microscope. The Anyouzok rocks have registered amphibolite, granulite and greenschist facies metamorphic conditions. This implies that the rocks were subjected to a retrograde, plurifacial metamorphic evolution. Ore enrichment occurred during upgrade from greenschist to amphibolite facies, upgrading BIF to a more enriched SBIF.

From a geochemical perspective, the Anyouzok area is made up essentially of metavolcanic and metasedimentary rocks. The metavolcanic rocks are composed of mafic granulites and garnet amphibolites, which are all of basaltic origin. These metavolcanic rocks show transitional to tholeiitic affinities with variable contents in trace and rare earth elements. The metasedimentary rocks are mainly pyroxene biotite gneiss which are of greywacke and arkosic origin. They were deposited within the active continental margin. Geochemical features of the Anyouzok IFs and interbedded metavolcanic rocks, indicate that these IFs are Algoma type and were formed distal to the hydrothermal vents in an arc /back-arc setting, under sub-oxic to anoxic conditions.

The Banded iron formations (BIF) Fe contents range from 26.05 wt% to 27.68 wt% while the SBIF Fe contents range from 49.6 wt% to 55.2 wt%. This qualifies the SBIF a potential low-grade iron ore, suitable for profitable exploitation.



### **Economic implications of this study**

It unravels the fact that low grade BIF through metamorphic related processes such as hydrothermalism has led to ore upgrade from banded iron formations to a more concentrated, sheared iron formation, thereby adding value to the deposit.

Secondly, the natural location of the deposit at about 80 Km from the Kribi deep seaport, and at an altitude of about 550 m above sea level, drained by many streams, puts it at the advantage over other iron ore deposits within the area as it makes exploitation easier and furthermore economic.

In perspective, the following has been suggested;

- Do a microprobe chemico-mineralogical study of the area to better understand for example the pressure and temperature conditions of formation.
- Carry out a geochronological and isotopic (Lu-Hf, Re-Os) analysis for a better comprehension of the geodynamic conditions.
- Develop knowledge on how to use the ore material to come out with finished products for the local markets.

## **REFERENCES**

- Aguilar, C., Alkmim, F.F., Lana, C., Farina, F., 2017. Palaeoproterozoic assembly of the São Francisco craton, SE Brazil: New insights from U–Pb titanite and monazite dating. *Precambrian Research*, 289, 95–115. <https://doi.org/10.1016/j.precamres.2016.12.001>
- Akame, J.M., Owona, S., Hublet, G., Debaille, V., 2020. Archean tectonics in the sangmelima granite-greenstone terrains, Ntem Complex (NW Congo craton), southern Cameroon. *Journal of African Earth Sciences*, 168, 103872. <https://doi.org/10.1016/j.jafrearsci.2020.103872>
- Alexander, B.W., Bau, M., Andersson, P., Dulski, P., 2008. Continentally-derived solutes in shallow Archean seawater: rare earth element and Nd isotope evidence in iron formation from the 2.9 Ga Pongola Supergroup, South Africa. *Geochimica et Cosmochimica Acta*, 72, 378–394.
- Alibo, D.S., Nozaki, Y., 1999. Rare earth elements in seawater: particle association, shale-normalization, and Ce oxidation. *Geochimica et Cosmochimica Acta*, 63, 363–372.
- Alkmim, F.F., Marshak, S., 1998. Transamazonian Orogeny in the Southern São Francisco Craton Region, Minas Gerais, Brazil: Evidence for Paleoproterozoic collision and collapse in the Quadrilátero Ferrífero. *Precambrian Research*, 90: 29–58.
- Armstrong-Altrin, J.S., Machain-Castillo, M.L., Rosales-Hoz, L., Carranza-Edwards, A., Sanchez-Cabeza, J.-A., Ruíz-Fernández, A.C., 2015. Provenance and depositional history of continental slope sediments in the Southwestern Gulf of Mexico unraveled by geochemical analysis. *Continental Shelf Research*, 95, 15–26.
- Aye, B.A., Sababa, E., Ndjigui, P.-D., 2017. Geochemistry of S, Cu, Ni, Cr and Au-PGE in the garnet amphibolites from the Akom II area in the Archaean Congo Craton, Southern Cameroon. *Geochemistry*, 77, 81–93. <https://doi.org/10.1016/j.chemer.2017.01.009>
- Bagnouls, F., Gaussen, H., 1957. LES CLIMATS BIOLOGIQUES ET LEUR CLASSIFICATION. *Annales de Géographie* 66, 193–220.
- Baker, H., Haythornthwaite, J., 2015. Mineral resource estimate for the FeO8 and Fe11 deposits of the Ntem Iron Project, South Province. *SRK Consulting (UK) Ltd.*
- Barbey, P., Macaudiere, J., Nzenti, J.P., 1990. High-Pressure Dehydration Melting of Metapelites: Evidence from the Migmatites of Yaounde (Cameroon)\*, *Journal of Petrology*. 31, 401–427. <https://doi.org/10.1093/petrology/31.2.401>
- Barbosa, J.S., Sabaté, P., 2002. Geological features and the Paleoproterozoic collision of four Archean crustal segments of the São Francisco Craton, Bahia, Brazil: a synthesis. *Anais da Academia Brasileira de Ciências*, 74, 343–359.
- Barrett, T.J., 1981. Chemistry and mineralogy of Jurassic bedded chert overlying ophiolites in the North Apennines, Italy. *Chemical Geology*, 34, 289–317. [https://doi.org/10.1016/0009-2541\(81\)90118-2](https://doi.org/10.1016/0009-2541(81)90118-2)
- Barth, M.G., McDonough, W.F., Rudnick, R.L., 2000. Tracking the budget of Nb and Ta in the continental crust. *Chemical Geology*, 165, 197–213.
- Basta, F.F., Maurice, A.E., Fontboté, L., Favarger, P.-Y., 2011. Petrology and geochemistry of the banded iron formation (BIF) of Wadi Karim and Um Anab, Eastern Desert, Egypt: implications for the origin of Neoproterozoic BIF. *Precambrian Research*, 187, 277–292.

- Bau, M., 1999. Scavenging of dissolved yttrium and rare earths by precipitating iron oxyhydroxide: experimental evidence for Ce oxidation, Y-Ho fractionation, and lanthanide tetrad effect. *Geochimica et Cosmochimica Acta*, 63, 67–77.
- Bau, M., Dulski, P., 1999. Comparing yttrium and rare earths in hydrothermal fluids from the Mid-Atlantic Ridge: implications for Y and REE behaviour during near-vent mixing and for the Y/Ho ratio of Proterozoic seawater. *Chemical Geology*, 155, 77–90.
- Bau, M., Dulski, P., 1996. Distribution of yttrium and rare-earth elements in the Penge and Kuruman iron-formations, Transvaal Supergroup, South Africa. *Precambrian Research*, 79, 37–55.
- Bekker, A., Slack, J.F., Planavsky, N., Krapež, B., Hofmann, A., Konhauser, K.O., Rouxel, O.J., 2010. Iron Formation: The Sedimentary Product of a Complex Interplay among Mantle, Tectonic, Oceanic, and Biospheric Processes. *Economic Geology*, 105, 467–508. <https://doi.org/10.2113/gsecongeo.105.3.467>
- Betsi, T.B., Ngo Bidjeck Bondje, L.M., Mvondo, H., Yannick Mama Nga, L.N., Molotouala, C.A., McFarlane, C., 2020. Rutile LA-ICP-MS U–Pb geochronology and implications for tectono-metamorphic evolution in the Yaoundé Group of the Neoproterozoic Central African Orogeny. *Journal of African Earth Sciences*, 171, 103939. <https://doi.org/10.1016/j.jafrearsci.2020.103939>
- Beukes, N.J., Gutzmer, J., 2008. Origin and paleoenvironmental significance of major iron formations at the Archean-Paleoproterozoic boundary. *Economic Geology*, 5–47.
- Bhatia, M.R., Crook, K.A., 1986. Trace element characteristics of graywackes and tectonic setting discrimination of sedimentary basins. *Contributions to Mineralogy and Petrology*, 92, 181–193.
- Binam Mandeng, E.P., Ngo Bidjeck, L.M., Takodjou Wambo, J.D., Taku, A., Bineli Betsi, T., Solange Ipan, A., Tchami Nfada, L., Bitom Dieudonné, L., 2018. Lithologic and structural mapping of the Abiete–Toko gold district in southern Cameroon, using Landsat 7 ETM+/SRTM. *Comptes Rendus Geoscience*, 350, 130–140. <https://doi.org/10.1016/j.crte.2017.11.003>
- Bolhar, R., Kamber, B.S., Moorbath, S., Fedo, C.M., Whitehouse, M.J., 2004. Characterisation of early Archaean chemical sediments by trace element signatures. *Earth Planetary Science Letters*, 222, 43–60.
- Boström, K., 1970. Submarine volcanism as a source for iron. *Earth Planetary Science Letters*, 9, 348–354.
- Braga, F.C.S., Rosière, C.A., Queiroga, G.N., Rolim, V.K., Santos, J.O.S., McNaughton, N.J., 2015. The Statherian itabirite-bearing sequence from the Morro Escuro Ridge, Santa Maria de Itabira, Minas Gerais, Brazil. *Journal of South American Earth Sciences*, 58, 33–53.
- Cabanis, B., Lecolle, M., 1989. Le diagramme La/10-Y/15-Nb/8: un outil pour la discrimination des séries volcaniques et la mise en évidence des processus de mélange et/ou de contamination crustale. *Comptes Rendus de l'Académie des Sciences Série 2, Mécanique-Physique, Chimie, Sciences de l'univers, Sciences de la Terre*, 309, 2023–2029.

- Castaing, C., Feybesse, J. L., Thiéblemont, D., Triboulet, C., Chèvremont, P. 1994. Palaeogeographical reconstructions of the Pan-African/Brasiliano orogen: closure of an oceanic domain or intracontinental convergence between major blocks? *Precambrian Research*, 69(1-4): 327-344.
- Chebeu, C., Diorlette Ngo Nlend, C., Paul Nzenti, J., Ganno, S., 2011. Neoproterozoic High-K Calc-Alkaline Granitoids from Bapa-Batie, North Equatorial Fold Belt, Central Cameroon: Petrogenesis and Geodynamic Significance. *The Open Geology Journal*, 5.
- Chombong, N.N., Suh, C.E., Lehmann, B., Vishiti, A., Ilouga, D.C., Shemang, E.M., Tantoh, B.S., Kedia, A.C., 2017. Host rock geochemistry, texture and chemical composition of magnetite in iron ore in the Neoarchean Nyong unit in southern Cameroon. *Applied Earth Science*. 126, 129–145. <https://doi.org/10.1080/03717453.2017.1345507>
- Condie, K.C., 1993. Chemical composition and evolution of the upper continental crust: contrasting results from surface samples and shales. *Chemical Geology*, 104, 1–37.
- Cox, K.G., Bell, J.D., Pankhurst, R.J., 1979. The Interpretation of Igneous Rocks. *London University, London*, 450 p.
- Cullers, R.L., Berendsen, P., 1998. The provenance and chemical variation of sandstones associated with the Mid-continent Rift System, USA. *European Journal of Mineralogy*, 10, 987–1002.
- D'Agrella-Filho, M.S., Feybesse, J.-L., Prian, J.-P., Dupuis, D., eko N'Dong, J., 1996. Palaeomagnetism of Precambrian rocks from Gabon, Congo craton, Africa. *Journal of African Earth Sciences*, 22, 65–80.
- Danielson, A., Möller, P., Dulski, P., 1992. The europium anomalies in banded iron formations and the thermal history of the oceanic crust. *Chemical Geology*, 97, 89–100.
- Deassou Sezine, E., Soh Tamehe, L., Ganno, S., Nzepang Tankwa, M., Brice Lemdjou, Y., Dadjio Djomo, H., Alberto Rosière, C., Paul Nzenti, J., Bekker, A., 2022. Geochronological and geochemical constraints for the metavolcanosedimentary succession of the Nyong Complex, northwestern margin of the Congo craton: Implications for depositional age and tectonic setting of associated banded iron formations. *Precambrian Research*, 383, 106910. <https://doi.org/10.1016/j.precamres.2022.106910>
- De Carvalho Mendes, L., dos Santos, T.J.S., Gomes, N.B., 2021. Geochemistry and provenance of the metasedimentary rocks surrounding the Santa Quitéria magmatic arc, NE Brazil: Tectonic and paleogeographic implications for the assembly of West Gondwana. *Precambrian Research*, 356, 106063.
- De la Roche, H., 1965. Sur l'existence de plusieurs faciès géochimiques dans les schistes paléozoïques des Pyrénées luchonnaises. *Geologische Rundschau*, 55, 274-301.
- De Wit, M.J., Stankiewicz, J., Reeves, C., 2008. Restoring Pan-African-Brasiliano connections: more Gondwana control, less trans-Atlantic corruption. *Geological Society, London Special Publication*, 294, 399–412.
- DePaolo, D.J., 1981. Trace element and isotopic effects of combined wallrock assimilation and fractional crystallization. *Earth and Planetary Science Letters*, 53, 189–202.

- Djoukouo Soh, A., Ganno, S., Zhang, L., Soh Tamehe, L., Wang, C., Peng, Z., Tong, X., Nzenti, J.P., 2021. Origin, tectonic environment and age of the Bibole banded iron formations, northwestern Congo Craton, Cameroon: geochemical and geochronological constraints. *Geological Magazine*, 158, 2245–2263. <https://doi.org/10.1017/S0016756821000765>
- Dumont, J.-F., 1986. Identification par télédétection de l'accident de la Sanaga (Cameroun) : sa position dans le contexte des grands accidents d'Afrique Centrale et de la limite nord du craton congolais. *Géodynamique I*, 13–19.
- Duuring, P., Hagemann, S., 2013. Leaching of silica bands and concentration of magnetite in Archean BIF by hypogene fluids: Beebyn Fe ore deposit, Yilgarn Craton, Western Australia. *Mineralium Deposita*, 48, 341–370.
- Ebah Abeng, S.A., Ndjigui, P.-D., Beyanu, A.A., Teutsong, T., Bilong, P., 2012. Geochemistry of pyroxenites, amphibolites and their weathered products in the Nyong unit, SW Cameroon (NW border of Congo craton): Implications for Au–PGE exploration. *Journal of Geochemical Exploration*, 114, 1–19. <https://doi.org/10.1016/j.gexplo.2011.11.003>
- El-Shazly, A.K., Khalil, K.I., Helba, H.A., 2019. Geochemistry of banded iron formations and their host rocks from the Central Eastern Desert of Egypt: a working genetic model and tectonic implications. *Precambrian Research*, 325, 192–216.
- Feybesse, J.L., Johan, V., Maurizot, P., Abessolo, A., 1987. Evolution tectonométamorphique libérienne et éburnéenne de la partie NW du craton zaïrois (SW Cameroun). *Presented at the Colloquium on African geology*, 14, pp. 9–12.
- Feybesse, J.L., Johan, V., Maurizot, P., Abessolo, A., 1986. Mise en évidence d'une nappe synmétamorphe d'âge Eburnéen dans la partie NW du craton Zairois (SW Cameroun). Publication Occasionelles - *Centre Internationale Pour la Formation et Échanges Géologiques*, 105–111.
- Feybesse, J.L., Johan, V., Triboulet, C., Guerrot, C., Mayaga-Mikolo, F., Bouchot, V., N'dong, J.E., 1998. The West Central African belt: a model of 2.5–2.0 Ga accretion and two-phase orogenic evolution. *Precambrian Research*, 87, 161–216.
- Floyd, P.A., Winchester, J.A., 1978. Identification and discrimination of altered and metamorphosed volcanic rocks using immobile elements. *Chemical Geology*, 21, 291–306. [https://doi.org/10.1016/0009-2541\(78\)90050-5](https://doi.org/10.1016/0009-2541(78)90050-5)
- Fossi, D.H., Ganno, S., Tankwa, M.N., Tamehe, L.S., Kenné, P.A., Kouayep Tchoundi, C.L., Kankeu, B., Nzenti, J.P., 2022. Petrogenesis and tectonic setting of the Pan-African Deng-Deng intrusive complex in the Lom series, Eastern Cameroon. *Journal of African Earth Sciences*, 104484. <https://doi.org/10.1016/j.jafrearsci.2022.104484>
- Fozing, E.M., Kwékam, M., Kouémo, J.T., Njanko, T., Njonfang, E., 2021. Kinematic analysis of the Dschang granitic pluton (West-Cameroon): Implications to the Pan-African deformation of the Central African Fold belt in Cameroon during the post-collisional history of western Gondwana. *Precambrian Research*, 359, 106231.
- Fuanya, C., Bolarinwa, A.T., Kankeu, B., Yongue, R.F., Tangko, E.T., Nkepguep, F.Y., 2019. Geochemical characteristics and petrogenesis of basic rocks in the Ako'ozam–Njabilobe area, Southwestern Cameroon: implications for Au genesis. *Springer Nature Applied Sciences I*, 904. <https://doi.org/10.1007/s42452-019-0959-5>



- Ganno, S., Ngnotue, T., Kouankap Nono, G.D., Nzenti, J.P., Notsa Fokeng, M., 2015. Petrology and geochemistry of the banded iron-formations from Ntem complex greenstones belt, Elom area, Southern Cameroon: Implications for the origin and depositional environment. *Geochemistry*, 75, 375–387. <https://doi.org/10.1016/j.chemer.2015.08.001>
- Ganno, S., Njiosseu Tanko, E.L., Kouankap Nono, G.D., Djoukouo Soh, A., Moudioh, C., Ngnotué, T., Nzenti, J.P., 2017. A mixed seawater and hydrothermal origin of superior-type banded iron formation (BIF)-hosted Kouambo iron deposit, Palaeoproterozoic Nyong series, Southwestern Cameroon: Constraints from petrography and geochemistry. *Ore Geology Reviews*, 80, 860–875. <https://doi.org/10.1016/j.oregeorev.2016.08.021>
- Ganno, S., Nzenti, J.P., Ngnotue, T., Kankeu, B., Kouankap Nono, G.D., 2010. Polyphase deformation and evidence for transpressive tectonics in the Kimbi area, northwestern Cameroon Pan-African fold belt. *Journal of Geology and Mining Research*, 2, 001–015. <https://doi.org/10.5897/JGMR.9000062>
- Ganwa, A.A., Klötzli, U.S., Hauzenberger, C., 2016. Evidence for Archean inheritance in the pre-Pan african crust of Central Cameroon: Insight from zircon internal structure and LA-MC-ICP-MS UPb ages. *Journal of African Earth Sciences*, 120, 12–22. <https://doi.org/10.1016/j.jafrearsci.2016.04.013>
- Gatsé Ebotehoua, C., Xie, Y., Adomako-Ansah, K., Gourcerol, B., Qu, Y., 2021. Depositional Environment and Genesis of the Nabeba Banded Iron Formation (BIF) in the Ivindo Basement Complex, Republic of the Congo: Perspective from Whole-Rock and Magnetite Geochemistry. *Minerals* 11, 579.
- Goodwin A.M. 1991. Precambrian Geology; The dynamic evolution of the continental crust, *Academic Press, Harcourt Brace Jovanovich Publishers, New York*, pp 1-666.
- Gourcerol, B., Blein, O., Chevillard, M., Callec, Y., Boudzoumou, F., Djama, L.-M.J., 2022. Depositional Setting of Archean BIFs from Congo: New Insight into Under-Investigated Occurrences. *Minerals* 12, 114.
- Gourcerol, B., Thurston, P.C., Kontak, D.J., Côté-Mantha, O., Biczok, J., 2016. Depositional setting of Algoma-type banded iron formation. *Precambrian Research*, 281, 47–79.
- Gross, G.A., 1980. A classification of iron formations based on depositional environments. *The Canadian Mineralogist*, 18, 215–222.
- Hagemann, S.G., Angerer, T., Duuring, P., Rosière, C.A., e Silva, R.F., Lobato, L., Hensler, A.S., Walde, D.H.G., 2016. BIF-hosted iron mineral system: a review. *Ore Geology Reviews*, 76, 317–359.
- Hamdja Ngoniri, A., Dadjo Djomo, H., Ngnotue, T., Ayonta Kenne, P., Mbianya, G., Ganno, S., Nzenti, J.P., 2021. Zircon Trace Element Geochemistry and Ti-in-Zircon Thermometry of the Ngazi-Tina Pan-African Post-Collisional Granitoids, Adamawa Cameroon. *International Journal of Geosciences*, 12, 307–328. <https://doi.org/10.4236/ijg.2021.124017>
- Hayashi, K., Fujisawa, H., Holland, H. D. and Ohmoto, H., 1997. Geochemistry of ~1.9 Ga sedimentary rocks from northeastern Labrador, Canada; *Geochim. Cosmochim. Acta* 61 4115–4137.

- Houketchang Bouyo, M., Penaye, J., Mouri, H., Toteu, S.F., 2019. Eclogite facies metabasites from the Paleoproterozoic Nyong Group, SW Cameroon: Mineralogical evidence and implications for a high-pressure metamorphism related to a subduction zone at the NW margin of the Archean Congo craton. *Journal of African Earth Sciences*, 149, 215–234. <https://doi.org/10.1016/j.jafrearsci.2018.08.010>
- Houketchang Bouyo, M., Penaye, J., Njel, U.O., Moussango, A.P.I., Sep, J.P.N., Nyama, B.A., Wassouo, W.J., Abaté, J.M.E., Yaya, F., Mahamat, A., Ye, H., Wu, F., 2016. Geochronological, geochemical and mineralogical constraints of emplacement depth of TTG suite from the Sinassi Batholith in the Central African Fold Belt (CAFB) of northern Cameroon: Implications for tectonomagmatic evolution. *Journal of African Earth Sciences*, 116, 9–41. <https://doi.org/10.1016/j.jafrearsci.2015.12.005>
- Huston, D.L., Logan, G.A., 2004. Barite, BIFs and bugs: evidence for the evolution of the Earth's early hydrosphere. *Earth and Planetary Science Letters*, 220, 41–55. [https://doi.org/10.1016/S0012-821X\(04\)00034-2](https://doi.org/10.1016/S0012-821X(04)00034-2)
- Ishikawa, Y., Sawaguchi, T., Iwaya, S., Horiuchi, M., 1976. Delineation of prospecting targets for Kuroko deposits based on modes of volcanism of underlying dacite and alteration haloes. *Journal of Mining and Geology*, 26, 105–117.
- James, H.L., 1954. Sedimentary facies of iron-formation. *Economic Geology*, 49, 235–293. <https://doi.org/10.2113/gsecongeo.49.3.235>
- Johnsson, M.J., 1993. The system controlling the composition of clastic sediments. In: Johnsson, M.J., Basu, A. (Eds.), Processes controlling the composition of clastic sediments, *Geological Society of America Special Paper* 284, pp. 1-19.
- Kamguia Woguia, B., Kouankap Nono, G.D., Nga Essomba Tsoungui, P.E., Njiosseu Tanko, E.L., Ayonta Kenne, P., Nzenti, J.P., 2022. Geochemistry and U–Pb zircon age of the Paleoproterozoic metasedimentary rocks from the Bidou I, Nyong Series, Cameroon: Implications for provenance and tectonic setting. *Arabian Journal of Geosciences*, 15, 1–21.
- Kamp, P.C. van de, Leake, B.E., 1985. Petrography and geochemistry of feldspathic and mafic sediments of the northeastern Pacific margin. *Earth and Environmental Science Transactions of the Royal Society of Edinburgh*, 76, 411–449. <https://doi.org/10.1017/S0263593300010646>
- Kankeu, B., Greiling, R.O., Nzenti, J.P., Ganno, S., Danguene, P.Y.E., Bassahak, J., Hell, J.V., 2018. Contrasting Pan-African structural styles at the NW margin of the Congo Shield in Cameroon. *Journal of African Earth Sciences, Precambrian Geology of Egypt: Stratigraphy, Geodynamics, and Mineral Resources* 146, 28–47. <https://doi.org/10.1016/j.jafrearsci.2017.06.002>
- Kankeu, B., Nzenti, J.P., Greiling, R.O., Ganno, S., Ngnotué, T., Basahak, J., Hell, J.V., 2010. Application de la technique de l'Anisotropie de la Susceptibilité Magnétique (ASM) à l'identification des structures géologiques: le cisaillement panafricain de Bétaré Oya dans le district aurifère de l'Est Cameroun. *Annales de la Faculté des Sciences, Série Sciences de la Terre*, 38 1 17 30.
- Kelemen, P.B., Hanghøj, K., Greene, A.R., 2014. One view of the geochemistry of subduction-related magmatic arcs, with an emphasis on primitive andesite and lower crust. *Elsevier*.

- Klein, C., 2005. Some Precambrian banded iron-formations (BIFs) from around the world: Their age, geologic setting, mineralogy, metamorphism, geochemistry, and origins. *American Mineralogist*, 90, 1473–1499. <https://doi.org/10.2138/am.2005.1871>
- Kouankap Nono, G.D., Nzenti, J.P., Suh, C.E., Ganno, S., 2010. Geochemistry of Ferriferous, High-K Calc-Alkaline Granitoids from the Banefo-Mvoutsaha Massif (NE Bafoussam), Central Domain of the Pan- African Fold Belt, Cameroon. *The Open Geology Journal*, 4, 15–28.
- Kwamou Wanang, Kouankap Nono, K.N.G., Nkouathio, D.G., Ayonta Kenne, P., 2021. Petrogenesis and U–Pb zircon dating of amphibolite in the Mewengo iron deposit, Nyong series, Cameroon: fingerprints of iron depositional geotectonic setting. *Arabian Journal of Geosciences*, 14, 872. <https://doi.org/10.1007/s12517-021-07235-8>
- Large, R.R., Gemmell, J.B., Paulick, H., Huston, D.L., 2001. The alteration box plot: A simple approach to understanding the relationship between alteration mineralogy and lithogeochemistry associated with volcanic-hosted massive sulfide deposits. *Economic Geology*, 96, 957–971.
- Lazaro, B.B., Burillo, M.J.M., Fernandez-Nieto, C., Lopez, J.M.G., 1995. Mineralogy and geochemistry of Devonian detrital rocks from the Iberian Range (Spain). *Clay Minerals*, 30, 381–394. <https://doi.org/10.1180/claymin.1995.030.4.10>
- Le Maitre, R.W., 1976. The Chemical Variability of some Common Igneous Rocks. *Journal of Petrology*, 17, 589–598. <https://doi.org/10.1093/petrology/17.4.589>
- Ledru, P., Cocherie, A., Barbosa, J., Johan, V., Onstott, T., 1994. Ages du métamorphisme granulitique dans le craton du São Francisco (Brésil). Implications sur la nature de l'orogène transamazonien. *Comptes Rendus de l'Academie des Sciences - Sereries II Science Terre Planetes*, 318, 251–257.
- Lerouge, C., Cocherie, A., Toteu, S.F., Penaye, J., Milési, J.-P., Tchameni, R., Nsifa, E.N., Fanning, C.M., Deloule, E., 2006. Shrimp U–Pb zircon age evidence for Paleoproterozoic sedimentation and 2.05 Ga syntectonic plutonism in the Nyong Group, South-Western Cameroon: consequences for the Eburnean–Transamazonian belt of NE Brazil and Central Africa. *Journal of African Earth Sciences*, 44, 413–427.
- Letouzey, R.-G. (1918-1989) C., 1985. Carte phytogéographique du Cameroun. *Institut de la Carte internationale de la végétation. Toulouse*.
- Loose, D., Schenk, V., 2018. 2.09 Ga old eclogites in the Eburnian-Transamazonian orogen of southern Cameroon: Significance for Palaeoproterozoic plate tectonics. *Precambrian Research*, 304, 1–11. <https://doi.org/10.1016/j.precamres.2017.10.018>
- Marchig, V., Gundlach, H., Möller, P., Schley, F., 1982. Some geochemical indicators for discrimination between diagenetic and hydrothermal metalliferous sediments. *Marine Geology*, 50, 241–256. [https://doi.org/10.1016/0025-3227\(82\)90141-4](https://doi.org/10.1016/0025-3227(82)90141-4)
- Maurizot, P., Abessolo, A., Feybesse, J.L., Lecomte, P.J., 1986. Etude de prospection minière du Sud-Ouest Cameroun: Synthèse des travaux de 1978 à 1985. *Rapport BRGM. 85, CMR 066*.
- McDonough, W.F., Sun, S. -s., 1995. The composition of the Earth. *Chemical Geology, Chemical Evolution of the Mantle*, 120, 223–253. [https://doi.org/10.1016/0009-2541\(94\)00140-4](https://doi.org/10.1016/0009-2541(94)00140-4)

- McLennan, S.M., Hemming, S., McDaniel, D.K., Hanson, G.N., 1993. Geochemical approaches to sedimentation, provenance, and tectonics. *Special Paper of the Geological Society of America*, 21–21.
- Meng, E., Liu, F.-L., Liu, P.-H., Liu, C.-H., Yang, H., Wang, F., Shi, J.-R., Cai, J., 2014. Petrogenesis and tectonic significance of Paleoproterozoic meta-mafic rocks from central Liaodong Peninsula, northeast China: Evidence from zircon U–Pb dating and in situ Lu–Hf isotopes, and whole-rock geochemistry. *Precambrian Research*, 247, 92–109.
- Metcalfe, R.V., Shervais, J.W., Wright, J.E., 2008. Suprasubduction-zone ophiolites: Is there really an ophiolite conundrum? *Special Paper of the Geological Society of America*, 438, 191.
- Motta Garcia, M. da G., Saraiva dos Santos, T.J., da Silva Amaral, W., 2014. Provenance and tectonic setting of Neoproterozoic supracrustal rocks from the Ceará Central Domain, Borborema Province (NE Brazil): constraints from geochemistry and detrital zircon ages. *International Geology Reviews*, 56, 481–500.
- Moudioh, C., Tamehe, L.S., Ganno, S., Nzepang Tankwa, M., Brando Soares, M., Ghosh, R., Kankeu, B., Nzenti, J.P., 2020. Tectonic setting of the Bipindi greenstone belt, northwest Congo craton, Cameroon: Implications on BIF deposition. *Journal of African Earth Sciences*, 171, 103971. <https://doi.org/10.1016/j.jafrearsci.2020.103971>
- Mvodo, H., Ganno, S., Kouankap Nono, G.D., Fossi, D.H., Nga Essomba, P.E., Nzepang Tankwa, M., Nzenti, J.P., 2022. Petrogenesis, LA-ICP-MS zircon U-Pb geochronology and geodynamic implications of the Kribi metavolcanic rocks, Nyong Group, Congo craton. *Acta Geochimica*, 41, 470–495. <https://doi.org/10.1007/s11631-022-00533-2>
- Mvondo, H., den Brok, S.W.J., Mvondo Ondo, J., 2003. Evidence for symmetric extension and exhumation of the Yaounde nappe (Pan-African fold belt, Cameroon). *Journal of African Earth Sciences*, 36, 215–231. [https://doi.org/10.1016/S0899-5362\(03\)00017-4](https://doi.org/10.1016/S0899-5362(03)00017-4)
- Mvondo, H., Owona, S., Ondo, J.M., Essono, J., 2007. Tectonic evolution of the Yaoundé segment of the Neoproterozoic Central African Orogenic Belt in southern Cameroon. *Canadian Journal of Earth Sciences*, 44, 433–444. <https://doi.org/10.1139/e06-107>
- Ndema Mbongue, J.L., Ngnotue, T., Ngo Nlend, C.D., Nzenti, J.P., Cheo Suh, E., 2014. Origin and evolution of the formation of the Cameroon Nyong Series in the western border of the Congo Craton. *Journal of Geosciences and Geomatics*, 2, 62–75.
- Ndema Mbongue, J.L., Segue, C., Nzenti, J.P., Suh, C.E., 2022. Mineral chemistry (EMPA) of monazites in metamorphic rocks from Edea region: implications of the monazite chemistry on the metamorphic evolution of the Nyong Complex. *Arabian Journal of Geosciences* 15,1665.
- Ndime, E.N., Ganno, S., Nzenti, J.P., 2019. Geochemistry and Pb–Pb geochronology of the Neoproterozoic Nkout West metamorphosed banded iron formation, southern Cameroon. *International Journal of Earth Sciences*, 108, 1551–1570.
- Ndime, E.N., Ganno, S., Tamehe, L.S., Nzenti, J.P., 2018. Petrography, lithostratigraphy and major element geochemistry of Mesoarchean metamorphosed banded iron formation-hosted Nkout iron ore deposit, north western Congo craton, Central West Africa. *Journal of African Earth Sciences*, 148, 80–98.

- Ndjigui, P.-D., Badinane, M.F.B., Nyeck, B., Nandjip, H.P.K., Bilong, P., 2013. Mineralogical and geochemical features of the coarse saprolite developed on orthogneiss in the SW of Yaoundé, South Cameroon. *Journal of African Earth Sciences*, 79, 125–142.
- Nédélec, A., Macaudière, J., Nzenti, J. P. et Barbey, P., 1986. Evolution structurale et métamorphisme des schistes de Mbalmayo (Cameroun). Informations pour la structure de la zone mobile panafricaine d'Afrique centrale au contact du craton du Congo. *Comptes Rendus Académie des Sciences de Paris*, tome 303, 75-80.
- Nedelec, A., Nsifa, E.N., Martin, H., 1990. Major and trace element geochemistry of the Archaean Ntem plutonic complex (south Cameroon): petrogenesis and crustal evolution. *Precambrian Research*, 47, 35–50. [https://doi.org/10.1016/0301-9268\(90\)90029-P](https://doi.org/10.1016/0301-9268(90)90029-P)
- Nesbitt, H.W., Young, G.M., 1982. Early Proterozoic climates and plate motions inferred from major element chemistry of lutites. *Nature*, 299, 715–717. <https://doi.org/10.1038/299715a0>
- Nga Essomba Tsoungui, P., Ganno, S., Tanko Njiosseu, E.L., Ndema Mbongue, J.L., Kamguia Woguia, B., Soh Tamehe, L., Takodjou Wambo, J.D., Nzenti, J.P., 2020. Geochemical constraints on the origin and tectonic setting of the serpentized peridotites from the Paleoproterozoic Nyong series, Eseka area, SW Cameroon. *Acta Geochimica*, 39, 404–422. <https://doi.org/10.1007/s11631-019-00368-4>
- Ngako, F., Jegouzo, P., Nzenti, J.P., 1991. Le cisaillement centre camerounais. Rôle structural et géodynamique dans l'orogénèse panafricaine. Cisaillement Centre Camerounaise. Rô-Crate Structure. *Géodynamique Dans Orognèse Panafricaine*, 313, 457–463.
- Ngako, V., Affaton, P., Nnange, J.M., Njanko, Th., 2003. Pan-African tectonic evolution in central and southern Cameroon: transpression and transtension during sinistral shear movements. *Journal of African Earth Sciences*, 36, 207–214. [https://doi.org/10.1016/S0899-5362\(03\)00023-X](https://doi.org/10.1016/S0899-5362(03)00023-X)
- Ngnotué, T., Ganno, S., Nzenti Jean, P., Schulz, B., Tchaptchet Tchato, D.I., Suh Cheo, E., 2012. Geochemistry and Geochronology of Peraluminous High-K Granitic Leucosomes of Yaoundé Series (Cameroon): Evidence for a Unique Pan-African Magmatism and Melting Event in North Equatorial Fold Belt. *Internal Journal of Geosciences*, 2012, 24. <https://doi.org/10.4236/ijg.2012.33055>
- Ngnotué, T., Nzenti, J.P., Barbey, P., Tchoua, F.M., 2000. The Ntui-Betamba high-grade gneisses: a northward extension of the Pan-African Yaoundé gneisses in Cameroon. *Journal of African Earth Sciences*, 31, 369–381. [https://doi.org/10.1016/S0899-5362\(00\)00094-4](https://doi.org/10.1016/S0899-5362(00)00094-4)
- Njiekak, G., Dörr, W., Tchouankoué, J.-P., Zulauf, G., 2008. U–Pb zircon and microfabric data of (meta) granitoids of western Cameroon: Constraints on the timing of pluton emplacement and deformation in the Pan-African belt of central Africa. *Lithos, Granites and Migmatites: Their Temporal, Spatial and Causal Relationships* 102, 460–477. <https://doi.org/10.1016/j.lithos.2007.07.020>
- Nomo Negue, E., Tchameni, R., Vanderhaeghe, O., Sun, F., Barbey, P., Tekoum, L., Tchunte, P.M.F., Eglinger, A., Fouotsa, N.A.S., 2017. Structure and LA-ICP-MS



- zircon U–Pb dating of syntectonic plutons emplaced in the Pan-African Banyo-Tcholliré shear zone (central north Cameroon). *Journal of African Earth Sciences*, 131, 251–271. <https://doi.org/10.1016/j.jafrearsci.2017.04.002>
- Nzenti, J. P., Barbey, P., Jegouzo, P. et Moreau, C., 1984. Un nouvel exemple de ceinture granulitique dans une chaîne protérozoïque de transition: les migmatites de Yaoundé au Cameroun. *Comptes Rendus de l'Académie des Sciences, Paris*, 299, 2, 1197–1199.
- Nzenti, J.P., Barbey, P., Macaudière, J., Soba, D., 1988a. Origin and evolution of the late Precambrian high-grade Yaounde gneisses (Cameroon). *Precambrian Research*. 38, 91–109.
- Nzenti, J. P., Barbey, P., Tchoua, F. M., 1999. Evolution crustale au Cameroun: éléments pour un modèle géodynamique de l'orogénèse néoproterozoïque. Géologie et environnements au Cameroun. *Collection Geocam*, 2, 397–407.
- Nzenti, J.P., Bertrand, S.M., Macaudière, J., 1994. La chaîne panafricaine au Cameroun: cherchons suture et modèle. *15e Réunion des Sciences de la Terre. Nancy Fr.*
- Nzenti, J.P., Kapajika, B., Wörner, G., Lubala, T.R., 2006. Synkinematic emplacement of granitoids in a Pan-African shear zone in Central Cameroon. *Journal of African Earth Sciences*, 45, 74–86. <https://doi.org/10.1016/j.jafrearsci.2006.01.005>
- Nzenti, J. P., 1992. Prograde and retrograde garnet zoning at high pressure and temperature in metapelitic and grenatite rocks from Yaounde (Cameroon Pan-African north-equatorial fold belt). *Journal of African Earth Science*, 15, 73–79.
- Nzenti, J. P., Njiosseu Tanko, E. L., Nzina, N. A., 2007. The metamorphic evolution of the Paleoproterozoic high grade Banyo gneisses (Adamawa, Cameroon, Central Africa). *Journal of Camerounian Academic Sciences*, 7, 95–109.
- Nzenti, J. P. et Tchoua, F.M., 1996. Les gneiss scapolitiques de la chaîne nord-équatoriale du craton du Congo. *Comptes Rendus de l'Académie des Sciences de Paris*, 323, 289–294.
- Nzepang Tankwa, M.N., Ganno, S., Okunlola, O.A., Njiosseu, E.L.T., Tamehe, L.S., Woguia, B.K., Mbita, A.S.M., Nzenti, J.P., 2020. Petrogenesis and tectonic setting of the Paleoproterozoic Kelle Bidjoka iron formations, Nyong group greenstone belts, southwestern Cameroon. Constraints from petrology, geochemistry, and LA-ICP-MS zircon U–Pb geochronology. *International Geology Review*, 0, 1–21. <https://doi.org/10.1080/00206814.2020.1793423>
- Nzolang, C., Kagami, H., Nzenti, J. P. et Holtz, F., 2003. Geochemistry and preliminary Sr–Nd isotopic data on the Neoproterozoic granitoids from the Bantoum area, West Cameroon: evidence for a derivation from a paleoproterozoic to Archaean crust. *Polar Geosciences*, 16, 196–226.
- Odigui Ahanda, D.H., Ndzana, G.M., Bekoa, E., Abossolo-Angue Abane, M., Bitom, L.D., 2019. Morphological, geochemical and mineralogical studies of two soil profiles developed on the itabirites of Ntem Complex, southern Cameroon. *Journal of African Earth Sciences*, 153, 111–129. <https://doi.org/10.1016/j.jafrearsci.2019.02.028>
- Onguene, N.A., Kuyper, T.W., 2001. Mycorrhizal associations in the rain forest of South Cameroon. *Forest Ecology and Management*, 140, 277–287.



- Owona, S., Ondoa, J.M., Tichomirowa, M., Ekodeck, G.E., 2020. The petrostructural characteristics and  $^{207}\text{Pb}/^{206}\text{Pb}$  zircon data from the Ngomedzap-Akongo area (Nyong complex, SW-Cameroon). *Journal of Geosciences*, 65, 201–219. <https://doi.org/10.3190/jgeosci.309>
- Owona, S., Ratschbacher, L., Afzal M, G., Nsangou Ngapna, M., Mvondo Ondoa, J., Ekodeck, G.E., 2021a. New U–Pb zircon ages of Nyong Complex meta-plutonites: Implications for the Eburnean/Trans-Amazonian Orogeny in southwestern Cameroon (Central Africa). *Geological Journal*, 56, 1741–1755.
- Owona, S., Ratschbacher, L., Ngapna, M.N., Gulzar, A.M., Ondoa, J.M., Ekodeck, G.E., 2021b. How diverse is the source? Age, provenance, reworking, and overprint of Precambrian meta-sedimentary rocks of West Gondwana, Cameroon, from zircon U–Pb geochronology. *Precambrian Research*, 359, 106220.
- Owona, S., Schulz, B., Minyem, D., Ratschbacher, L., Tchamabe, B.C., Olinga, J.B., Ondoa, J.M., Ekodeck, G.E., 2022. Eburnean/Trans-Amazonian orogeny in the Nyong complex of southwestern Cameroon: Meta-basite geochemistry and metamorphic petrology. *Journal of African Earth Sciences*, 190, 104515.
- Owona, S., Tichomirowa, M., Ratschbacher, L., Ondoa, J.M., Youmen, D., Pfänder, J., Tchoua, F.M., Affaton, P., Ekodeck, G.E., 2012. New igneous zircon Pb/Pb and metamorphic Rb/Sr ages in the Yaounde Group (Cameroon, Central Africa): implications for the Central African fold belt evolution close to the Congo Craton. *International Journal of Earth Sciences*, 101, 1689–1703. <https://doi.org/10.1007/s00531-012-0751-x>
- Paolo Sighinolfi, G., 1974. Geochemistry of early precambrian carbonate rocks from the Brazilian Shield: Implications for archean carbonate sedimentation. *Contributions to Mineralogy and Petrology*, 46, 189–200.
- Pearce, J.A., 2008. Geochemical fingerprinting of oceanic basalts with applications to ophiolite classification and the search for Archean oceanic crust. *Lithos*, 100, 14–48.
- Penaye, J., Kröner, A., Toteu, S.F., Van Schmus, W.R., Doumnang, J.-C., 2006. Evolution of the Mayo Kebbi region as revealed by zircon dating: An early (ca. 740Ma) Pan-African magmatic arc in southwestern Chad. *Journal of African Earth Sciences*, The Precambrian of Central Africa 44, 530–542. <https://doi.org/10.1016/j.jafrearsci.2005.11.018>
- Penaye, J., Toteu, S.F., Tchameni, R., Van Schmus, W.R., Tchakounté, J., Ganwa, A., Minyem, D., Nsifa, E.N., 2004. The 2.1 Ga West central African belt in Cameroon: extension and evolution. *Journal of African Earth Sciences*, 39, 159–164.
- Penaye, J., Toteu, S. F., Michard, A., Van Schmus, W. R. et Nzenti, J. P., 1993. U-Pb and Sm-Nd preliminary geochronologic data on the Yaoundé serie, Cameroon: reinterpretation of granulitic rock as the suture of the collision in the « Centrafricain » belt. *Compte Rendu de l'Académie des Sciences*, 317, 789-794.
- Peters, W.S., 2011. Aeromagnetic –Radiometric survey: Structural interpretation for Iron ore, Gold and other commodities for Aureus Mining Inc. (No. 1). *Southern Geoscience Consulting Pty Ltd, Cameroon*.
- Pettijohn, F.J., Potter, P.E., Siever, R., 1987. Sand and sandstone. *Springer, New York*.

- Planavsky, N., Bekker, A., Rouxel, O.J., Kamber, B., Hofmann, A., Knudsen, A., Lyons, T.W., 2010. Rare earth element and yttrium compositions of Archean and Paleoproterozoic Fe formations revisited: new perspectives on the significance and mechanisms of deposition. *Geochimica et Cosmochimica Acta* 74, 6387–6405.
- Polat, A., Hofmann, A.W., 2003. Alteration and geochemical patterns in the 3.7–3.8 Ga Isua greenstone belt, West Greenland. *Precambrian Research, Early Archean Processes and the Isua Greenstone Belt, West Greenland* 126, 197–218. [https://doi.org/10.1016/S0301-9268\(03\)00095-0](https://doi.org/10.1016/S0301-9268(03)00095-0)
- Polat, A., Hofmann, A.W., Rosing, M.T., 2002. Boninite-like volcanic rocks in the 3.7–3.8 Ga Isua greenstone belt, West Greenland: geochemical evidence for intra-oceanic subduction zone processes in the early Earth. *Chemical Geology*, 184, 231–254.
- Poucllet, A., Tchameni, R., Mezger, K., Vidal, M., Nsifa, E., Shang, C., Penaye, J., 2007. Archean crustal accretion at the northern border of the Congo Craton (South Cameroon). The charnockite-TTG link. *Bulletin de la Société Géologique de France*, 178, 331–342. <https://doi.org/10.2113/gssgfbull.178.5.331>
- Rooney, T.O., 2010. Geochemical evidence of lithospheric thinning in the southern Main Ethiopian Rift. *Lithos*, 117, 33–48.
- Roser, B.P., Korsch, R.J., 1986. Determination of Tectonic Setting of Sandstone-Mudstone Suites Using SiO<sub>2</sub> Content and K<sub>2</sub>O/Na<sub>2</sub>O Ratio. *The Journal of Geology*, 94, 635–650. <https://doi.org/10.1086/629071>
- Ross, P.-S., Bédard, J.H., 2009. Magmatic affinity of modern and ancient subalkaline volcanic rocks determined from trace-element discriminant diagrams. *Canadian Journal of Earth Sciences*, 46, 823–839.
- Roy, S., Venkatesh, A.S., 2009. Mineralogy and geochemistry of banded iron formation and iron ores from eastern India with implications on their genesis. *Journal of Earth System Science*, 118, 619–641.
- Rudnick, R., Gao, S., 2003. The role of lower crustal recycling in continent formation. *Geochimica et Cosmochimica Acta*, 67, 403.
- Rudnick, R.L., McLennan, S.M., Taylor, S.R., 1985. Large ion lithophile elements in rocks from high-pressure granulite facies terrains. *Geochimica et Cosmochimica Acta*, 49, 1645–1655.
- Saha-Fouotsa, A.N., Vanderhaeghe, O., Barbey, P., Eglinger, A., Tchameni, R., Zeh, A., Tchunte, P.F., Nomo, E.N., 2019. The geologic record of the exhumed root of the Central African Orogenic Belt in the central Cameroon domain (Mbé–Sassa–Mbersi region). *Journal of African Earth Sciences*, 151, 286–314.
- Schmus, V., Oliveira, E.P., Filho, A.F. da S., Toteu, S.F., Penaye, J., Guimarães, I.P., 2008. Proterozoic links between the Borborema Province, NE Brazil, and the Central African Fold Belt. *Geological Society of London Special Publication*, 294, 69–99. <https://doi.org/10.1144/SP294.5>
- Segalen, P., 1967. Les sols et la géomorphologie du Cameroun. *Office de la Recherche Scientifique et Technique Outre-Mer*.
- Sep Nlomngan, J.P., Penaye, J., Tchameni, R., Owona, S., Patrice, A., Ibohn, M., Nsifa, E.N., Félix, T.S., 2019. Geochemical Characterization of Boula Ibi Granitoids and Implications in Geodynamic Evolution. *Journal of Geography and Geology* 11.

- Shang, C.K., Liégeois, J.P., Satir, M., Frisch, W., Nsifa, E.N., 2010. Late Archaean high-K granite geochronology of the northern metacratonic margin of the Archaean Congo craton, Southern Cameroon: Evidence for Pb-loss due to non-metamorphic causes. *Gondwana Research*, 18, 337–355. <https://doi.org/10.1016/j.gr.2010.02.008>
- Shang, C.K., Satir, M., Nsifa, E.N., Liégeois, J.-P., Siebel, W., Taubald, H., 2007. Archaean high-K granitoids produced by remelting of earlier Tonalite–Trondhjemite–Granodiorite (TTG) in the Sangmelima region of the Ntem complex of the Congo craton, southern Cameroon. *International Journal of Earth Sciences*, 96, 817–841. <https://doi.org/10.1007/s00531-006-0141-3>
- Shang, C.K., Satir, M., Siebel, W., Nsifa, E.N., Taubald, H., Liégeois, J.-P., Tchoua, F.M., 2004. TTG magmatism in the Congo craton; a view from major and trace element geochemistry, Rb–Sr and Sm–Nd systematics: case of the Sangmelima region, Ntem complex, southern Cameroon. *Journal of African Earth Sciences*, 40, 61–79.
- Shido, F., Miyashiro, A., Ewing, M., 1974. Compositional variation in pillow lavas from the Mid-Atlantic Ridge. *Marine Geology*, 16, 177–190.
- Sighomnou, D., 2004. Analyse et redéfinition des régimes climatiques et hydrologiques du Cameroun : perspectives d'évolution des ressources en eau (*PhD Thesis*). Université de Yaoundé I, Yaoundé.
- Singh, L.K., Jha, M.K., Chowdary, V.M., 2018. Assessing the accuracy of GIS-based Multi-Criteria Decision Analysis approaches for mapping groundwater potential. *Ecological Indicators*, 91, 24–37. <https://doi.org/10.1016/j.ecolind.2018.03.070>
- Soba, D., 1989. La serie du lom : etude geologique et geochronologique d'un bassin volcano-sedimentaire de la chaine panafricaine a l'est du cameroun (*These de doctorat*). Paris 6.
- Soh Tamehe, L., Chongtao, W., Ganno, S., Simon, S.J., Kouankap Nono, G.D., Nzenti, J.P., Lemdjou, Y.B., Lin, N.H., 2019. Geology of the Gouap iron deposit, Congo craton, southern Cameroon: Implications for iron ore exploration. *Ore Geology Review*, 107, 1097–1128. <https://doi.org/10.1016/j.oregeorev.2019.03.034>
- Soh Tamehe, L., Nzepang Tankwa, M., Chongtao, W., Ganno, S., Ngnotue, T., Kouankap Nono, G.D., Simon, S.J., Zhang, J., Nzenti, J.P., 2018. Geology and geochemical constrains on the origin and depositional setting of the Kpwa–Atog Boga banded iron formations (BIFs), northwestern Congo craton, southern Cameroon. *Ore Geology Review*, 95, 620–638. <https://doi.org/10.1016/j.oregeorev.2018.03.017>
- Soh Tamehe, L., Wei, C., Ganno, S., Rosière, C.A., Li, H., Soares, M.B., Nzenti, J.P., Santos, J.O.S., Bekker, A., 2022. Provenance of metasiliciclastic rocks at the northwestern margin of the East Gabonian Block: Implications for deposition of BIFs and crustal evolution in southwestern Cameroon. *Precambrian Research*, 376, 106677.
- Soh Tamehe, L., Wei, C., Ganno, S., Rosière, C.A., Nzenti, J.P., Gatse Ebotehoua, C., Lu, G., 2021. Depositional age and tectonic environment of the Gouap banded iron formations from the Nyong group, SW Cameroon: Insights from isotopic, geochemical and geochronological studies of drillcore samples. *Geoscience Frontiers*, 12, 549–572. <https://doi.org/10.1016/j.gsf.2020.07.009>

- Suh C. E., Cabral A., Shemang E. M., Mbinkar L., Mboudou G. G. M. 2008. Two contrasting iron-ore deposits in the Precambrian mineral belt of Cameroon, West Africa. *Explore Mineral Geology*, 17: 197 - 207.
- Suh C. E., Cabral A. R., Ndime E. N., 2009. Geology and ore fabrics of the Nkout high-grade haematite deposit, southern Cameroon. *Smart Science for Exploration and Mining*, 1: 558 - 560.
- Taylor, S. R. et McLennan, S., 1985. The Continental Crust: Its Composition and Evolution. An Examination of the Geochemical Record Preserved in Sedimentary Rocks. *Blackwell, Oxford*, 312 p.
- Tchakounté, J., Eglinger, A., Toteu, S.F., Zeh, A., Nkoumbou, C., Mvondo-Ondoa, J., Penaye, J., de Wit, M., Barbey, P., 2017. The Adamawa-Yadé domain, a piece of Archaean crust in the Neoproterozoic Central African Orogenic belt (Bafia area, Cameroon). *Precambrian Research*, 299, 210–229. <https://doi.org/10.1016/j.precamres.2017.07.001>.
- Tchameni, R., 1997. Géochimie et géochronologie des formations de l'archéen et du paléoproterozoïque du sud-cameroun (groupe du ntem, craton du congo) (*PhD Thesis*).
- Tchameni, R., Mezger, K., Nsifa, N.E., Pouclet, A., 2001. Crustal origin of Early Proterozoic syenites in the Congo Craton (Ntem Complex), South Cameroon. *Lithos*, 57, 23–42. [https://doi.org/10.1016/S0024-4937\(00\)00072-4](https://doi.org/10.1016/S0024-4937(00)00072-4)
- Teutsong, T., Bontognali, T.R.R., Ndjigui, P.-D., Vrijmoed, J.C., Teagle, D., Cooper, M., Vance, D., 2017. Petrography and geochemistry of the Mesoarchean Bikoula banded iron formation in the Ntem complex (Congo craton), Southern Cameroon: Implications for its origin. *Ore Geology Review*, 80, 267–288. <https://doi.org/10.1016/j.oregeorev.2016.07.003>
- Thurston, P.C., Kamber, B.S., Whitehouse, M., 2012. Archean cherts in banded iron formation: insight into Neoarchean ocean chemistry and depositional processes. *Precambrian Research*, 214, 227–257.
- Toteu, S.F., Penaye, J., Deloule, E., Van Schmus, W.R., Tchameni, R., 2006. Diachronous evolution of volcano-sedimentary basins north of the Congo craton: Insights from U–Pb ion microprobe dating of zircons from the Poli, Lom and Yaoundé Groups (Cameroon). *Journal of African Earth Sciences*, The Precambrian of Central Africa 44, 428–442. <https://doi.org/10.1016/j.jafrearsci.2005.11.011>
- Toteu, S.F., Penaye, J., Djomani, Y.P., 2004. Geodynamic evolution of the Pan-African belt in central Africa with special reference to Cameroon. *Canadian Journal of Earth Sciences*, 41, 73–85.
- Toteu, S.F., Van Schmus, W.R., Penaye, J., Michard, A., 2001. New U/Pb and Sm/Nd data from North-Central Cameroon and its bearing on the pre-pan African history of Central Africa. *Precambrian Research*, 108, 45–73.
- Toteu, S.F., Van Schmus, W.R., Penaye, J., Nyobé, J.B., 1994. U/Pb and Sm/Nd evidence for Eburnian and Pan-African high-grade metamorphism in cratonic rocks of southern Cameroon. *Precambrian Research*, 67, 321–347. [https://doi.org/10.1016/0301-9268\(94\)90014-0](https://doi.org/10.1016/0301-9268(94)90014-0)

- Wang, C., Peng, Z., Tong, X., Huang, H., Zheng, M., Zhang, L., Zhai, M., 2017. Late Neoproterozoic supracrustal rocks from the Anshan-Benxi terrane, North China craton: New geodynamic implications from the geochemical record. *American Journal of Science*, 317, 1095–1148.
- Wang, C., Zhang, L., Lan, C., Dai, Y., 2014. Petrology and geochemistry of the Wangjiazhuang banded iron formation and associated supracrustal rocks from the Wutai greenstone belt in the North China Craton: implications for their origin and tectonic setting. *Precambrian Research*, 255, 603–626.
- Wang, X., Peng, P., Wang, C., Yang, S., 2016. Petrogenesis of the 2115 Ma Haicheng mafic sills from the Eastern North China Craton: Implications for an intra-continental rifting. *Gondwana Research*, 39, 347–364.
- Whitney, D.L., Evans, B.W., 2010. Abbreviations for names of rock-forming minerals. *American Mineralogist*, 95, 185–187. <https://doi.org/10.2138/am.2010.3371>
- Wilson, M., 1989. Igneous petrogenesis. Unwin Hyman. *Geological Society of America Bulletin*, 466.
- Workman, R.K., Hart, S.R., 2005. Major and trace element composition of the depleted MORB mantle (DMM). *Earth and Planetary Science Letters*, 231, 53–72.
- Yonta-Ngoune, C., Nkoumbou, C., Barbey, P., Le Breton, N., Montel, J.-M., Villieras, F., 2010. Geological context of the Boumnyebel talcschists (Cameroun): Inferences on the Pan-African Belt of Central Africa. *Comptes Rendus Geoscience*, 342, 108–115. <https://doi.org/10.1016/j.crte.2009.12.007>

## **APPENDIX**



### Appendix 1. Anyouzok iron deposit drillhole details

Hole ID	Easting	Northing	Elevation	End of Hole	Azimuth	Dip angle
TH9	657797	323609	545	83	180	-50
TH31	657607	324482	350	81	135	-50
TD35	657828	323809	575	281	180	-55
TD37	657809	323698	556	179	180	-55
TD46	658098	323893	573	306	180	-55
TD47	658400	324101	602	329	180	-55
TD60	657794	324605	385	110	140	-70
TE4	660816	317370	686	245	60	-50
TE5	660775	317343	687	182	60	-50
TE6	660705	317321	686	300	60	-50
TE9	660651	317460	680	220	55	-50
TE22	660886	317253	679	139	70	-50
TD65	657564	323327	467	111	140	-70

### Appendix 2. Anyouzok deposit logging details.

Northern prospect					
Drillhole	From	To (m)	Interval (m)	Rock type	Contact
TH9	0	3	3	Lateritic cover	Gradational
TH9	3	16.4	13.4	Hematite cap	Gradational
TH9	16.4	83	66.6	SBIF	EOH
TD37	0	3.3	3.3	Lateritic cover	Gradational
TD37	3.3	15	11.7	Hematite cap	Gradational
TD37	15	97.83	82.83	SBIF	Sharp
TD37	97.83	106.9	9.07	Biotite gneiss	Sharp
TD37	106.9	143.41	36.51	SBIF	Sharp
TD37	143.41	179	35.59	Mafic granulite	EOH
TD35	0	4	4	Lateritic cover	Gradational
TD35	4	23.4	19.4	Hematite cap	Gradational
TD35	23.4	107.08	83.68	SBIF	Sharp
TD35	107.08	114.2	7.12	Garnet amphibolite	Sharp
TD35	114.2	120.74	6.54	SBIF	Sharp
TD35	120.74	133.4	12.66	Mafic granulite	Sharp
TD35	133.4	220.2	86.8	Biotite gneiss	Sharp
TD35	220.2	281	60.8	Mafic granulite	EOH
TD46	0	5.44	5.44	Lateritic cover	Gradational
TD46	5.44	21.44	16	Hematite cap	Gradational
TD46	21.44	84.9	63.46	Biotite gneiss	Sharp
TD46	84.9	96.4	11.5	Mafic granulite	Sharp
TD46	96.4	102.4	6	SBIF	Sharp
TD46	102.4	110	7.6	Mafic granulite	Sharp
TD46	110	118	8	SBIF	Sharp
TD46	118	126.9	8.9	Mafic granulite	Sharp
TD46	126.9	154.3	27.4	SBIF	Sharp

TD46	154.3	186	31.7	Mafic granulite	Sharp
TD46	186	216	30	SBIF	Gradational
TD46	216	240	24	Garnet amphibolite	Sharp
TD46	240	306	66	Mafic granulite	EOH
TH31	0	3.6	3.6	Lateritic cover	Gradational
TH31	3.6	17.9	14.3	Garnet amphibolite	Gradational
TH31	17.9	31.9	14	SBIF	Sharp
TH31	31.9	49.9	18	Mafic granulite	Sharp
TH31	49.9	62.88	12.98	Garnet amphibolite	Sharp
TH31	62.88	81	18.12	Mafic granulite	EOH
TD47	0	25.4	25.4	Lateritic cover	Gradational
TD47	25.4	55.9	30.5	Garnet amphibolite	Gradational
TD47	55.9	70.2	14.3	SBIF	Gradational
TD47	70.2	82.9	12.7	Garnet amphibolite	Gradational
TD47	82.9	184.9	102	SBIF	Sharp
TD47	184.9	189.1	4.2	Biotite gneiss	Sharp
TD47	189.1	195.1	6	Garnet amphibolite	Sharp
TD47	195.1	197	1.9	Biotite gneiss	Sharp
TD47	197	204.7	7.7	Garnet amphibolite	Sharp
TD47	204.7	212.1	7.4	Biotite gneiss	Sharp
TD47	212.1	214.6	2.5	Mafic granulite	Sharp
TD47	214.6	242	27.4	Biotite gneiss	Gradational
TD47	242	273	31	SBIF	Sharp
TD47	273	315.9	42.9	Biotite gneiss	Sharp
TD47	315.9	329	13.1	Garnet amphibolite	EOH
TD60	0	12.6	12.6	Lateritic cover	Gradational
TD60	12.6	16.9	4.3	Biotite gneiss	Sharp
TD60	16.9	40	23.1	Mafic granulite	Sharp
TD60	40	67	27	Garnet amphibolite	Gradational
TD60	67	72.2	5.2	SBIF	Sharp
TD60	72.2	79.3	7.1	Garnet amphibolite	Sharp
TD60	79.3	84.4	5.1	SBIF	Gradational
TD60	84.4	110	25.6	Garnet amphibolite	EOH
TD65	0	1.3	1.3	Lateritic cover	Gradational
TD65	1.3	8.7	7.4	Hematite cap	Gradational
TD65	8.7	22.06	13.36	Mafic granulite	Gradational
TD65	22.06	56.55	34.49	SBIF	Sharp
TD65	56.55	111	54.45	Mafic granulite	EOH
<b>Southern prospect</b>					
TE6	0	11	11	Lateritic cover	Gradational
TE6	11	91.3	80.3	Biotite gneiss	Gradational
TE6	91.3	95.9	4.6	Mafic granulite	Gradational
TE6	95.9	125	29.1	Biotite gneiss	Sharp
TE6	125	153.8	28.8	Garnet amphibolite	Sharp
TE6	153.8	192.8	39	SBIF	Sharp
TE6	192.8	218.3	25.5	Mafic granulite	Gradational
TE6	218.3	246.9	28.6	SBIF	Gradational
TE6	246.9	300	53.1	Biotite gneiss	EOH

TE5	0	6.56	6.56	Lateritic cover	Gradational
TE5	6.56	88.93	82.37	Biotite gneiss	Gradational
TE5	88.93	123.25	34.32	SBIF	Sharp
TE5	123.25	155	31.75	Mafic granulite	Sharp
TE5	155	168.4	13.4	SBIF	Sharp
TE5	168.4	182	13.6	Biotite gneiss	EOH
TE4	0	8.5	8.5	Lateritic cover	Gradational
TE4	8.5	44.65	36.15	Biotite gneiss	Sharp
TE4	44.65	81.35	36.7	SBIF	Sharp
TE4	81.35	106.25	24.9	Mafic granulite	Sharp
TE4	106.25	115.55	9.3	SBIF	Sharp
TE4	115.55	245	129.45	Biotite gneiss	EOH
TE9	0	11.65	11.65	Lateritic cover	Gradational
TE9	11.65	80.7	69.05	Biotite gneiss	Gradational
TE9	80.7	93.7	13	Garnet amphibolite	Gradational
TE9	93.7	119.5	25.8	SBIF	Gradational
TE9	119.5	134.75	15.25	Garnet amphibolite	Gradational
TE9	134.75	141	6.25	Mafic granulite	Gradational
TE9	141	186.4	45.4	SBIF	Sharp
TE9	186.4	220	33.6	Biotite gneiss	EOH
TE22	0	19.4	19.4	Lateritic cover	Gradational
TE22	19.4	21.6	2.2	SBIF	Sharp
TE22	21.6	33.4	11.8	Mafic granulite	Sharp
TE22	33.4	37.3	3.9	SBIF	Sharp
TE22	37.3	42	4.7	Mafic granulite	Sharp
TE22	42	45.5	3.5	SBIF	Sharp
TE22	45.5	46.5	1	Mafic granulite	Gradational
TE22	46.5	48	1.5	BIF	Gradational
TE22	48	50.5	2.5	Mafic granulite	Sharp
TE22	50.5	133.5	83	SBIF	Sharp
TE22	133.5	137.6	4.1	Mafic granulite	Sharp
TE22	137.6	139	1.4	Biotite gneiss	EOH

**Appendix 3.** Table showing geochemical analysis for Bidou garnet gneiss and garnet micaschist (Kamguia Woguia et al., 2022)

Rock type Major elements	Garnet gneiss							Garnet micaschist				
	OB 37A	OB 37B	OB 37C	OB 40A	OB 40B	OB 42A	OB 42B	OB 38A	OB 38B	OB 39A	OB 39B	OB 39C
SiO <sub>2</sub>	85.05	82.42	81.32	83.06	88.06	74.34	80.31	77.41	77.01	61.57	61.75	54.64
TiO <sub>2</sub>	0.35	0.41	0.44	0.47	0.26	0.51	0.35	0.45	0.47	0.82	0.82	1.39
Al <sub>2</sub> O <sub>3</sub>	7.67	9.41	9.51	8.57	5.81	13.72	9.75	10.35	10.34	15.42	15.93	19.66
Fe <sub>2</sub> O <sub>3</sub>	2.73	2.77	3.15	3.24	2.38	4.67	3.79	4.5	4.71	7.57	7.05	7.13
MgO	0.42	0.48	0.56	0.63	0.48	0.92	0.67	1.27	1.3	4.17	3.84	4.24
MnO	0.11	0.11	0.13	0.07	0.06	0.1	0.08	0.07	0.07	0.11	0.11	0.08
CaO	0.05	0.05	0.06	0.07	0.05	0.11	0.08	1.25	1.24	3.58	3.8	4.36
Na <sub>2</sub> O	0.06	0.07	0.07	0.06	0.06	0.22	0.19	1.64	1.61	2.21	2.55	3.45
K <sub>2</sub> O	1.26	1.5	1.59	1.12	1	3.14	2.72	1.73	1.76	2.62	2.28	2.86
Cr <sub>2</sub> O <sub>3</sub>	0.01	0.01	0.01	0.01	0.01	0.01	0.01	0.01	0.01	0.04	0.04	0.03
P <sub>2</sub> O <sub>5</sub>	0.02	<0.01	<0.01	0.02	0.01	0.02	0.04	0.04	0.04	0.26	0.25	0.14
LOI	2.2	2.6	3	2.5	1.7	2.1	1.9	1.1	1.2	1.3	1.3	1.5
Total	99.94	99.93	99.92	99.93	99.95	99.89	99.92	99.88	99.88	99.78	99.78	99.66
Trace and Rare earth elements	OB 37A	OB 37B	OB 37C	OB 40A	OB 40B	OB 42A	OB 42B	OB 38A	OB 38B	OB 39A	OB 39B	OB 39C
V	33	49	48	61	34	79	58	76	73	142	136	325
Ba	307	348	401	423	255	610	458	586	585	1182	1096	1614
Rb	37.9	43.6	46.7	40.4	31.8	97.9	85.9	55.3	58.3	96.3	78	112.1
Ga	7.9	9.3	8.8	7.3	5.3	14.3	10.5	9.8	9.8	16.6	16.1	22.2
Cs	0.1	<0.1	<0.1	0.2	0.1	<0.1	<0.1	0.3	0.2	0.9	0.6	0.8
Th	11.2	15.3	11.3	10.2	9.2	19.8	18.5	18.9	18.8	16.4	16.5	13
U	1.2	1.4	1.5	1.3	1.1	1.7	1.7	2.3	2.2	1	1.1	1
Sr	19.9	17.6	18	23.6	25	49.7	38.9	161.7	163	454.2	529.4	631.5
Nb	8.8	8.6	10.1	9.8	4.3	11.6	7.6	8.1	8.6	5.7	6.8	6.7
Ta	0.8	0.8	0.9	0.6	0.3	0.8	0.6	0.8	0.9	0.4	0.4	0.4
Hf	7.6	7.9	9.2	8.5	6.7	6.9	6.2	5.4	5.7	4	4.7	14.1
Zr	272.3	277.4	330.4	304.1	239.2	252.1	222.1	192	213.3	149.9	170.5	581.7
Y	17.1	18.7	23.7	18.1	14.9	23.1	17.9	26.3	24.9	22.7	22.2	17.4
La	21.7	29.2	23.3	24.6	18.2	38.7	35.3	57.6	61.8	63.2	63.1	75.3
Ce	39.8	52.9	40.6	40.4	31.9	70.5	64.3	82.5	90.4	113.2	114.6	126.1
Pr	4.09	5.23	3.98	4.13	3.3	7.41	6.73	10.21	11.33	12.48	12.47	13
Nd	14.5	18.4	15.2	14.5	11.2	26.5	23.3	35.1	39.2	46.6	45.6	43.6
Sm	2.56	3.21	2.86	2.67	2.18	4.14	3.87	6.13	6.6	6.87	6.38	5.46
Eu	0.54	0.65	0.64	0.62	0.49	1	0.87	1.17	1.14	1.66	1.76	2.41
Gd	2.52	2.99	3.17	3.02	2.27	3.86	3.43	5.54	5.42	5.53	5.3	4.49
Tb	0.46	0.5	0.56	0.48	0.36	0.61	0.49	0.85	0.8	0.73	0.71	0.58
Dy	2.78	3.13	3.45	2.91	2.38	3.86	3.13	4.55	4.47	4.18	4.03	3.12
Ho	0.58	0.65	0.81	0.63	0.55	0.81	0.64	0.9	0.96	0.77	0.77	0.61
Er	1.88	2.18	2.62	1.84	1.84	2.42	1.95	2.79	2.71	2.42	2.24	1.84
Tm	0.29	0.32	0.4	0.29	0.28	0.34	0.29	0.39	0.39	0.34	0.34	0.27
Yb	1.98	2.25	2.81	1.91	1.91	2.31	1.93	2.74	2.66	2.29	2.3	1.65
Lu	0.31	0.34	0.44	0.33	0.31	0.38	0.32	0.42	0.4	0.34	0.34	0.25
ΣREE	110.78	140.31	124.1	116.1	91.76	185.56	164.13	236.77	252.78	282.97	281.8	295.83

**Appendix 4.** Table showing Bipindi mafic granulites (Moudioh et al., 2020) and Kribi mafic granulites (Mvodo et al., 2022).

SAMPLE	Bipindi mafic granulites			Kribi mafic granulites						
	BRV6	GZ1	GZ2	MV1	MV2	KR16A	KR16B	KR16C	KR19A	KR19B
SiO <sub>2</sub>	48.05	47.78	48.79	51.6	51.6	50	48.3	50.3	51.5	51.1
TiO <sub>2</sub>	1.12	0.69	0.67	1.24	1.24	1.31	1.41	1.28	1.22	1.24
Al <sub>2</sub> O <sub>3</sub>	13.55	17.31	16.95	13.2	13.65	12.75	13.05	13.2	13.05	13
Fe <sub>2</sub> O <sub>3</sub>	14.65	13.91	13.3	14.4	14.75	15.95	16.8	15.5	14.45	14.8
MgO	7.28	8.99	8.55	5.35	5.21	6.05	6.22	5.79	5.3	5.52
MnO	0.23	0.19	0.19	0.21	0.21	0.24	0.24	0.23	0.21	0.21
CaO	11.24	9.19	9.43	9.46	9	10.15	10.35	10.1	9.01	9.82
Na <sub>2</sub> O	0.79	1.45	1.56	2.99	2.9	2.97	2.89	3.15	3.08	3.05
K <sub>2</sub> O	0.36	0.12	0.12	0.37	0.4	0.35	0.33	0.35	0.36	0.35
Cr <sub>2</sub> O <sub>3</sub>	0.04	0.06	0.06	0.01	0.01	0.01	0.01	0.01	0.01	0.01
P <sub>2</sub> O <sub>5</sub>	0.08	0.04	0.03	0.11	0.09	0.14	0.1	0.17	0.13	0.18
Total	99.77	99.76	99.77	99.41	99.57	100.62	100.13	100.58	98.79	99.85
Trace and Rare earth elements										
Ba	125	29	25	228	246	126	129.5	122	129	130
Ga	15.7	15.7	14.4	22	20.5	20	22.1	20.4	19.1	19.4
Hf	1.8	1.4	1	2.6	1.9	2.2	2.6	1.9	2.4	2.2
Nb	2.4	2	2.1	5.4	4.7	4.9	5	4.5	4.3	4.5
Rb	7.9	2.7	2.4	3	2.8	2.7	2.2	2.2	2.4	2.5
Sr	112.3	107.3	83.6	222	237	95.4	97.8	99.1	122	123
Ta	0.1	0.1	0.2	0.6	0.5	0.6	0.5	0.7	0.3	0.4
Th	0.2	0.2	0.2	0.47	0.43	0.65	0.71	0.58	0.49	0.64
U	0.1	0.1	0.1	0.28	0.26	0.2	0.26	0.22	0.18	0.19
V	288	263	255	379	371	409	430	383	359	378
Y	23	8.6	10.5	27.7	24.1	31.3	29.5	29.3	23.1	26.1
Zr	57.9	49	36.6	87	60	57	73	53	68	55
La	5.1	3.9	2.8	10.8	10.3	7.4	6.8	7.7	6.8	8.3
Ce	10.1	6.3	5.1	22.7	21	17.3	15.8	17.7	15.6	19.4
Pr	1.55	0.84	0.71	3.07	2.67	2.38	2.25	2.42	2.19	2.63
Nd	7.9	3.5	3.4	13.7	11.8	11.2	10.6	11.2	10.1	12.4
Sm	2.56	0.86	0.83	3.73	3.17	3.64	3.25	3.44	2.95	3.37
Eu	0.9	0.52	0.49	1.2	1.12	1.16	1.12	1.12	1.08	1.12
Gd	3.6	1.17	1.18	4.1	3.96	4.11	4.16	4.1	3.69	4.25
Tb	0.64	0.22	0.22	0.67	0.66	0.72	0.7	0.71	0.62	0.72
Dy	4.3	1.5	1.52	4.49	4.15	4.99	4.71	4.69	4	4.55
Ho	0.94	0.36	0.35	0.97	0.9	1.06	1.05	0.99	0.86	0.99
Er	2.63	1.16	1.1	2.9	2.62	3.05	3.27	2.89	2.4	2.78
Tm	0.38	0.19	0.17	0.39	0.36	0.5	0.46	0.44	0.35	0.41
Yb	2.51	1.2	1.22	2.58	2.44	3.22	3.13	2.88	2.29	2.54
Lu	0.39	0.21	0.19	0.4	0.39	0.48	0.48	0.46	0.34	0.4

## Appendix 5. Structural data: Foliations, lineations and fold axis

Foliation									
N14	30NW	N142	20NE	N132	82SW	N146	64SW	N164	66SW
N30	50NW	N142	38NE	N132	60SW	N146	68SW	N168	64SW
N34	32NW	N142	24NE	N132	74SW	N150	60SW	N170	68SW
N34	42NW	N150	26NE	N132	60SW	N150	66SW	N170	70SW
N36	46NW	N180	42E	N132	66SW	N150	70SW	N172	64SW
N39	22NW	N114	62S	N136	60SW	N150	60SW	N174	72SW
N40	30NW	N114	62S	N136	72SW	N150	60SW	N176	54SW
N40	22NW	N118	70SW	N136	60SW	N154	60SW	N178	54SW
N40	30NW	N118	70SW	N138	66SW	N156	68SW	N178	66W
N42	50NW	N124	68SW	N138	66SW	N156	60SW		
N44	34NW	N124	68SW	N140	64SW	N158	62SW		
N50	30NW	N124	74SW	N140	60SW	N158	66SW		
N62	30NW	N128	66SW	N140	70SW	N158	62SW		
N74	36NW	N128	68SW	N140	66SW	N158	66SW		
N88	20NW	N128	78SW	N140	64SW	N158	62SW		
N105	38NE	N128	34SE	N140	70SW	N160	64SW		
N106	42NE	N128	66SW	N140	64SW	N160	64SW		
N106	42NE	N130	80SW	N140	60SW	N160	68SW		
N110	45NE	N130	80SW	N140	60SW	N162	78SW		
N120	25NE	N130	64SW	N144	82SW	N162	70SW		
N124	38NE	N132	76SW	N144	58SW	N162	70SW		
N125	26NE	N132	80SW	N144	58SW	N162	68SW		
N129	34NE	N132	76SW	N146	64SW	N162	70SW		
N133	30NE	N132	80SW	N146	68SW	N164	70SW		

Fold axis						
N50,90						
Mineral lineations						
65NW	36NW	46NW	30NW	38W	44W	46NW
50W	48W	20SW	20SW	24SW	46SW	28SW



## **Appendix 6. Publication**

## Article

# Lithostratigraphy, Origin, and Geodynamic Setting of Iron Formations and Host Rocks of the Anyouzok Region, Congo Craton, Southwestern Cameroon

Isaac Swiffa Fajong <sup>1</sup>, Marvine Nzepang Tankwa <sup>2</sup> , Donald Hermann Fossi <sup>1,2</sup>, Sylvestre Ganno <sup>1,\*</sup> , Cyriel Moudioh <sup>2</sup>, Landry Soh Tamehe <sup>3</sup>, Cheo Emmanuel Suh <sup>4</sup> and Jean Paul Nzenti <sup>1</sup>

<sup>1</sup> Department of Earth Sciences, Faculty of Science, University of Yaounde I, Yaounde P.O. Box 812, Cameroon

<sup>2</sup> Institute for Geological and Mining Research, Yaounde P.O. Box 4110, Cameroon

<sup>3</sup> School of Geosciences and Info-Physics, Central South University, Changsha 410083, China

<sup>4</sup> Economic Geology Unit, Department of Geology, University of Buea, Buea P.O. Box 63, Cameroon

\* Correspondence: sganno2000@gmail.com; Tel.: +237-677-752-579

**Abstract:** In Cameroon, most of the iron formation occurrences reported are found within the Nyong and Ntem Complexes. The Anyouzok iron deposit is located in the Nyong Complex greenstone belts, which represent the NW margin of this Congo craton. The main lithological units comprise the iron formations (IFs) unit, consisting of banded IFs (BIFs) and sheared BIFs (SBIFs), and the associated metavolcanic rocks unit consisting of mafic granulite, garnet amphibolite, and biotite gneiss. Within the Anyouzok area, BIFs are rare, while SBIFs are ubiquitous. This study reports the petrography, mineralogy, and whole rock geochemistry of IFs and interbedded metavolcanic rocks of the Anyouzok iron deposit. The abundance of cavities, higher Fe contents (49.60–55.20 wt%), and strong Eu anomalies ( $\text{Eu}/\text{Eu}^* = 2.14\text{--}3.17$ ) within the SBIFs compared to the BIFs suggest that SBIFs were upgraded through post-depositional hydrothermal alteration activities. REE signatures indicate the contribution of both seawater and hydrothermal fluids during BIFs precipitation. Mafic granulite and garnet amphibolite protoliths were derived from the partial melting of a metasomatized spinel lherzolite depleted mantle source. The overall compositional variations of the Anyouzok IFs and interbedded metavolcanic rocks endorse an Algoma-type formation deposited in the back-arc basin under suboxic to anoxic conditions.

**Keywords:** BIFs; seawater; hydrothermal fluids; back-arc/arc settings; Nyong Complex greenstone belts; Anyouzok; Congo craton



**Citation:** Swiffa Fajong, I.; Nzepang Tankwa, M.; Fossi, D.H.; Ganno, S.; Moudioh, C.; Soh Tamehe, L.; Suh, C.E.; Nzenti, J.P. Lithostratigraphy, Origin, and Geodynamic Setting of Iron Formations and Host Rocks of the Anyouzok Region, Congo Craton, Southwestern Cameroon. *Minerals* **2022**, *12*, 1198. <https://doi.org/10.3390/min12101198>

Academic Editors: Matías Reolid and Santanu Banerjee

Received: 8 July 2022

Accepted: 15 September 2022

Published: 23 September 2022

**Publisher's Note:** MDPI stays neutral with regard to jurisdictional claims in published maps and institutional affiliations.



**Copyright:** © 2022 by the authors. Licensee MDPI, Basel, Switzerland. This article is an open access article distributed under the terms and conditions of the Creative Commons Attribution (CC BY) license (<https://creativecommons.org/licenses/by/4.0/>).

## 1. Introduction

Iron formations (IFs) are Precambrian sedimentary rocks, typically thin-bedded or laminated, containing 15% or more iron of sedimentary origin and commonly but not necessarily containing chert layers [1]. Iron ore is an essential raw material for several industrialization products, especially for developing nations. Despite the increasing demand for high-grade (>55 wt% Fe), high-purity (e.g., low phosphorus) Fe concentrates, hematite/goethite-rich ore bodies are increasingly difficult to find. Therefore, industries and policymakers are getting more and more interested in low-grade iron ore [2]. Exploration efforts are thus geared towards Archaean and Paleoproterozoic IFs-hosted magnetite-rich deposits [2,3]. Several exploration works have been carried out on the Anyouzok iron ore deposit [4,5], the latest of them being the prefeasibility studies conducted by Caminex Sarl, the Cameroonian subsidiary of the British-based International Mining and Infrastructure Corporation (IMIC). These studies reported magnetite ore deposits, with 96.9 Mt at 34.92% Fe indicated and 79.4 Mt at 35.04% Fe inferred [5]. Besides their high economic value in the steel and construction industries, IFs provide invaluable information in the understanding of the evolution of the atmosphere, biosphere, and coeval ocean composition,

as well as the origin and growth of continents [6–15]. In spite of the extensive studies in the last century, many controversies still persist concerning their origin as well as regarding how these formations are upgraded to iron ore [2,3,7,16,17]. Early classifications divided IFs into Algoma- and Superior-type [18]. Superior-type IFs are extensive, closely associated with clastic to carbonate rocks, and were deposited in near-shore continental shelf environments with no direct correlation with volcanic rocks [18]. Conversely, Algoma-type IFs are less extensive, closely affiliated with volcanic rocks in greenstone belts, and generally deposited in intracratonic rifts or in back-arc/arc basins [18]. Texturally, iron formations were also divided into two groups: banded iron formation (BIFs), widespread in Archaean to early Paleoproterozoic successions, and granular iron formations (GIFs), much more common in Paleoproterozoic successions [7].

In Cameroon, IFs are mainly found within the Nyong and Ntem Complexes (Figure 1), which correspond to the Northwestern extension of the Congo Craton [19]. The Nyong Complex (Figure 1), where the Anyouzok iron ore deposit lies, hosts several greenstone belts mainly comprising metavolcanic-sedimentary rocks associated with IFs [11,12,14,19–31]. It constitutes an emerging iron ore province of south Cameroon. This complex has experienced deformation and high-grade metamorphism, rendering the reconstruction of the depositional environment of the hosted IFs difficult. As a palliative, several workers worldwide have investigated interbedded igneous and/or sedimentary rocks to better constrain IFs' depositional setting [9–12,14,28]. In this regard, the present study provides a comprehensive geochemical dataset for IFs and interbedded metavolcanic rocks, which were intercepted in drillholes of the Anyouzok iron deposit (Figure 2a). Lithostratigraphy and petrography are presented, in combination with bulk-rock major, trace, and rare earth elements (REE) geochemistry, with the aim of determining the origin and depositional environment of the Anyouzok IFs, which is important for the understanding of the Nyong Complex geodynamic evolution.

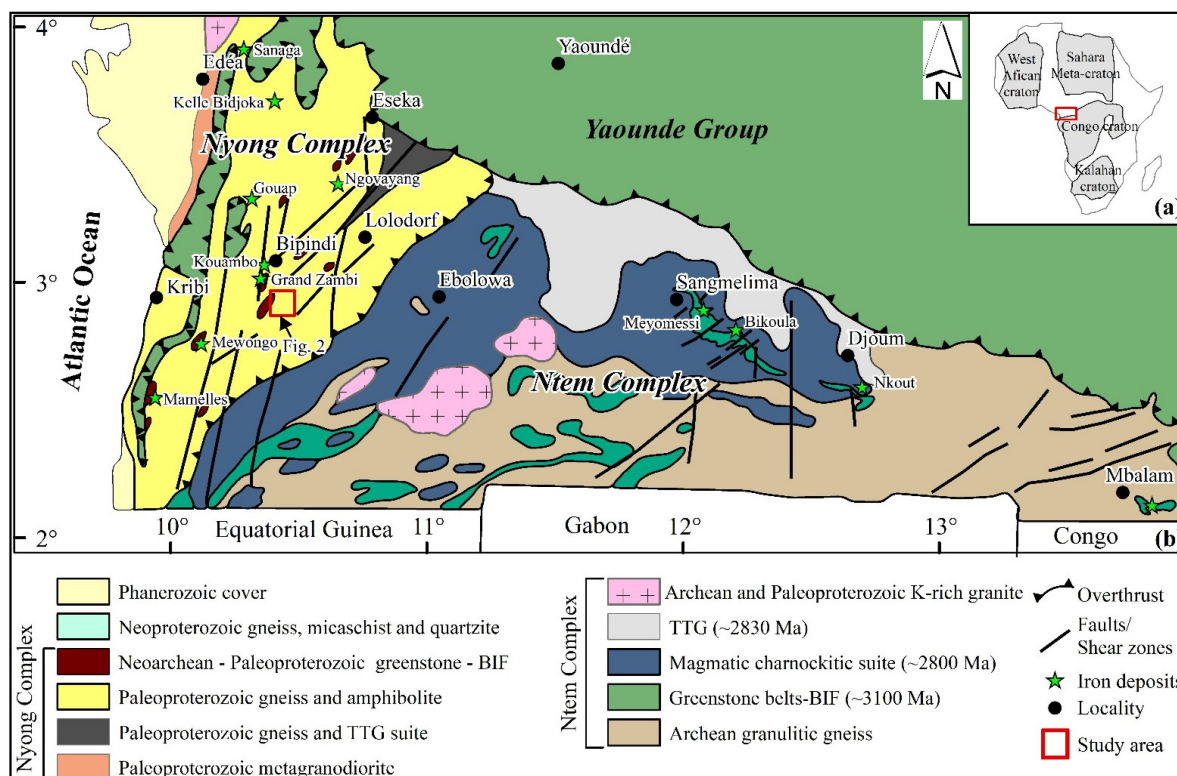


**Figure 1.** Sketch geological map of SW Cameroon (modified after [19]), with insert showing the Congo craton in relation to other African cratons.

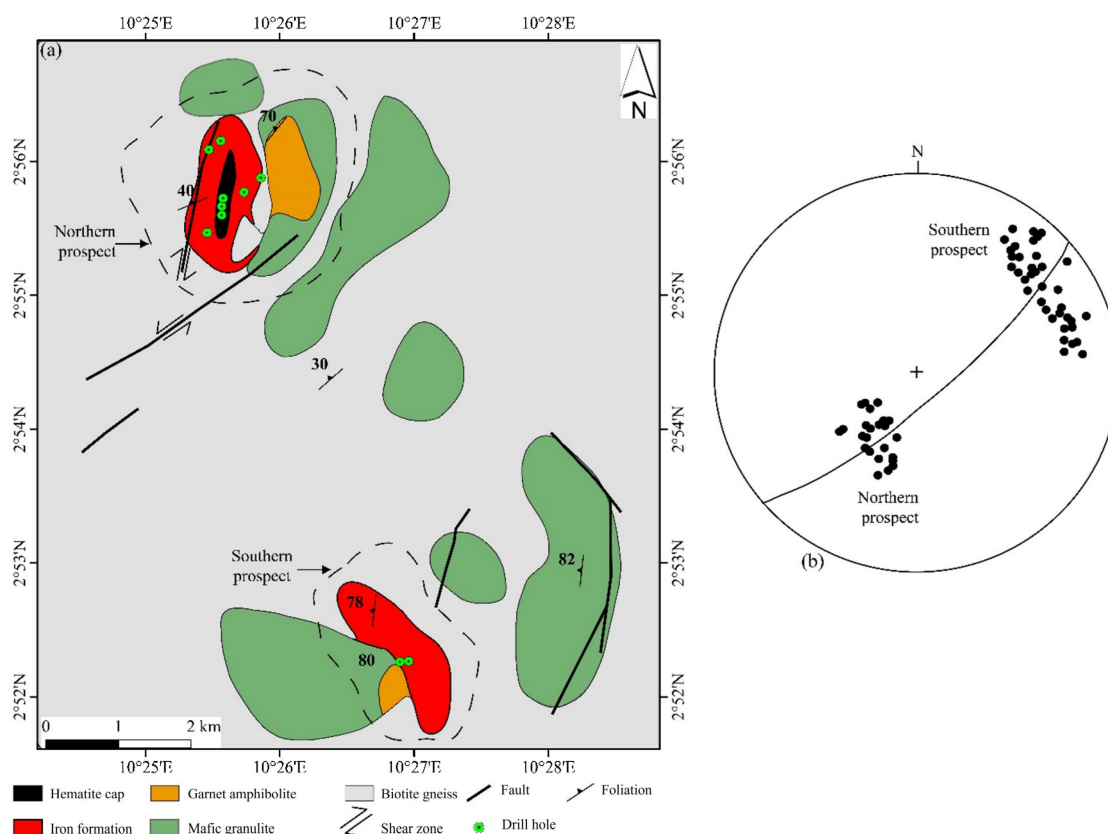


**Figure 2.** (a) Geological map of the Anyouzok iron deposit with drillholes and prospects (northern and southern) locations; (b) orientation diagram presenting the  $S_1/S_2$  foliations of the Anyouzok northern and southern prospects.

## 2. Geological Setting

### 2.1. Regional Geology

Pioneer studies reported that the NW extension of the Congo Craton (CC) in Cameroon is represented by the Nyong and Ntem Complexes (Figure 1) [19]. Subsequent geophysical investigations reported that the cratonic basement in Cameroon extends northwards to the Adamawa Yade region, as revealed by the existence of high-gravity anomalies from denser material beneath this region [32–34]. These results are consistent with recent petrological investigations and U-Pb on zircon LA-ICP-MS [35], LA-MC-ICP-MS, and SHRIMP dating [36], suggesting an extension of the northern edge of the Congo Craton in the Central domain of the Pan-African North Equatorial fold belt and eastward to Central African Republic.

The Anyouzok iron ore deposit is located within the Nyong Complex (Figure 1), which is considered as a segment of the Archean Ntem Complex that was reactivated during the Paleoproterozoic Eburnean/Trans-Amazonian orogeny [14,37–39] or as a Paleoproterozoic suture zone contemporaneous to a nappe tectonic event between the São Francisco and Congo Cratons [20,23,24,40,41]. The Nyong Complex consists of various gneisses, micaschists, amphibolites, IFs, metagranodiorites, charnockites, dolerites, quartzites, tonalite-trondhjemite-granodiorite suite, syenites, serpentinites, and eclogites [11,12,14,20,22–24,28,30,31,42,43].

Few geochronological investigations characterized the geodynamic evolution of the Nyong Complex during Precambrian times [12,14,27,29,31,35,39,43,44]. LA-ICP-MS U-Pb on zircon dating of the Nyong Complex metabasic rocks (amphibolites) yielded Archean ages of  $3072 \pm 28$  Ma [45] and  $2819 \pm 12$  Ma [46], interpreted as the crystallization age of their precursor. The Neoarchaean age ( $2699 \pm 7$  Ma) obtained from SHRIMP zircon U-Pb isotope data on magnetite gneiss (IFs) has been interpreted as the onset age of IFs deposition in the Nyong Complex [47]. Few workers using SHRIMP U-Pb on zircon analyses [20]

and LA-ICP-MS U-Pb on zircon [27] from metasediments, constrained the maximum depositional age of the Nyong Complex at ca. 2423 Ma. Owona et al. [39], using LA-ICP-MS U-Pb on zircon suggested that the Nyong Complex metasediments have a depositional age bracketed between 2400 and 2200 Ma. Paleoproterozoic ages between 2000 and 2100 Ma have been widely reported within the Nyong Complex [12,20,27,29,43,44]. These ages have been linked to a high-grade metamorphic event and metasomatism, to the tectonic emplacement of plutonic rocks, or to an eclogite facies metamorphism. More recently, Soh Tamehe et al. [14] combining SIMS and LA-ICP-MS U-Pb analyses on zircon from the Gouap metasiliciclastic rocks constrained the depositional age of a BIF sequence at 2100–2000 Ma. These Neoarchaean and Paleoproterozoic formations generally bear Neoproterozoic imprints (600–500 Ma), corresponding to later Pan-African tectonometamorphic activities [12,43,47–49].

The Nyong Complex exhibits shallow dipping  $S_1/S_2$  foliations with variably oriented axial fold (N-S to NNE-SSW) and stretching (E-W to NW-SE) lineations and local large open folds associated with N-S sinistral strike slip faults [19,20,43,50].

## 2.2. Anyouzok Deposit Geology

The Anyouzok iron ore deposit is found between longitudes  $10^{\circ}24'12''$  E to  $10^{\circ}28'54''$  E and latitudes  $2^{\circ}51'38''$  N to  $2^{\circ}56'51''$  N, covering a total surface area of about 80 km<sup>2</sup> (Figure 2a). Field investigations revealed that the study area consists of banded IFs (BIFs) associated with mafic granulite, garnet amphibolite, biotite gneiss, and mylonitized gneiss. All BIFs encountered on the field are sheared and will be called Sheared BIF (SBIF) in this study. SBIFs occur as road cuttings and on river beds (Figure 3a,b) generally associated with mafic granulite (Figure 3b). Previous workers reported that rocks within this region have undergone greenschist to granulite facies metamorphism [11,21]. From a combination of Landsat image processing, field mapping, and geostatistical analysis carried out around the neighboring Abiete-Toko gold district, this area is known to have undergone a ductile/brittle polyphase deformation, ( $D_1$ – $D_3$ ), represented by the  $S_1$  foliation/schistosity,  $L_1$  lineation,  $S_2$  foliation, and  $F_2$  folds with  $F_3$  shear zones and faults. The second deformation phase,  $D_2$ , is dominant, characterized by regular folds. It is therefore suggested that there was an N-S and NE-SW shortening direction, as expressed by the folds and localized strike-slip shear zones [51].

Based on IFs occurrences on the field, the Anyouzok iron deposit is subdivided into a northern and a southern prospect (Figure 2a). The northern prospect is an N-S trending ore body with a strike length of 2100 m by 800 m (Figure 2a). The southern prospect is an NW-SE trending ore body with a strike-length of 2000 m by 300 m (Figure 2a). In these prospects, compositional layering  $S_1$  represents the earliest fabric observed within the mafic granulite, garnet amphibolite, biotite gneiss, and SBIFs. The SBIFs portray a dominant  $S_2$  foliation, parallel to the  $S_1$  gneissic compositional layering (Figure 3c). The  $S_1/S_2$  in the northern prospect represents an NW shallow-dipping composite fabric with a mean direction of  $N126^{\circ}E32NE$ , whereas, in the southern prospect,  $S_2$  (Figure 3d), which affected SBIFs and biotite gneiss, is steeply dipping  $60$ – $75^{\circ}$  towards the SW. The average direction of  $S_1/S_2$  is  $N145^{\circ}E66SW$ . Broad mesoscale gentle folds are observed on the SBIFs and biotite gneiss (Figure 3e). The C-planes of these fabrics are parallel to  $S_1/S_2$ , suggesting a component of layer parallel shearing (Figure 3f). The disposition of the foliation planes  $S_1/S_2$  from the two prospects in the diagram of poles (Figure 2b) reflects the existence of a regional fold with axial plane oriented  $N049E$  and dipping  $78^{\circ}$  to the SE.





**Figure 3.** Outcrop views and deformation features: sheared banded iron formation (SBIF) outcropping as (a) road cuttings; (b) river bed generally associated with mafic granulite; (c)  $S_1$  foliation in Biotite gneiss; (d)  $S_2$  foliation in SBIF; (e)  $P_2$  fold in biotite gneiss; (f) Shear zone in biotite gneiss.

### 3. Lithostratigraphy of the Anyouzok Iron Ore Deposit

The lithostratigraphy of the study area was determined via the logging of thirteen representative holes drilled by Caminex SARL. Eight drillholes (TH9, TD37, TD35, TD46, TH31, TD47, TD60, and TD65) were logged from the northern prospect (Figure 4a), while five drillholes (TE4, TE5, TE6, TE9, and TE22) were considered for the southern prospect (Figure 4b). The drillhole details are presented in Supplementary Tables S1 and S2. The units intercepted along the stratigraphy in both prospects are metamorphosed and consist of an IFs unit and country rocks unit (mafic granulite, garnet amphibolite, and biotite gneiss).

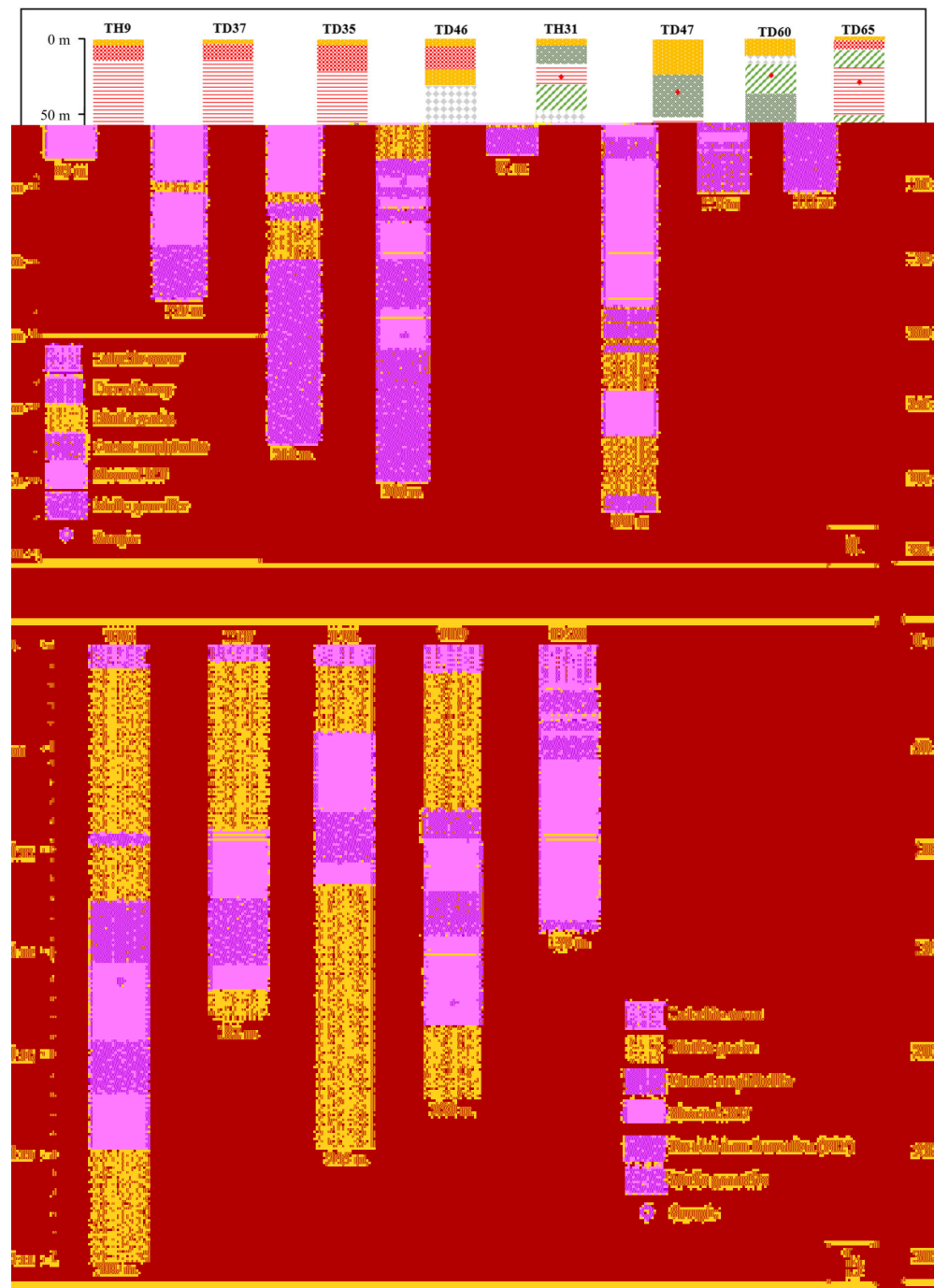


**Figure 4.** Stratigraphic logs with sample locations at the Anyouzok (a) northern prospect and (b) southern prospect.

### 3.1. The Northern Prospect

#### Iron formations unit

In this part of the deposit, IFs consist of SBIFs, intercepted below the surface at variable depths from 15 m (hole TD37), with cumulative thicknesses ranging from 10.30 m (hole TD60; Figure 4a) to 147.3 m (hole TD47; Figure 4a). SBIFs are found in sharp to gradational contact with interbedded biotite gneiss, mafic granulite, and garnet amphibolite. The core specimen consists mainly of medium- to coarse-grained magnetite and quartz.



### Country rocks unit

Biotite gneiss is intercepted from a 12.6 m depth (hole TD60) with various intercalations along the section and a cumulative thickness up to 86.80 m (hole TD35). Biotite gneiss at the hanging wall was intercepted from ca. 32–84 m, just below the hematite cap (hole TD46; Figure 5b). At the footwall, biotite gneiss is found in sharp contact with mafic granulite and garnet amphibolite. The core specimen is mainly made up of fine- to coarse-grained biotite, quartz, and feldspar.

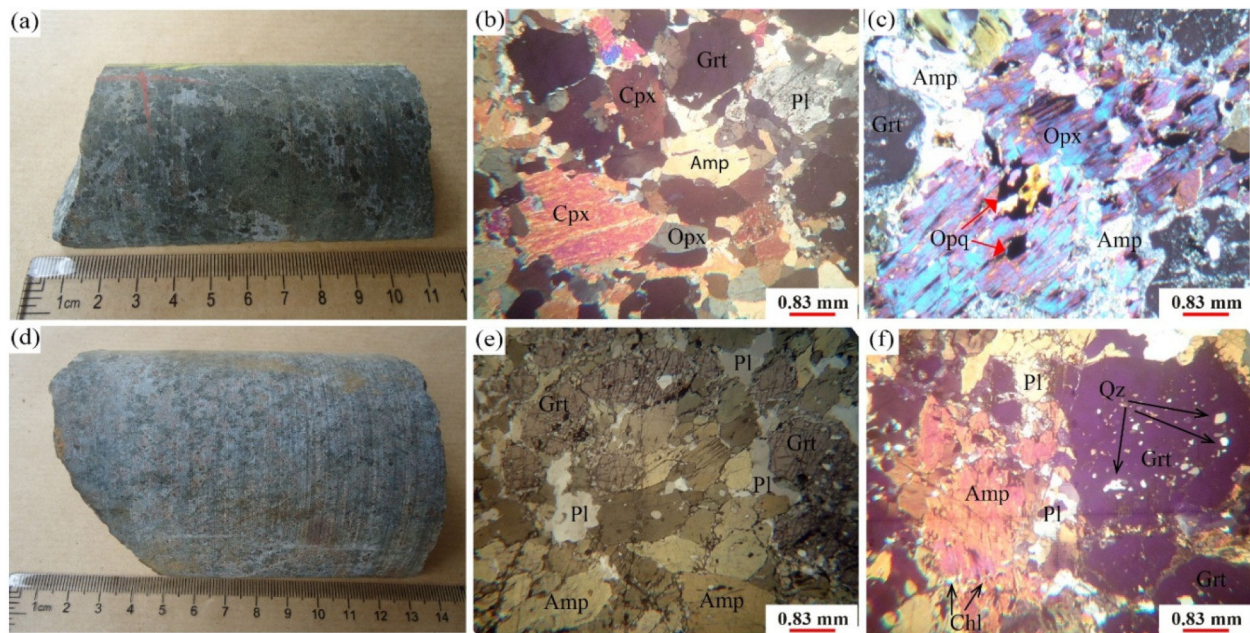


**Figure 5.** Drill core samples and photomicrographs of the Anyouzok metavolcanic rocks: (a) hand specimen of mafic granulite; (b) granoblastic heterogranular microstructure with pyroxene, hornblende, and garnet association (Plane polarized light: PPL); (c) anhedral orthopyroxene undergoing transformation into amphibole along the rims; (d) core sample of garnet amphibolite; (e) granoblastic heterogranular microstructure with amphibole, garnet, and quartz association (PPL); (f) amphibole grain boundaries partially replaced by chlorite (Cross Polarized Light: XPL). Abbreviations: Grt: garnet; Cpx: clinopyroxene; Opx: orthopyroxene; Amp: amphibole; Qz: quartz; Chl: chlorite; Pl: plagioclase.

Mafic granulite represents the major lithotype along the stratigraphy of the northern prospect (Figure 4a) and generally shows a sharp and conformable contact with the SBIFs and other country rocks. At the hanging wall, it is intercepted in holes TD46, TD60, and TH31, with thicknesses of 11.5 m, 23.1 m, and 13.36 m, respectively. The core specimen consists of medium- to coarse-grained pyroxene, garnet, amphibole, and quartz.

Garnet amphibolite represents the less abundant lithotype along the stratigraphy of the northern prospect (Figure 4a). It is intercepted from 3.60 m below the surface (hole TH31) to a 329.16 m depth (hole TD47), with a cumulative thickness ranging from 7.12 m (hole TD35) to 70.16 m (hole TD47). The hand specimen shows visible amphibole, garnet, and quartz crystals.

### 3.2. The Southern Prospect

#### Iron formation unit

The IFs unit within the southern prospect comprises ubiquitous SBIFs and minor BIFs, the latter only intercepted along the section of the drillhole TE22.

SBIFs are exposed in the drill core at various depths from 19.4 m (hole TE22) below the surface and show cumulative thicknesses ranging from 46.0 m (hole TE4) to 92.6 m (hole

TE22; Figure 4b). In this prospect, SBIFs mainly show sharp and conformable contacts with intercalated mafic granulite and garnet amphibolite. Likewise, on the northern prospect, the drill core specimen mainly consists of magnetite and quartz.

BIFs were not encountered during surface mapping but are exposed in the drill core of the hole TE22 from 46.5 to 48.0 m, with a thickness of 1.5 m. They occur sandwiched with gradational contacts between mafic granulite (Figure 4b). The core specimen is banded, with alternating white and dark millimeter- to centimeter-thick quartz-rich and magnetite-rich bands, respectively. Within the dark bands, the magnetite is fine- to medium-grained, while the white bands show fine-grained quartz.

#### Country rocks unit

Biotite gneiss is intercepted at various depths from 8.5 m (hole TE4) below the surface (Figure 4b) and shows cumulative thicknesses ranging from 1.51 m (hole TE22) to 165.95 m (hole TE4). It represents the most abundant lithology of the southern prospect (Figure 4b). Biotite gneiss mainly shows gradational contacts with interbedded mafic granulite, SBIFs, and garnet amphibolite (Supplementary Table S2). It is mainly made up of fine- to coarse-grained biotite, quartz, and feldspar crystals.

Mafic granulite mainly occurs as intercalations between SBIFs with generally sharp contacts and has cumulative thicknesses ranging from 6.25 m (Hole TE9) to 31.75 m (hole TE5). Along the section of hole TE22, mafic granulite represents the only lithology intercalated between SBIFs and BIFs. The core specimen consists of medium- to coarse-grained pyroxene, garnet, amphibole, and quartz.

Garnet amphibolite in the southern prospect (Figure 4b) as well as in the northern prospect represents the least abundant lithotype. The intercepts extend from 80.7 m (hole TE9) below the surface to 125 m (hole TE6), with cumulative thicknesses ranging from 28.25 m (Hole TE9) to 28.8 m (hole TE6). The drill core specimen shows medium to coarse amphibole, garnet, and quartz.

#### 4. Sampling and Analytical Methods

Diamond drill cores were logged at the Caminex camp core shed. For each hole, drill cores were observed from the beginning to the end of the hole. Based on color, texture, and mineral composition, different rock units were distinguished and rock boundaries were delimited. Using a measuring tape, lithologic boundaries and thicknesses were measured and recorded progressively. Half and quarter core samples were systematically collected from the representative drillholes with respect to their lithology and texture. Drill core samples were carefully selected to ensure that the full variability of the iron mineralized unit (SBIFs and BIFs) and interbedded un-mineralized unit (barren zones) were represented, as they need to reflect the geology of the deposit. A total of 31 samples (8 SBIFs, 4 BIFs, 8 mafic granulites, and 11 garnet amphibolites) from 8 drillholes (TH31, TD46, TD60, TE6, TE9, TD47, TE22, and TD65) were collected for this study. Details of holes logged and/or sampled are presented in Supplementary Tables S1 and S2. Selected samples were placed in plastic bags and sealed up to prevent contamination. Labels and codes were given to the samples, which were written on the bags.

Twenty standard thin sections of metavolcanic rocks (ten for mafic granulite and ten for garnet amphibolite) and ten polished thin sections of IFs were prepared at Vanpetro and Geotech Lab, Vancouver (Canada). Detailed microscopic description was carried out at the Earth Sciences Department, University of Yaoundé I (Cameroon) and at Vanpetro Lab, Vancouver (Canada). The IFs' mineral composition was further determined by the X-ray diffraction (XRD) method with the Bruker D8-Advanced Eco 1Kw diffractometer (Bruker Corporation, Billerica, MA, USA) at AGES (University of Liège, Liège, Belgium). A total of 100 g of fresh rock sample were carefully selected, cut, manually crushed, and sieved to 250  $\mu\text{m}$ , using a mortar and pestle. X-ray wavelengths  $\lambda$  ( $0.1 < \lambda < 10 \text{ nm}$ ) are incident on the mineral sample. Excited atoms emit radiations consistent with Bragg's law,  $n\lambda = 2d(\text{hkl})\sin\theta$ , where  $n$  = whole numbers corresponding to the order of diffraction;  $\lambda$  = incident wavelength,  $d$  = distance between layers, and  $\theta$  = angle of diffraction. Based

on the petrographic results, twenty-seven representative fresh samples (six mafic granulites, ten garnet amphibolites, seven SBIFs, and four BIFs) were selected for whole rock geochemical analysis.

Whole rock geochemical analysis for major elements was conducted using rock pulp by inductively coupled plasma-atomic emission spectrometry (ICP-AES), while inductively coupled plasma mass spectrometry (ICP-MS) was conducted for trace element and rare earth element (REE) analysis at ALS Lab, Tipperary, Ireland. The samples were initially pulverized, and 50–60 g were extracted for analysis. Rock powder (0.2 g) was then fused with  $\text{LiBO}_2$  and dissolved in 100 mm<sup>3</sup> of 5%  $\text{HNO}_3$ . Analytical uncertainties vary from 0.1% to 0.04% for major elements, from 0.1 to 0.5 ppm for trace elements, and from 0.01 to 0.5 ppm for rare earth elements. Loss on ignition (LOI) was determined by weight difference after ignition at 1000 °C. Various standards were used, and data quality assurance was verified by running these standards between samples as unknowns. Analysis precision for rare earth elements is estimated at 5% for concentrations >10 ppm and 10% when lower. After data curation, 7 altered samples were screened out, and 20 samples (4 mafic granulites, 7 garnet amphibolites, 5 SBIFs, and 4 BIFs) were selected for geochemical studies. Since Y is more similar to Ho and has been extensively used in REE studies of aqueous solutions and their precipitates [52], it has been inserted between Dy and Ho. REE-Y concentrations of IFs were normalized to Post Archaean Australian Shale (PAAS; [53]). The Eu, Ce, La, Gd, Y, and Pr anomalies of IFs discussed in this study are calculated following the procedure of Bau and Dulski [54] and Bolhar et al. [6]:

$$\begin{aligned} (\text{Eu}/\text{Eu}^*)_{\text{SN}} &= (\text{Eu})_{\text{SN}} / (0.67\text{Sm}_{\text{SN}} + 0.33\text{Tb}_{\text{SN}}); (\text{Ce}/\text{Ce}^*)_{\text{SN}} = \text{Ce}_{\text{SN}} / (0.5\text{La}_{\text{SN}} + 0.5\text{Pr}_{\text{SN}}); \\ (\text{La}/\text{La}^*)_{\text{SN}} &= (\text{La})_{\text{SN}} / (3\text{Pr}_{\text{SN}} - 2\text{Nd}_{\text{SN}}); (\text{Gd}/\text{Gd}^*)_{\text{SN}} = (\text{Gd})_{\text{SN}} / (0.33\text{Sm}_{\text{SN}} + 0.67\text{Tb}_{\text{SN}}); \\ (\text{Y}/\text{Y}^*)_{\text{SN}} &= 2\text{Y}_{\text{SN}} / (\text{Dy}_{\text{SN}} + \text{Ho}_{\text{SN}}); (\text{Pr}/\text{Pr}^*)_{\text{SN}} = \text{Pr}_{\text{SN}} / (0.5\text{Ce}_{\text{SN}} + 0.5\text{Nd}_{\text{SN}}). \end{aligned}$$

## 5. Results

### 5.1. Petrography and Mineralogy

#### 5.1.1. Metavolcanic Rocks

Metavolcanic rocks appear as mafic granulite and garnet amphibolite.

Mafic granulite tends to be massive and generally dark grey, with coarse-grained pyroxene associated with garnet and patchy amphibole crystals (Figure 5a). In thin sections, the rock shows a granoblastic heterogranular microstructure (Figure 5b), consisting of pyroxene (35 vol.%), garnet (30 vol.%), amphibole (10 vol.%), plagioclase (10 vol.%), quartz (5 vol.%), opaque (2 vol.%), and chlorite (<2 vol.%). Pyroxene occurs mainly as clinopyroxene and orthopyroxene in lesser volumes. They are medium- to coarse-grained (up to 2 mm in size). They show transformation into amphibole and opaque minerals along their rims and cleavages (Figure 5c). Garnet is medium- to coarse-grained (up to 2 mm), sub-angular to rounded, and fractured. It sometimes contains quartz inclusions (Figure 5b,c). Quartz is fine- to coarse-grained and generally appears either as aggregates mixed with opaque minerals or as occupying interstices between minerals. Amphibole is medium- to coarse-grained (0.5–2 mm) and occurs generally as angular to sub-angular crystals, associated with garnet, clinopyroxene, and quartz. It shows transformation into chlorite. Plagioclase is anhedral, fine- to medium-grained (up to 2 mm), and shows transformation into sericite (Figure 5b). Opaque minerals are rare and found as inclusions within pyroxene, garnet, and amphibole.

Garnet amphibolite is generally medium- to coarse-grained and brownish-gray in color, with coarse-grained garnet surrounded by amphibole (Figure 5d). In thin sections, the rock shows a granoblastic heterogranular microstructure (Figure 5e) consisting of amphibole (50 vol.%), garnet (15 vol.%), plagioclase (25 vol.%), pyroxene (5 vol.%), quartz (<2 vol.%), and opaque (<3 vol.%). Amphibole is medium- to coarse-grained (1–2 mm) and occurs as rounded to sub-angular crystals. It sometimes shows transformation into chlorite and opaque minerals along the rims and cleavages (Figure 5f). Garnet is generally sub-rounded to polygonal, medium- to coarse-grained (1–2 mm in size), and fractured. Plagioclase is fine- to medium-grained (<0.5 mm) and occurs as a crushed mosaic crystal,



in association with garnet, hornblende, and pyroxene. Minute quartz inclusions are also found in garnet and hornblende (Figure 5f). Pyroxene occurs as medium-grained (~1 mm) and angular to sub-rounded crystals. Opaque minerals are fine-grained and appear as inclusions in garnet and amphibole crystals or along their rims (Figure 5e).

### 5.1.2. Iron Formations

The Anyouzok IFs comprise banded iron formations (BIFs) and sheared banded iron formations (SBIFs).

BIF is fine- to medium-grained, foliated, and made up of alternating white silica-rich bands and dark magnetite-rich bands (Figure 6a). The white bands range from 1 to 10 mm in thickness, while the dark bands range from 2 to 16 mm in thickness. In thin sections, the rock has a granoblastic heterogranular microstructure (Figure 6b), consisting of quartz (50 vol.%), magnetite (30 vol.%), amphibole (15 vol.%), pyrite (2 vol.%), biotite (1 vol.%), chlorite (<1 vol.%), and hematite (<1 vol.%). Magnetite is fine-grained ( $0.5 \times 0.5$  mm on average), anhedral, and in association with amphibole and biotite. It sometimes appears intergrown with pyrite and, less likely, with hematite (Figure 6c). Some magnetite crystals contain minute quartz inclusions. Amphibole crystals are generally stretched and occur as tremolite and actinolite of 1.5 mm, on average (Figure 6b). They are mostly found partly altered into chlorite and contain diffuse magnetite inclusions (Figure 6b). Biotite ( $0.25 \times 0.5$  mm) is anhedral and generally stretched, and it is closely associated with amphibole, magnetite, and, rarely, quartz. It sometimes presents transformation into chlorite, mostly along the rims. Quartz crystals are anhedral and in close association with amphibole, magnetite, and biotite. Pyrite is fine- to medium-grained and anhedral to subhedral. Hematite is rare and occurs as traces at intimate intergrowths of pyrite with magnetite (Figure 6c).

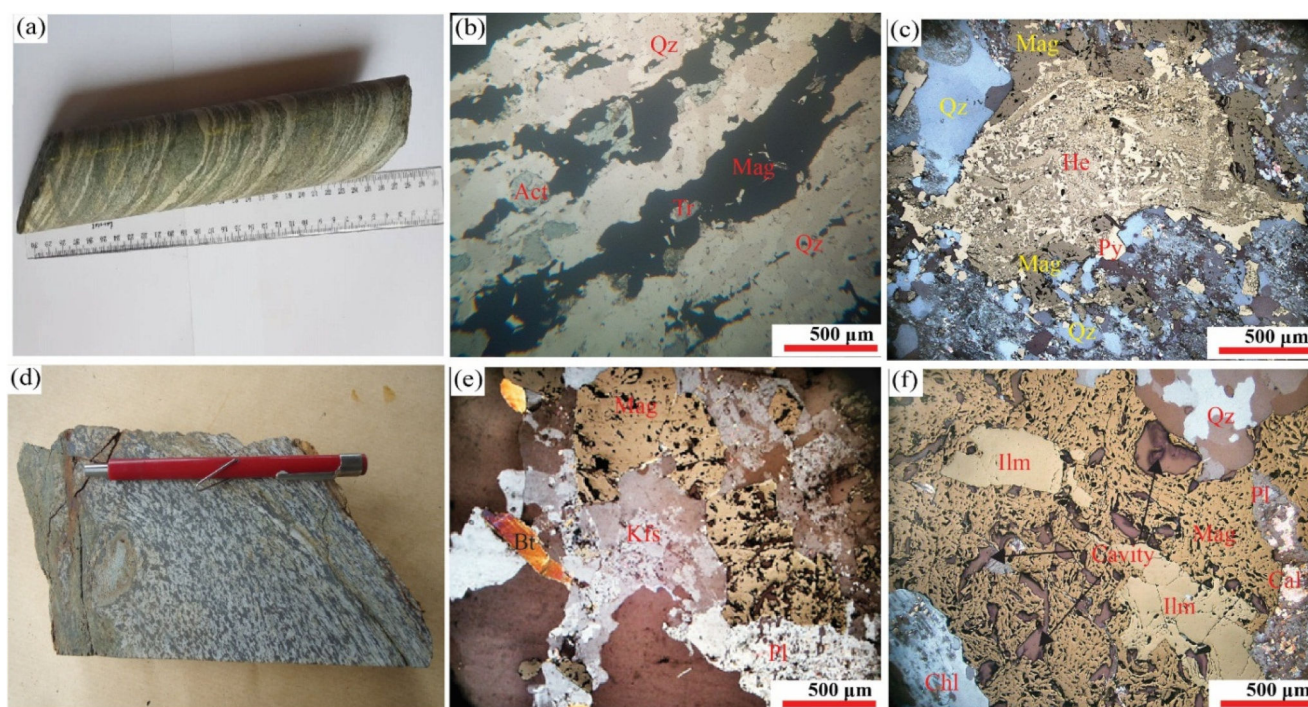


**Figure 6.** Drill core and photomicrographs (partially crossed and reflected light) of the Anyouzok IFs: (a) hand specimen of Banded iron formation (BIF) showing alternating silica and magnetite-rich bands; (b) photomicrograph of BIF showing granoblastic heterogranular microstructure; (c) anhedral magnetite crystal partially replaced by hematite and pyrite; (d) core specimen of SBIF; (e) granoblastic magnetite associated with biotite and intensely sericitized plagioclase and K-feldspar; (f) anhedral magnetite exhibiting several cavities, in association with ilmenite and secondary calcite. Abbreviations: Act: actinolite; Mag: magnetite; Bt: biotite; Ilm: Ilmenite; Qz: Quartz; Cal: Calcite; Pl: Plagioclase; Kfs: K-feldspar; Py: pyrite; Chl: chlorite.

SBIF is dark grey, medium- to coarse-grained, and massive to highly strained; it is mainly composed of magnetite and quartz (Figure 6d). In thin sections, the rock shows a mylonitic and granoblastic heterogranular microstructure (Figure 6e), consisting of magnetite (60 vol.%), quartz (20 vol.%), amphibole (10 vol.%), plagioclase (2 vol.%), ilmenite (2 vol.%), biotite (2 vol.%), chlorite (3 vol.%), calcite (1 vol.%), and K-feldspar (<1 vol.%). Magnetite is found as anhedral and coarse crystals, though very few euhedral grains are also present (Figure 6e). It contains several cavities and is occasionally associated with ilmenite (Figure 6f). Where magnetite crystals lack cavities, quartz is found as minute inclusions in magnetite. Quartz is anhedral, generally coarse-grained, and associated with magnetite and amphibole. Plagioclase and K-feldspar are anhedral, medium- to coarse-grained, and generally altered to sericite. Amphibole occurs as tremolite and actinolite. It is anhedral, coarse-grained ( $1 \times 1.5$  mm), and generally altered into chlorite (Figure 6f). Biotite is anhedral, fine- to medium-grained, and associated with plagioclase, K-feldspar, quartz, and, to a lesser extent, magnetite. Calcite is anhedral and is generally found at the rims of magnetite crystals (Figure 6f).

### 5.1.3. Mineralogy of IFs

The mineralogy of the Anyouzok BIFs investigated by the XRD method (Figure 7a) is simple, with main mineral peaks consisting of magnetite (2.53 Å), hematite (1.49 Å), quartz (2.34 Å), biotite (10.10 Å), pyrite (2.42 Å), and tremolite (6.37 Å). Like the BIFs, the SBIFs (Figure 7b) present a similar mineralogy, with peaks of magnetite (2.53 Å), hematite (1.49 Å), quartz (3.34 Å), biotite (10.10 Å), pyrite (2.42 Å), and tremolite (2.70 Å). In addition, peaks of secondary minerals not detected in BIF, such as calcite (2.29 Å) and chlorite (7.07 Å), are also detected.

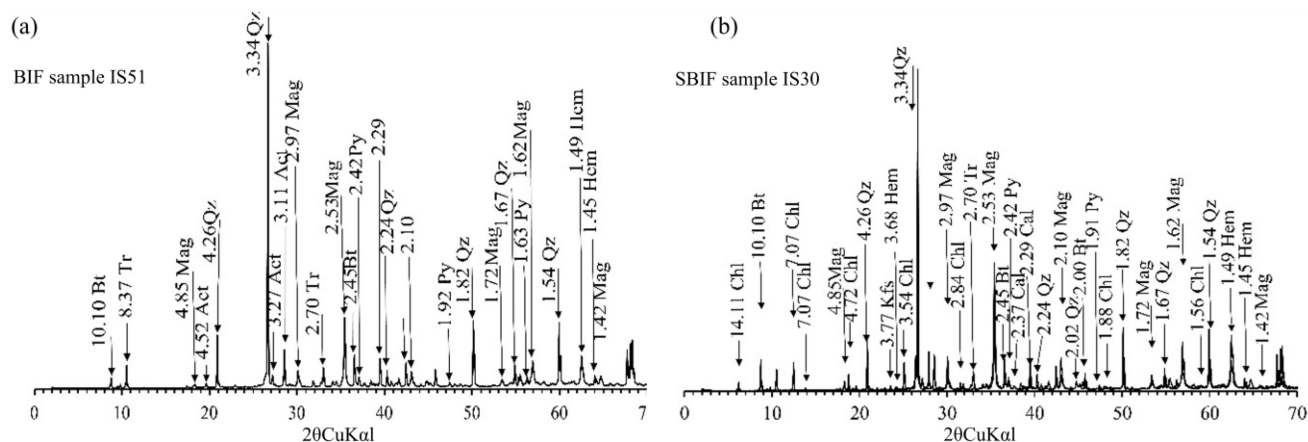


**Figure 7.** X-ray diffraction spectra for the Anyouzok BIF (a) and SBIF (b) samples, indicating prominent quartz and magnetite peaks. Magnetite (Mag), biotite (Bt), hematite (Hem), quartz (Qz), chlorite (Chl), tremolite (Tr), actinolite (Act), pyrite (Py), Calcite (Cal).

### 5.2. Geochemistry

Whole rock geochemical compositions of the Anyouzok metavolcanic rocks and interbedded IFs are presented in Tables 1 and 2, respectively.

**Table 1.** Major elements (wt%) and trace elements (ppm) compositions of the Anyouzok metavolcanic rocks.

Rock Type	Mafic Granulite						Garnet Amphibolite				
Major Elements	IS20	IS40	IS26	IS17	IS15b	IS24	IS27b	IS28	IS33	IS37	IS39
SiO <sub>2</sub>	44.70	48.80	50.60	51.20	44.10	44.80	49.30	46.50	49.10	50.80	46.50
TiO <sub>2</sub>	0.57	0.90	2.24	1.77	1.84	0.64	1.37	1.46	1.34	0.99	0.77
Al <sub>2</sub> O <sub>3</sub>	14.25	14.75	11.95	13.50	12.90	14.05	13.20	14.35	12.05	13.30	13.65

Table 1. Cont.

Rock Type		Mafic Granulite					Garnet Amphibolite				
Major Elements	IS20	IS40	IS26	IS17	IS15b	IS24	IS27b	IS28	IS33	IS37	IS39
Fe <sub>2</sub> O <sub>3</sub>	14.65	16.60	21.50	18.15	18.10	12.25	17.45	15.80	18.60	16.45	14.25
MgO	9.91	5.92	4.01	5.07	7.72	11.30	6.28	8.99	5.50	6.37	11.40
MnO	0.21	0.27	0.25	0.22	0.26	0.17	0.21	0.20	0.22	0.21	0.20
CaO	13.95	8.28	7.82	8.14	11.85	13.25	9.31	7.73	9.37	8.65	9.33
Na <sub>2</sub> O	1.70	1.48	0.41	1.16	1.25	1.70	1.06	2.04	1.58	1.15	1.73
K <sub>2</sub> O	0.29	0.55	0.07	0.48	0.53	0.54	0.43	0.75	0.45	0.57	0.91
Cr <sub>2</sub> O <sub>3</sub>	0.07	0.01	<0.01	0.01	0.02	0.06	0.01	0.02	0.02	0.02	0.12
P <sub>2</sub> O <sub>5</sub>	0.05	0.32	0.25	0.22	0.30	0.05	0.13	0.18	0.19	0.17	0.06
LOI	0.04	1.02	−0.97	0.05	0.38	0.49	−0.15	2.21	0.17	0.41	1.71
Total	100.39	98.92	98.13	99.98	99.26	99.30	98.61	100.24	98.60	99.10	100.65
mg#	57.27	41.40	26.98	35.62	45.80	64.63	41.62	52.99	36.94	43.41	61.31
K <sub>2</sub> O/Na <sub>2</sub> O	0.17	0.37	0.17	0.41	0.42	0.32	0.41	0.37	0.28	0.50	0.53
Trace and rare earth elements											
Cr	460.00	100.00	20.00	80.00	150.00	440.00	80.00	120.00	130.00	100.00	820.00
Sn	1.00	1.00	2.00	1.00	1.00	1.00	1.00	1.00	1.00	1.00	1.00
V	361.00	287.00	392.00	391.00	475.00	258.00	429.00	392.00	242.00	338.00	231.00
Ba	24.10	82.60	6.00	103.50	90.80	31.60	63.60	126.50	52.80	53.80	70.80
Rb	2.50	7.30	1.20	15.00	8.90	2.90	7.50	10.00	9.10	5.30	10.60
Ga	16.80	13.70	18.70	15.00	18.80	13.30	16.90	18.40	18.70	14.10	16.30
Cs	0.02	0.17	0.05	0.65	0.44	0.01	0.30	0.18	0.12	0.07	0.31
Th	0.15	0.93	1.33	1.64	<0.5	0.07	0.40	0.16	0.69	0.50	0.44
U	0.10	0.51	0.31	2.63	0.24	0.08	0.24	0.27	0.27	0.35	0.31
Sr	48.40	86.40	20.70	62.10	69.50	37.50	32.30	53.10	57.00	38.60	40.70
Nb	0.60	3.70	6.90	6.60	6.60	1.30	4.70	4.70	6.30	3.10	3.00
Ta	<0.1	0.30	0.30	0.30	0.30	<0.1	0.30	0.20	9.70	<0.1	0.10
Hf	1.30	1.80	4.80	3.80	3.40	1.10	2.60	2.80	3.80	2.40	2.50
Zr	37.00	76.00	176.00	140.00	115.00	34.00	91.00	103.00	125.00	87.00	94.00
Y	16.70	36.10	53.10	39.20	34.20	16.20	31.50	35.10	37.80	29.40	22.50
La	2.10	7.00	9.80	8.70	6.60	2.10	4.60	7.30	6.60	5.10	4.00
Ce	6.80	16.30	26.10	20.90	19.50	6.00	13.20	21.30	18.10	13.40	10.00
Pr	1.19	2.43	3.51	2.82	2.97	0.93	2.09	3.24	2.68	1.87	1.54
Nd	7.30	11.30	18.00	14.60	15.00	4.80	10.80	17.10	14.50	9.20	7.10
Sm	2.58	3.19	5.78	4.35	4.37	1.63	3.77	5.19	4.04	2.80	2.19
Eu	0.89	1.14	1.89	1.59	1.54	0.69	1.49	1.50	1.56	0.99	0.64
Gd	2.62	4.07	8.14	6.14	5.11	2.30	4.97	5.63	5.99	3.69	2.72
Tb	0.43	0.81	1.48	1.07	0.88	0.41	0.84	0.93	1.03	0.69	0.56
Dy	3.14	5.49	9.93	7.80	6.44	2.86	5.74	6.33	6.88	5.20	3.66
Ho	0.64	1.29	2.06	1.49	1.29	0.63	1.27	1.30	1.42	1.15	0.76
Er	1.98	3.84	6.28	4.50	4.08	2.17	3.77	3.77	4.45	3.71	2.44
Tm	0.24	0.59	0.77	0.62	0.50	0.26	0.50	0.49	0.56	0.42	0.34
Yb	1.85	4.01	6.15	4.24	3.99	2.03	3.58	3.84	4.54	3.45	2.89
Lu	0.25	0.65	0.85	0.63	0.56	0.29	0.52	0.52	0.60	0.51	0.47
ΣREE	32.01	62.11	100.74	79.45	72.83	27.10	57.14	78.44	72.95	52.18	39.31
(La/Yb) <sub>CN</sub>	0.77	1.19	1.08	1.39	1.12	0.70	0.87	1.29	0.99	1.00	0.94
(La/Sm) <sub>CN</sub>	0.51	1.37	1.06	1.25	0.94	0.80	0.76	0.88	1.02	1.14	1.14
(Gd/Yb) <sub>CN</sub>	1.15	0.82	1.07	1.17	1.04	0.92	1.12	1.19	1.07	0.87	0.76
(Eu/Eu*) <sub>CN</sub>	1.04	0.96	0.84	0.94	0.99	1.09	1.05	0.85	0.97	0.94	0.80
(Ce/Ce*) <sub>CN</sub>	1.04	0.96	1.08	1.02	1.07	1.04	1.03	1.06	1.04	1.05	0.97
Th/Nb	0.25	0.25	0.19	0.25	0.00	0.05	0.09	0.03	0.11	0.16	0.15
Nb/Y	0.04	0.10	0.13	0.17	0.19	0.08	0.15	0.13	0.17	0.11	0.13
La/Nb	3.50	1.89	1.42	1.32	1.00	1.62	0.98	1.55	1.05	1.65	1.33
Dy/Yb	1.70	1.37	1.61	1.84	1.61	1.41	1.60	1.65	1.52	1.51	1.27
Zr/Nb	61.67	20.54	25.51	21.21	17.42	26.15	19.36	21.91	19.84	28.06	31.33
Zr/Hf	28.46	42.22	36.67	36.84	33.82	30.91	35.00	36.79	32.89	36.25	37.60
Th/Yb	0.08	0.23	0.22	0.39	0.01	0.03	0.11	0.04	0.15	0.14	0.15



**Table 2.** Major elements (wt%) and trace elements (ppm) compositions of the Anyouzok Iron formations.

Rock Type	BIF						SBIF		
Major Elements	IS13	IS50	IS51	IS52	IS18	IS19	IS35	IS41	IS54
SiO <sub>2</sub>	44.40	60.78	59.02	59.45	43.70	43.50	43.30	45.70	47.26
TiO <sub>2</sub>	0.12	0.07	0.07	0.05	0.01	0.04	0.03	0.08	<0.01
Al <sub>2</sub> O <sub>3</sub>	1.83	2.37	2.52	1.84	0.26	0.94	0.70	0.99	0.74
Fe <sub>2</sub> O <sub>3</sub>	48.40	26.37	26.05	27.68	55.20	51.30	53.20	50.20	49.60
MgO	2.55	5.27	5.98	5.73	1.94	1.94	2.08	2.21	1.82
MnO	0.04	0.40	0.46	0.46	0.03	0.04	0.03	0.04	0.05
CaO	1.46	2.44	3.39	2.76	1.16	1.10	1.03	0.75	1.10
Na <sub>2</sub> O	0.52	0.14	0.18	0.10	0.04	0.27	0.10	0.01	0.20
K <sub>2</sub> O	0.47	1.16	1.20	0.84	0.06	0.40	0.08	0.03	0.32
Cr <sub>2</sub> O <sub>3</sub>	0.01	0.00	0.00	0.00	<0.01	0.01	0.01	0.01	0.00
P <sub>2</sub> O <sub>5</sub>	0.12	0.09	0.07	0.09	0.09	0.16	0.14	0.11	0.10
LOI	−0.69	0.80	0.90	0.90	−1.32	−1.20	−0.88	−0.58	−1.30
Total	99.24	99.88	99.87	99.87	101.17	98.51	99.82	99.56	99.96
Fe	33.88	18.46	18.24	19.38	38.64	35.91	37.24	35.14	34.72
Fe/Si	1.63	0.65	0.66	0.70	1.89	1.77	1.84	1.65	1.57
Trace and rare earth elements									
Sn	<1	<1	<1	<1	<1	<1	<1	<1	<1
V	28.00	<8	<8	<8	6.00	13.00	9.00	32.00	<8
Ba	66.10	71.00	74.00	39.00	9.70	134.00	5.10	3.80	74.00
Rb	23.60	85.40	88.00	54.50	2.80	33.70	3.40	1.90	15.90
Ga	3.50	1.50	2.40	1.40	0.50	1.90	1.00	3.40	3.60
Cs	0.77	8.70	8.70	4.40	0.07	0.88	0.10	0.14	0.40
Th	1.23	1.50	1.30	1.10	0.05	<0.05	0.13	0.16	<0.2
U	0.32	0.30	0.30	0.20	0.10	0.08	0.38	0.09	0.10
Sr	10.50	8.90	11.50	6.60	7.10	20.70	5.00	5.30	15.00
Nb	1.00	0.50	0.60	0.40	0.20	0.40	1.00	0.70	<0.1
Ta	<0.1	<0.1	<0.1	<0.1	<0.1	<0.1	0.10	<0.1	<0.1
Hf	0.50	0.40	0.50	0.30	0.20	0.20	0.20	0.20	0.10
Zr	18.00	17.00	16.90	12.40	4.00	7.00	7.00	5.00	3.70
Y	9.10	6.60	7.50	6.80	5.80	7.20	5.90	5.50	6.90
La	6.00	6.80	6.50	6.20	1.70	2.50	1.40	3.70	3.20
Ce	11.40	12.70	12.50	12.00	3.50	5.90	3.50	7.20	5.30
Pr	1.29	1.36	1.31	1.36	0.43	0.74	0.44	0.92	0.62
Nd	5.00	5.30	5.20	5.40	1.80	3.10	2.30	3.10	2.70
Sm	1.15	1.00	1.08	0.98	0.44	0.71	0.54	0.84	0.54
Eu	0.66	0.45	0.45	0.45	0.36	0.47	0.36	0.38	0.35
Gd	1.27	1.19	1.16	1.10	0.70	0.95	0.74	0.69	0.87
Tb	0.17	0.18	0.18	0.17	0.10	0.13	0.11	0.12	0.12
Dy	1.43	1.05	1.04	1.14	0.86	1.02	0.89	0.75	0.76
Ho	0.30	0.25	0.26	0.24	0.20	0.22	0.17	0.20	0.18
Er	0.93	0.74	0.79	0.70	0.59	0.64	0.56	0.43	0.55
Tm	0.09	0.10	0.11	0.10	0.05	0.05	0.05	0.07	0.08
Yb	0.81	0.74	0.82	0.68	0.66	0.66	0.56	0.41	0.51
Lu	0.09	0.11	0.13	0.11	0.06	0.04	0.04	0.09	0.08
ΣREE-Y	39.69	38.57	39.03	37.43	17.25	24.33	17.56	24.40	22.76
(Eu/Eu*) <sub>SN</sub>	2.68	1.94	1.86	2.01	3.17	2.83	2.72	2.14	2.54
(Ce/Ce*) <sub>SN</sub>	0.94	0.96	0.99	0.95	0.94	0.99	1.02	0.90	0.86
(La/La*) <sub>SN</sub>	1.10	1.19	1.23	1.13	1.12	0.96	2.66	0.75	1.63
(Gd/Gd*) <sub>SN</sub>	1.35	1.26	1.21	1.22	1.41	1.40	1.32	1.03	1.45
(Y/Y*) <sub>SN</sub>	0.86	0.80	0.89	0.81	0.87	0.94	0.94	0.88	1.16
(Pr/Pr*) <sub>SN</sub>	1.01	0.98	0.96	0.99	1.00	1.01	0.89	1.15	0.96
(Eu/Eu*) <sub>CN</sub>	1.66	1.26	1.23	1.32	1.98	1.74	1.74	1.52	1.56
(Eu/Eu*) <sub>NASC</sub>	2.70	1.97	1.88	2.04	3.26	2.88	2.78	2.16	2.61
Y/Ho	30.33	26.40	28.85	28.33	29.00	32.73	34.71	27.50	38.33
Pr/Yb	1.59	1.84	1.60	2.00	0.65	1.12	0.79	2.24	1.22
Th/U	3.84	5.00	4.33	5.50	0.50	0.31	0.34	1.78	1.00

### 5.2.1. Metavolcanic Rocks

#### Major elements

The metavolcanic samples present wide compositional variations in their major elements (Table 1), such as SiO<sub>2</sub> (44.7–1.2 wt%; 44.1–50.8 wt%), Fe<sub>2</sub>O<sub>3</sub> (14.65–21.5 wt%; 12.25–18.6 wt%), MgO (4.01–9.91 wt%; 5.5–11.4 wt%), and CaO (7.82–13.95 wt%; 7.73–13.25 wt%) for mafic granulite and garnet amphibolite, respectively. The analyzed samples show low to moderate contents in Al<sub>2</sub>O<sub>3</sub> (11.95–14.75 wt%; 12.05–14.35 wt%), TiO<sub>2</sub> (0.57–2.24 wt%; 0.64–1.84 wt%), MnO (0.21–0.27 wt%; 0.17–0.26 wt%), P<sub>2</sub>O<sub>5</sub> (0.05–0.32 wt%; 0.05–0.30 wt%), and Cr<sub>2</sub>O<sub>3</sub> (<0.01–0.07 wt%; 0.01–0.12 wt%). Na<sub>2</sub>O (0.41–1.7 wt%; 1.15–2.04 wt%) contents are higher than K<sub>2</sub>O (0.07–0.55 wt%; 0.43–0.91 wt%) contents in both rock types, yielding to low K<sub>2</sub>O/Na<sub>2</sub>O ratios (0.17–0.41; 0.28–0.53). LOI values range from −0.97 to 1.02 wt% and −0.15 to 2.21 wt% for mafic granulite and garnet amphibolite, respectively.

#### Trace and rare earth elements (REE)

Except for Zr (37–176 ppm; 34–125 ppm) and Y (16.7–53.1 ppm; 16.2–37.8 ppm), the high field strength elements (HFSEs) in mafic granulite and garnet amphibolite samples are generally low, <10 ppm (Table 1). Large ion lithophile elements (LILEs) such as Rb (1.2–15 ppm; 2.9–10.6 ppm) show very low concentrations, whereas Sr (20.7–86.4 ppm; 32.3–69.5 ppm) and Ba (6–103.5 ppm; 31.6–126.5 ppm) show slightly higher values. Cr contents range from 20 to 460 ppm and from 80 to 820 ppm in mafic granulite and garnet amphibolite, respectively.

REE contents are variable and higher in mafic granulite samples ( $\Sigma$ REE: 32.01–100.74 ppm) compared to garnet amphibolite ( $\Sigma$ REE: 27.1–78.44 ppm). Chondrite-normalized [55] REE diagrams show homogeneous and coherent patterns for most of the analyzed samples, comparable to both NMORB and EMORB (Figure 8a,c). The Nyong Complex mafic granulites from Kribi [31] and Bipindi [11] and the Nyong Complex garnet amphibolites from Akom II [22] are plotted for comparison. Both the Anyouzok mafic granulite and garnet amphibolite samples, as well as the Nyong Complex mafic granulite samples, show relatively flat patterns ((La/Yb)<sub>CN</sub> = 0.77–1.39; 0.70–1.29 for mafic granulite and garnet amphibolite, respectively) (Figure 8a,c). In contrast, the Nyong Complex garnet amphibolite patterns are more fractionated, with LREE enriched over the HREE. The Anyouzok samples generally present slightly negative to no Eu anomalies ((Eu/Eu\*)<sub>CN</sub> = 0.84–1.04; 0.80–1.09) and exhibit no Ce anomalies (Ce/Ce\*: 0.96–1.08; 0.97–1.07) compared to the Nyong Complex mafic granulite and garnet amphibolite. Primitive mantle-normalized [52] multi-element diagrams (Figure 8b,d) show peaks in K and U and troughs in Nb, Ta, Sr, and Ti for mafic granulite samples and in Th, Nb, Ta, and Sr for garnet amphibolite samples.

### 5.2.2. Iron Formations

#### Major elements

The major element compositions of the Anyouzok IFs show that SiO<sub>2</sub> and Fe<sub>2</sub>O<sub>3</sub> are the main constituents, representing ca 96 wt% of the bulk composition of SBIFs and ca 87 wt% of BIFs (Table 2). BIFs show higher SiO<sub>2</sub> (44.4–60.78 wt%) and lower Fe<sub>2</sub>O<sub>3</sub> (26.05–48.40 wt%) contents, while SBIFs show lower SiO<sub>2</sub> (43.3–47.26 wt%) and higher Fe<sub>2</sub>O<sub>3</sub> (49.6–55.2 wt%) contents. Likewise, MgO (2.55–5.98 wt%), CaO (1.46–3.39 wt%), Al<sub>2</sub>O<sub>3</sub> (1.83–2.52 wt%), MnO (0.04–0.46 wt%), TiO<sub>2</sub> (0.05–0.12 wt%), and K<sub>2</sub>O (0.47–1.2 wt%) are of higher contents in BIFs than in SBIFs (MgO: 1.82–2.21 wt%; CaO: 0.75–1.16 wt%; Al<sub>2</sub>O<sub>3</sub>: 0.26–0.99 wt%; MnO: 0.03–0.05 wt%; TiO<sub>2</sub>: 0.01–0.08 wt%; K<sub>2</sub>O: 0.03–0.08 wt%). P<sub>2</sub>O<sub>5</sub> concentrations have a narrow range for both IF types, ranging from 0.07–0.12 wt% and from 0.09–0.16 wt% for BIFs and SBIFs, respectively. LOI values range from −0.69 to 0.9 wt% in BIFs and from −1.32 to −0.58 wt% in SBIFs.

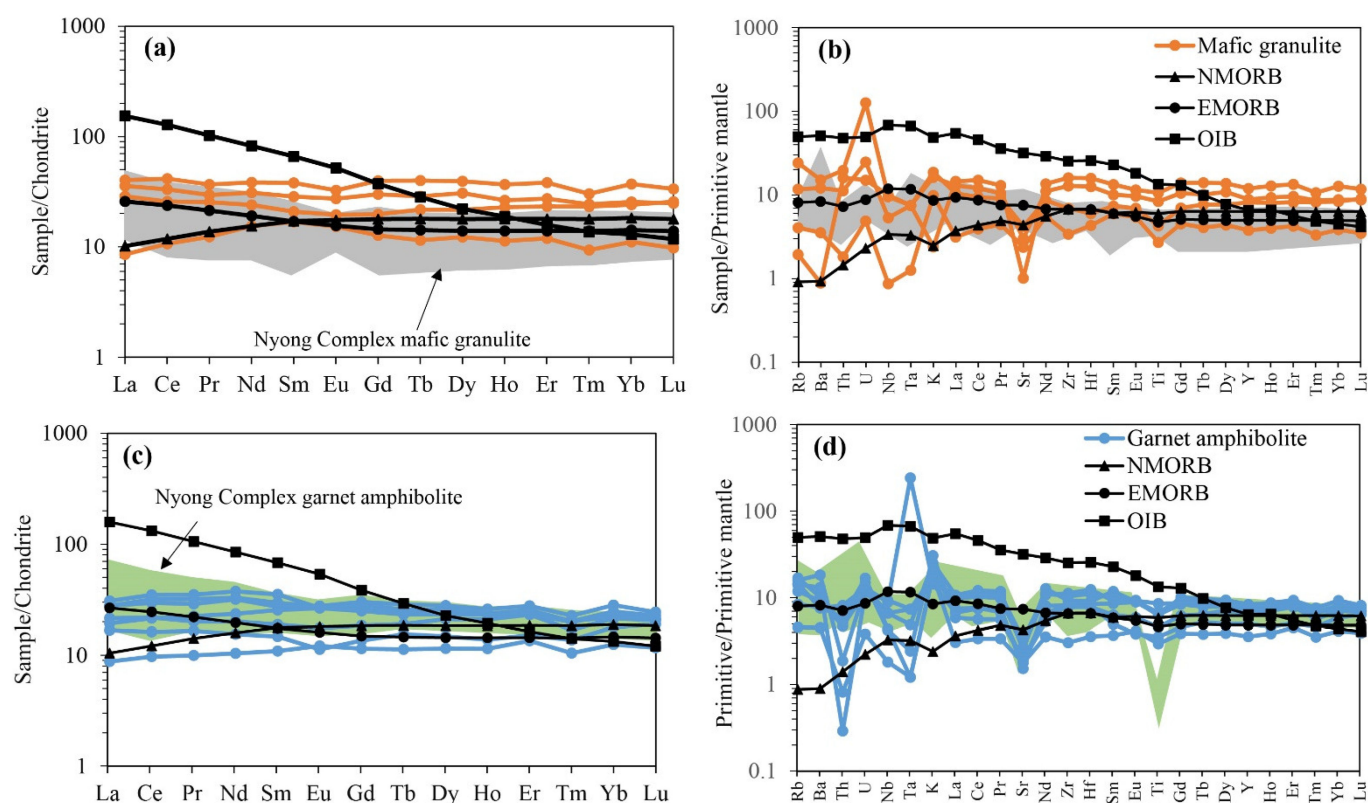


**Figure 8.** (a,c) Chondrite-normalized (normalization values after [55] REE plots for the Anyouzok mafic granulite and garnet amphibolite, respectively); (b,d) primitive mantle-normalized (normalization values after [52] multielement diagrams for the Anyouzok mafic granulite and garnet amphibolite, respectively). Nyong Complex mafic granulite data are from [11,31]. Nyong Complex garnet amphibolite data are from [22].

#### Trace and rare earth elements

The Anyouzok IFs generally show low trace element contents, <10 ppm. However, relatively high values are observed in some LILEs, such as Sr (6.6–11.5 ppm; 5.0–20.7 ppm), Rb (23.6–88 ppm; 2.8–33.7 ppm), and Ba (39–74 ppm; 3.8–134 ppm) contents for BIFs and SBIFs, respectively. HFSEs such as Zr (12.4–18 ppm; 3.7–7 ppm) and Th (1.1–1.5 ppm; <0.05–0.16 ppm) present higher contents in BIFs compared to SBIFs, respectively.

The total REE-Y concentrations are higher for BIFs (37.43–39.69 ppm) compared to SBIFs (17.25–24.4 ppm). The chondrite-normalized [55] plot shows homogenous patterns with LREE enrichment over the HREE (Figure 9a) and positive Eu anomalies ( $(\text{Eu}/\text{Eu}^*)_{\text{CN}}$ ) ranging from 1.23 to 1.66 and from 1.52 to 1.98 for BIFs and SBIFs, respectively. PAAS-normalized REE-Y plots (normalization after [53]) are consistent for both BIFs and SBIFs (Figure 9b). Heavy rare earth elements (HREE) are enriched over light rare earth elements (LREE) with prominent positive Eu anomalies  $(\text{Eu}/\text{Eu}^*)_{\text{SN}}$  ranging from 1.86 to 2.68 in BIFs and from 2.14 to 3.17 in SBIFs. Y/Ho ratios range from 26.4 to 30.33 for BIFs and from 27.50 to 38.33 for SBIFs. Pr/Yb ratios vary between 1.22 and 2 and between 0.65 and 2.24 for BIFs and SBIFs, respectively. BIFs show positive La  $((\text{La}/\text{La}^*)_{\text{SN}} = 1.1\text{--}1.23)$  and Gd  $((\text{Gd}/\text{Gd}^*)_{\text{SN}} = 1.21\text{--}1.35)$  anomalies, whereas the SBIFs display positive Gd  $((\text{Gd}/\text{Gd}^*)_{\text{SN}} = 1.03\text{--}1.45)$  and positive to negative La  $((\text{La}/\text{La}^*)_{\text{SN}} = 0.75\text{--}2.66)$  anomalies. Except for one SBIF sample (IS54), all the analyzed IFs present negative Y anomalies  $((\text{Y}/\text{Y}^*)_{\text{SN}} = 0.80\text{--}0.89)$  and  $0.87\text{--}0.94)$ .

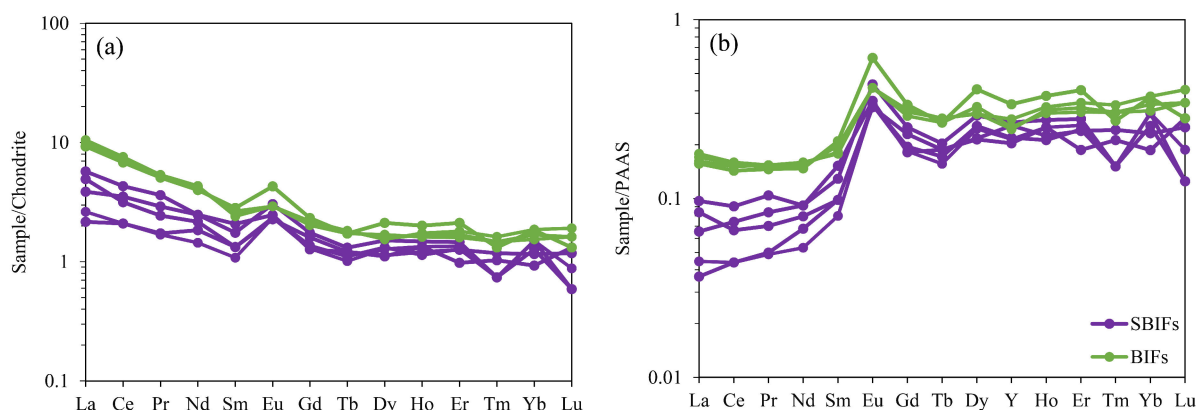


**Figure 9.** Chondrite—(a) and (b) PAAS-normalized REE-Y of the Anyouzok iron formations (BIFs and SBIFs). Normalization values after [53,55].

## 6. Discussion

### 6.1. Alteration, Metamorphism, and Element Mobility Assessment

Most Precambrian rocks have been affected by processes such as metamorphism, metasomatism, and deformation, which tend to modify their primary geochemical features [56–59]. In the current study, field investigations combined with petrographic and geochemical studies show that the rocks from the Anyouzok deposit have been subjected to some deformation, high-grade metamorphism, and alteration. Similar processes are widely reported within the whole Nyong Complex [11,12,20,24–26,28,30,31,60]. In this regard, the effects of post-emplacement processes on the mobility of major, trace, and rare earth elements should be assessed before any petrogenetic and geodynamic interpretations.

#### 6.1.1. Effects on Metavolcanic Rocks

The Anyouzok metavolcanic rocks have experienced high-grade metamorphism and some alteration, as reflected by the retrograde transformation of pyroxene into amphibole (Figure 5c) and the occurrence of secondary sericite and chlorite (Figure 5b,f). However, they mainly show low LOI (mean: 0.37 wt% and 0.90 wt% for mafic granulite and garnet amphibolite samples, respectively), indicating insignificant hydration or alteration during post-igneous processes, except for one mafic granulite sample (IS26 (LOI: −0.97 wt%)) and one garnet amphibolite sample (IS27b (LOI: −0.15 wt%)). The degrees of alteration of the analyzed metavolcanic rock samples were quantified using the chlorite-carbonate-pyrite index (CCPI; [61]) and the Ishikawa alteration index (AI; [62]). The analyzed rocks show relatively low AI (33.14–39.86 and 35.21–52.67) and moderate CCPI (50.53–67.51 and 52.88–71.00) for mafic granulite and garnet amphibolite, respectively, indicating minor to moderate alteration. In the CCPI vs AI diagram (Figure 10), the overall samples plot within the least altered box for mafic to felsic rocks, although some samples follow the chlorite-pyrite-(sericite) alteration trend, which also suggests some degrees of alteration and weak compositional modification of the major elements. Polat et al. [56] proposed that metavolcanic rock samples with  $0.90 < \text{Ce}/\text{Ce}^* < 1.10$  lack LREE mobility, while samples with  $0.90 > \text{Ce}/\text{Ce}^* > 1.10$  had undergone high LREE mobility. In the case of the Anyouzok metavolcanic rocks, Ce anomalies range from 0.96 to 1.08 and from 0.97 to 1.07, respectively, for mafic granulite and garnet amphibolite (Table 1), consistent with LREE immobility [56]. Furthermore, according to these previous authors, a positive correlation between Zr and other elements suggests the lack of mobility of these elements via alteration, since Zr is generally considered to be immobile. The analyzed samples show positive correlations with REEs (such as La, Ce, Sm, Eu, Gd, Dy, and Yb; not shown) and HFSEs (such as Nb, Y, and Hf; not shown) and scattered data points with some LILEs (such as Ba and Rb; not shown). In addition, their REE and HFSE patterns (Figure 8) are generally homogeneous and coherent, suggesting insignificant mobility during post-igneous metamorphism and

alteration. Therefore, immobile elements were considered to depict the igneous affinities, petrogenesis, and tectonic setting of the investigated metavolcanic rocks.

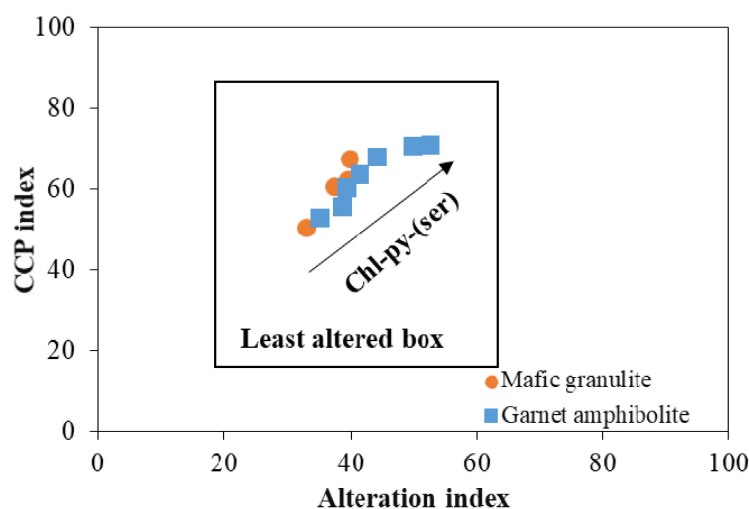


**Figure 10.** Alteration box plot [61] for the Anyouzok metavolcanic rocks. Overall samples fall within the least altered box and follow the chlorite alteration trend.

#### 6.1.2. Effects on IFs

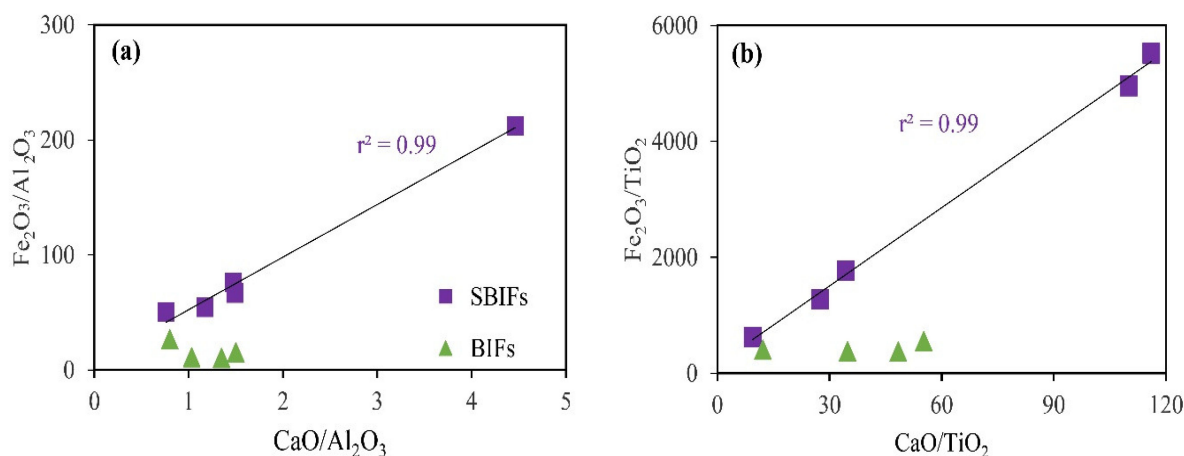
The effects of hydrothermal alteration on BIFs within the Nyong Complex have been recently reported by a few authors [27,29]. Polished thin section observations of the Anyouzok IFs revealed secondary minerals such as calcite, pyrite, hematite, and chlorite (Figure 6c,e). These secondary minerals are mainly encountered in SBIFs, which have experienced shearing, but are less obvious in BIFs. Geochemical data present a general increase in  $\text{Fe}_2\text{O}_3$  and a decrease in  $\text{SiO}_2$  within the SBIFs, in contrast to BIFs (except for sample IS13), resulting in the increase in Fe/Si ratios from 0.67 in BIFs to 1.72 in SBIFs. Moreover, the SBIFs matrix presents numerous cavities (Figure 6f), which are most likely a result of the leaching of silica [2]. Therefore, the ubiquitous shearing that affected the Anyouzok SBIFs may have created paths for fluid circulation, facilitating hydrothermal alteration and leaching processes. The formation of Ca-bearing minerals such as calcite or epidote are generally linked with hydrothermal alteration [10]. In this view, these authors proposed the use of  $\text{Fe}_2\text{O}_3/\text{Al}_2\text{O}_3$  vs.  $\text{CaO}/\text{Al}_2\text{O}_3$  and  $\text{Fe}_2\text{O}_3/\text{TiO}_2$  vs.  $\text{CaO}/\text{TiO}_2$  binary diagrams to assess the effect of hydrothermal alteration. In these diagrams (Figure 11), the SBIF samples show strong positive correlations ( $r^2 = 0.99$ ), suggesting that the increase in  $\text{Fe}_2\text{O}_3$  concentrations is linked with hydrothermal alteration. In contrast, such correlations are not observed in BIFs. In addition, PAAS-normalized REE-Y patterns of the investigated IFs (Figure 9b) exhibit prominent positive Eu anomalies and HREE enrichment over LREE, comparable to many Archean to Paleoproterozoic IFs worldwide [6,8,10,15,54,60,63], suggesting that most samples kept their primary REE-Y systematics. Based on the above discussion, we suggest that BIFs are more reliable in determining the characteristics of the Anyouzok IFs during their deposition, while SBIFs characteristics should be used with caution.

#### 6.2. Petrogenesis of the Metavolcanic Rocks

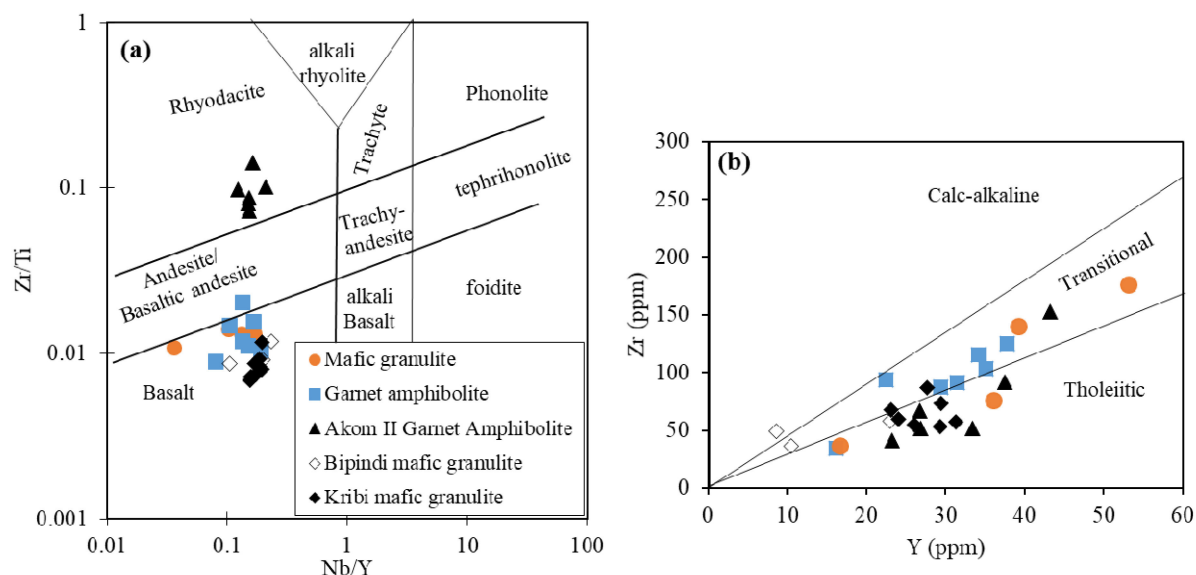
Considering previous investigations on the geochemical features of metabasic rocks within the Nyong Complex greenstone belts [11,28,30,31,37,64], it is suggested in the current study that the Anyouzok metabasic rocks are of volcanic origin. In the Zr/Ti vs. Nb/Y plot [65], all the Anyouzok metavolcanic rock samples, along with the Kribi and Bipindi mafic granulites, show basaltic compositions (Figure 12a). In contrast, the Akom II garnet amphibolites show more evolved compositions and fall in the rhyodacitic rocks field. The Anyouzok metavolcanic rock samples mainly show flat patterns in chondrite-normalized REE diagrams (Figure 8a,c), suggesting that they are of the tholeiitic series. In the Zr vs. Y



diagram (Figure 12b; [66]), their data points show tholeiitic to transitional affinities, similar to the Kribi and Bipindi mafic granulites and the Akom II garnet amphibolites.



**Figure 11.** (a)  $\text{Fe}_2\text{O}_3/\text{Al}_2\text{O}_3$  vs.  $\text{CaO}/\text{Al}_2\text{O}_3$  and (b)  $\text{Fe}_2\text{O}_3/\text{TiO}_2$  vs.  $\text{CaO}/\text{TiO}_2$  binary plots [10]; hydrothermal alteration effect on the Anyouzok IFs.



**Figure 12.** Classification plots for the Anyouzok metavolcanic rocks: (a)  $\text{Zr}/\text{TiO}_2$  vs.  $\text{Nb}/\text{Y}$  [65]; (b)  $\text{Y}$  vs.  $\text{Zr}$  plot [66].

Mafic to ultramafic source magmas tend to assimilate crustal components during their ascent to the surface, resulting in variable degrees of crustal contamination [67,68]. The extent and nature of this input could be evaluated using elemental concentrations and various ratios, showing different variations in crustal- and mantle-derived materials [52,67–70]. For instance, the troughs in Nb and Ta exhibited by most analyzed samples in multi-element diagrams (Figure 8b,d) suggest crustal input [67–69]. The  $\text{Th}/\text{Nb}$  (0.19–0.36; mean: 0.24 and 0.004–0.16; mean: 0.08 for mafic granulite and garnet amphibolite, respectively) and  $\text{Nb}/\text{Y}$  (0.036–0.17; mean: 0.11 and 0.08–0.19; mean: 0.14 for mafic granulite and garnet amphibolite, respectively) ratios of the analyzed samples are lower than those of UCC ( $\text{Th}/\text{Nb}$ : 0.87;  $\text{Nb}/\text{Y}$ : 0.57; [70]), suggesting insignificant to minor crustal contamination.

The Anyouzok metavolcanic rocks present variable  $\text{MgO}$  (4.01–11.4 wt%) and  $\text{Mg\#}$  (26.98–64.63) contents, suggesting that their precursor primary melts experienced fractional crystallization during magma ascent [71]. This is further supported by the variable Cr contents (20–820 ppm) of the analyzed samples, with values lower than those of mantle-derived melts ( $\text{Cr} > 1000$  ppm; [71]), suggesting some degree of fractional crystallization.



The MgO contents show a wide compositional range within the dataset, which serves as an index of differentiation in the binary plots of mafic rocks [71]. When plotted against MgO, Cr shows a strong positive correlation ( $r^2 = 0.98$ ) and a weak positive correlation ( $r^2 = 0.67$ ) for mafic granulite and garnet amphibolite, respectively (Figure 13a), suggesting a higher degree of clinopyroxene and/or spinel fractionation within mafic granulite samples. CaO decrease with decreasing MgO for the mafic granulite, indicating the fractionation of clinopyroxene (Figure 13b). Such fractionation lacks in garnet amphibolite, as suggested by their scattered data points (Figure 13b), which could be attributed to Ca mobility. Moreover, clinopyroxene fractionation in the mafic granulite samples is also depicted via the increase in  $\text{SiO}_2$  with decreasing MgO (Figure 13c). The chondrite-normalized REE diagrams (Figure 8a,c) show slightly negative to null Eu anomalies ( $(\text{Eu}/\text{Eu}^*)_{\text{CN}} = 0.84\text{--}1.04$  and  $0.80\text{--}1.09$  for mafic granulite and garnet amphibolite, respectively), suggesting minor to no plagioclase fractionation. The troughs in Sr observed in multi-element diagrams (Figure 8b,d) could reflect post-magmatic processes such as alteration or metamorphism. Moreover, the relatively flat chondrite-normalized REE patterns (Figure 8a,c) presented by most samples also suggest minor fractional crystallization. Based on these characteristics, the investigated rocks were plotted in the La/Yb vs. Yb [72] binary diagram (Figure 13d) and indicated that fractional crystallization is subordinate to partial melting in the parental melt genesis.

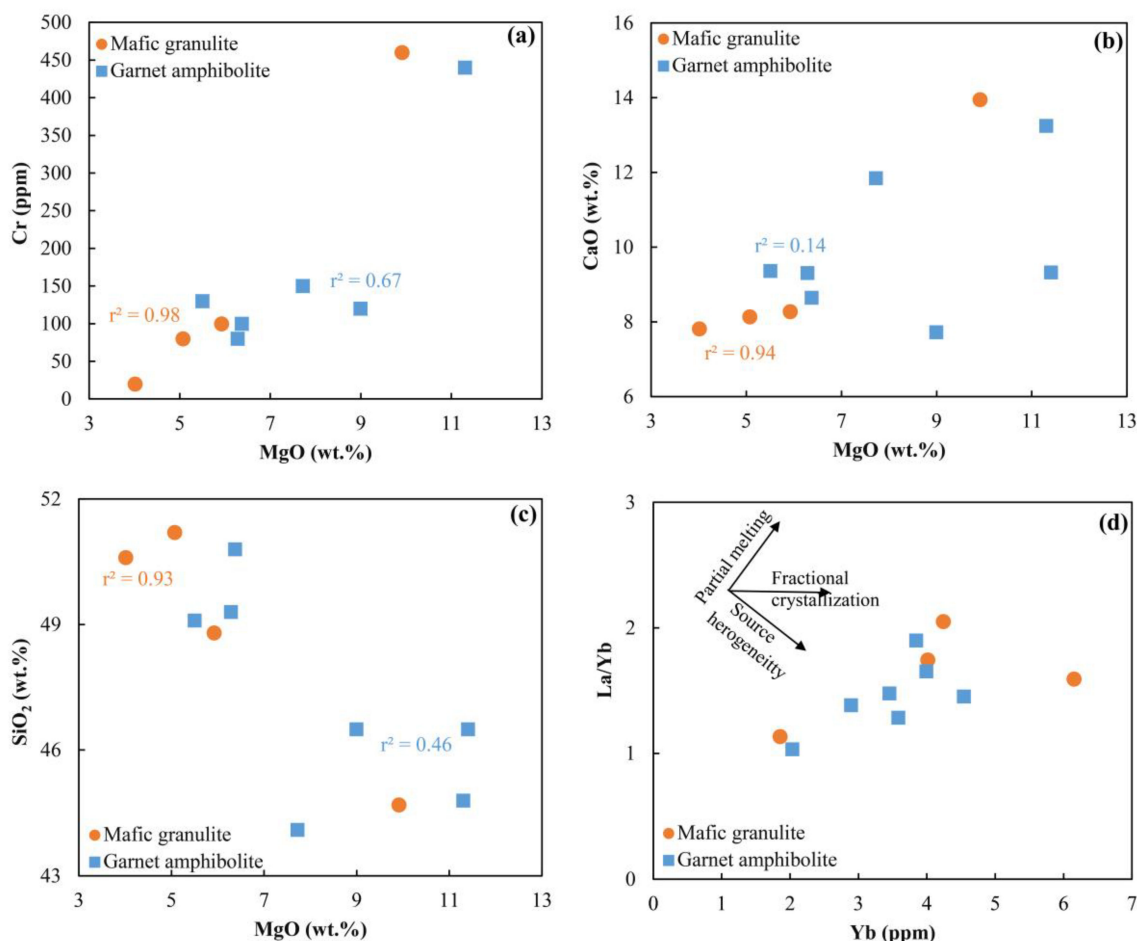


**Figure 13.** Binary plots of (a) Cr vs. MgO; (b) CaO vs. MgO; (c)  $\text{SiO}_2$  vs. MgO; and (d) Yb vs. La/Yb [72].

Compositional variations of REE and HFSE and their elemental ratios generally assist in the depiction of the source and melting conditions of mantle melts [73–76]. For instance, the flat HREE patterns of most analyzed samples (Figure 8a,c), Dy/Yb ( $1.37\text{--}1.84$  and  $1.27\text{--}1.65$ ) and the  $(\text{Gd}/\text{Yd})_{\text{CN}}$  ( $0.82\text{--}1.17$  and  $0.76\text{--}1.19$ ) ratios of the mafic granulite and

garnet amphibolite samples, respectively, point toward a shallow mantle source lacking residual garnet [73,74]. Excluding one mafic granulite sample (IS20), the Zr/Nb (20.54–25.51 and 17.42–31.33) and Zr/Hf (36.67–42.22 and 30.91–37.60) ratios of mafic granulite and garnet amphibolite, respectively, are comparable to the primitive mantle (Zr/Nb = 15.71 and Zr/Hf = 36.25; [52]) and NMORB (Zr/Nb = 31.76 and Zr/Hf = 36.10; [52]), suggesting a depleted mantle source. Moreover, the chondrite-normalized REE diagrams of the Anyouzok metavolcanic rocks show MORB-like patterns (Figure 8a,c), also hinting at source derivation from a depleted mantle.

In the Nb vs. Zr binary diagram proposed by [75], the analyzed samples, similar to the Nyong Complex mafic granulite and garnet amphibolite samples, plot within or close to the depleted mantle source field (Figure 14a). Furthermore, in the Dy/Yb vs. La/Yb diagram (Figure 14b; [73]), the data points mainly indicate ca. 4% partial melting of a spinel-peridotite source, with no residual garnet. Primitive mantle-normalized multi-element diagrams of the Anyouzok metavolcanic rocks present HFSEs (Nb, Ta, Zr, and Ti) depletion for most samples, coupled with relatively high Th/Yb (0.08–0.39; 0.006–0.15) and La/Nb (1.32–3.5; 0.98–1.65) ratios compared to those of depleted mantle (Th/Yb = 0.02 and La/Nb = 1.29; [77]). These features generally reflect the source metasomatism of the precursors by melts or by subduction-related fluids [68,71]. In this view, the analyzed samples were plotted in the Rb/Y vs. Nb/Y [78] diagram (Figure 14c) and show that the mantle source of the Anyouzok metavolcanic rock precursors slightly experienced fluid metasomatism. Based on these geochemical characteristics, it is suggested that the primary melt of the Anyouzok metavolcanic rock protoliths originated from shallow depth partial melting of a slightly metasomatized spinel peridotite source, which has experienced various degrees of fractional crystallization and minor crustal contamination. A comparable origin has been proposed for precursors of metabasic to ultrabasic rocks also occurring within the Nyong Complex [24,30,31].

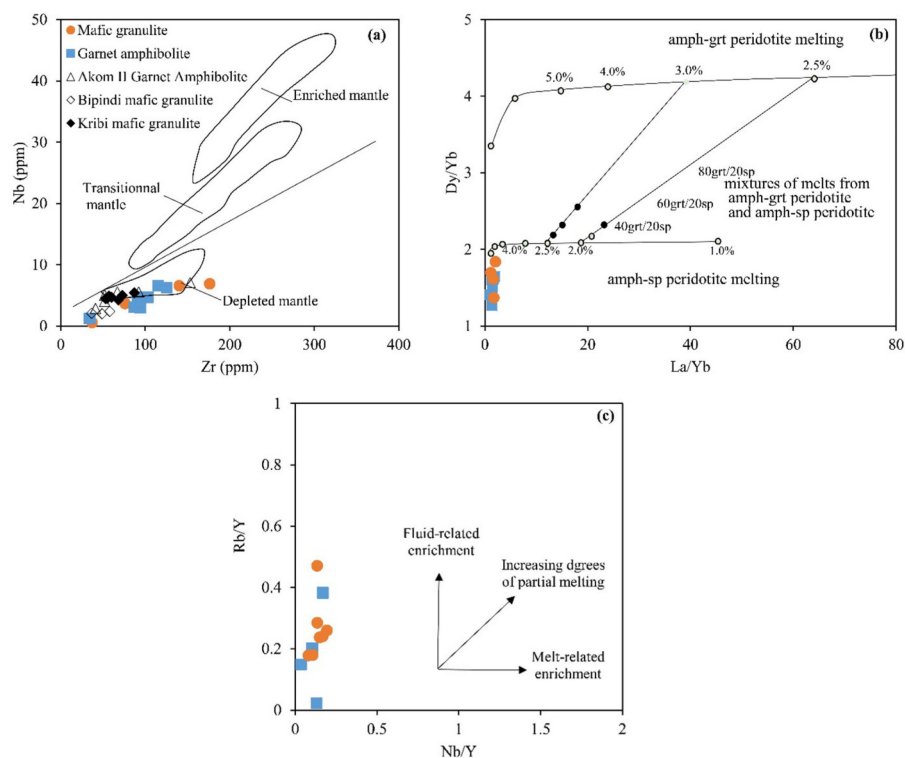


**Figure 14.** Binary plots for magma source characteristics of the Anyouzok metavolcanic rocks: (a) Zr vs. Nb [75]; (b) La/Yb vs. Dy/Yb [73]; (c) Rb/Y vs. Nb/Y [78].

### 6.3. Tectonic Setting of the Metavolcanic Rocks

Previous workers reported various tectonic environments for the Nyong Complex metabasic rocks, including back-arc, within-plate, NMORB, EMORB, and OIB settings [11,28,30,31,64]. Chondrite-normalized diagrams show that the Anyouzok metabasaltic rocks mainly show NMORB and EMORB affinities (Figure 8a,c). Furthermore, in the primitive mantle-normalized multi-element plots (Figure 8b,d), most samples exhibit depletion in Nb, Ta, Ti, and Zr, which are commonly observed in the arc basalt setting [79–81]. Various tectonic discrimination diagrams based on immobile elements are generally used to constrain the geodynamic setting of metamorphosed mafic rocks [68,82]. In the La/10-Nb/8-Y/15 ternary diagram (Figure 15a) proposed by [82], the studied garnet amphibolite samples, like the Akom II garnet amphibolite plotted for comparison, show back-arc and EMORB characteristics. In contrast, the analyzed mafic granulite samples mainly have arc tholeiites and back-arc features, similar to other Nyong Complex mafic granulites. In the Th/Yb vs. Nb/Yb discrimination diagram (Figure 15b), the Anyouzok samples are scattered within and above the mantle array. The garnet amphibolite samples fall within the back-arc field and NMORB area, while the mafic granulite samples plot along the arc field and follow the within-plate enrichment trend defined by [68]. Based on these geochemical features and earlier studies of metabasic rocks within the Nyong Complex, an association between back-arc and arc setting is suggested for the emplacement of the Anyouzok metavolcanic rocks precursors.

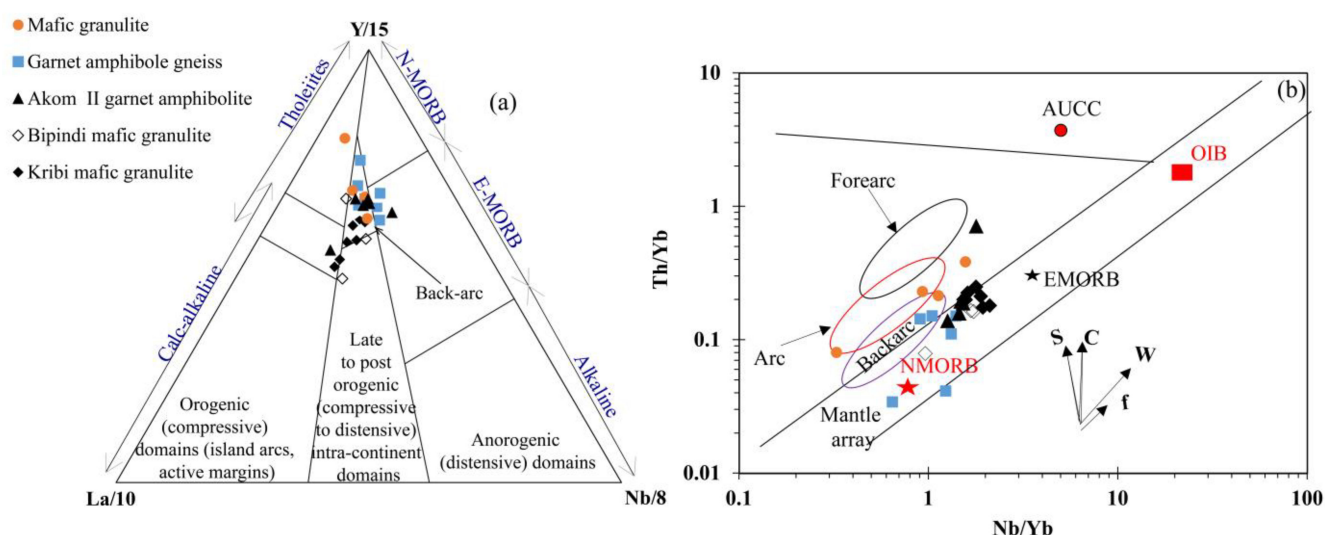


**Figure 15.** Tectonic discrimination plots for the Anyouzok metavolcanic rocks: (a) La/10-Nb/8-Y/15 [82]; (b) Th/Yb vs. Nb/Yb. NMORB: Normal Mid-Ocean Ridge Basalts, E-MORB: Enriched Mid-Ocean Ridge Basalts, OIB: Ocean Island Basalts, AUCC: Archean Upper Continental Crust. The vectors f, W, C, and S refer to fractional crystallization, within-plate fractionation, crustal contamination, and subduction zone.

### 6.4. Nature, Source, and Assessment of Detrital Input during the Anyouzok IF Deposition

The primary features of IFs could be influenced by the occurrence of clastic and/or volcanic components, yielding to high contents of some trace elements generally considered immobile and which lack in seawater (e.g.,  $\text{Al}_2\text{O}_3$ ,  $\text{TiO}_2$ , Zr, Th, Nb, and Sc; [6,8,9,83–85]). In addition, these detritus produce correlations between the former listed immobile elements and some REE and HFSE ratios such as Y/Ho and Pr/Yb [8]. A petrography study has revealed the presence of detrital components within the Anyouzok IFs depicted by minerals such as plagioclase and K-feldspar (Figure 6b,c,e,f). The Anyouzok BIFs show  $\text{Al}_2\text{O}_3$  (mean: 2.14 wt%),  $\text{TiO}_2$  (mean: 0.08 wt%), and Zr (mean: 16.08 ppm) contents and Pr/Yb ratios (mean: 1.76), suggesting a slight detritus contribution during the deposition of BIFs.

The estimation of the detrital input in the Anyouzok IFs was based on the Fe/Ti vs. Al/(Al + Fe + Mn) diagram by [86], displaying the ideal mixing between terrigenous and metalliferous sediments. In this plot (Figure 16a), the analyzed BIFs reveal up to 15% detritus in their composition, whereas the SBIFs reflect insignificant contamination for most samples (except for sample IS41, with ca. 10% crustal input). As discussed in Section 6.1.2., an increase in Fe within the SBIFs is associated with hydrothermal alteration, which facilitated leaching processes and, thus, the position of their data points being closer to the hydrothermal sediments area (Figure 16a). Th/U ratios < 5 have been proposed as an indicator of the presence of phosphate (e.g., apatite, monazite) and contaminants during chemical sediment deposition [8], since volcanic and clastic materials generally have values ranging from ca. 3–5 [52,70,87]. In the current study, phosphate minerals such as monazite or apatite have neither been identified in thin sections nor via XRD investigations. The studied BIFs have Th/U ratios ranging from 3.84–5.50, similar to those of volcanic and clastic materials [52,70,87]. In addition, Figure 16b indicates increasing Th/U ratios with decreasing Zr concentrations in the Anyouzok BIFs, suggesting the influence of volcanic or clastic detritus in the Anyouzok BIFs [8]. Lower concentrations and ratios, and a lack of correlations between Zr and Th/U presented by the SBIF samples (Table 2), could be attributed to the leaching of materials during hydrothermal activities [2]. To further evaluate the influence of detritus on the REE-Y systematics of the Anyouzok IFs, binary plots such as Zr and Pr/Yb vs. Y/Ho (La/La\*)<sub>SN</sub> and (Ce/Ce\*)<sub>SN</sub> were used (Figure 16c–h). In Figure 16e, (Ce/Ce\*)<sub>SN</sub> highlighted the positive correlation against Zr for the SBIFs and no correlation against Pr/Yb. In contrast, no other important positive correlation is observed with Y/Ho and (La/La\*)<sub>SN</sub>, suggesting that the presence of detritus and/or alterations have not significantly influenced the REE-Y systematics of the Anyouzok IFs.

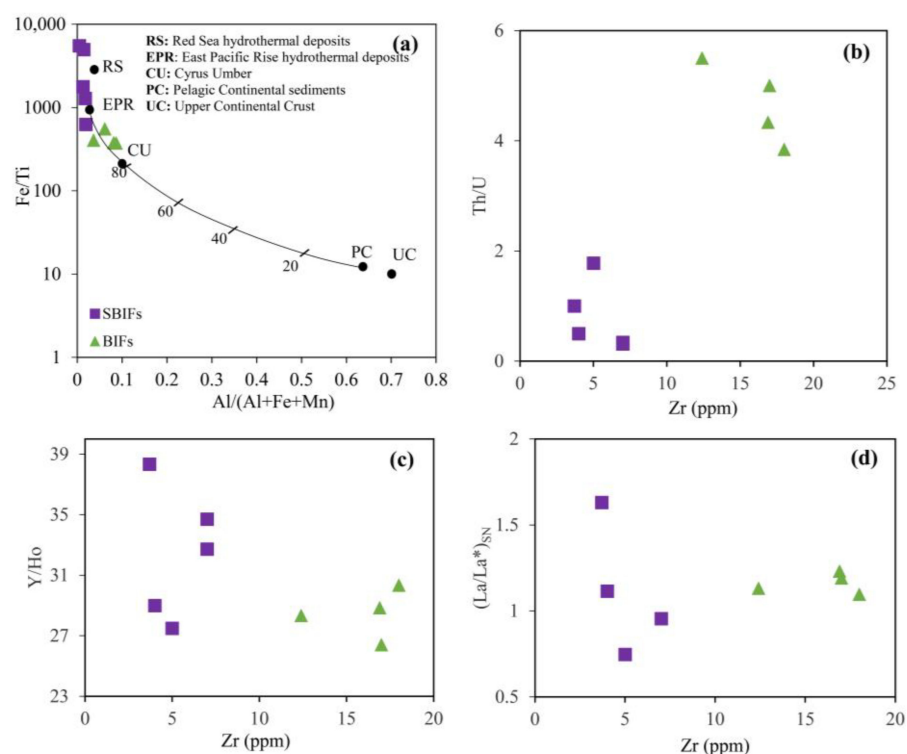
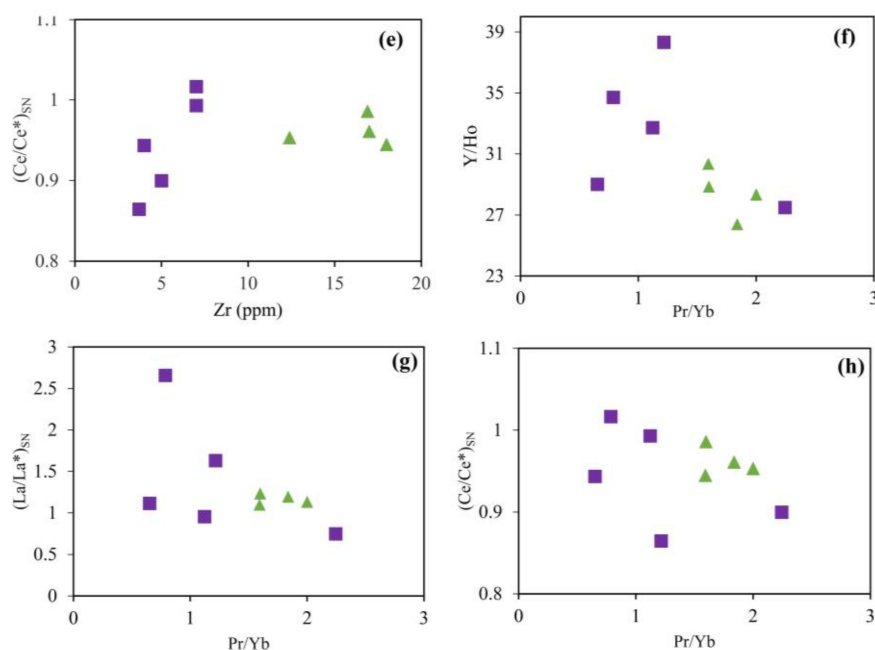


Figure 16. Cont.



**Figure 16.** Detrital input assessment of the Anyouzok IFs: (a) Fe/Ti vs. Al/(Al + Fe + Mn). The curve represents the mixing of pelagic sediments (PC) with East Pacific Rise deposits (EPR); the approximate amount of EPR in the mixture [88] is indicated by the numbers in percentages. CU: Cyprus umber, UC: Upper continental crust, RS: Red sea hydrothermal deposits [53,89]; (b) Th/U vs. Zr; (c) Y/Ho vs. Zr; (d) (La/La\*)<sub>SN</sub> vs. Zr; (e) (Ce/Ce\*)<sub>SN</sub> vs. Zr; (f) Y/Ho vs. Pr/Yb; (g) (La/La\*)<sub>SN</sub> vs. Pr/Yb; (h) (Ce/Ce\*)<sub>SN</sub> vs. Pr/Yb.

### 6.5. Origin of the Anyouzok Iron Formations

#### 6.5.1. Seawater and Hydrothermal Fluid Contribution

REE-Y systematics is widely used to assess the origin of Si and Fe in IFs [6,7,15,54,83–85,90]. Chemical sediments originating from seawater are characterized by super-chondritic Y/Ho ratios (>44), shale-normalized REE-Y patterns exhibiting positive La, Y, and Gd anomalies, negative Ce anomalies, and HREE enrichment over LREE and MREE [6,8,54]. In PAAS-normalized REE-Y diagrams, the Anyouzok IFs show consistent patterns (Figure 9b), with LREE depletion over HREE, positive Gd and La anomalies (except for two SBIF samples: IS19 and IS41), and negative Y anomalies (except for one SBIF sample: IS54). They show chondritic to super-chondritic Y/Ho ratios in both BIF (26.40–30.33) and SBIF (27.5–38.33) samples. Almost all BIF samples (except for IS13) exhibit negative Y anomalies and chondritic Y/Ho ratios, indicating they could be derived from slow rates of Fe oxyhydroxide precipitation [83,91,92].

Several workers reported that prominent positive Eu anomalies in IFs reflect the influence of high-temperature hydrothermal fluids, whereas a lack of Eu anomalies is considered reflective of low-temperature hydrothermal fluids [6,84,85,92–97]. The Anyouzok IFs show positive (Eu/Eu\*)<sub>SN</sub> anomalies ranging from 1.86–2.68 and from 2.14–3.17 for the BIFs and SBIFs, respectively, suggesting the influence of high-temperature hydrothermal fluids. In addition, [54] reported that high-temperature hydrothermal fluids (>250 °C) have (Eu/Eu\*)<sub>CN</sub> > 1, while low-temperature hydrothermal fluids (<250 °C) have (Eu/Eu\*)<sub>CN</sub> ≈ 1. In this view, the Eu anomalies ((Eu/Eu\*)<sub>CN</sub>) of 1.23–1.66 and 1.52–1.98 observed for the analyzed BIFs and SBIFs, respectively, could account for high-temperature hydrothermal fluids contribution. However, in the (Eu/Eu\*)<sub>SN</sub> vs. LREE diagram (Figure 17a), excluding sample IS13, showing secondary enrichment, all BIFs samples lack correlation, suggesting hydrothermal fluids input during their precipitation [6,84,85,92,93]. In contrast, the increase in Eu anomalies with decreasing LREE in SBIFs samples could indicate the influence of post-depositional processes, such as hydrothermal alteration, as previously discussed in Section 6.1.2. [84,85] proposed binary diagrams based on the Eu/Sm, Y/Ho, and Sm/Yb



ratios and defined the mixing line using seawater and high-temperature hydrothermal fluid end-members in order to evaluate their contribution in the solute sources of IFs. Figure 17b shows that small quantities of high-temperature hydrothermal fluids (0.1%) could account for the Eu/Sm and Y/Ho ratios presented by the Anyouzok IFs. Furthermore, the analyzed IFs fall along the mixing line (Figure 17c) defined by [85] and suggest an input of ca. 5% of high-temperature hydrothermal fluids in the Anyouzok BIFs and that they were deposited distal to the hydrothermal vent. It is therefore suggested that a mixture of seawater, low proportions of high-temperature hydrothermal fluids, and variable quantities of detrital materials influenced the deposition of the Anyouzok IFs. Comparable results were reported for several IF occurrences within the Congo Craton in Cameroon [12,25,27,63,98] and Congo [13,15].

### 6.5.2. Palaeoredox State of IF

Ce anomalies in chemical sediments are widely used to assess the palaeoredox state of the ancient seawater [7,17,54,99]. Suboxic and anoxic seawaters lack negative Ce anomalies, unlike oxygenated seawater, which displays strong negative Ce anomalies [7,54]. To distinguish “true” from “false” negative Ce anomalies, the  $(\text{Ce}/\text{Ce}^*)_{\text{SN}}$  vs.  $(\text{Pr}/\text{Pr}^*)_{\text{SN}}$  diagram (Figure 17d) has been proposed by [54]. In this plot, most of the Anyouzok IF samples show no Ce anomalies, suggesting that they were deposited in a suboxic to anoxic environment. Only the SBIF sample IS41, with a negative La (0.75) anomaly, plots within the oxic environment field. This could be attributed to post-depositional processes, which affected the SBIFs, as discussed in Section 6.1.2, since IFs deposited in the oxic environment show positive La anomalies (e.g., [6,96,97]). Therefore, we suggest that the Anyouzok IFs were deposited under anoxic conditions, similar to most of the Nyong Complex and Archean to Paleoproterozoic IFs worldwide [7,12,13,47,63,90,100].

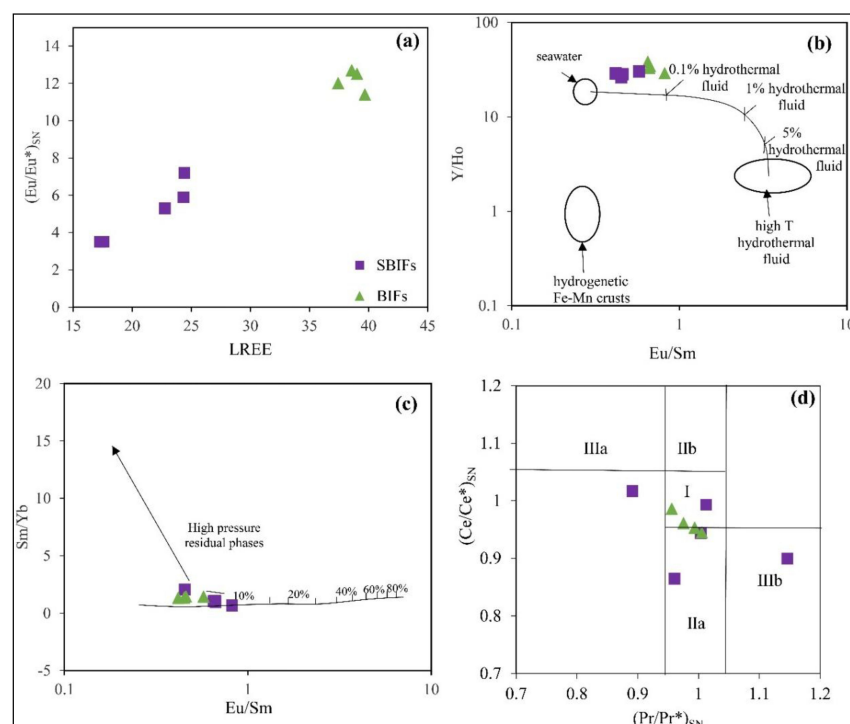


**Figure 17.** Contribution of seawater and hydrothermal fluids for the Anyouzok IFs precipitation: (a)  $(\text{Eu}/\text{Eu}^*)_{\text{SN}}$  vs. LREE diagram for the Anyouzok IFs; (b)  $\text{Eu}/\text{Sm}$  vs.  $\text{Y}/\text{Ho}$  [84] with a conservative mixing line of high-temperature hydrothermal fluid [92] and seawater [101]; (c)  $\text{Eu}/\text{Sm}$  vs.  $\text{Sm}/\text{Yb}$  plot [85] with a conservative mixing line of high-temperature hydrothermal fluid [8] and seawater [101]; (d)  $(\text{Ce}/\text{Ce}^*)_{\text{SN}}$  vs.  $(\text{Pr}/\text{Pr}^*)_{\text{SN}}$  plot [54] for the Anyouzok IFs. I: neither Ce nor La anomaly; IIa: positive La anomaly, no Ce anomaly; IIb: negative La anomaly, no Ce anomaly; IIIa: positive Ce anomaly; IIIb: negative Ce anomaly.



### 6.6. Depositional Setting

Based on associated or interbedded rocks, IFs have been classified as Algoma-type when deposited close to volcanic centers within greenstone belts or as Superior-type when deposited distal from volcanic centers, on continental shelves, or on submerged platforms [17,18,102]. Previous workers suggested both superior- [25,27,60] and Algoma-type [11] affinities for the Nyong Complex IFs. Furthermore, several depositional environments were proposed for Nyong Complex IFs, including the island arc setting with MORB-like signatures [28], the volcanic arc setting [12], back-arc or continental margin sea environments [25,60], a large basin between a continental margin and an oceanic volcanic center [27], and an extensional basin between a continental margin and a back-arc setting [11]. The Anyouzok IFs are interbedded with metavolcanic rocks comprising mafic granulite and garnet amphibolite along the stratigraphy (Figure 4a and b), suggesting an Algoma-type deposit. Considering the conspicuous higher Shale-normalized Eu anomalies of the Algoma type IFs, [103] proposed a threshold with  $(\text{Eu}/\text{Eu}^*)_{\text{NASC}} > 1.8$  for Algoma-type IFs and values  $< 1.8$  for the superior-type IFs. On this view, the high  $(\text{Eu}/\text{Eu}^*)_{\text{NASC}}$  anomalies presented by the studied BIFs (1.88–2.7) and SBIFs (2.16–3.26) suggest an Algoma-type deposit for the Anyouzok IFs, although the higher values presented by SBIFs may reflect the influence of hydrothermal alteration. Taking into consideration our results and those of previous IF investigations within the Nyong Complex, we suggest that the Anyouzok IFs are Algoma-type and were deposited distal to the hydrothermal vents in the back-arc setting.

## 7. Conclusions

This work integrates field and petrographic investigations, coupled with whole rock geochemical data of rocks from the Anyouzok area in the Nyong Complex greenstone belts. The following conclusions can be provided:

1. The lithostratigraphy of this area comprises an IF unit, consisting of BIFs and SBIFs, and a country rock unit made up of mafic granulite and garnet amphibolite. These rocks were intensely deformed and metamorphosed up to granulite facies. BIFs are absent in surface outcrops and were uniquely intercepted in one drillhole, sandwiched between mafic granulites.
2. The Anyouzok metavolcanic rocks have tholeiitic to transitional basalt precursors. The latter originated from the partial melting of a metasomatized spinel lherzolite source, which experienced various degrees of fractional crystallization and was emplaced in an arc/back-arc setting.
3. The Anyouzok IFs are mainly composed of magnetite, quartz, and metamorphic amphibole (actinolite and tremolite), with subordinate biotite, plagioclase, K-feldspar, hematite, pyrite, calcite, and ilmenite. These rocks were primarily deposited as BIFs and enriched to SBIFs through hydrothermal alteration activities and the leaching of silica.
4. The Anyouzok BIFs recorded the contribution of detrital components during their deposition. In addition, the REE-Y systematics of both BIFs and SBIFs suggest the influence of seawater and high-temperature hydrothermal fluids distal to the vent source during their precipitation in an anoxic to suboxic environment. The ubiquitous negative Y anomalies and chondritic Y/Ho ratios observed in almost all BIF samples suggest slow rates of Fe oxyhydroxide precipitation.
5. Based on the geochemical features of the Anyouzok IFs and interbedded metavolcanic rocks, we propose that these IFs are Algoma-type and were formed distal to the hydrothermal vents in a back-arc setting.

**Supplementary Materials:** The following supporting information can be downloaded at: <https://www.mdpi.com/article/10.3390/min12101198/s1>, Table S1: Anyouzok iron ore deposit drillhole details; Table S2: Anyouzok iron ore deposit logging details.

**Author Contributions:** Conceptualization, I.S.F., M.N.T. and D.H.F.; formal analysis, J.P.N., C.E.S., S.G. and I.S.F.; investigation, I.S.F. and J.P.N.; writing—original draft preparation, I.S.F., M.N.T., D.H.F. and L.S.T.; writing—review and editing, I.S.F., M.N.T., D.H.F., C.M., L.S.T., S.G., C.E.S. and J.P.N.; project administration, J.P.N.; funding acquisition, I.S.F. All authors have read and agreed to the published version of the manuscript.

**Funding:** This research did not receive any specific grant from funding agencies in the public, commercial, or not-for-profit sectors.

**Data Availability Statement:** The data used to support the findings of this study are available with the corresponding author upon request.

**Acknowledgments:** This paper represents part of the first author's PhD thesis at the Department of Earth Sciences of the University of Yaoundé I. The authors are grateful to the International Mining and Infrastructure Corporation PLC (IMIC) via Caminex for providing logistic support during the field work. We would also like to thank two anonymous referees for their constructive review comments that greatly improved the manuscript.

**Conflicts of Interest:** The authors declare no conflict of interest.

## References

- James, H.L. Sedimentary facies of iron-formation. *Econ. Geol.* **1954**, *49*, 235–293. [\[CrossRef\]](#)
- Hagemann, S.; Angerer, T.; Duuring, P.; Rosière, C.; E Silva, R.F.; Lobato, L.; Hensler, A.; Walde, D. BIF-hosted iron mineral system: A review. *Ore Geol. Rev.* **2016**, *76*, 317–359. [\[CrossRef\]](#)
- Duuring, P.; Hagemann, S. Leaching of silica bands and concentration of magnetite in Archean BIF by hypogene fluids: Beebyn Fe ore deposit, Yilgarn Craton, Western Australia. *Miner. Depos.* **2012**, *48*, 341–370. [\[CrossRef\]](#)
- Peters, W.S. *Aeromagnetic-Radiometric Survey: Structural Interpretation for Iron Ore, Gold and Other Commodities for Aureus Mining Inc*; Aeromagnetic (Southern Geoscience Consulting Pty Ltd.): Yaoundé, Cameroon, 2011.
- Baker, H.; Haythornthwaite, J. *Mineral Resource Estimate for the FeO8 and Fe11 Deposits of the Ntem Iron Project*; SRK Consulting Ltd.: Gauteng, China, 2015.
- Bolhar, R.; Kamber, B.S.; Moorbath, S.; Fedo, C.M.; Whitehouse, M.J. Characterisation of early Archaean chemical sediments by trace element signatures. *Earth Planet. Sci. Lett.* **2004**, *222*, 43–60. [\[CrossRef\]](#)
- Bekker, A.; Slack, J.F.; Planavsky, N.; Krapez, B.; Hofmann, A.; Konhauser, K.; Rouxel, O.J. Iron Formation: The Sedimentary Product of a Complex Interplay among Mantle, Tectonic, Oceanic, and Biospheric Processes. *Econ. Geol.* **2010**, *105*, 467–508. [\[CrossRef\]](#)
- Thurston, P.; Kamber, B.; Whitehouse, M. Archean cherts in banded iron formation: Insight into Neoarchean ocean chemistry and depositional processes. *Precambrian Res.* **2012**, *214–215*, 227–257. [\[CrossRef\]](#)
- Wang, C.; Zhang, L.; Lan, C.; Dai, Y. Petrology and geochemistry of the Wangjiazhuang banded iron formation and associated supracrustal rocks from the Wutai greenstone belt in the North China Craton: Implications for their origin and tectonic setting. *Precambrian Res.* **2014**, *255*, 603–626. [\[CrossRef\]](#)
- El-Shazly, A.; Khalil, K.; Helba, H. Geochemistry of banded iron formations and their host rocks from the Central Eastern Desert of Egypt: A working genetic model and tectonic implications. *Precambrian Res.* **2019**, *325*, 192–216. [\[CrossRef\]](#)
- Moudioh, C.; Tamehe, L.S.; Ganno, S.; Tankwa, M.N.; Soares, M.B.; Ghosh, R.; Kankeu, B.; Nzenti, J.P. Tectonic setting of the Bipindi greenstone belt, northwest Congo craton, Cameroon: Implications on BIF deposition. *J. Afr. Earth Sci.* **2020**, *171*, 103971. [\[CrossRef\]](#)
- Tankwa, M.N.; Ganno, S.; Okunlola, O.A.; Njiosseu, E.L.T.; Tamehe, L.S.; Woguia, B.K.; Mbita, A.S.M.; Nzenti, J.P. Petrogenesis and tectonic setting of the Paleoproterozoic Kelle Bidjoka iron formations, Nyong group greenstone belts, southwestern Cameroon. Constraints from petrology, geochemistry, and LA-ICP-MS zircon U-Pb geochronology. *Int. Geol. Rev.* **2020**, *63*, 1737–1757. [\[CrossRef\]](#)
- Ebotohoua, C.G.; Xie, Y.; Adomako-Ansah, K.; Gourcerol, B.; Qu, Y. Depositional Environment and Genesis of the Nabeba Banded Iron Formation (BIF) in the Ivindo Basement Complex, Republic of the Congo: Perspective from Whole-Rock and Magnetite Geochemistry. *Minerals* **2021**, *11*, 579. [\[CrossRef\]](#)
- Soh Tamehe, L.; Li, H.; Ganno, S.; Chen, Z.; Lemdjou, Y.B.; Elatikpo, S.Y. Insight into the Origin of Iron Ore Based on Elemental Contents of Magnetite and Whole-Rock Geochemistry: A Case of the Bipindi Banded Iron Formations. *J. Earth Sci.* **2022**. *submitted for publication*.
- Gourcerol, B.; Blein, O.; Chevillard, M.; Callec, Y.; Boudzoumou, F.; Djama, L.-M.J. Depositional Setting of Archean BIFs from Congo: New Insight into Under-Investigated Occurrences. *Minerals* **2022**, *12*, 114. [\[CrossRef\]](#)
- Taylor, D.; Dalstra, H.J.; Harding, A.E.; Broadbent, G.C.; Barley, M.E. Genesis of High-Grade Hematite Orebodies of the Hamersley Province, Western Australia. *Econ. Geol.* **2001**, *96*, 837–873. [\[CrossRef\]](#)
- Klein, C. Some Precambrian banded iron-formations (BIFs) from around the world: Their age, geologic setting, mineralogy, metamorphism, geochemistry, and origins. *Am. Miner.* **2005**, *90*, 1473–1499. [\[CrossRef\]](#)

18. Gross, G.A. A classification of iron formations based on depositional environments. *Can. Mineral.* **1980**, *18*, 215–222.
19. Maurizot, P.; Abessolo, A.; Feybesse, J.L.; Johan Lecomte, P. Etude de prospection minière du Sud-Ouest Cameroun, Synthèse des travaux de 1978 à 1985. *J. Sci. Res.* **1986**, 247.
20. Lerouge, C.; Cocherie, A.; Toteu, S.F.; Penaye, J.; Milési, J.-P.; Tchameni, R.; Nsifa, E.N.; Fanning, C.M.; Deloule, E. Shrimp U–Pb zircon age evidence for Paleoproterozoic sedimentation and 2.05Ga syntectonic plutonism in the Nyong Group, South-Western Cameroon: Consequences for the Eburnean–Transamazonian belt of NE Brazil and Central Africa. *J. Afr. Earth Sci.* **2006**, *44*, 413–427. [\[CrossRef\]](#)
21. Ganno, S.; Moudioh, C.; Nchare, A.N.; Nono, G.D.K.; Nzenti, J.P. Geochemical Fingerprint and Iron Ore Potential of the Siliceous Itabirite from Palaeoproterozoic Nyong Series, Zambi Area, Southwestern Cameroon. *Resour. Geol.* **2015**, *66*, 71–80. [\[CrossRef\]](#)
22. Aye, B.A.; Sababa, E.; Ndjigui, P.-D. Geochemistry of S, Cu, Ni, Cr and Au-PGE in the garnet amphibolites from the Akom II area in the Archaean Congo Craton, Southern Cameroon. *Geochemistry* **2017**, *77*, 81–93. [\[CrossRef\]](#)
23. Bouyo, M.H.; Penaye, J.; Mouri, H.; Toteu, S. Eclogite facies metabasites from the Paleoproterozoic Nyong Group, SW Cameroon: Mineralogical evidence and implications for a high-pressure metamorphism related to a subduction zone at the NW margin of the Archean Congo craton. *J. Afr. Earth Sci.* **2018**, *149*, 215–234. [\[CrossRef\]](#)
24. Tsoungui, P.N.E.; Ganno, S.; Njiosseu, E.L.T.; Mbongue, J.L.N.; Woguia, B.K.; Tamehe, L.S.; Wambo, J.D.T.; Nzenti, J.P. Geochemical constraints on the origin and tectonic setting of the serpentinized peridotites from the Paleoproterozoic Nyong series, Eseka area, SW Cameroon. *Acta Geochim.* **2019**, *39*, 404–422. [\[CrossRef\]](#)
25. Tamehe, L.S.; Tankwa, M.N.; Chongtao, W.; Ganno, S.; Ngnotue, T.; Nono, G.D.K.; Simon, S.J.; Zhang, J.; Nzenti, J.P. Geology and geochemical constraints on the origin and depositional setting of the Kpwa–Atog Boga banded iron formations (BIFs), northwestern Congo craton, southern Cameroon. *Ore Geol. Rev.* **2018**, *95*, 620–638. [\[CrossRef\]](#)
26. Tamehe, L.S.; Chongtao, W.; Ganno, S.; Simon, S.J.; Nono, G.D.K.; Nzenti, J.P.; Lemdjou, Y.B.; Lin, N.H. Geology of the Gouap iron deposit, Congo craton, southern Cameroon: Implications for iron ore exploration. *Ore Geol. Rev.* **2019**, *107*, 1097–1128. [\[CrossRef\]](#)
27. Tamehe, L.S.; Wei, C.; Ganno, S.; Rosière, C.A.; Nzenti, J.P.; Ebotehoua, C.G.; Lu, G. Depositional age and tectonic environment of the Gouap banded iron formations from the Nyong group, SW Cameroon: Insights from isotopic, geochemical and geochronological studies of drillcore samples. *Geosci. Front.* **2020**, *12*, 549–572. [\[CrossRef\]](#)
28. Marion, K.W.M.; Djibril, K.N.G.; Guimollaire, N.D.; Patrick, A.K. Petrogenesis and U–Pb zircon dating of amphibolite in the Mewengo iron deposit, Nyong series, Cameroon: Fingerprints of iron depositional geotectonic setting. *Arab. J. Geosci.* **2021**, *14*, 1–15. [\[CrossRef\]](#)
29. Soh, A.P.D.; Ganno, S.; Zhang, L.; Tamehe, L.S.; Wang, C.; Peng, Z.; Tong, X.; Nzenti, J.P. Origin, tectonic environment and age of the Bibole banded iron formations, northwestern Congo Craton, Cameroon: Geochemical and geochronological constraints. *Geol. Mag.* **2021**, *158*, 2245–2263. [\[CrossRef\]](#)
30. Owona, S.; Schulz, B.; Minyem, D.; Ratschbacher, L.; Tchamabe, B.C.; Olinga, J.B.; Ondoa, J.M.; Ekodeck, G.E. Eburnean/Trans-Amazonian Orogeny in the Nyong Complex of Southwestern Cameroon: Meta-Basite Geochemistry and Meta-morphic Petrology. *J. Afr. Earth Sci.* **2022**, *190*, 104515. [\[CrossRef\]](#)
31. Mvodo, H.; Ganno, S.; Nono, G.D.K.; Fossi, D.H.; Essomba, P.E.N.; Tankwa, M.N.; Nzenti, J.P. Petrogenesis, LA-ICP-MS zircon U–Pb geochronology and geodynamic implications of the Kribi metavolcanic rocks, Nyong Group, Congo craton. *Acta Geochim.* **2022**, *41*, 470–495. [\[CrossRef\]](#)
32. Djomani, Y.P.; Diamant, M.; Wilson, M. Lithospheric structure across the Adamawa plateau (Cameroon) from gravity studies. *Tectonophysics* **1997**, *273*, 317–327. [\[CrossRef\]](#)
33. Toteu, S.F.; Penaye, J.; Djomani, Y.P. Geodynamic evolution of the Pan-African belt in central Africa with special reference to Cameroon. *Can. J. Earth Sci.* **2004**, *41*, 73–85. [\[CrossRef\]](#)
34. Ngalamo, J.F.G.; Bisso, D.; Abdelsalam, M.G.; Atekwana, E.A.; Katumwehe, A.B.; Ekodeck, G. Geophysical imaging of metacratonization in the northern edge of the Congo craton in Cameroon. *J. Afr. Earth Sci.* **2017**, *129*, 94–107. [\[CrossRef\]](#)
35. Tchakounté, J.; Eglinger, A.; Toteu, S.F.; Zeh, A.; Nkoubou, C.; Mvondo-Ondoa, J.; Penaye, J.; De Wit, M.; Barbey, P. The Adamawa–Yadé domain, a piece of Archaean crust in the Neoproterozoic Central African Orogenic belt (Bafia area, Cameroon). *Precambrian Res.* **2017**, *299*, 210–229. [\[CrossRef\]](#)
36. Toteu, S.F.; De Wit, M.; Penaye, J.; Drost, K.; Tait, J.A.; Bouyo, M.H.; Van Schmus, W.R.; Jelsma, H.; Moloto-A-Kenguemba, G.R.; Filho, A.F.D.S.; et al. Geochronology and correlations in the Central African Fold Belt along the northern edge of the Congo Craton: New insights from U–Pb dating of zircons from Cameroon, Central African Republic, and south-western Chad. *Gondwana Res.* **2022**, *107*, 296–324. [\[CrossRef\]](#)
37. Ndema Mbongue, J.L.; Ngnotue, T.; Ngo Nlend, C.D.; Nzenti, J.P.; Cheo Suh, E. Origin and Evolution of the Formation of the Cameroon Nyong Series in the Western Border of the Congo Craton. *J. Geosci. Geomat.* **2014**, *2*, 62–75. [\[CrossRef\]](#)
38. Owona, S.; Ondoa, J.M.; Tichomirowa, M.; Ekodeck, G.E. The petrostructural characteristics and 207Pb/206Pb zircon data from the Ngomedzap-Akongo area (Nyong complex, SW-Cameroon). *J. Geosci.* **2020**, *65*, 201–219. [\[CrossRef\]](#)
39. Owona, S.; Ratschbacher, L.; Ngapna, M.N.; Gulzar, A.M.; Ondoa, J.M.; Ekodeck, G.E. How diverse is the source? Age, provenance, reworking, and overprint of Precambrian meta-sedimentary rocks of West Gondwana, Cameroon, from zircon U–Pb geochronology. *Precambrian Res.* **2021**, *359*, 106220. [\[CrossRef\]](#)
40. Kankeu, B.; Greiling, R.O.; Nzenti, J.P.; Ganno, S.; Danguene, P.Y.; Bassahak, J.; Hell, J.V. Contrasting Pan-African structural styles at the NW margin of the Congo Shield in Cameroon. *J. Afr. Earth Sci.* **2018**, *146*, 28–47. [\[CrossRef\]](#)

41. Penaye, J.; Toteu, S.; Tchameni, R.; Van Schmus, W.; Tchakounté, J.; Ganwa, A.; Minyem, D.; Nsifa, E. The 2.1Ga West Central African Belt in Cameroon: Extension and evolution. *J. Afr. Earth Sci.* **2004**, *39*, 159–164. [\[CrossRef\]](#)
42. Abeng, S.A.E.; Ndjigui, P.-D.; Beyanu, A.A.; Teutsong, T.; Bilong, P. Geochemistry of pyroxenites, amphibolites and their weathered products in the Nyong unit, SW Cameroon (NW border of Congo craton): Implications for Au–PGE exploration. *J. Geochem. Explor.* **2012**, *114*, 1–19. [\[CrossRef\]](#)
43. Toteu, S.; Van Schmus, W.; Penaye, J.; Nyobé, J. UPb and SmN edvidence for Eburnian and Pan-African high-grade metamorphism in cratonic rocks of southern Cameroon. *Precambrian Res.* **1994**, *67*, 321–347. [\[CrossRef\]](#)
44. Loose, D.; Schenk, V. 2.09 Ga old eclogites in the Eburnian-Transamazonian orogen of southern Cameroon: Significance for Palaeoproterozoic plate tectonics. *Precambrian Res.* **2018**, *304*, 1–11. [\[CrossRef\]](#)
45. Nkoubou, C.; Barbey, P.; Yonta-Ngouné, C.; Paquette, J.; Villiéras, F. Pre-collisional geodynamic context of the southern margin of the Pan-African fold belt in Cameroon. *J. Afr. Earth Sci.* **2014**, *99*, 245–260. [\[CrossRef\]](#)
46. Owona, S.; Ratschbacher, L.; Afzal, M.G.; Nsangou Ngapna, M.; Mvondo Ondoa, J.; Ekodeck, G.E. New U–Pb Zircon Ages of Nyong Complex Meta-Plutonites: Implications for the Eburnean/Trans-Amazonian Orogeny in Southwestern Cameroon (Central Africa). *Geol. J.* **2021**, *56*, 1741–1755. [\[CrossRef\]](#)
47. Chombong, N.N.; Suh, E.; Lehmann, B.; Vishiti, A.; Ilouga, D.C.; Shemang, E.; Tantoh, B.S.; Kedia, A.C. Host rock geochemistry, texture and chemical composition of magnetite in iron ore in the Neoarchean Nyong unit in southern Cameroon. *Appl. Earth Sci.* **2017**, *126*, 129–145. [\[CrossRef\]](#)
48. Toteu, S.F.; Penaye, J.; Deloule, E.; VanSchmus, W.; Tchameni, R. Diachronous evolution of volcano-sedimentary basins north of the Congo craton: Insights from U–Pb ion microprobe dating of zircons from the Poli, Lom and Yaoundé Groups (Cameroon). *J. Afr. Earth Sci.* **2006**, *44*, 428–442. [\[CrossRef\]](#)
49. Penaye, J.; Toteu, S.F.; Van Schmus, W.R.; Nzenti, J.-P. U-Pb and Sm-Nd Preliminary Geochronologic Data on the Yaoundé Series, Cameroon: Re-Interpretation of the Granulitic Rocks as the Suture of a Collision in the Centrafrican Belt. *C. R. Acad. Sci. Sér. 2 Méc. Phys. Chim. Sci. Univers Sci. Terre* **1993**, *317*, 789–794.
50. Feybesse, J.L.; Johan, V.; Maurizot, P.; Abessolo, A. Mise En Évidence d’une Nappe Symmétamorphe d’âge Eburnéen Dans La Partie NW Du Craton Zairois (SW Cameroun). *Publ. Occas.-Cent. Int. Form. Échanges Géol.* **1986**, *10*, 105–111.
51. Mandeng, E.P.B.; Bidjeck, L.M.B.; Wambo, J.D.T.; Taku, A.; Betsi, T.B.; Ipan, A.S.; Nfada, L.T.; Dieudonné, L.B. Lithologic and structural mapping of the Abiete–Toko gold district in southern Cameroon, using Landsat 7 ETM+ /SRTM. *C. R. Geosci.* **2018**, *350*, 130–140. [\[CrossRef\]](#)
52. Sun, S.S.; McDonough, W.F. Chemical and isotopic systematics of oceanic basalts: Implications for mantle composition and processes. In *Magmatism in the Ocean Basin*; Geological Society Special Publication: London, UK, 1989; Volume 42, pp. 313–345.
53. Taylor, S.R.; McLennan, S.M. *The Continental Crust: Its Composition and Evolution*; U.S. Department of Energy: Washington, DC, USA, 1985.
54. Bau, M.; Dulski, P. Anthropogenic origin of positive gadolinium anomalies in river waters. *Earth Planet. Sci. Lett.* **1996**, *143*, 245–255. [\[CrossRef\]](#)
55. McDonough, W.F.; Sun, S.-S. The composition of the Earth. *Chem. Geol.* **1995**, *120*, 223–253. [\[CrossRef\]](#)
56. Polat, A.; Hofmann, A.; Rosing, M. Boninite-like volcanic rocks in the 3.7–3.8 Ga Isua greenstone belt, West Greenland: Geochemical evidence for intra-oceanic subduction zone processes in the early Earth. *Chem. Geol.* **2002**, *184*, 231–254. [\[CrossRef\]](#)
57. Wang, C.; Peng, Z.; Tong, X.; Huang, H.; Zheng, M.; Zhang, L.; Zhai, M. Late Neoarchean supracrustal rocks from the Anshan-Benxi terrane, North China Craton: New geodynamic implications from the geochemical record. *Am. J. Sci.* **2017**, *317*, 1095–1148. [\[CrossRef\]](#)
58. Sun, X.-H.; Zhu, X.-Q.; Tang, H.-S.; Zhang, Q.; Luo, T.-Y. The Gongchangling BIFs from the Anshan–Benxi Area, NE China: Petrological–Geochemical Characteristics and Genesis of High-Grade Iron Ores. *Ore Geol. Rev.* **2014**, *60*, 112–125. [\[CrossRef\]](#)
59. Sun, X.-H.; Zhu, X.-Q.; Tang, H.-S.; Zhang, Q.; Luo, T.-Y.; Han, T. Protolith reconstruction and geochemical study on the wall rocks of Anshan BIFs, Northeast China: Implications for the provenance and tectonic setting. *J. Geochem. Explor.* **2014**, *136*, 65–75. [\[CrossRef\]](#)
60. Sylvestre, G.; Laure, N.T.E.; Djibril, K.N.G.; Arlette, D.S.; Cyriel, M.; Timoléon, N.; Paul, N.J. A mixed seawater and hydrothermal origin of superior-type banded iron formation (BIF)-hosted Kouambo iron deposit, Palaeoproterozoic Nyong series, Southwestern Cameroon: Constraints from petrography and geochemistry. *Ore Geol. Rev.* **2017**, *80*, 860–875. [\[CrossRef\]](#)
61. Large, R.R.; Gemmell, J.B.; Paulick, H.; Huston, D.L. The Alteration Box Plot: A Simple Approach to Understanding the Relationship between Alteration Mineralogy and Lithogeochemistry Associated with Volcanic-Hosted Massive Sulfide Deposits. *Econ. Geol.* **2001**, *96*, 957–971. [\[CrossRef\]](#)
62. Ishikawa, Y.; Sawaguchi, T.; Iwaya, S.; Horiuchi, M. Delineation of Prospecting Targets for Kuroko Deposits Based on Modes of Volcanism of Underlying Dacite and Alteration Haloes. *Min. Geol.* **1976**, *26*, 105–117. [\[CrossRef\]](#)
63. Ndimé, E.N.; Ganno, S.; Nzenti, J.P. Geochemistry and Pb–Pb Geochronology of the Neoarchean Nkout West Metamorphosed Banded Iron Formation, Southern Cameroon. *Int. J. Earth Sci.* **2019**, *108*, 1551–1570. [\[CrossRef\]](#)
64. Fuanya, C.; Bolarinwa, A.T.; Kankeu, B.; Yongue, R.F.; Tangko, E.T.; Nkepguep, F.Y. Geochemical characteristics and petrogenesis of basic rocks in the Ako’ozam–Njabilobe area, Southwestern Cameroon: Implications for Au genesis. *SN Appl. Sci.* **2019**, *1*, 904. [\[CrossRef\]](#)



65. Winchester, J.; Floyd, P. Geochemical discrimination of different magma series and their differentiation products using immobile elements. *Chem. Geol.* **1977**, *20*, 325–343. [\[CrossRef\]](#)
66. Ross, P.-S.; Bédard, J.H. Magmatic affinity of modern and ancient subalkaline volcanic rocks determined from trace-element discriminant diagrams. *Can. J. Earth Sci.* **2009**, *46*, 823–839. [\[CrossRef\]](#)
67. DePaolo, D.J. A neodymium and strontium isotopic study of the Mesozoic calc-alkaline granitic batholiths of the Sierra Nevada and Peninsular Ranges, California. *J. Geophys. Res. Earth Surf.* **1981**, *86*, 10470–10488. [\[CrossRef\]](#)
68. Pearce, J.A. Geochemical fingerprinting of oceanic basalts with applications to ophiolite classification and the search for Archean oceanic crust. *Lithos* **2008**, *100*, 14–48. [\[CrossRef\]](#)
69. Barth, M.G.; McDonough, W.F.; Rudnick, R.L. Tracking the budget of Nb and Ta in the continental crust. *Chem. Geol.* **2000**, *165*, 197–213. [\[CrossRef\]](#)
70. Rudnick, R.L.; Gao, S. The role of lower crustal recycling in continent formation. *Geochim. Cosmochim. Acta Suppl.* **2003**, *67*, 403.
71. Wilson, M. *Igneous Petrogenesis*; Springer: Dordrecht, The Netherlands, 1989; 466p. [\[CrossRef\]](#)
72. Fan, W.-M.; Guo, F.; Wang, Y.-J.; Zhang, M. Late Mesozoic Volcanism in the Northern Huaiyang Tectono-Magmatic Belt, Central China: Partial Melts from a Lithospheric Mantle with Subducted Continental Crust Relicts beneath the Dabie Orogen? *Chem. Geol.* **2004**, *209*, 27–48. [\[CrossRef\]](#)
73. Jung, C.; Jung, S.; Hoffer, E.; Berndt, J. Petrogenesis of Tertiary Mafic Alkaline Magmas in the Hoheifel, Germany. *J. Pet.* **2006**, *47*, 1637–1671. [\[CrossRef\]](#)
74. Rooney, T.O. Geochemical evidence of lithospheric thinning in the southern Main Ethiopian Rift. *Lithos* **2010**, *117*, 33–48. [\[CrossRef\]](#)
75. Geng, H.; Sun, M.; Yuan, C.; Zhao, G.; Xiao, W. Geochemical and geochronological study of early Carboniferous volcanic rocks from the West Junggar: Petrogenesis and tectonic implications. *J. Southeast Asian Earth Sci.* **2011**, *42*, 854–866. [\[CrossRef\]](#)
76. Singh, S.P.; Subramanyam, K.S.V.; Manikyamba, C.; Santosh, M.; Singh, M.R.; Kumar, B.C. Geochemical Systematics of the Mauranipur-Babina Greenstone Belt, Bundelkhand Craton, Central India: Insights on Neoarchean Mantle Plume-Arc Accretion and Crustal Evolution. *Geosci. Front.* **2018**, *9*, 769–788. [\[CrossRef\]](#)
77. Workman, R.K.; Hart, S.R. Major and trace element composition of the depleted MORB mantle (DMM). *Earth Planet. Sci. Lett.* **2005**, *231*, 53–72. [\[CrossRef\]](#)
78. Bhat, I.M.; Ahmad, T.; Rao, D.S. The tectonic evolution of the Dras arc complex along the Indus Suture Zone, western Himalaya: Implications for the Neo-Tethys Ocean geodynamics. *J. Geodyn.* **2019**, *124*, 52–66. [\[CrossRef\]](#)
79. Kelemen, P.B.; Hanghøj, K.; Greene, A.R. *One View of the Geochemistry of Subduction-Related Magmatic Arcs, with an Emphasis on Primitive Andesite and Lower Crust*; Elsevier: Amsterdam, The Netherlands, 2014. [\[CrossRef\]](#)
80. Meng, E.; Liu, F.-L.; Liu, P.-H.; Liu, C.-H.; Yang, H.; Wang, F.; Shi, J.-R.; Cai, J. Petrogenesis and tectonic significance of Paleoproterozoic meta-mafic rocks from central Liaodong Peninsula, northeast China: Evidence from zircon U–Pb dating and in situ Lu–Hf isotopes, and whole-rock geochemistry. *Precambrian Res.* **2014**, *247*, 92–109. [\[CrossRef\]](#)
81. Wang, X.; Peng, P.; Wang, C.; Yang, S. Petrogenesis of the 2115 Ma Haicheng mafic sills from the Eastern North China Craton: Implications for an intra-continental rifting. *Gondwana Res.* **2016**, *39*, 347–364. [\[CrossRef\]](#)
82. Cabanis, B.; Lecolle, M. Le Diagramme La/10-Y/15-Nb/8: Un Outil Pour La Discrimination Des Séries Volcaniques et La Mise En Évidence Des Processus de Mélange et/Ou de Contamination Crustale. *C. R. Acad. Sci. Sér. 2 Méc. Phys. Chim. Sci. Univers Sci. Terre* **1989**, *309*, 2023–2029.
83. Basta, F.F.; Maurice, A.E.; Fontboté, L.; Favarger, P.-Y. Petrology and Geochemistry of the Banded Iron Formation (BIF) of Wadi Karim and Um Anab, Eastern Desert, Egypt: Implications for the Origin of Neoproterozoic BIF. *Precambrian Res.* **2011**, *187*, 277–292. [\[CrossRef\]](#)
84. Alexander, B.W.; Bau, M.; Andersson, P.; Dulski, P. Continentally-derived solutes in shallow Archean seawater: Rare earth element and Nd isotope evidence in iron formation from the 2.9Ga Pongola Supergroup, South Africa. *Geochim. Cosmochim. Acta* **2008**, *72*, 378–394. [\[CrossRef\]](#)
85. Gourcerol, B.; Thurston, P.; Kontak, D.; Côté-Mantha, O.; Biczok, J. Depositional setting of Algoma-type banded iron formation. *Precambrian Res.* **2016**, *281*, 47–79. [\[CrossRef\]](#)
86. Boström, K. Submarine volcanism as a source for iron. *Earth Planet. Sci. Lett.* **1970**, *9*, 348–354. [\[CrossRef\]](#)
87. Condie, K.C. Chemical composition and evolution of the upper continental crust: Contrasting results from surface samples and shales. *Chem. Geol.* **1993**, *104*, 1–37. [\[CrossRef\]](#)
88. Barrett, T. Chemistry and mineralogy of Jurassic bedded chert overlying ophiolites in the North Apennines, Italy. *Chem. Geol.* **1981**, *34*, 289–317. [\[CrossRef\]](#)
89. Marchig, V.; Gundlach, H.; Möller, P.; Schley, F. Some geochemical indicators for discrimination between diagenetic and hydrothermal metalliferous sediments. *Mar. Geol.* **1982**, *50*, 241–256. [\[CrossRef\]](#)
90. Planavsky, N.; Bekker, A.; Rouxel, O.J.; Kamber, B.; Hofmann, A.; Knudsen, A.; Lyons, T.W. Rare Earth Element and Yttrium Compositions of Archean and Paleoproterozoic Fe Formations Revisited: New Perspectives on the Significance and Mechanisms of Deposition. *Geochim. Cosmochim. Acta* **2010**, *74*, 6387–6405. [\[CrossRef\]](#)
91. Bau, M. Scavenging of dissolved yttrium and rare earths by precipitating iron oxyhydroxide: Experimental evidence for Ce oxidation, Y-Ho fractionation, and lanthanide tetrad effect. *Geochim. Cosmochim. Acta* **1999**, *63*, 67–77. [\[CrossRef\]](#)

92. Bau, M.; Dulski, P. Comparing yttrium and rare earths in hydrothermal fluids from the Mid-Atlantic Ridge: Implications for Y and REE behaviour during near-vent mixing and for the Y/Ho ratio of Proterozoic seawater. *Chem. Geol.* **1999**, *155*, 77–90. [[CrossRef](#)]
93. Danielson, A.; Möller, P.; Dulski, P. The europium anomalies in banded iron formations and the thermal history of the oceanic crust. *Chem. Geol.* **1992**, *97*, 89–100. [[CrossRef](#)]
94. Chen, Y.; Fu, S. Variation of Ree Patterns in Early Precambrian Sediments—Theoretical Study And Evidence from the Southern Margin of the North China Craton. *Chin. Sci. Bull.* **1991**, *36*, 1100–1104.
95. Deng, X.-H.; Chen, Y.-J.; Yao, J.-M.; Bagas, L.; Tang, H.-S. Fluorite REE-Y (REY) geochemistry of the ca. 850 Ma Tumen molybdenite–fluorite deposit, eastern Qinling, China: Constraints on ore genesis. *Ore Geol. Rev.* **2014**, *63*, 532–543. [[CrossRef](#)]
96. Frei, R.; Dahl, P.S.; Duke, E.F.; Frei, K.M.; Hansen, T.R.; Frandsson, M.M.; Jensen, L.A. Trace Element and Isotopic Characterization of Neoproterozoic and Paleoproterozoic Iron Formations in the Black Hills (South Dakota, USA): Assessment of Chemical Change during 2.9–1.9 Ga Deposition Bracketing the 2.4–2.2 Ga First Rise of Atmospheric Oxygen. *Precambrian Res.* **2008**, *162*, 441–474. [[CrossRef](#)]
97. Tang, H.-S.; Chen, Y.-J.; Santosh, M.; Zhong, H.; Yang, T. REE geochemistry of carbonates from the Guanmenshan Formation, Liaohe Group, NE Sino-Korean Craton: Implications for seawater compositional change during the Great Oxidation Event. *Precambrian Res.* **2012**, *227*, 316–336. [[CrossRef](#)]
98. Teutsong, T.; Bontognali, T.R.; Ndjigui, P.-D.; Vrijmoed, J.C.; Teagle, D.; Cooper, M.; Vance, D. Petrography and geochemistry of the Mesoarchean Bikoula banded iron formation in the Ntem complex (Congo craton), Southern Cameroon: Implications for its origin. *Ore Geol. Rev.* **2017**, *80*, 267–288. [[CrossRef](#)]
99. Braga, F.C.S.; Rosière, C.A.; Queiroga, G.N.; Rolim, V.K.; Santos, J.O.S.; McNaughton, N.J. The Statherian itabirite-bearing sequence from the Morro Escuro Ridge, Santa Maria de Itabira, Minas Gerais, Brazil. *J. South Am. Earth Sci.* **2015**, *58*, 33–53. [[CrossRef](#)]
100. Sylvestre, G.; Timoleon, N.; Djibril, K.N.G.; Paul, N.J.; Marianne, N.F. Petrology and geochemistry of the banded iron-formations from Ntem complex greenstones belt, Elom area, Southern Cameroon: Implications for the origin and depositional environment. *Geochemistry* **2015**, *75*, 375–387. [[CrossRef](#)]
101. Alibo, D.S.; Nozaki, Y. Rare earth elements in seawater: Particle association, shale-normalization, and Ce oxidation. *Geochim. Cosmochim. Acta* **1999**, *63*, 363–372. [[CrossRef](#)]
102. Beukes, N.J.; Gutzmer, J. Origin and Paleoenvironmental Significance of Major Iron Formations at the Archean–Paleoproterozoic Boundary. In *Reviews in Economic Geology*; Society of Economic Geologists: Littleton, CO, USA, 2008; pp. 5–47.
103. Huston, D.L.; Logan, G.A. Barite, BIFs and bugs: Evidence for the evolution of the Earth’s early hydrosphere. *Earth Planet. Sci. Lett.* **2004**, *220*, 41–55. [[CrossRef](#)]